Quench Study for FAIR Magnets

Quench Studie an FAIR Magneten
Zur Erlangung des akademischen Grades Doktor-Ingenieur (Dr.-Ing.)
genehmigte Dissertation von Piotr Szwangruber, Dipl.-Ing., aus Kwidzyn / Polen
Tag der Einreichung: 20. Juni 2017, Tag der Prüfung: 27. November 2017
Darmstadt 2018 — D 17

1. Gutachten: Prof. Dr. Oliver Boine-Frankenheim TUD
2. Gutachten: Prof. Dr. Rüdiger Schmidt CERN

TECHNISCHE
UNIVERSITÄT
DARMSTADT

Fachbereich 18 - Elektrotechnik
und Informationstechnik
Institut für Theorie
Elektromagnetischer Felder

Quench Study for FAIR Magnets
Quench Studie an FAIR Magneten

Genehmigte Dissertation von Piotr Szwangruber, Dipl.-Ing., aus Kwidzyn / Polen

1. Gutachten: Prof. Dr. Oliver Boine-Frankenheim TUD
2. Gutachten: Prof. Dr. Rüdiger Schmidt CERN

Tag der Einreichung: 20. Juni 2017
Tag der Prüfung: 27. November 2017

Darmstadt 2018 — D 17

URN: urn:nbn:de:tuda-tuprints-72079
URL: http://tuprints.ulb.tu-darmstadt.de/7207

Das Dokument wird bereitgestellt von tuprints,
E-Publishing-Service der TU Darmstadt
http://tuprints.ulb.tu-darmstadt.de
tuprints@ulb.tu-darmstadt.de

Die Veröffentlichung steht unter folgender Creative Commons Lizenz:
Namensnennung – Keine kommerzielle Nutzung – Keine Bearbeitung 4.0
Deutschland
http://creativecommons.org/licenses/by-nc-nd/4.0/

Andrzejowi Jarynowskiemu

Erklärung zur Dissertation

Hiermit versichere ich, die vorliegende Dissertation ohne Hilfe Dritter nur mit den angegebenen Quellen und Hilfsmitteln angefertigt zu haben. Alle Stellen, die aus Quellen entnommen wurden, sind als solche kenntlich gemacht. Diese Arbeit hat in gleicher oder ähnlicher Form noch keiner Prüfungsbehörde vorgelegen.

Darmstadt, den 20. Juni 2017

(Piotr Szwangruber)

Abstract

FAIR – the Facility for Antiproton and Ion Research is a new international accelerator facility which is built in Darmstadt, Germany. The core machines of the project are the superconducting synchrotron SIS100 and the superconducting fragment separator Super–FRS. Design and construction of superconducting machines require a comprehensive study of cases when the superconducting state is lost (quench). This dissertation covers two subjects.

The first subject aims the development of a novel calculation tool (called GSI quench software) dedicated to the quench study of the FAIR magnets. Quench calculations done with the GSI software serve as an input for the proper design of SIS100 and Super–FRS quench detection and energy extraction systems. The software uses the unconditionally stable implicit scheme for the solution of the partial–differential equations that describe the thermal model of the coil. An innovative adaptive time stepping algorithm is used in order to limit the maximum temperature increase of the individual mesh elements to a predefined level. The thermal model of the coil gives the possibility to include the cooling by a liquid helium bath. The electrical circuit topology including the magnet protection system (energy extraction resistors and/or by–pass diodes) is implemented. The properties of the magnet's yoke are taken into account in the inductance function $L_\mathrm{d}(I)$. The implemented electro–thermal model was verified and validated by comparison to quench measurements conducted on SIS100 dipole and Super–FRS dipole prototypes. The testing campaign on the SIS100 dipole prototype (magnet training, quench propagation velocity, hot–spot temperature, MIITs, RRR_Cu, inductance, splice resistance, current leads) was performed in the scope of this work. The quench measurements on the Super–FRS dipole prototype were received from the FAIR China Group. The results of calculations performed with the GSI software are either in good agreement with the measurement data or they represent the worst case scenario, e.g. the calculated hot–spot temperature or quench voltage is higher than measured.

The second subject concerns the design challenges of the SIS100 quench detection system. An outstanding cycling rate of the dipole circuit (4 T/s), high voltage ($U_0/U = 1$ kV/2 kV), radiation hardness required for the equipment to be installed in the accelerator tunnel (≥ 1 MGy) and long signal lines between the magnets and quench detection racks (up to 200 m) implies a customised design of the key components of the system. Selected contributions to the SIS100 quench detection system, concerning the reduction of the parasitic capacitance in the main magnet circuits (by utilising magnetic amplifiers and a new overlapping structure of balance bridges) and the development of a quench detector dedicated to corrector magnets (mutual inductance detector) are presented.

Kurzfassung

FAIR (Facility for Antiproton and Ion Research) ist eine neue Teilchenbeschleunigeranlage, geplant am Standort Darmstadt in Deutschland. Die Kernkomponenten sind der Ringbeschleuniger SIS100 und ein Fragmentseparator Super–FRS, jeweils unter Verwendung von supraleitenden Magneten. Die Planung und Entwicklung solcher Anlagen erfordert die umfassende Betrachtung der Fälle, in denen Komponenten plötzlich vom supraleitenden in den normalleitenden Zustand übergehen (Quench). Diese Dissertation behandelt zwei Themenbereiche dazu.

Erstes Thema ist die Entwicklung einer neuartigen Berechnungssoftware (GSI Quench Software) zur Untersuchung von Quenchen bei FAIR–Magneten. Diese Berechnungen dienen als ein Parameter für die korrekte Auslegung der SIS100 bzw. Super–FRS Quench–Erkennungs– und Energieausleitungssysteme. Die Software nutzt dabei den Ansatz des bedingungslos stabilen, geschlossenen Systems zur Lösung der partiellen Differentialgleichungen, die das thermische Verhalten der Magnetspule beschreiben. Ein innovativer, adaptiver Zeitstufenalgorithmus wird dabei zur Begrenzung des Temperaturanstiegs der einzelnen Gitterzellen auf einen vordefinierten Wert eingesetzt. Das Thermomodell der Spule erlaubt auch den Einsatz einer Kühlung in einem Bad mit flüssigem Helium. Die Struktur der elektrischen Stromkreise einschließlich des Magnetschutz–Systems (Ausleitungswiderstände und/oder Bypass–Dioden) sind ebenfalls implementiert. Die Eigenschaften des Magnetjochs sind mit der Induktivitätsfunktion $L_\mathrm{d}(I)$ berücksichtigt. Das eingesetzte elektrothermische Modell wurde im Vergleich mit realen Quench–Messungen an einem SIS100 Dipol Prototyp bzw. Super–FRS Dipol Prototyp überprüft und bestätigt. Die Testreihe am SIS100 Dipol (Magnettraining, Quench–Ausbreitungsgeschwindigkeit, Hot–Spot Temperatur, MIITs, RRR_Cu, Induktivität, Widerstand elektrischer Verbindungen, Stromzuführungen) wurde im Rahmen dieser Arbeit durchgeführt. Messergebnisse zum Super–FRS Dipol wurden von einer FAIR Gruppe in Lanzhou, China, zur Verfügung gestellt. Die Berechnungen zeigen entweder eine gute Übereinstimmung mit den Messergebnissen oder sie stellen den ungünstigsten Fall dar, z.B. die Hot–Spot Temperatur oder die elektrische Quench–Spannung ist höher als der Messwert.

Der zweite Themenbereich befasst sich mit den Herausforderungen beim Entwurf des SIS100 Quench–Erkennungssystems. Eine außergewöhnliche Arbeitsgeschwindigkeit des Dipol–Magnetkreises (4 T/s), hohe elektrische Spannungswerte ($U_0/U = 1$ kV/2 kV), Strahlenfestigkeit der im Beschleunigertunnel eingesetzten Komponenten (≥ 1 MGy) und lange Signalwege zwischen den Magneten und der Quench–Erkennungselektronik (bis zu 200 m) deuten auf einen maßgeschneiderten Entwurf der Schlüsselbauteile des Systems hin. Ausgewählte Beiträge zum SIS100 Quench–Erkennungssystem bezüglich der Reduzierung parasitärer Kapazitäten in den Haupt–Magnetkreisen (unter Nutzung von magnetischen Verstärkern sowie einer neuen Anschlussstruktur der Quench–Brückenschaltungen) und der Entwicklung eines speziellen Quench–Detektors für Korrekturmagnete (Mutual Inductance Detector) werden vorgestellt.

Contents

1 Introduction

The Facility for Antiproton and Ion Research (FAIR) is a new international accelerator facility which is built in Darmstadt, Germany. The physics research program at FAIR will address a broad variety of topics ranging from fundamental question of the evolution of the universe to the structure of matter [1]. The scheme of the FAIR complex is presented in Fig. 1.1. The linear accelerator UNILAC (11 MeV/u) and the normal conducting synchrotron SIS18 (200 MeV/u for $^{238}U^{28+}$) are existing machines (GSI Helmholtz Centre for Heavy Ion Research) and are currently being upgraded in order to be utilised as pre–accelerators for FAIR. The machines including the beam lines marked in red are new machines which are currently being developed. The P-LINAC is a linear accelerator for protons. The SIS100 (2.7 GeV/u for $^{238}U^{28+}$) and SIS300 (34 GeV/u for $^{238}U^{92+}$) are superconducting synchrotrons that will be situated in a common tunnel on top of each other. Depending on the required beam energy, experiments will be fed with the beam coming from either SIS100 or SIS300. While using SIS300, SIS100 plays the role of a pre–accelerator. The beam can be stored and modified for a variety of experiments in storage rings: the High Energy Storage Ring (HESR), the Recycled Experimental Storage Ring (RESR), the Collector Ring (CR), and the New Experimental Storage Ring (NESR). The Superconducting FRagment Separator (Super–FRS) is a highly complex magnetic spectrometer that will be used for exotic atoms and exotic nuclei studies.

1.1 Motivation

Design and construction of superconducting machines require a comprehensive study of quench cases. Quenching of a superconducting magnet denotes the transition from the superconducting state to the resistive (normal conducting) state. Most of the accelerator magnets are not self–protecting (see Section 2.5) and require a properly designed energy extraction system. In order to define the input parameters for the protection system or to ensure that the magnet design provides self–protection, a detailed quench analysis has to be performed. Quench calculation must take into account the magnet design and the topology of the superconducting circuit. Moreover, quench calculations enable to estimate the maximum time within which a quench shall be detected and validated. Although there exist several quench calculation software solutions [2–14], it was decided to develop a new quench calculation software that will be used for the FAIR magnets. Such approach provides full knowledge concerning the software details, awareness of the program limitations and unlimited access to the source code. The development, verification and validation of this new calculation tool (called GSI quench calculation software) is the primary

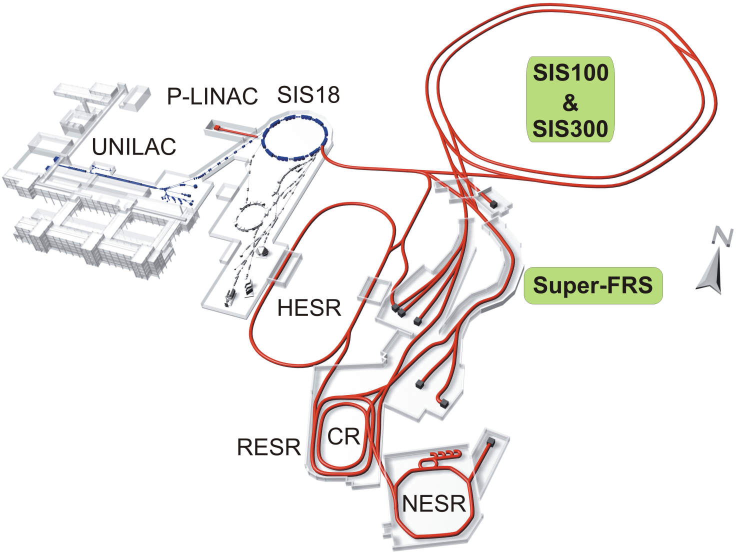

Figure 1.1.: Existing GSI facility and future FAIR facility [1].

objective of this Ph.D. work.

SIS100 is a unique synchrotron (worldwide) with a cycling rate of the dipole magnets up to 4 T/s. Such a high rate generates additional requirements for the quench detection system of the main magnet circuits (high insulation voltage, low parasitic capacitance of the long signal cables). In addition, all the equipment installed in the accelerator tunnel shall be characterised by high radiation hardness (≥ 1 MGy). Analysing quench detection systems used for existing superconducting machines, interesting components, called magnetic amplifiers, were utilised at the HERA[1] synchrotron. Magnetic amplifiers are suitable for high voltage, radiation hard and provide galvanic isolation of the detection circuit (reduction of cabling capacitance). Therefore, the aptitude of magnetic amplifiers for the modern quench detection system of SIS100 shall be investigated which becomes one of the objectives of this Ph.D. work.

The corrector magnets of SIS100 are utilising a special Nuclotron–type cable with individual superconducting wires being insulated from each other. Such a construction is sensitive to symmetrical quenches, e.g. beam induced quenches that cannot be detected by a typical balance bridge detector. The issue can be resolved by utilising so–called mutual inductance detectors (MID). The contribution to the research and

---

[1] HERA – Hadron-Electron-Ring-Anlage at the German Electron Synchrotron research center (DESY), Hamburg, Germany.

development program of SIS100 MID (including validation of a detector prototype) is a part of this dissertation.

The importance level of the quench study can be emphasised by giving the example of an incident during the commissioning of LHC[2] (known as the 2008 incident, see Appendix N). Despite of an excellent work done on the superconducting circuit protection, the 2008 incident caused a severe damage of over 50 superconducting magnets and delayed the start of LHC operation for approximately 14 months – that is a good lesson that is seriously taken into account at FAIR.

1.2 Overview

After the introductory chapter, the required fundamentals are presented. The reader is guided through the phenomenon of superconductivity, superconducting materials, superconducting wires & cables, superconducting magnets and machines. Then a closer look is taken at magnet quenching. Consequences of a quench are discussed and the potential danger for superconducting machines is emphasised. Furthermore, typical ways of magnet protection and quench detection are described.

Next two chapters describe a new quench calculation software (called GSI software). Chapter 3 starts with a simple analysis of a zero–dimensional case (instantaneous quench and $MIIT$s calculation). Further, an implementation of the electro–thermal magnet model is presented. First, the 1D case is described followed by an introduction to the innovative adaptive time stepping algorithm. In the next section, it is shown how the electro–thermal model is expanded to a 3D case. The last section describes the implementation of the cooling model of the coil (case of a liquid helium bath).

In Chapter 4, the GSI quench calculation software is validated by a comparison to measurements conducted on the SIS100 dipole prototype and the Super–FRS dipole prototype.

Chapter 5 presents contributions to the quench detection system of SIS100. The first section aims the main detectors dedicated to dipole and quadrupole circuits. The main topic concerns reduction of the parasitic capacitance introduced by the long signal line. The line can be decoupled (galvanic isolation) by utilising magnetic amplifiers and the parasitic capacitance of cables can be reduced by a new concept of an overlapping structure of balance bridges. Investigation on magnetic amplifiers, including prototype construction and testing is presented. The next section concerns study of the mutual inductance detector (MID) – a quench detector which is planned to survey all corrector magnets of SIS100. Measurements performed on a superconducting corrector magnet model surveyed by a MID prototype are reported.

Finally, Chapter 6 concludes with a summary and outlook.

---

[2] LHC – Large Hadron Collider at the Centre Européen pour la Recherche Nucléaire (CERN), Switzerland.

As a supplement, additional information concerning: superconductivity (Appendices A–C), current leads and their protection (Appendix D), optimal composition for the NbTi alloy (Appendix E), fundamentals on electromagnetism and synchrotrons (Appendix F), parameters of world's largest superconducting machines (Appendix G), *RRR* measurements (Appendix H), existing quench calculation software solutions (Appendix I), magnet inductance (Appendix J), Wiedemann–Franz law and material properties (Appendix K), analytical and numerical solutions for the heat–balance problem (Appendix L), Paschen's law (Appendix M), magnet protection at LHC and the 2008 incident (Appendix N), magnet protection at FAIR (Appendix O), and SIS100–type splice resistance measurements (Appendix P); is attached.

2 Fundamentals

2.1 Superconductivity

Superconductivity was discovered by Heike Kamerlingh Onnes who observed “zero resistance” in pure mercury at the temperature below 4.2 K. Superconductivity occurs in certain materials when they are cooled down below a certain critical temperature T_c (often called the transition temperature). When the material is superconducting, it looses electrical resistivity [15]. The historical steps of superconductivity are presented in Tab. A.1 (Appendix A).

Superconductivity of Type I and Type II

One can distinguish two types of superconducting materials: type I and type II. Both types show a certain critical temperature T_c below which superconductivity reveals. The superconductor of type I is characterised by a certain critical magnetic field B_c below which it remains superconducting. That means if such a superconductor at $T < T_\mathrm{c}$ is immersed into an external magnetic field B_a which is lower than B_c, its superconducting properties are preserved. Moreover, B_a does not penetrate its interior which is called the Meissner effect (see Appendix B).

In contrast with superconductors of type I, superconductors of type II are characterised by two critical fields: a lower B_c1 and an upper B_c2. At temperatures $T < T_\mathrm{c}$ and for $B_\mathrm{a} < B_\mathrm{c1}$, a superconductor of type II is in a superconducting state like a superconductor of type I. When the external magnetic field exceeds B_c1, the superconductor of type II enters a mixed state in which B_a penetrates into the material by formation of flux–tubes (see Fig. 2.1). Each flux tube is surrounded by a super–vortex current and it is carrying a quantum flux (fluxoid) [2]. In the mixed state, a “mixed state Meisner effect” is observed – the magnetic field is expelled out of the superconducting regions. At $B_\mathrm{a} > B_\mathrm{c2}$ the mixed state is destroyed and the material gets normal conducting. More details on type I and type II superconductors can be found in Appendix C.

The critical fields for type I and type II superconductors are shown in Fig. 2.2. For type II superconductors, $H_\mathrm{c} = B_\mathrm{c}/\mu$ (μ states for the magnetic permeability) is the thermodynamic critical field strength and it can be interpreted as the critical field strength that would be characteristic for an equivalent type I superconductor [15].

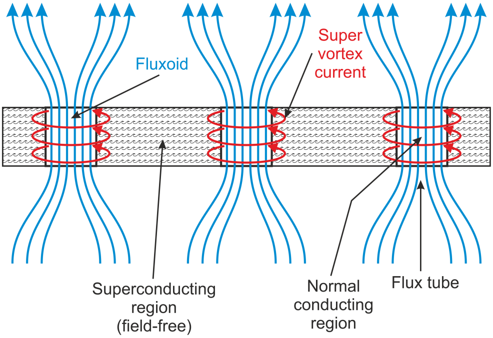

Figure 2.1.: Flux tubes, fluxoids and super-vortex currents in a type II superconductor at $T < T_\mathrm{c}$ and $B_\mathrm{c1} < B_\mathrm{a} < B_\mathrm{c2}$.

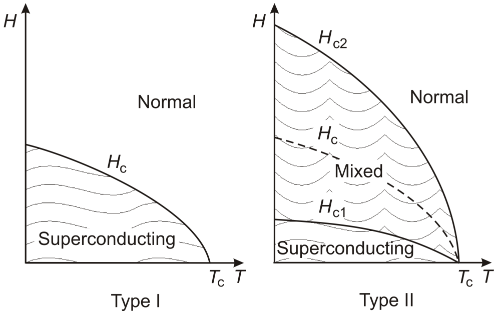

Figure 2.2.: Critical field strength for type I and type II superconductors.

Critical Parameters

In order to hold a conductor in the superconducting state it is required to provide working conditions under which the critical parameters: T_c, B_c2 and critical current density J_c are not exceeded. J_c is defined as a maximum transport current density which does not destroy superconductivity. In Fig. 2.3, the critical parameters form a critical current surface of a LTS type II superconductor [3]. The point “P” represents the working point. When “P” is located below the critical surface, the material is in the superconducting state. Beyond the critical surface the material is in the resistive state (normal conducting). T_c0 is the critical temperature at zero magnetic field and zero transport current. T_cB is the critical temperature at a finite magnetic field B_op and zero transport current. T_cs is the so–called current–sharing temperature. It is

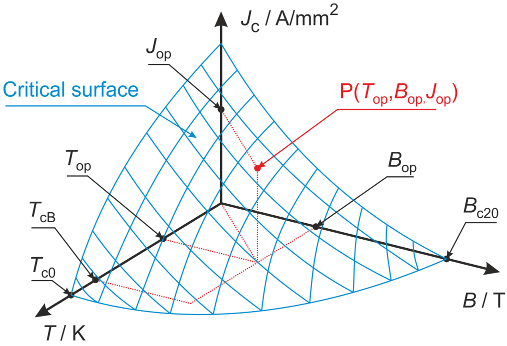

Figure 2.3.: Critical surface of a type II superconductor. T_{op}, B_{op} and J_{op} are: the temperature of the superconductor, the magnetic field inside the superconductor and the current density in the superconductor, respectively.

the actual critical temperature at which the superconductor looses superconducting properties. T_{cs} varies with the magnetic field and the transport current. B_{c20} is the critical magnetic field of type II superconductors defined at zero temperature and zero transport current.

Temperature Margin and Load Line

The temperature margin of a superconductor is defined as $T_{\mathrm{cs}} - T_{\mathrm{op}}$, where T_{cs} is the current–sharing temperature and T_{op} is the operating temperature of the superconductor, (see Fig. 2.4a). The higher $T_{\mathrm{cs}} - T_{\mathrm{op}}$ is, the less probable is the transition to the normal state. The load line shows how the applied current density differs from the critical current density at the working point (see Fig. 2.4b).

Low and High Temperature Superconductors

Superconducting materials with T_{c} lower than 77 K (boiling point of liquid nitrogen) are called low temperature superconductors (LTS) or conventional superconductors. Superconducting materials for which $T_{\mathrm{c}} > 77$ K are called high temperature superconductors (HTS).

Up to now there are only six commercially available superconductors: NbTi, Nb_3Sn, BSCCO-2212, BSCCO-2223, REBCO, and MgB_2 [16]. Critical parameters and the compound type of these and other selected superconductors are given in Tab. 2.1. Almost all type I superconductors have a very small critical magnetic field

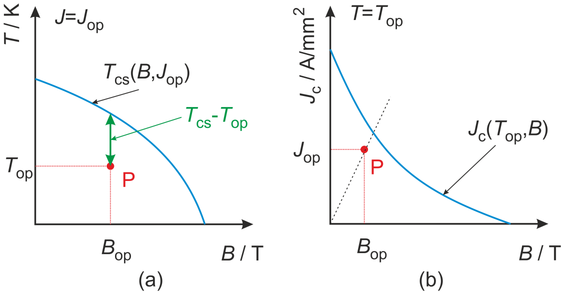

Figure 2.4.: Temperature margin and the load line of a superconducting wire.

B_c below 0.1 T which makes them out of interest for applications in electrical machines like superconducting magnets. In contrast, the upper critical magnetic field of type II superconductors B_{c2} can exceed tens of Teslas while carrying high electrical current. Therefore all superconducting machines are build with the use of type II superconductors.

The superconducting wire industry was born in the 1960s with two LTS superconductors: niobium titanium (NbTi) and niobium tin (Nb_3Sn) [3]. Even nowadays, NbTi is still the most popular material used for the superconducting magnet production. Although NbTi is an alloy, it is too brittle to be fabricated by the conventional wire-drawing method. This problem was solved in the middle of the 1960s by embedding the NbTi filaments in a ductile Cu, CuMn, CuNi or rarely Al matrix (inter–filamentary matrix) and then drawing the multi–filament wire[1] [3, 17]. Figure 2.5 shows NbTi wires with and without an outer shell. The amount of the superconducting material in the naked wire (without insulation) is given by $\alpha = A_{\mathrm{nosc}}/A_{\mathrm{sc}}$, where A_{nosc} and A_{sc} are the total cross–section of the non–superconductor and of the superconductor, respectively. NbTi is typically used for coils of superconducting magnets that generate magnetic fields up to 6.5 T at 4.2 K or up to 9 T when cooled down with super–fluid helium (2 K).

Nb_3Sn has higher T_c and B_{c2} than NbTi. However it is more expensive and its manufacturing process is more complicated. As an inter–metallic compound, Nb_3Sn is very brittle. The most popular Nb_3Sn wire production method is the bronze process in which unreacted Nb and Sn are first wound and then heat treated at a reaction temperature of $\approx 700\ ^\circ\mathrm{C}$.

The most popular HTS conductors are of the REBCO and BSCCO families. REBCO stands for (Rare-Earth)$Ba_2Cu_3O_7$. Typically yttrium is the rare-earth

---

[1] Superconducting wires are often called strands.

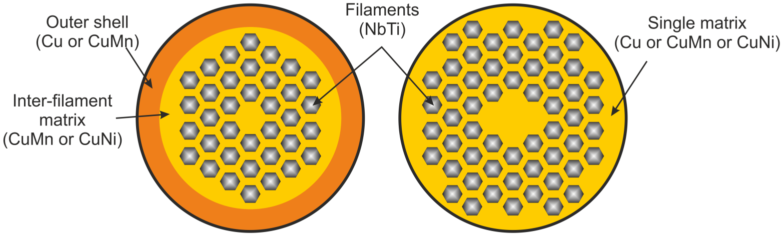

Figure 2.5.: Simple NbTi conductors with and without an outer shell.

Table 2.1.: Critical parameters of selected superconducting materials [15, 16]

Material	T_c (K)	B_c or B_{c2} (T)	Type	Compound
Al	1.2	$9.9 \cdot 10^{-3}$ at 0 K	I	metal
In	3.4	$27.6 \cdot 10^{-3}$ at 0 K	I	metal
Pb	7.2	$80.3 \cdot 10^{-3}$ at 0 K $55.0 \cdot 10^{-3}$ at 4 K	I	metal
Hg α Hg β	4.2 4.0	$41.3 \cdot 10^{-3}$ at 0 K $34.0 \cdot 10^{-3}$ at 0 K	I	metal
Ta	4.5	$83.0 \cdot 10^{-3}$ at 0 K	I	metal
Sn	3.7	$30.6 \cdot 10^{-3}$ at 0 K	I	metal
Nb	9.3	-	II	metal
NbTi	9.2	15 at 4 K	II	alloy
Nb_3Sn	18	20 at 4 K	II	alloy
Nb_3Ge	23	37 at 4 K	II	alloy
MgB_2	39	3.3 - 74*	II	ionic binary compound
YBCO	93	120 $\perp$** 250 $\|\|$**	II	ceramic copper oxide
BSCCO 2212 BSCCO 2223	90 107	~200	II	ceramic copper oxide

* depends on the field direction and the sample geometry (e.g. tape, fiber)
** case of a single crystal; $\perp$ or $||$ to the Cu_2O plane

element and then the corresponding material is called YBCO. YBCO is a ceramics and, thus, it is very brittle. For practical applications YBCO-based multi–layer tapes are produced. Typical tape thickness is around 100 μm where YBCO represents only 1% or less of the total conductor thickness [18].

The most popular superconducting ceramic compounds of the BISCCO family are Bi-2223 ($Bi_2Sr_2Ca_2Cu_3O_{10}$) and Bi-2212 ($Bi_2Sr_2CaCu_2O_8$). Similarly to YBCO, the Bi-2223 conductors can be made in form of multi-layer tapes. For temperatures below 30 K both YBCO and Bi-2223 can hold high current densities in a magnetic field range which is inaccessible for LTS superconductor (e.g. NbTi, Nb_3Sn). However, the cabling of these HTS tapes is still challenging. It seems that Bi-2212 can be manufactured as a round wire with a reasonable current density [19]. The HTS wires/tapes are still significantly more expensive than LTS wires. Nevertheless, the HTS conductors are often used for current leads (see Appendix D), e.g. they are used at LHC and will be used at SIS100.

Magnesium diboride (MgB_2) is a compound known since the early 1950s. However, it was only in 2001 when MgB_2 was discovered to be a superconductor. Due to the fact that both MgB_2 and B are hard materials, MgB_2 conductors have to be prepared using a powder in tube (PIT) method. In the PIT method, a metal tube or a sheath is filled with the precursor powder. Then a wire is drawn out of it and rolled into a tape. The production cost of this simple compound is attractive. Up to now MgB_2 is at the stage to change into a commonly used superconductor [18].

2.2 NbTi–based Wires and Cables

The superconducting magnets of the FAIR machines are constructed with the most popular superconductor which is Niobium Titanium. In order to describe the critical current surface of a particular NbTi wire (see Appendix E for the optimal alloy composition), one can use one of the available empirical fitting functions. The most popular are Lubell's fit and Bottura's fit.

Lubell's Fit for the Critical Surface

In the early 1980s, Lubell [20] proposed fitting functions for $B_{c2}(T)$, $T_c(B)$, and $J_c(B,T)$ of the commercially available NbTi alloys of nominal composition 44–48 weight percent Ti. Equation (2.1) describes the fitting function for B_{c2}. Figure 2.6 shows Lubell's function for B_{c2} that fits the measurement data. Equation (2.2) is derived from Eq. (2.1) and shows the fit for $T_{cB}(B)$. According to Lubell, the best fit is achieved when $T_{c0} = 9.2$ K, $B_{c20} = 14.5$ T and n =1.7 for $B < 10$ T and $B_{c20} = 14.8$ T for $B > 10$ T.

$$B_{c2}(T) = B_{c20} \cdot \left[1 - \left(\frac{T}{T_{c0}}\right)^n\right] \tag{2.1}$$

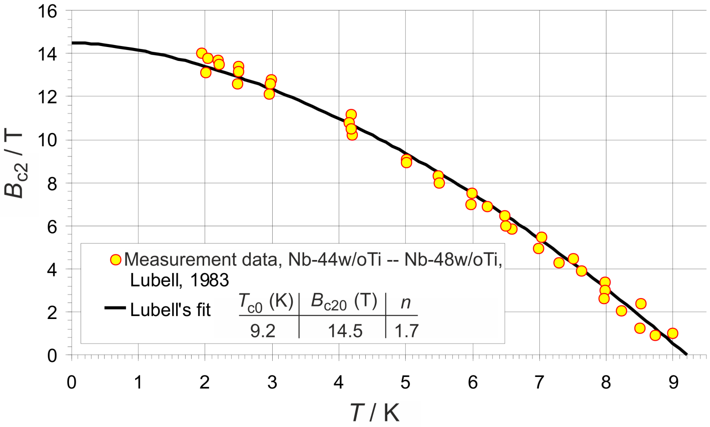

Figure 2.6.: Measured temperature dependence of B_{c2} for NbTi conductors of nominal composition 44–48 weight percent Ti and corresponding Lubell's fit [20].

$$T_{cB}(B) = T_{c0} \cdot \left(1 - \frac{B}{B_{c20}}\right)^{\frac{1}{n}} \tag{2.2}$$

The critical current density fit is given by

$$J_c(B, T) = J_0(B = 0, T) \cdot \left(1 - \frac{B}{B_{c20}}\right) \cdot \left(1 - \frac{T}{T_{cB}(B)}\right), \tag{2.3}$$

where $J_0(B = 0, T)$ can be found for any sample via a single measurement. Figure 2.7 shows the Lubell's fits for selected J_c measurement data. One can see that the Lubell's fit is sufficient only at higher fields. For data provided by Hudson [21] and Boulbout [22] a good fit is obtained for $B > 2$ T and $B > 4$ T, respectively.

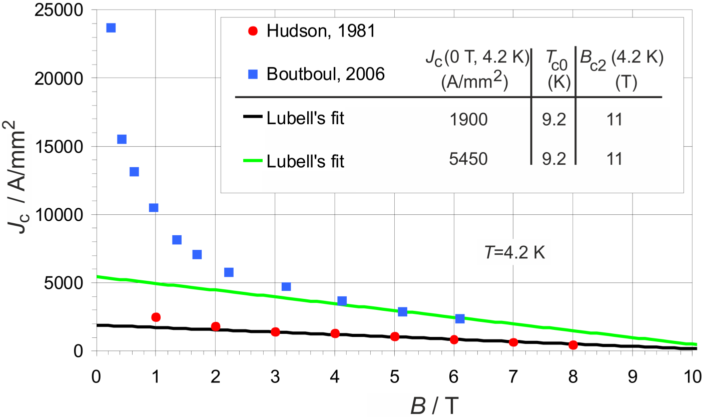

Figure 2.7.: Lubell's fits for selected J_c measurement data [21, 22].

Bottura's Fit for the Critical Surface

In order to take into account the non–linear dependence of J_c on B, Bottura proposed the following formulation for the critical surface [23]:

$$J_c(B,T) = J_{cref}(T_{ref}, B_{ref}) \cdot \frac{C_0}{B} \cdot \left[\frac{B}{B_{c2}(T)}\right]^{\alpha} \cdot \left[1 - \frac{B}{B_{c2}(T)}\right]^{\beta} \cdot \left[1 - \left(\frac{T}{T_{c0}}\right)^{1.7}\right]^{\gamma} \quad , \tag{2.4}$$

where B_{c2} is derived from Eq. (2.1). Bottura's fit parameters are explained in Tab. 2.2. Figure 2.8 shows the Bottura's fits for selected J_c measured data. In both cases the fitting curves show a very good agreement with the measured data.

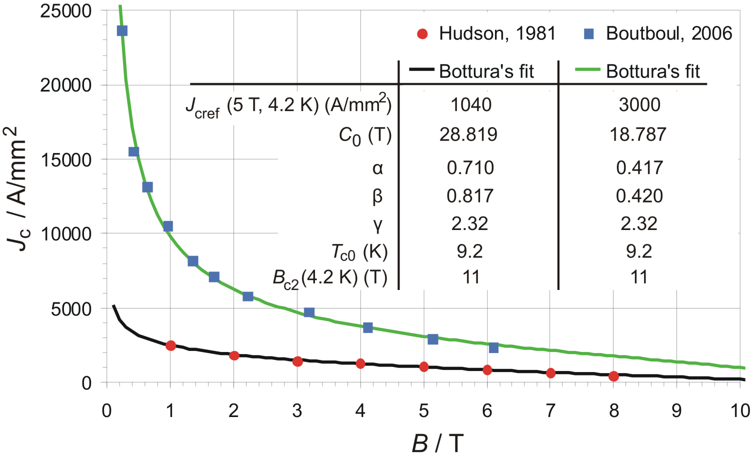

Figure 2.8.: Bottura's fits for selected J_c measured data [21, 22].

Table 2.2.: Bottura's fit parameters

Parameter	Description	Typical range
$J_{cref}(T_{ref}, B_{ref})$	Reference current density in A/mm^2. The value is provided by the manufacturer and typically measured at $T = 4.2$ K and $B = 5$ T.	1000 – 3000
C_0	Normalization constant, in T	> 20
α	Fit parameter (dependence on B)	0.5 – 0.8
β	Fit parameter (dependence on B)	≈ 1
γ	Fit parameter* (dependence on T)	≈ 2

*In most cases the wire manufacturer provides only few values of J_c which are measured at a constant temperature. Thus it is impossible to derive the γ–parameter. For NbTi conductors Bottura proposes $\gamma = 2.32$ [23].

AC Losses in Superconducting Wires

When operating a superconducting wire with alternating currents, AC losses are generated due to the magnetic hysteresis inside the filaments and the inter–filament coupling (induced eddy currents between the filaments). Equations (2.5) describe the AC losses dependency on the filament size (d_f – filament diameter), filament twist pitch t_pf and inter-filamentary matrix resistivity ϱ_IF. The twist pitch of filaments is defined as the axial length in which a filament returns to its original relative position in a superconducting wire. To reduce the hysteresis loss P_h one should reduce the filament size. In order to reduce the coupling between filaments (inter–filamentary coupling loss P_ifc) one should twist the filaments more (make the twist pitch t_pf shorter) and increase the resistance of the inter–filamentary matrix [3].

$$P_\mathrm{h} \propto d_\mathrm{f}, \quad P_\mathrm{ifc} \propto \frac{t_\mathrm{pf}^2}{\varrho_\mathrm{IF}} \tag{2.5}$$

There is a broad spectrum of superconducting wires available on the market. A few wire examples with different geometry and dimensions are depicted in Fig. 2.9 and summarised in Tab. 2.3. d_f and d_s correspond to the diameter of a single filament and a single strand, respectively. ϱ_IF is the resistivity of the inter–filamentary matrix. Figure 2.10 shows 37 sets of J_c data measured for various NbTi wires with weight percent Ti from 44 to 53. The wires differ from each other with d_f, t_pf, d_s and the inter-filamentary matrix material. The wire selection depends on considered application. J_c is higher when:

- the NbTi cross–section is larger (lower α),
- filaments are twisted (shorter t_pf → less AC losses).

The right choice for the filament size and the inter–filamentary matrix material depends on the operation conditions of the wire. For DC machines, one can choose a larger filament size (AC losses due to hysteresis are of low importance) and a soft matrix (low ϱ_IF and high thermal conductivity, e.g. Cu) in order to provide good thermal stability. On the contrary, for AC machines, very small filaments and a hard matrix (higher ϱ_IF, e.g. CuMn, CuNi) are strongly recommended in order to reduce the AC losses. Furthermore, J_c also depends on the mechanical and thermal treatment during the wire production process.

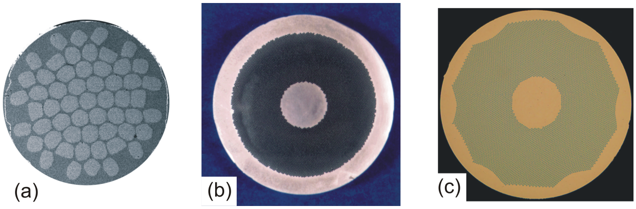

Figure 2.9.: Various designs of NbTi multi–filamentary wires: (a) Super–FRS main dipole prototype: $d_{\mathrm{s}} = 0.63$ mm, $d_{\mathrm{f}} =66$ μm (courtesy of IMP Lanzhou); (b) LHC dipole outer layer: $d_{\mathrm{s}} = 0.825$ mm, $d_{\mathrm{f}} =6$ μm [24]; (c) SIS100 two layer dipole prototype: $d_{\mathrm{s}} = 0.5$ mm, $d_{\mathrm{f}} =4.3$ μm (courtesy of GSI).

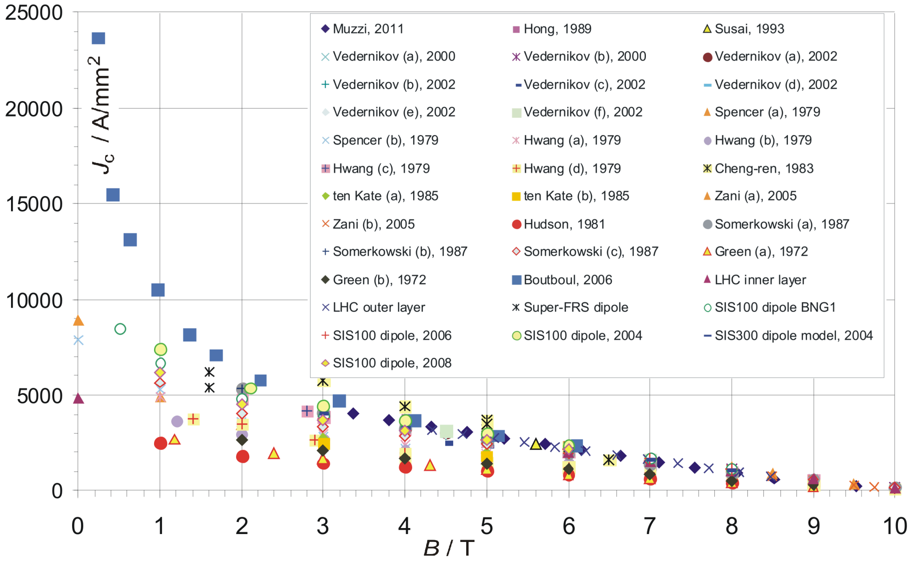

Figure 2.10.: J_c data measured for different wires at T =4.2 K [21, 22, 24–36].

Table 2.3.: Parameters of selected NbTi strands

Used in	d_s (mm)	α	d_f (μm)	Inter-filament matrix	ϱ_{IF} at 4 K (Ωm)	t_{pf} (mm)
Super–FRS dipole prototype (wire core)	0.63	1.3	66	Cu	$1.3{\cdot}10^{-10}$	13
LHC dipole (outer layer)	0.825	1.9	6	Cu	$1.1{\cdot}10^{-10}$	15
SIS100 2 layer dipole	0.5	1.46	4.3	Cu	$1.0{\cdot}10^{-10}$	4
SIS100 1 layer dipole	0.8	1.4	2.9	Cu-0.5 w/oMn	$1.8{\cdot}10^{-8}$	6.5
"R"-strand (Alstom) [37]	0.178	4.81	0.192	Cu-30 w/oNi	$3.415{\cdot}10^{-7}$	1.8

Superconducting Cables

In the construction of a superconducting machine, the required operating current is typically much higher than the critical current of a single superconducting wire. In order to increase the current, the superconducting wires are connected in parallel and form a cable. When powering the cables with alternating currents, AC losses are generated due to the inter–wire coupling by induced eddy currents between the wires. In order to reduce the AC losses, the wires shall be twisted or braided with respect to each other. There are various types of cables. Among them, the most popular are the Rutherford–type cable, the Nuclotron–type cable and cable–in–conduct (CIC). The Rutherford cable consists of two layers of braided superconducting strands which stick to each other in such a way that the liquid He is able to flow between them and cool them down. Usually, the cable is insulated with polyimide tape. Figure 2.11a shows the Rutherford cable used in LHC (outer layer in dipoles, quadrupoles and bus–bars). Another type of cable was developed for the Nuclotron accelerator at JINR[2], see Fig. 2.11b. In this cable, the superconducting strands are placed around a CuNi tube in which the liquid He flows and cools down the wires. In case of CIC, a bundle of strands is cabled together and

---

[2] JINR – Joint Institute for Nuclear Research, Russia.

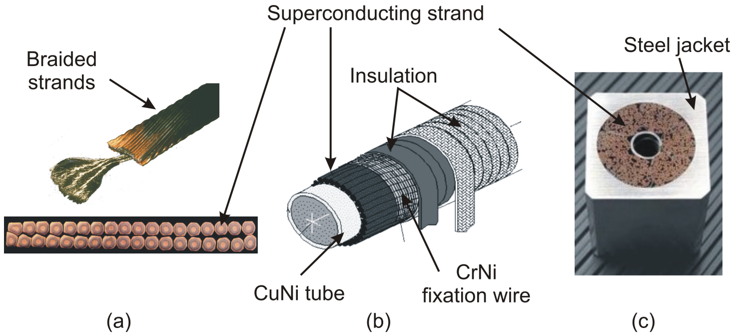

Figure 2.11.: Various types of superconducting cables: (a) Rutherford cable [19, 38], (b) Nuclotron–type cable [39], (c) cable–in–conduct (courtesy of University of Twente).

suited in a structural steel jacket. The liquid He flows inside the jacket and cools down the strands. Figure 2.11c shows CIC of the ITER[3] central solenoid magnet.

2.3 Magnets, Particle Accelerators and Fragment Separators (Superconducting)

A superconducting magnet is an electromagnet in which the coils are wound from a superconducting cable instead of a classical copper cable. The superconducting coil has to be operated at cryogenic condition which means cooling with liquid helium for LTS coils and with liquid helium or nitrogen for HTS coils. The use of a superconducting coil increases the operating current density from a few A/mm^2 for a classical (normal conducting) coil to a few kA/mm^2. Thus, for the same number of Ampere–turns, a superconducting coil will have much smaller size than an equivalent normal conducting coil. Furthermore, the operation cost of superconducting magnets is significantly lower than of normal conducting magnets due to the vanishing DC resistance of the coil. Stand–alone superconducting magnets are used for MRI[4] magnets and scientific equipment, e.g. small mass spectrometers. Larger superconducting magnet installations are used in research facilities, e.g. particle accelerators, fragment separators, etc. In case of superconducting magnet installations, typically large effort is spent to provide the operating condition by

---

[3] ITER – International Thermonuclear Experimental Reactor, a fusion reactor constructed in the south of France.

[4] Magnetic Resonance Imaging (MRI) – medical imaging technique used in radiology to visualise in detail the internal structure of the object (definition from WIKIPEDIA).

utilising cryogenic facilities. At the temperature of 4 K, one Watt of heat loss calls for approximately 300 W of cooling power [3].

There are two major types of superconducting magnets:

- coil dominated magnets for high magnetic field applications and
- super–ferric (yoke dominated) magnets for fields up to 2–2.5 T and quadrupole gradients up to 20 T/m, at which the natural limit for the magnetic yoke (iron) is reached [40].

Coil Dominated Magnets: cosϑ–type

In superconducting machines that operate at high fields ($B > 2$ T), coil–dominated cosϑ–approximation magnets are used. In these magnets, the shape of the magnetic field is determined by the conductor arrangement. Thus, in order to achieve sufficient field precision (a typical requirement for accelerator magnets is 10^{-4}), the magnet coil is built with an extreme accuracy. In the ideal case, the current distribution in the coil cross–section follows the cosine function of the azimuthal angle ϑ. In order to get as close as possible to the ideal conductor distribution, the cross–section of the coil is shaped by discrete blocks of superconducting cable assembled in one or two layers as shown in Fig. 2.12a. For quadrupole and sextupole magnets, the current distribution follows $\cos(2\vartheta)$ and $\cos(3\vartheta)$, respectively [40]. In cosϑ magnets, the yoke provides only the return path for the magnetic field.

Super–ferric Magnets: H–type and Window–Frame

Super–ferric magnets are iron dominated magnets where the field shape is determined by the magnetic yoke. For most of the designs, the coil and the iron yoke are situated in a common helium bath. However, there are magnets where only the coil is immersed into the helium bath and the magnetic yoke remains warm (at ambient temperature), e.g. the Super–FRS dipole magnet has such a construction. Figures 2.12b and 2.12c show super–ferric H–type and window–frame magnets, respectively. In H–type magnets, the coil has a racetrack shape and the yoke has distinctive magnetic poles. In contrary, in window–frame magnets, the magnetic yoke cross–section is simply rectangular and the magnetic poles are further apart (the superconducting coil is embedded into the inner part of the yoke in the way shown in Fig. 2.12c).

As reported in [42], a window–frame configuration could be used for coil dominated high field (14–16 T) dipole magnets. Reaching such a high field becomes

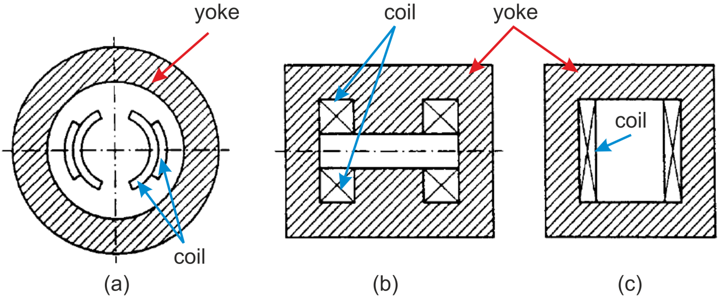

Figure 2.12.: Superconducting dipole magnet configurations [41]: (a) coil–dominated cosϑ–type, (b) super–ferric H–type and (c) super–ferric window–frame.

feasible when applying high field superconductors (such as Nb_3Sn – see Section 2.1). Unfortunately, these high field superconducting materials are brittle and mechanically less stable than NbTi and therefore the coil manufacturing process becomes challenging. Nevertheless, the coil geometry of a window–frame magnet is much simpler than in a cosϑ magnet and a construction with the use of Nb_3Sn is achievable.

Superconducting Magnets at FAIR

In the SIS100 accelerator, the nominal magnetic field of a dipole is only 1.9 T. Although this field can be achieved by normal–conducting magnets, it was decided to use super-ferric window–frame magnets. Since both SIS100 and SIS300 require an ultra-high vacuum (UHV) in the beam pipe, a cryogenic infrastructure is required in any case (the vacuum chamber has to be cooled down to $\approx 10 - 15$ K). The use of cosϑ magnets was the only reasonable choice for SIS300 where the required dipole field is 4.5 T.

The Super–FRS machine mainly operates at a DC mode. Thus applying superconducting magnets significantly reduces the cost of operation. The Super–FRS magnets have very large apertures. In order to avoid collisions of the large beam pipe with the coil ends at the magnet extremities and also to simplify the coil geometry, a H–type magnet construction was chosen.

Superconducting Particle Accelerators and Fragment Separators

Typically, particle accelerators utilise an electric field to accelerate the beam and an magnetic field for beam guiding (see Appendix F). The dipole and quadrupole magnets are used to bend and focus the beam, respectively. The particles can be accelerated either along a linear path (case of linear accelerators) or along a circular path (case of cyclotrons and synchrotrons). In linear accelerators, the beam is accelerated only once along its path. In a cyclotron, the bending magnetic field is constant and the ions travel along a spiral path outward from the centre while in a synchrotron, the radius is fixed and the bending and focusing magnetic fields vary with time according to the increasing kinetic energy of the particles. Since in circular accelerators the beam passes through the accelerating unit(s) many times, they are featured with a higher energy compared to linear accelerators. In circular accelerators at very high particle velocities in order to hold the beam within the designed orbit/spiral, one has to either increase the radius (increase the machine size) or (and) increase the magnetic field by using stronger magnets. For both synchrotrons and cyclotrons the energy limit that comes from the maximal magnetic field is identical. However, when considering the machine size, a synchrotron forms a ring which can have a diameter of few kilometres (e.g. 8.5 km for LHC) while a cyclotron forms a circular area limited to a diameter of tens of metres[5]. Therefore synchrotrons are able to hold the beam at energies not accessible for cyclotrons and the most powerful particle accelerators in the world indeed have a synchrotron construction.

Fragment Separators are large aperture magnet systems that work as mass spectrometers where only the magnetic field is used in order to deflect and focus the particles, and to select the desired ions.

The world's largest synchrotrons, fragment separators and their main parameters are listed in Appendix G.

---

[5] The largest cyclotron in the world has a diameter of 18 m and was built at TRIUMF (Canada's national laboratory for particle and nuclear physics and accelerator–based science) located in Vancouver, British Columbia, Canada [43].

In order to successfully operate a superconducting magnet, it is required to provide such operating conditions at which the superconducting state is enabled. The operating point of the superconductor must be kept below the critical current surface (see Fig. 2.3, Section 2.1). When the operating point crosses the critical current surface, the superconductor becomes resistive. The transition from the superconducting state to the resistive state is called quench. Most of the time, a quench occurs because of a temperature increase due to the conductor movement (friction), eddy currents in the conductor, poor cooling or beam losses (in particle accelerators and fragment separators).

In order to understand the development of the resistive zone (conductor quenching), first let us have a closer look at the resistivity of primary materials used for superconducting wires, that are copper and niobium-titanium. The resistivity of Cu (ϱ_{Cu}) decreases with temperature. When the temperature approaches absolute zero, ϱ_{Cu} does not vanish. It settles at a constant value called residual resistivity ϱ_0 which depends on the impurity level. The ratio of the resistivity at 300 K to the resistivity at 4 K (at zero applied magnetic field) is called the residual resistivity ratio (RRR). RRR of Cu used for superconducting wires is typically of 70–200. Figure 2.13a shows the influence of RRR on ϱ_{Cu}. The purer the copper is (higher RRR), the lower ϱ_0 it has. ϱ_{Cu} is sensitive to the applied magnetic field (magnetoresistance effect) what is shown in Fig. 2.13b [15, 44]. See Appendix H for a RRR measurement technique.

For a typical NbTi/Cu wire in the superconducting state, the current is carried by NbTi filaments. However, when a quench occurs, the resistivity of NbTi (ϱ_{NbTi}) jumps from 0 to $6{\cdot}10^{-7}$ Ωm which is three orders of magnitude higher than the resistivity of the Cu matrix (ϱ_{Cu}). Therefore the current moves from the NbTi filaments to the Cu matrix. When the temperature further rises, ϱ_{Cu} increases more rapidly than ϱ_{NbTi} and a small portion (1–2%) of the current comes back to the NbTi filaments. The resistivity of NbTi in comparison to Cu is presented in Fig. 2.14a. Figure 2.14b shows the current sharing dependence on temperature for a wire with Cu to NbTi ratio α equal to one.

Quench Propagation

In a superconducting wire, a quench starts within a certain conductor length. This corresponds to an initial normal zone within which heat is generated due to the Joule effect. If the generated heat power is larger than the conduction power, the normal zone expands and contrariwise for generated power lower than the

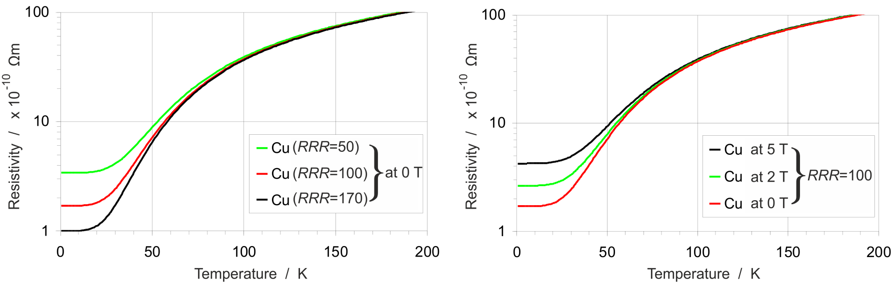

(a)

(b)

Figure 2.13.: Influence of RRR (a) and of the applied magnetic field (b) on the resistivity of Cu [45].

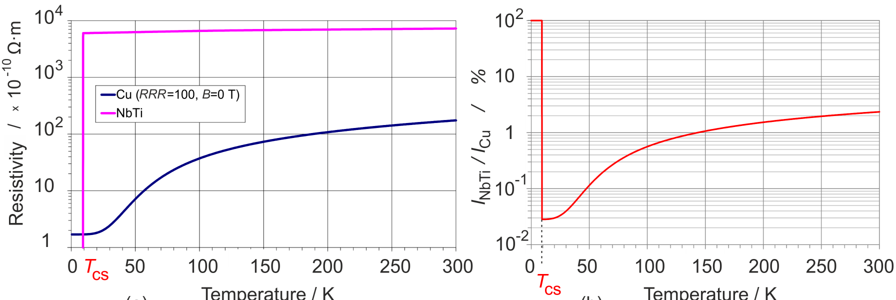

(a)

(b)

Figure 2.14.: (a) Resistivity of NbTi and Cu ($RRR = 100$, $B = 0$ T) [24,37]. (b) Current sharing in NbTi/Cu wire ($\alpha = 1$).

conduction power, the normal zone shrinks and finally disappears. The shrinking of the the normal zone is called quench recovery. For the case when the generated heat power equals the conduction power, the initial normal zone is called the minimum propagation zone[6] (MPZ). The corresponding energy is called the minimal quench energy (MQE). Figure 2.15 shows a quench propagation in a simple conductor (1D case) which is immersed into a helium bath characterised by a temperature T_{He}. $T(t_1)$ and $T(t_2)$ represent temperature profiles at time moments t_1 and t_2 ($t_2 > t_1$), respectively. A normal front is defined as a location on the normal zone edge at which the temperature is equal to T_{cs} (current sharing temperature). The quench propagation velocity v_{fp} is the velocity of the normal front propagation.

---

[6] For a 1D case, one uses the expression: minimum propagation length.

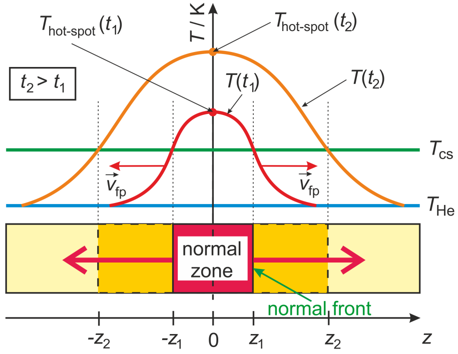

Figure 2.15.: Normal zone expansion and the temperature profiles during a quench (1D model).

The hot–spot is located at the quench origin and it is featured by a temperature $T_{\text{hot-spot}}$.

A one–dimensional representation of the quench behaviour is a good approximation when the quench is confined within a single conductor. This is the case of a Nuclotron–type magnet where each turn in the coil is well insulated from the other with a thick insulating layer[7]. Thus, a large disproportion between the quench propagation in the longitudinal and transverse direction exists. In the longitudinal direction (along the conductor), due to the high thermal conductivity, the normal zone expands very rapidly. In the transverse direction, the normal zone expansion takes a much longer time due to the insulation barrier with low thermal conductivity. For example, in the SIS100 dipole magnet the normal zone will expand to the adjacent cable via the longer longitudinal path than through the shorter transverse path due to the thickness of the insulation between the adjacent superconducting cables, see Fig. 2.16.

---

[7] Usually a glass–reinforced plastic known as either GRP (English) or GFK (German) is used as insulation.

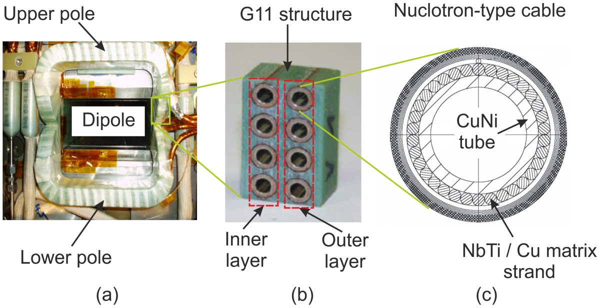

Figure 2.16.: SIS100 two–layer straight dipole prototype magnet: (a) coil, (b) coil cross–section, (c) Nuclotron–type cable.

In contrast with Nuclotron–type magnets, for magnet coils with relatively thin turn–to–turn insulation, a one–dimensional representation is insufficient. A good example of such a case is a potted coil magnet. A potted coil is a multilayer coil (usually with a large cross–section) in which the insulation is reinforced by impregnation with epoxy resin and then multi–step baking. In order to model the quench behaviour in a potted coil, a three–dimensional representation is required since the quench propagates in longitudinal and transverse direction, see Fig. 2.17.

Magnet Training

When constructing coils for superconducting magnets, it was discovered that the quenching current – a current at which a natural quench occurs, is lower than it might have been expected from the measurements done on short wire/cable samples. This phenomenon is called coil degradation and it is caused by the mechanical and thermal stress applied to the superconducting cable during the production of the coil. Besides, when the coil is powered, its turns tend to slightly move due to the Lorentz force. The latter creates friction between the cable and the coil fixation structure which may induce a quench. For a magnet which is powered for the first time, it is very likely that a quench occurs at a current which is lower than the nominal current I_{n}. After a few quenches, the coil becomes more stable mechanically and in most of the cases, at the next powering session, a quench occurs at a higher current. The procedure of consecutive powering of the magnet in order to reach a quenching current above the nominal and to mechanically stabilize the coil, is called magnet training [3].

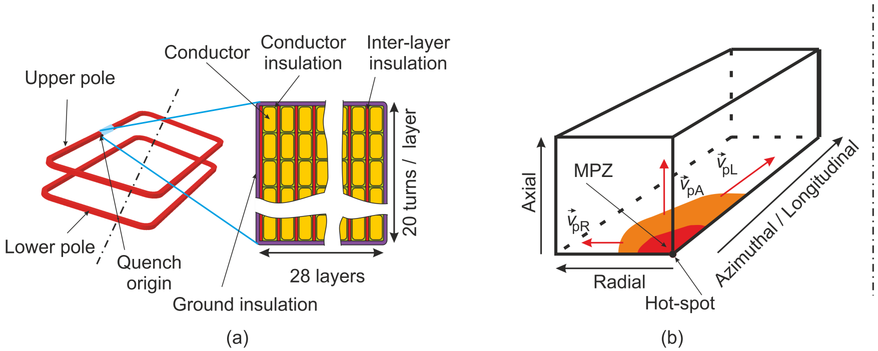

Figure 2.17.: Potted coil of the Super–FRS dipole: (a) 3D model of the dipole coil (upper and lower pole) and its cross–section, (b) normal zone expansion.

The maximum quenching current that was reached in the superconducting magnet during its training, can be compared to the short sample limit (SSL) defined by the cross of the magnet's load line and the $J_c - B$ characteristics of the used superconducting wire as shown in Fig. 2.18a (example of the SIS100 dipole prototype). The $J_c - B$ characteristics (Fig. 2.18b) is obtained by applying the Bottura's fit to the measurement data of wire samples delivered by the wire manufacturer. The fit is constructed in order to obtain the minimum J_c. The training curve of the SIS100 dipole prototype[8] is shown in Fig. 2.19. For this magnet, the quenching current has already exceeded the nominal current ($I_n = 13.1$ kA) at the second powering. During the consecutive powering, the maximum current before the quench has increased from initial 12.4 to 15.7 kA. The runs "1", "2" and "3" correspond to the successive thermal cycles[9]. The magnet reached 88% of the estimated short sample limit (17.8 kA) what indicates a very stable mechanical construction. If a magnet reveals a bad training curve, the quench performance might be improved by subjecting the magnet for the next thermal cycle in order to increase the mechanical stability by locking the coil stronger into its position in the magnetic yoke.

---

[8] Fitting the measurement data of the SIS100 main cable with the Bottura's formula and conducting the training campaign of the dipole prototype belong to coarse of this Ph.D. work.

[9] In terms of superconducting magnet testing, a thermal cycle corresponds to magnet cooling from the ambient temperature to its operating temperature and warming it up again to the ambient temperature.

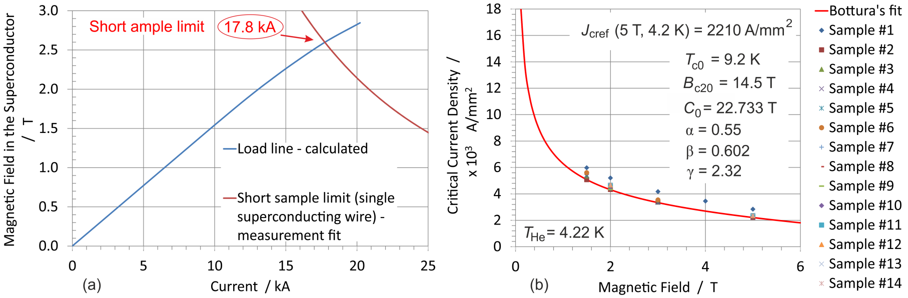

Figure 2.18.: SIS100 dipole magnet prototype: (a) load line and short sample limit, (b) Bottura's fit for the used superconducting wire.

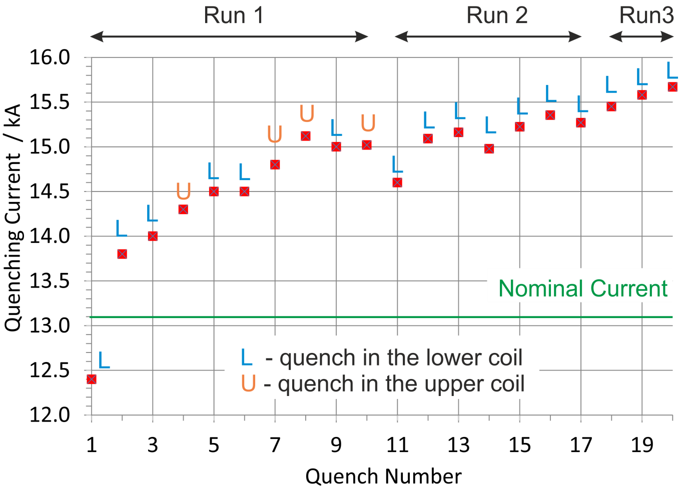

Figure 2.19.: Training curve of the SIS100 dipole magnet prototype.

A quench in a superconducting magnet results in development of a resistive voltage, temperature increase due to Joule heating and pressure build–up in the helium vessel or cooling channels. For a stand–alone magnet in a helium bath (see Fig. 2.20a), once a current i is injected into the coil, it circulates there for a very long time (the time constant of the current decay is in the range of years). If a quench occurs (see Fig. 2.20b), a normal zone featured with a quench resistance R_{q} develops. The current in the quenched magnet starts to decrease according to

$$L(i) \cdot \frac{di(t)}{dt} + R_{\mathrm{q}}(t) \cdot i(t) = 0, \tag{2.6}$$

where L is the magnet inductance.

Figure 2.20c shows the current decay i, the temperature at the hot–spot $T_{\text{hot-spot}}$ and the developing quench voltage V_{q} defined by $i \cdot R_{\mathrm{q}}$. In case the hot–spot temperature and the voltage induced by the quench do not damage the insulation and the pressure build–up stays within the design level, such a magnet will be autonomously discharged, and all the stored energy will be dissipated within the coil.

In case of an AC operation, the magnet is connected to a power supply via current leads (CL) as shown in Fig. 2.21. A current lead is a conductor which communicate the electric power from the power supply circuit (situated at ambient temperature) to the magnet which is operated at cryogenic conditions (4 K). The simplest current lead is a conduction cooled piece of copper. During a normal operation, the switch S1 is opened and the switch S2 is closed. In case of a quench, S1 is closed and S2 is opened. The current decays due to the developing quench resistance R_{q} according to Eq. (2.6). Since during a quench the magnet is simply short–circuited, the total magnet energy is dissipated within the coil. In order to trigger the switches S1 and S2, a quench detection system (see Section 2.6) is required.

A magnet is called self–protecting if dissipating all its magnetic energy within the coil does not cause damage to the coil and its insulation. Most of the magnet designers consider 300 K (sometimes 350 K) as the maximum temperature at the hot–spot (T_{max}) which do not cause destructive effects [24].

In contrast, a not self–protecting magnet powered as in Fig. 2.21 will be damaged in case of quench due to the too high temperature. In order to reduce the temperature, the current decay needs to be accelerated. The most common protection scheme which speeds up the current decay considers an energy extraction

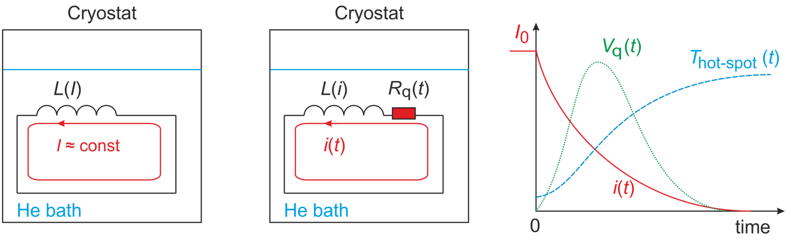

(a) (b) (c)

Figure 2.20.: Quench behaviour in a short-circuited magnet: (a) normal operation, (b) quench case, (c) current decay (i), development of quench voltage (V_q) and temperature rise at the hot–spot ($T_\text{hot-spot}$).

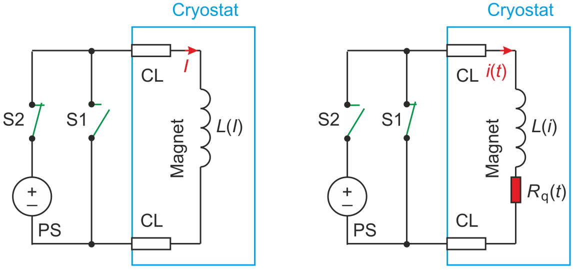

(a) (b)

Figure 2.21.: A self–protecting magnet with its current leads and the power supply: (a) normal operation, (b) quench case; PS – power supply, S1, S2 – switches, CL – current lead.

resistor[10] R_d, located at ambient temperature. Then, in case of a quench, R_d is activated and the power supply is cut off as shown in Fig. 2.22. When a quench is detected (see Section 2.6), switch S1 is closed, switch S2 is opened and the current is dumped due to the developing R_q and activated R_d as described in Eq. (2.7).

$$L(i) \cdot \frac{di(t)}{dt} + (R_\mathrm{q}(t) + R_\mathrm{d}) \cdot i(t) = 0 \tag{2.7}$$

---

[10] The energy extraction resistor is often called the dump resistor.

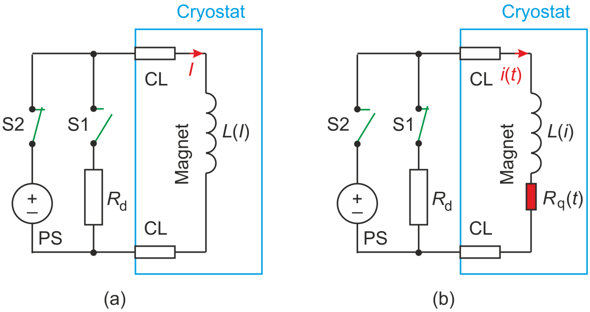

Figure 2.22.: A not self–protecting magnet protected with a dump resistor; (a) normal operation, (b) quench case: dump resistor (R_d) activation and power supply cut off; PS – power supply, S1, S2 – switches, CL – current lead.

A significant part of the energy initially stored in the magnet is extracted and dissipated in R_d at ambient temperature – as mentioned in Section 2.3, in a 4 K cryo–system, dissipation of one Watt at cold calls for 300 W of refrigerating power. Therefore it is very desirable to reduce the amount of the energy dissipated within the coil. Furthermore, the overall temperature reduction, especially reduction at the hot-spot results in a smaller pressure build–up in the helium channels/vessel.

Magnet Protection Schemes

A protection scheme that only includes an energy extraction resistor (or resistors) can be insufficient for some magnet designs or magnet circuits, for example when:

- the quench propagation velocity is very slow which results in a very high temperature rise at the hot–spot and extremely non–uniform temperature distribution along the conductor or within the coil cross–section;
- the use of a high dump resistance generates a too high voltage which can break the electrical insulation;
- the protected circuit consists of many magnets connected in series and therefore stores a huge magnetic energy; in this case, a quench in a single magnet results in an enormous energy dissipation within the quenched coil.

Energy Extraction Resistor

Let us consider a magnet or a magnet string[11] characterised by the inductance L and protected with an energy extraction resistor R_d as illustrated in Fig. 2.23. When R_d is activated, the voltage across the magnet is initially equal to $|I_0 \cdot R_\mathrm{d}|$ and later it decreases to zero following the current. $|I_0 \cdot R_\mathrm{d}|$ is limited by the design of the extraction system and by the circuit insulation. Therefore the designed insulation level determines the maximum value of R_d. On the other hand, R_d has a direct influence on the current decay constant τ. The shorter the current decay is, the less energy is dissipated within the coil and the lower is the hot–spot temperature. Assuming that $R_\mathrm{d} \gg R_\mathrm{q}$, τ can be estimated as L/R_d. In order to accelerate the current decay, one shall use as high R_d as possible.

Switches for the Quench Protection System

In order to activate the quench protection system, a number of reliable power switches is required. One could use:

- mechanical switches – there are variants that provide opening functionality, closing functionality or both (switching time could be from 40 to 300 ms);
- semiconductor switches – power thyristors or IGBT transistors (switching time < 1 ms).

The quench protection system at the prototype test facility (PTF) at GSI (see Fig. 2.24a) uses an energy extraction resistor which can be activated via a thyristor switch. The power converter can be disconnected by a DC circuit breaker which is realised as multiple parallel branches of IGBT transistors and fuses (see Fig. 2.24b). In each branch IGBT is connected in series with a fuse. When a quench is detected, a trigger is sent to the power converter control unit. Then, the power thyristor is activated (via an adequate driver) and all the IGBT transistors are opened simultaneously, disconnecting the power converter from the magnet circuit. The magnet energy is discharged and its major part is dissipated within the dump resistor. If there is a malfunction of one or more IGBT switch(es) within the circuit breaker, all the current will be conducted through the branch(es) with the corrupted transistor(s). Since a single branch (or even a few branches) is not designed to conduct the full magnet current, the fuse (or fuses) will burn out in a short time and finally the power supply will be disconnected anyway.

---

[11] Magnet string – many magnets connected in series forming a common electrical circuit.

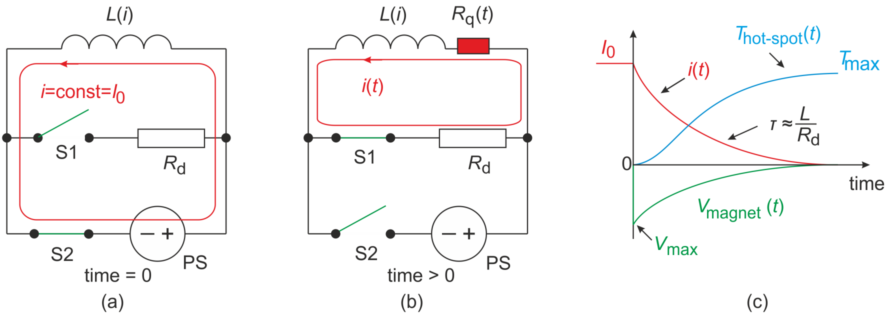

Figure 2.23.: Quench in a magnet protected with a dump resistor: (a) normal operation, (b) after activation of the protection circuit, (c) current decay, magnet voltage and temperature rise; PS – power supply, S1, S2 – switches.

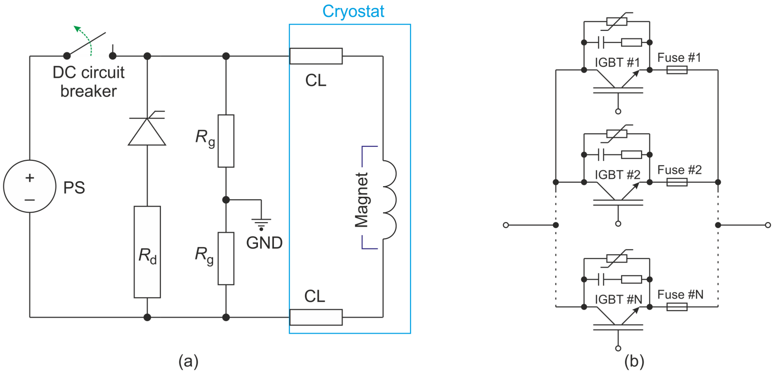

Figure 2.24.: Magnet protection at the facility at GSI: (a) electrical circuit, (b) DC circuit breaker; PS – power supply, R_g – grounding resistor, R_d – dump resistor, CL – current lead, GND – system grounding point.

Two other examples of quench protection schemes are presented in Fig. 2.25. Figure 2.25a shows a protection scheme with a bipolar crowbar and a mechanical opening switch. Such a scheme was initially proposed by CERN for testing of the Super–FRS dipole and quadrupole magnets [46]. Figure 2.25b shows a protection concept used for the GLAD magnet of the R3B experiment [47] and proposed for

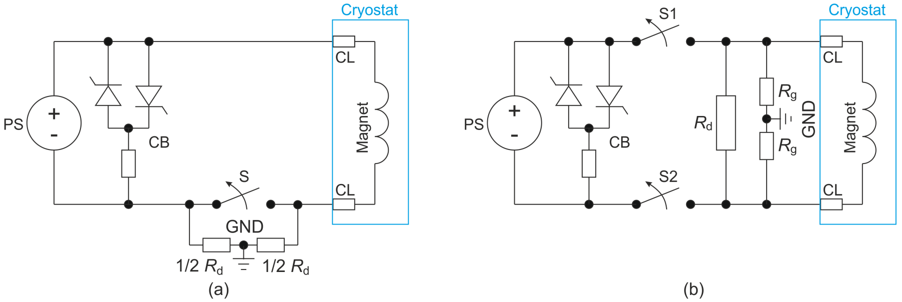

Figure 2.25.: A protection circuit with a mechanical switch (hot opening) and crowbar (a); circuit proposed for the CBM magnet with “always on” dump resistor and two mechanical switches (b); PS – power supply, CB – crowbar, R_g – grounding resistor, R_d – dump resistor, CL – current lead, S/S1/S2 – switches, GND – system grounding point.

the CBM[12] dipole magnet [48]. This scheme is characterised by an “always on” dump resistor and two mechanical circuit breakers. The protection scheme with “always on” R_d is recommended only when R_d is much higher than the resistance of the magnet circuit (magnet coil + current leads + warm cables of PS) and for magnets operated in a DC mode.

Grounding of the Power Supply

In order to reduce the high voltage that occurs when activating the energy extraction resistor, one can fix the grounding point[13] of the magnet circuit at the optimal location. The most common grounding schemes are shown in Fig. 2.26. The scheme (a) is used for low voltage systems. Then the ground is located at an extremity of the power supply (Fig. 2.26a) and the maximum voltage which is seen at the magnet extremity is $V_A = -R_d \cdot I_n$. In contrast, in the scheme presented in Fig. 2.26b, the ground is fixed in the middle of the power supply by two grounding resistors R_g (tens or hundreds of kΩ each). In this case, the maximum voltage at the magnet extremity equals $\pm 0.5 \cdot R_d \cdot I_n$. For a string of magnets, the grounding scheme could be equipped with emergency grounding switches that will be activated during energy extraction. See [49] for more explanation concerning grounding concepts in superconducting machines.

---

[12] CBM – Compressed Baryonic Matter Experiment at FAIR.

[13] The grounding point means here the global ground = protective earth (PE).

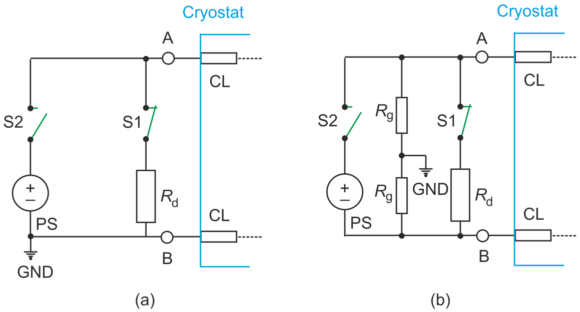

Figure 2.26.: Typical grounding schemes: (a) GND fixed at a one extremity of PS, (b) GND fixed in the middle of PS; PS – power supply, GND – ground, R_g – grounding resistors, S1/S2 – switches.

Quench Back

Despite the high voltage which arises when using a large dump resistor, the fast current dump is also characterised by a high current rate di/dt which may provoke quenches in other sections of the coil that were not quenched by the expansion of the initial resistive zone. This effect is called quench back and it increases the overall quench resistance R_q. The resistive zones that can occur because of a quench back effect are distributed over the whole circuit which, first of all, reduces the hot–spot temperature and makes the temperature distribution more flat. Furthermore, it reduces the stress on the electrical insulation by decentralising the quench voltage within the circuit.

Quench Heaters

In magnets that are characterised by a low quench propagation velocity, a quench back can be provoked by special quench heaters[14] installed directly at the magnet coils [3]. Those quench heaters are usually constructed as resistive strips, glued to the outer surface of the coil to provide a good thermal contact. For example, a scheme of the LHC dipole quench heaters is shown in Fig. 2.27. When a quench is detected, the quench heaters are fired, creating normal zones in the coil parts that are located close to the heaters. The expansion of these normal zones increases the overall quench resistance and therefore speeds up the current decay.

---

[14] often called quench back heaters

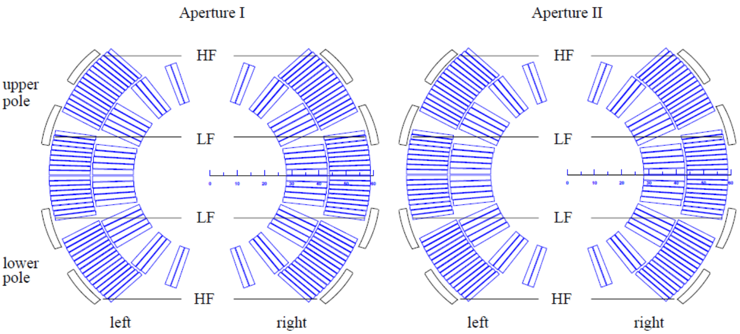

Figure 2.27.: Resistive heater strips in the twin aperture dipole magnet of LHC; HF – heaters installed in the high-field regions, LF – heaters installed in the low–field regions [19].

Quench heaters could also be constructed as inductive heaters[15] that quench the magnet coil with induced magnetic field. A protection system with quench heaters requires an installation of capacitor discharge cabinets, powering cables and additional feedthroughs at the magnet cryostat.

A new and very interesting magnet protection system called "Coupling–Loss Induced Quench (CLIQ)" was recently developed at CERN [50]. In CLIQ, the activation of a special capacitor discharge system introduces a few oscillations in the magnet current what result in a rapid change of the local magnetic field in the coil. This leads to local heating of the coil cable due to the inter–filament and inter–strand losses[16]. This local temperature increase provokes a quench in the coil what accelerates the dump of the magnet current. The CLIQ system has the potential to replace quench heaters in the future superconducting magnet applications.

---

[15] Inductive spot heater – an inductive element in form of a solenoid wound around the magnet bus–bar (Nuclotron–type cable). The heater is connected to a capacitor bank. Discharging the capacitor on the spot heater generates a transient magnetic field which quenches the bus–bar.

[16] The study of the CLIQ protection system refers to coils built with Rutherford–type cable.

Magnet By–pass

It is more challenging to provide quench protection for a string of magnets than for a stand–alone magnet. In the string, the total inductance of the circuit sums up to a very large value which significantly increases the time constant of the current decay. Moreover, when a single magnet quenches, the resistive zone only occurs within this magnet. Thus all the energy stored in the string is dissipated in the quenched coil (assuming no external energy extraction system). In order to safe the quenched magnet from a burnout, each magnet can be equipped with a cold diode stack[17] that will be switched on when the quench voltage exceeds the turn on voltage (e.g. 6–8 V for cold diodes used for LHC dipoles and quadrupoles [51]). A protection system with a cold diode by–pass is presented in Fig. 2.28. $R_{\text{By-pass}}$ denotes the resistance of the by-pass section (resistance of the diode stack and cabling). The diode stacks are often connected "back to back" (as shown in Fig. 2.28) which allows to conduct the current regardless of the magnet polarity. The use of cold diodes has certain disadvantages:

- cold diodes are not recommended for fast cycling machines (e.g. SIS100) due to the too low turn on voltage (even when considering a diode stack);
- diodes are located in the direct surroundings of the magnet (e.g. beneath the magnet), close to the vacuum chamber with the beam, hence they have to be radiation hard[18] for the designed time of operation (usually 20–30 years);
- tendency to overheat;
- variations of the voltage–current characteristics from one diode to the other at cryogenic conditions.

Coil Subdivision

In case of a magnet with a very large inductance, quench protection could be as challenging as for a string of magnets. In case of a quench, due to the large inductance of the magnet and consequently a slow current decay, all the magnet energy will be dissipated within the quenched region of the coil. In order to prevent the coil overheating, one can implement the cold diode by–pass system and divide the coil into subsections as shown in Fig. 2.29. An example of a quench protection scheme with coil subdivision for a 13 MJ magnet is reported in [52].

---

[17] Cold diode stack – few diodes connected in series in order to increase the total turn on voltage.

[18] Studies on the radiation hardness of cold diodes are reported in [51].

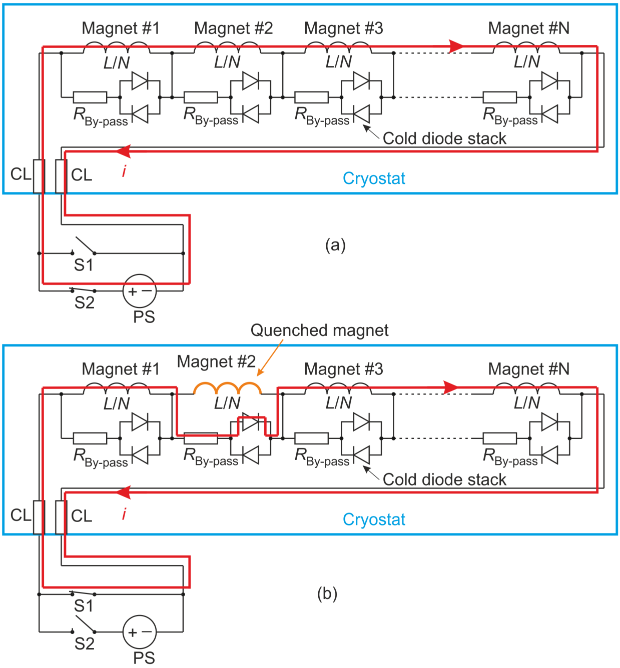

Figure 2.28.: Quench protection with cold diodes: (a) normal operation, (b) when the developed quench voltage reached the turn on voltage of the cold diode stack; PS – power supply, S1, S2 – switches, N – number of magnets in the string, L/N – inductance of a single magnet, CL – current lead.

2.6 Quench Detection

A quench can be detected by monitoring of temperature, pressure or voltage. The voltage signal is the fastest and the most reliable. Therefore, it was used for the most large superconducting magnet systems in the world, e.g. Tevatron, RHIC, HERA, Nuclotron, LHC and it will be used at FAIR as well.

Balance Bridge

The most common detection scheme utilises a balance bridge composed of two high precision resistors R_{b1} and R_{b2}. Figure 2.30 shows a not self–protecting dipole

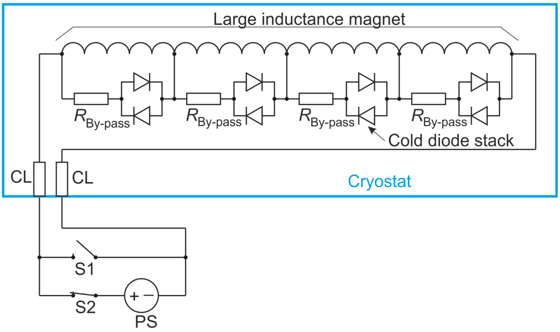

Figure 2.29.: Quench protection with coil subdivision for a large inductance magnets.

magnet with a quench detection system based on a resistive bridge. During normal operation (no quench), the bridge voltage V_b is equal to zero[19] regardless of the operation mode of the magnet (DC or AC). When a normal zone develops in one of the magnet coil–halves, V_b immediately rises up which clearly indicates a quench.

Looking at the electrical circuit shown in Fig. 2.30, one can distinguish three currents: the current given by the power supply (I), the current in the magnet (i_{m}) and the current in the balance bridge (i_{b}). The relation between them is given by

$$I = i_{\text{m}} + i_{\text{b}}, \qquad i_{\text{b}} = \frac{V_1 + V_2}{R_{\text{b1}} + R_{\text{b2}}}, \tag{2.8}$$

where V_1 and V_2 are the voltages across the magnet coil halves. V_1 and V_2 are given by

$$V_1 = L_{\text{s1}}\frac{di_{\text{m}}}{dt} + M\frac{di_{\text{m}}}{dt} + R_{\text{q1}} \cdot i_{\text{m}}, \qquad V_2 = L_{\text{s2}}\frac{di_{\text{m}}}{dt} + M\frac{di_{\text{m}}}{dt} + R_{\text{q2}} \cdot i_{\text{m}}, \tag{2.9}$$

where L_{s1} & L_{s2} are the self inductances of the corresponding coil halves, $M = k\sqrt{L_{\text{s1}}L_{\text{s2}}}$ is the mutual inductance between the coil halves and R_{q1} & R_{q2} are the resistances of the normal zone which can develop in case of a quench in either the first or the second coil half. Since the coil halves of a dipole magnet are strongly coupled with the coupling factor k close to 1, $M \approx \sqrt{L_{\text{s1}}L_{\text{s2}}}$.

---

[19] assuming ideal balance of the bridge

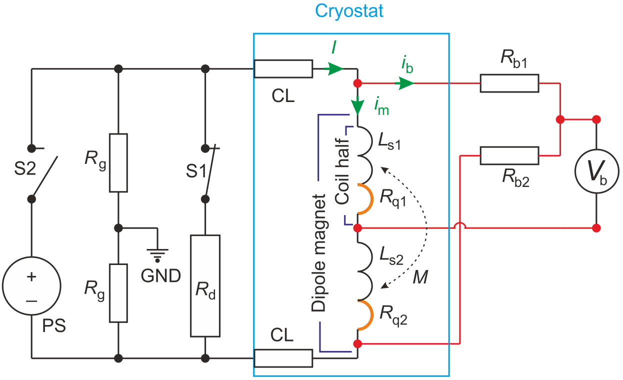

Figure 2.30.: Detection and protection system for a stand–alone, not self-protecting dipole magnet: PS – power supply; GND – ground; R_g – grounding resistor; S1, S2 – switches; CL – current lead; R_d – dump resistor; R_b1, R_b2 – balance resistors of the bridge; L_s1, L_s2 – self inductances of coil halves; M – mutual inductance; R_q1, R_q2 – possible quench resistances in corresponding poles; V_b – differential voltage seen by the bridge; I – current given by PS; i_m – magnet current; i_b – current in the balance bridge.

Applying Kirchoff's law, V_b equals to

$$V_\mathrm{b} + i_\mathrm{b} \cdot R_\mathrm{b1} - V_1 = 0 \tag{2.10}$$

or

$$V_\mathrm{b} - i_\mathrm{b} \cdot R_\mathrm{b2} + V_2 = 0. \tag{2.11}$$

Adding Eq. (2.10) to Eq. (2.11) and substituting i_b from Eq. (2.8), one gets Eq. (2.12) which defines V_b.

$$V_\mathrm{b} = \frac{1}{2} \cdot [V_1 - V_2 + i_\mathrm{b} \cdot (R_\mathrm{b2} - R_\mathrm{b1})] = \frac{1}{2} \cdot \left[V_1 - V_2 + \frac{R_\mathrm{b2} - R_\mathrm{b1}}{R_\mathrm{b1} + R_\mathrm{b2}} \cdot (V_1 + V_2)\right] \tag{2.12}$$

Substituting V_1 and V_2, one gets the final formula for V_b:

$$V_\mathrm{b} = \frac{1}{2} \cdot \left\{ \frac{di_\mathrm{m}}{dt} \cdot \left[L_\mathrm{s1} - L_\mathrm{s2} + \frac{R_\mathrm{b2} - R_\mathrm{b1}}{R_\mathrm{b1} + R_\mathrm{b2}} \cdot (L_\mathrm{s1} + L_\mathrm{s2} + 2M) \right] \right\} + \\ + \frac{1}{2} \cdot \left\{ i_\mathrm{m} \cdot \left[R_\mathrm{q1} - R_\mathrm{q2} + \frac{R_\mathrm{b2} - R_\mathrm{b1}}{R_\mathrm{b1} + R_\mathrm{b2}} \cdot (R_\mathrm{q1} + R_\mathrm{q2}) \right] \right\}. \quad (2.13)$$

For a large impedance bridge[20], one can assume that $i_\mathrm{m} \approx I$. If $L_\mathrm{s1} = L_\mathrm{s2}$ and $R_\mathrm{b1} = R_\mathrm{b2}$ (ideal symmetry), Eq. (2.13) simplifies to

$$V_\mathrm{b} = \pm \frac{1}{2} \cdot R_\mathrm{q} \cdot I = \pm \frac{V_\mathrm{q}}{2}, \quad (2.14)$$

where R_q denotes the resistance of the quenched half coil.

The resistive bridge has a very serious disadvantage. It is unable to detect a symmetrical quench – a quench which develops simultaneously in both coil halves ($R_\mathrm{q1} = R_\mathrm{q2}$) and gives an identical quench voltage across each coil half. A beam loss which deposits energy in the magnet coil is a possible origin for a symmetrical quench. Other reasons are less likely. In order to protect the magnet against a symmetrical quench, one usually designs a second layer of detection. For a stand–alone magnet, the second layer of detection could be realised by monitoring the voltage across the whole magnet. In that case a quench trigger will be released when the magnet voltage exceeds the predefined threshold voltage. In a magnet string, the second layer of detection can be realised by comparing voltages across two adjacent magnets.

Mutual Inductance Detector

Another way to detect a quench is to utilise a pick–up coil that is strongly coupled with the magnet coil [24]. Such a detector is called a mutual inductance detector (MID) and its functional scheme is shown in Fig. 2.31. The pick–up coil, in conjunction with the magnet coil and its yoke, forms a transformer where the voltage of the magnet coil and the induced voltage in the pick-up coil are given by:

$$V_1 = L_1 \frac{di_1}{dt} + M \frac{di_2}{dt} + (R_1 + R_\mathrm{q}) \cdot i_1, \quad (2.15)$$

---

[20] Large impedance bridge means that R_b1 and R_b2 are in the range of hundreds of kΩ or more.

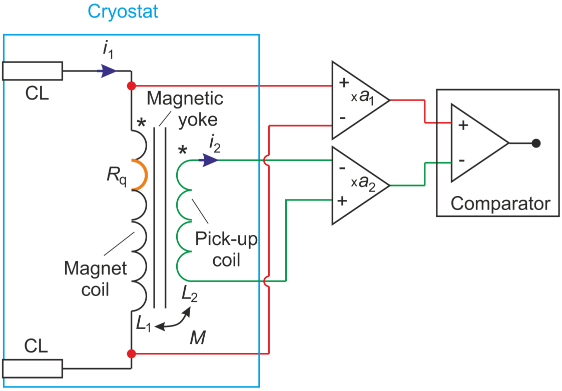

Figure 2.31.: Scheme of a mutual inductance detector.

$$V_2 = L_2 \frac{di_2}{dt} + M \frac{di_1}{dt} + R_2 \cdot i_2, \tag{2.16}$$

where i_1 & i_2 are the currents in the magnet coil and in the pick–up coil, respectively; L_1 is the self inductance of the magnet coil; R_1 is the resistance of the magnet coil; L_2 is the self inductance of the pick–up coil; R_2 is the resistance of the pick–up coil; M is the mutual inductance between the magnet coil and the pick–up coil; $V_\mathrm{q} = R_\mathrm{q} \cdot i_1$ is the quench voltage which arises in case of a quench.

The mutual inductance is defined by

$$M = k\sqrt{L_1 L_2}, \tag{2.17}$$

where $k \approx 1$ due to a good overlapping of the magnet and pick–up coils that share the magnetic flux.

The considered magnet has a superconducting coil, thus the coil resistance R_1 equals zero. The pick–up coil is connected to an amplifier characterised by a very high impedance input, hence $i_2 \approx 0$. Therefore:

$$V_1 = L_1 \frac{di_1}{dt} + V_\mathrm{q} \quad \Rightarrow \quad V_\mathrm{q} = V_1 - L_1 \frac{di_1}{dt}, \tag{2.18}$$

$$V_2 = M \frac{di_1}{dt} \quad \Rightarrow \quad \frac{di_1}{dt} = \frac{V_2}{M}. \tag{2.19}$$

Inserting Eq. (2.19) into Eq. (2.18), one gets the expression for the quench voltage:

$$V_\mathrm{q} = V_1 - \frac{L_1}{M} V_2. \tag{2.20}$$

Generally speaking, MID is a quench detector which compares the magnet voltage with the voltage induced in the pick–up coil. In case of a quench, an additional resistive voltage V_q occurs in the magnet coil. Since V_q is not transferred to the pick–up coil, the voltage comparator (Fig. 2.31) sees a voltage difference which indicates a quench. Although MID has the advantage over the resistive bridge concerning the ability of symmetrical quench detection, its use requires an additional pick–up coil, built into the magnet which is not possible for every magnet design.

Time Sequence for Quench Detection

From the moment when the transition to the resistive state starts, to the moment when a quench trigger is given, a certain time elapses. This particular time can be divided into sequences as presented in Figures 2.32a and 2.32b for a quench which originates in a magnet (quench detection realised with a balance bridge) and for a thermal runaway[21] in a copper current lead (CL), respectively. With the normal zone development (temp. increase in case of CL), the quench voltage V_q (voltage drop V_CLq for CL) increases and reaches the threshold V_th (V_thCL for CL) at the time t_rt. Then, the detection system “waits“ for a predefined validation time t_v (typically 10 ms). If V_q at $t_\mathrm{rt}+t_\mathrm{v}$ is still higher than V_th (or V_thCL), a quench trigger is released. The validation time is introduced in order to eliminate false quench signals caused by the noise (voltage spikes, etc.). t_o is the time to open/close the switches S1 and S2 (see Fig. 2.30). Typically, t_o is up to 300 ms for a mechanical

---

[21] A thermal runaway of a conductor is an uncontrolled positive feedback where an increase in temperature caused by the Joule heating results in further increase in temperature and leads to a destructive effect.

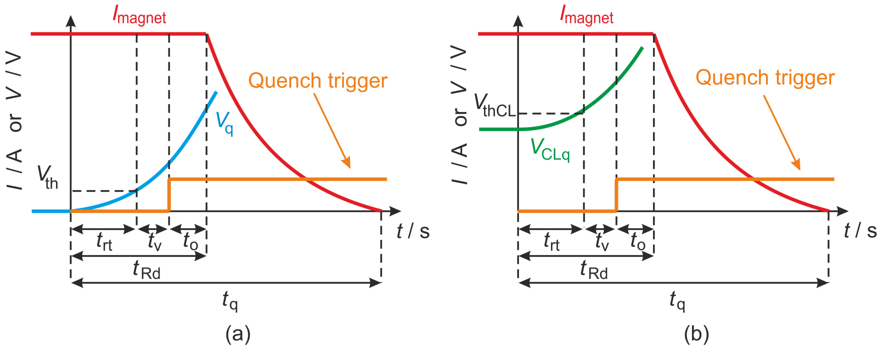

Figure 2.32.: Time sequence for quench detection: (a) quench voltage seen by a resistive bridge, (b) thermal runaway in a copper current lead.

switch and up to 1 ms for a semiconductor switch (power transistor/thyristor). Table 2.4 gives definitions for the time sequence of quench detection.

Table 2.4.: Time sequence for quench detection

Symbol	Definition
$t = 0$	1. origin of a quench 2. origin of a thermal runaway in the current lead
V_{th}	voltage threshold (magnet)
V_{thCL}	voltage threshold (current lead)
t_{rt}	time to reach the threshold
t_{v}	validation time
t_{o}	delay of the energy extraction system
t_{Rd}	$t_{\mathrm{Rd}} = t_{\mathrm{rt}} + t_{\mathrm{v}} + t_{\mathrm{o}}$ time between the quench (thermal runaway) origin and the start of current extraction
t_{q}	total time between the quench (thermal runaway) origin and the moment when the magnet current is discharged to zero

3 Development of a Quench Calculation Software

Although there exist several quench calculation software solutions [2–14] (see Appendix I), it was decided to develop a new quench calculation software that will be used for the FAIR magnets. Such an approach provides the full knowledge concerning the software details, awareness of the program limitations and unlimited access to the source code.

3.1 Zero–Dimensional Approach

In order to perform a preliminary quench calculation, it is very useful to have a simple computation tool which enables to estimate the temperature and the maximum voltage at a quench. The simplest calculation can be performed under the assumption of an instantaneous quench or with the calculation of $\mathrm{M}IIT$s.

3.1.1 Instantaneous Quench

Let us consider a simple dipole magnet with two racetrack–shape coils (one per magnetic pole). Each coil is wound from an insulated superconducting wire constructed from NbTi filaments in a Cu matrix. An instantaneous quench means that the considered magnet coil simultaneously quenches in its whole volume (homogeneous quench). In that case the coil has an uniform temperature called T_{av} (the subscript "av" states for average) which increases with time. Without an energy extraction system, all the magnet energy is dissipated within the quenched coil. When T_{av} exceeds the critical temperature, a quench resistance $R_{\mathrm{q}}^{\mathrm{av}}$ occurs. $R_{\mathrm{q}}^{\mathrm{av}}$ can be calculated as:

$$R_{\mathrm{q}}^{\mathrm{av}}(RRR, B_{\mathrm{coil}}^{\mathrm{av}}, T_{\mathrm{av}}) = \varrho_{\mathrm{av}}(RRR, B_{\mathrm{coil}}^{\mathrm{av}}, T_{\mathrm{av}}) \cdot \frac{n_{\mathrm{tpp}} \cdot l_{\text{1-turn}}}{A_{\mathrm{cond}}}, \tag{3.1}$$

where A_{cond} is the conductor cross–section (NbTi+Cu), n_{tpp} is the number of turns per pole and $l_{\text{1-turn}}$ is the average turn length. $B_{\mathrm{coil}}^{\mathrm{av}}$ is the average magnetic field which penetrates the conductor. For most of the cases, B_{coil} is calculated from a 2D magneto–static simulation during the phase of magnet design. Thus,

B_{coil} is typically given as the input parameter – if not, one can use the following assumption:

- $B_{\text{coil}}^{\text{av}} = B_{\text{coil}}^{\max}(I_n)/2$ or
- $B_{\text{coil}}^{\text{av}}(i) = i(t) \cdot B_{\text{coil}}^{\max}(I_n)/(2 \cdot I_n)$, where I_n is the nominal current and i is the actual current in the conductor.

The average resistivity of the conductor ϱ_{av} is defined by:

$$\varrho_{\text{av}}(RRR, B_{\text{coil}}^{\text{av}}, T_{\text{av}}) = A_{\text{cond}} \left(\frac{A_{\text{Cu}}}{\varrho_{\text{Cu}}(RRR, B_{\text{coil}}^{\text{av}}, T_{\text{av}})} + \frac{A_{\text{NbTi}}}{\varrho_{\text{NbTi}}(T_{\text{av}})} \right)^{-1}, \tag{3.2}$$

where A_{Cu} and A_{NbTi} are the cross–sections of Cu and NbTi, respectively.

The Joule energy E_{Joule} generated in the quenched coil within the time Δt is given by:

$$E_{\text{Joule}} = i^2(t) \cdot R_{\text{q}}^{\text{av}}(RRR, B_{\text{coil}}^{\text{av}}, T_{\text{av}}) \cdot \Delta t. \tag{3.3}$$

Assuming adiabatic conditions, E_{Joule} heats up the quenched coil volume by ΔT. Therefore the energy portion absorbed by the coil is equal to:

$$E_{\text{heating}\uparrow} = A_{\text{coil}} \cdot l_{\text{1-turn}} \cdot C_{\text{V}}^{\text{av}}(B_{\text{coil}}^{\text{av}}, T_{\text{av}}) \cdot \Delta T, \tag{3.4}$$

where A_{coil} is the coil cross–section and C_{V}^{av} is the averaged volumetric specific heat of the coil. C_{V}^{av} is weighted by the volumetric proportion of the involved materials as following:

$$C_{\text{V}}^{\text{av}}(B_{\text{coil}}^{\text{av}}, T_{\text{av}}) = \frac{A_{\text{Cu}} \cdot C_{\text{V}}^{\text{Cu}}(T_{\text{av}}) + A_{\text{NbTi}} \cdot C_{\text{V}}^{\text{NbTi}}(B_{\text{coil}}^{\text{av}}, T_{\text{av}}) + A_{\text{ins}} \cdot C_{\text{V}}^{\text{ins}}(T)}{A_{\text{Cu}} + A_{\text{NbTi}} + A_{\text{ins}}}, \tag{3.5}$$

where A_{ins} is the cross–section of the coil insulation.

Looking at the energy balance:

$$E_{\text{Joule}} = E_{\text{heating}\uparrow} \Rightarrow i^2 \cdot R_{\text{q}}^{\text{av}}(RRR, B_{\text{coil}}^{\text{av}}, T_{\text{av}}) \cdot \Delta t = A_{\text{coil}} \cdot l_{\text{1-turn}} \cdot C_{\text{V}}(B_{\text{coil}}^{\text{av}}, T_{\text{av}}) \cdot \Delta T, \tag{3.6}$$

one can calculate the temperature increase ΔT during the time Δt:

$$\Delta T = \frac{i^2 \cdot R_{\text{q}}^{\text{av}}(RRR, B_{\text{coil}}^{\text{av}}, T_{\text{av}})}{A_{\text{coil}} \cdot l_{\text{1-turn}} \cdot C_{\text{V}}(B_{\text{coil}}^{\text{av}}, T_{\text{av}})} \cdot \Delta t. \tag{3.7}$$

At the quench, the magnet is short–circuited (a self–protecting magnet is assumed) and the current is given by:

$$L\frac{\Delta i}{\Delta t} + R_{\mathrm{q}}^{\mathrm{av}}(RRR, B_{\mathrm{coil}}^{\mathrm{av}}, T_{\mathrm{av}}) \cdot i(t) = 0. \tag{3.8}$$

Assuming that the magnet inductance L does not vary with the magnetising current, the current change Δi during the time Δt is equal to:

$$\Delta i = -\frac{R_{\mathrm{q}}^{\mathrm{av}}(RRR, B_{\mathrm{coil}}^{\mathrm{av}}, T_{\mathrm{av}}) \cdot i(t)}{L}\Delta t. \tag{3.9}$$

Combining Equations (3.1), (3.7) and (3.9) one can compute the increase of $R_{\mathrm{q}}^{\mathrm{av}}$, the current decay and the temperature profile at the following time steps. The correlated quench voltage V_{q} and its maximum $V_{\mathrm{q}}^{\mathrm{max}}$ can be calculated by $i(t) \cdot R_{\mathrm{q}}^{\mathrm{av}}(t)$. A typical time profile of a current, temperature, quench voltage and quench resistance for a magnet without any energy extraction system, is presented in Fig. 3.1.

At the end of the quench, the temperature reaches its maximum $T_{\mathrm{av}\infty}$ which can be derived from the following integral:

$$\frac{E_{\mathrm{mag}}}{V_{\mathrm{vol}}} = \int_{T_{\mathrm{He}}}^{T_{\mathrm{av}\infty}} C_{\mathrm{V}}^{\mathrm{av}}(T) \cdot dT, \tag{3.10}$$

where $E_{\mathrm{mag}} = L \cdot I_{\mathrm{n}}^2/2$ is the magnetic energy of the magnet, $V_{\mathrm{vol}} = A_{\mathrm{cond}} \cdot n_{\mathrm{tpp}} \cdot l_{\text{1-turn}}$ is the volume of the quenched coil and T_{He} is the He bath temperature. Although $T_{\mathrm{av}\infty}$ is lower than the hot–spot temperature that occurs during a real quench, the presented calculation can indicate a badly designed conductor without sufficient amount of stabilising copper.

The instantaneous quench calculation can also be used for a magnet protected with a dump resistor R_{d}. Then, the electrical circuit is described by

$$L\frac{\Delta i}{\Delta t} + [R_{\mathrm{q}}^{\mathrm{av}}(RRR, B_{\mathrm{coil}}^{\mathrm{av}}, T_{\mathrm{av}}) + R_{\mathrm{d}}] \cdot i = 0 \Rightarrow \Delta i = -\frac{[R_{\mathrm{q}}^{\mathrm{av}}(RRR, B_{\mathrm{coil}}^{\mathrm{av}}, T_{\mathrm{av}}) + R_{\mathrm{d}}] \cdot i}{L}\Delta t. \tag{3.11}$$

Since a part of the initially stored magnetic energy will be extracted from the magnet and dissipated in R_{d}, Eq. (3.10) cannot be used to estimate $T_{\mathrm{av}\infty}$.

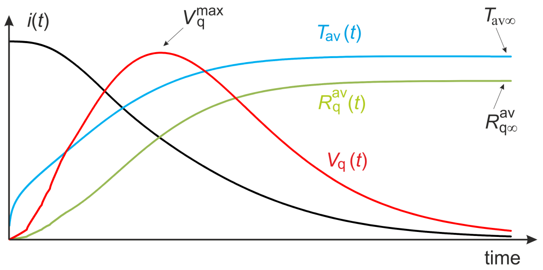

Figure 3.1.: Typical time profiles of the current, temperature, quench voltage and quench resistance for a magnet without any energy extraction system.

3.1.2 MIITs Calculation

The MIITs calculation is a tool which enables a quick estimation of the maximum temperature during a quench. The abbreviation MIITs states for:

"M" – Mega (prefix), "II" – current × current, "Ts" – time in seconds

and it is equal to the integral of the current square over the time counted from the quench origin moment to the time when the magnet current is discharged to zero:

$$IITs = \int_{t=0}^{t=\infty} i^2(t)dt. \tag{3.12}$$

MIITs sometimes is called simply IITs without the prefix Mega, thus MIITs $= 10^6 \cdot IIT$s. Although the abbreviation MIITs is more popular than IITs, all equations contained in this thesis, refer to IITs (SI unit system).

In the MIITs calculation, adiabatic conditions (no heat exchange to the coolant) are considered. Thus, the calculated conductor temperature is typically higher than the real temperature that occurs in the magnet coil. This overestimation of the temperature can be interpreted as the worst case scenario [24].

Coming back to the energy balance considered in the previous section, the Joule energy E_{Joule} generated by the electrical current i in the conductor of the length Δz and cross–section A can be calculated as

$$E_{\text{Joule}} = i^2(i) \cdot \varrho(T)\frac{\Delta z}{A} \cdot \Delta t. \tag{3.13}$$

This energy is dissipated within the coil and used for heating up of the coil. Therefore, the energy absorbed by the coil ($E_{\text{heating}\uparrow}$) is equal to

$$E_{\text{heating}\uparrow} = A \cdot \Delta z \cdot C_{\text{V}}(T) \cdot \Delta T \tag{3.14}$$

In adiabatic conditions it is true that

$$E_{\text{Joule}} = E_{\text{heating}\uparrow} \quad \Rightarrow \quad i^2(t) \cdot \varrho(T) \frac{\Delta z}{A} \cdot \Delta t = A \cdot \Delta z \cdot C_{\text{V}}(T) \cdot \Delta T \tag{3.15}$$

Integrating the left side of Eq. (3.15) over the time and the right side over the temperature increase one gets:

$$\int_{t=0}^{t=\infty} i^2(t) dt = A^2 \int_{T=T_{\text{cs}}}^{T_{\text{max}}} \frac{C_{\text{V}}(T)}{\varrho(T)} dT. \tag{3.16}$$

From the right side of Eq. (3.16), one also gets the formula for IITs that takes into account the adiabatic heating of the conductor:

$$IIT\text{s} = A^2 \int_{T_{\text{cs}}}^{T_{\text{max}}} \frac{C_{\text{V}}(T)}{\varrho(T)} dT. \tag{3.17}$$

When computing the current decay using the instantaneous quench approach summarised in Equations (3.1), (3.7) and (3.9), one can calculate IITs from Eq. (3.12). Knowing IITs for the considered conductor design, it is possible to derive the temperature at the hot–spot T_{max} from Eq. (3.17). IITs has direct influence on T_{max}. If T_{max} is too high and must be reduced, a reduction in IITs is required.

For not self–protecting magnets, another type of MIITs calculation can be used in order to estimate the minimum value for the dump resistance of the magnet protection system. When looking at a typical current waveform of a quenched magnet protected with R_{d} (see Fig. 3.2), the current remains constant up to the moment when the protection system is activated (the current is regulated by the power supply controller with an active feedback loop). When the protection system is activated, the current starts to decay. Assuming $R_{\text{d}} \gg R_{\text{q}}$ and that the magnetic yoke stays unsaturated (L =const), the current drops exponentially with a time constant $\tau = L/R_{\text{d}}$. If one marks the time moment of the quench protection system activation as the reference (t =0), the current waveform can be approximated by:

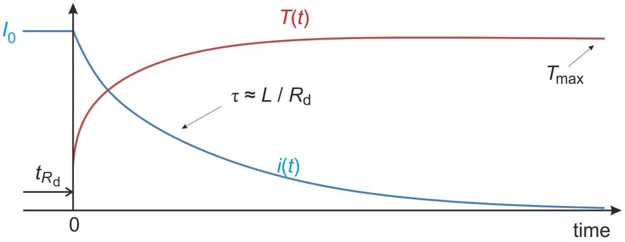

Figure 3.2.: Typical current decay and temperature increase of a magnet protected with R_d.

$$i(t) = \begin{cases} I_0, & t \in (-t_{R_\mathrm{d}}, 0); \\ I_0 \cdot \mathrm{e}^{-\frac{t}{\tau}}, & t > 0; \end{cases} \tag{3.18}$$

where t_{R_d} is the time counted from the quench origin to the moment of the extraction system activation (see Section 2.6). Using Eq. (3.12), one gets:

$$IIT\mathrm{s} = \int_{t=-t_{R_\mathrm{d}}}^{t=\infty} i^2(t)dt = \int_{t=-t_{R_\mathrm{d}}}^{t=0} I_0^2 dt + \int_{t=0}^{t=\infty} I_0^2 \cdot \mathrm{e}^{-2\frac{t}{\tau}} dt \Rightarrow IIT\mathrm{s} = I_0^2 \left(t_{R_\mathrm{d}} + \frac{\tau}{2} \right). \tag{3.19}$$

Since IITs is a function of the hot–spot temperature, the maximum time constant τ could be calculated as:

$$\tau_\mathrm{max} = 2 \left(\frac{IIT\mathrm{s}(T_\mathrm{max})}{I_0^2} - t_{R_\mathrm{d}} \right). \tag{3.20}$$

The time t_{R_d} equals to $t_\mathrm{rt} + t_\mathrm{o} + t_\mathrm{v}$ (see Section 2.6). t_o can be assumed as 1 ms or 40–300 ms for a semiconductor or a mechanical switch, respectively. t_v is the delay given by the quench detection electronics (usually 5–10 ms). t_rt is the time to reach the quench detection threshold V_th. The longer t_rt is, with a shorter τ the quench protection system shall be characterised. Knowing the quench propagation velocity (v_fp) along the coil – which for the considered conductor, can be either estimated in the way proposed by M. Wilson (Appendix I, Eq. (I.1)) or measured in advance – one can estimate t_rt by comparing the developed quench voltage V_q to the quench detection threshold V_th as following:

$$V_\mathrm{q} = V_\mathrm{th} = I_0 \cdot \varrho \frac{v_\mathrm{fp} \cdot t_\mathrm{rt}}{A} \quad \Rightarrow \quad t_\mathrm{rt} = \frac{V_\mathrm{th} \cdot A}{I_0 \cdot \varrho \cdot v_\mathrm{fp}}. \tag{3.21}$$

In order to simulate the quench behaviour in a superconducting magnet, a simplified thermal model has to be created. The choice of the model depends on the magnet type (coil structure, conductor type, cooling scheme, etc.). Let us consider a magnet with potted coils. In that case a single coil can be represented by a number of uniform conductors, e.g. a single turn is represented by an uniform conductor. Such a conductor is characterised by its physical properties such as specific heat C_V, thermal conductivity k (anisotropic) and resistivity ϱ that are weighted by the volumetric proportion of the involved materials (Cu, NbTi, insulation, etc.). An electrical current I applied to the the conductor is included in the model as a current density $J = I/A_\mathrm{conductor}$ ($A_\mathrm{conductor}$ – conductor cross–section). The thermal model is governed by the heat–balance equation:

$$\varrho(RRR, B, T) \cdot J^2(t) + \nabla\left(k(T) \cdot \nabla T(x,y,z,t)\right) = C_\mathrm{V}(B,T) \cdot \frac{\partial T(x,y,z,t)}{\partial t}, \tag{3.22}$$

where the first term of the left side describes the Joule heating within the normal zone expressed in [W/m^3]. The second term represents the heat propagation in the conductor. At the right side the warming of the conductor is included.

The current density $J = I/A_\mathrm{conductor}$ is derived from the electrical equation which takes into account the powering and protection circuit of the considered magnet system. For instance, a magnet circuit protected with an energy extraction resistor R_d is described by

$$L_\mathrm{d}(I) \cdot \frac{dI(t)}{dt} + \left(R_\mathrm{q}(t) + \delta(t) \cdot R_\mathrm{d}\right) \cdot I(t) = V_\mathrm{PS}(t), \tag{3.23}$$

where $\delta(t)$ is a step function which takes 0–value before and 1–value after the activation of R_d. V_PS is the voltage given by the power supply. L_d is the differential inductance (see Appendix J).

The heat–balance problem is of a parabolic partial differential type and in principle could be solved analytically. However, taking into account that the all coefficients (namely material properties) are non–linear, and vary with temperature and magnetic field (see Figures 3.3, 3.4 and Appendix K), the analytical calculation becomes a challenging task which requires expert knowledge concerning mathematical methods in physics. Therefore, it is more convenient to solve the heat–balance equation with numerical methods. An example of an analytical and numerical solutions for a simplified 1D case are presented in Appendix L.

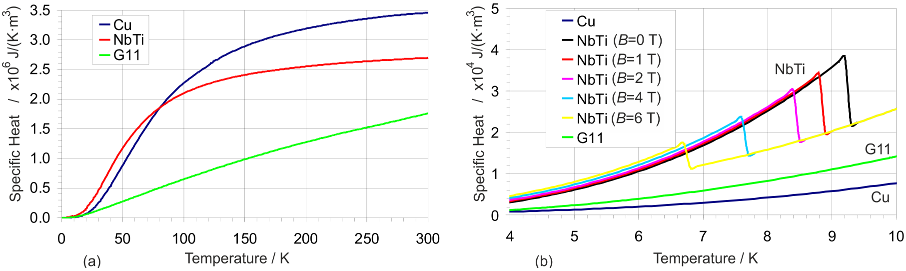

Figure 3.3.: Specific heat for Cu, NbTi and G11: (a) range from 0 to 300 K; (b) zoom at 4–10 K and applied magnetic field influence on C_V of NbTi.

3.2.1 One–Dimensional Case

A 1D quench calculation gives satisfactory results for superconducting coils with well insulated turns. In such a coil, the quench propagates much slower in the transverse direction than longitudinally along the conductor. Thus, the transverse quench propagation can be neglected. In the 1D approach, there is no advanced thermal model of the coil. All coil turns are connected in series and represented as a long 1D conductor, as shown in Fig. 3.5. The model is featured by resistivity, specific heat and thermal conductivity that are averaged according to the volumetric proportion of the involved materials, i.e. NbTi, Cu, CuMn, CuNi, insulation, etc. – see Equations (3.24), (3.25) and (3.27). Since the quench propagates symmetrically in the both directions, it is sufficient to consider only one half of the bar.

$$\varrho(RRR,B,T) = (A_\mathrm{NbTi} + A_\mathrm{Cu} + \ldots) \cdot \left(\frac{A_\mathrm{NbTi}}{\varrho_\mathrm{NbTi}(T)} + \frac{A_\mathrm{Cu}}{\varrho_\mathrm{Cu}(RRR,B,T)} + \ldots \right)^{-1} \tag{3.24}$$

$$k(RRR,T) = \frac{A_\mathrm{NbTi} \cdot k_\mathrm{NbTi}(T) + A_\mathrm{Cu} \cdot k_\mathrm{Cu}(RRR,T) + \ldots + A_\mathrm{ins} \cdot k_\mathrm{ins}(T)}{A_\mathrm{NbTi} + A_\mathrm{Cu} + \ldots + A_\mathrm{ins}} \tag{3.25}$$

Since $k_\mathrm{Cu} \gg k_\mathrm{NbTi}$ & $k_\mathrm{Cu} \gg k_\mathrm{ins}$, Eq. (3.25) can be simplified to

$$k(RRR,T) = \frac{A_\mathrm{Cu} \cdot k_\mathrm{Cu}(RRR,T)}{A_\mathrm{NbTi} + A_\mathrm{Cu} + \ldots + A_\mathrm{ins}}. \tag{3.26}$$

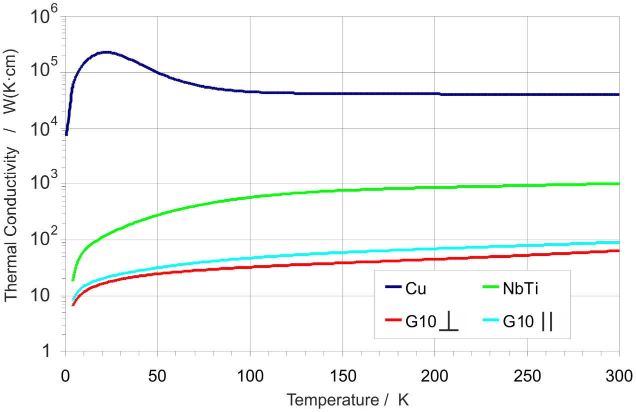

Figure 3.4.: Thermal conductivity for Cu, NbTi and G10 (insulating material): $\|$ – propagation along glass fibre, $\perp$ – propagation perpendicular to glass fibre.

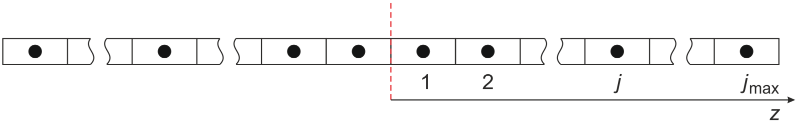

Figure 3.5.: One–dimensional model of the superconducting coil.

$$C_\mathrm{V}(B,T) = \frac{A_\mathrm{NbTi} \cdot C_\mathrm{V}^\mathrm{NbTi}(B,T) + A_\mathrm{Cu} \cdot C_\mathrm{V}^\mathrm{Cu}(T) + \ldots + A_\mathrm{ins} \cdot C_\mathrm{V}^\mathrm{ins}(T)}{A_\mathrm{NbTi} + A_\mathrm{Cu} + \ldots + A_\mathrm{ins}} \tag{3.27}$$

In order to avoid numerical instability, the implicit scheme is used to solve the heat–balance of the bar (see Section L.2.2). The thermal model of the considered conductor (ti is used for the time step index) is given by:

$$\begin{aligned} J^2(t) \cdot \varrho(RRR,B,T) + k(RRR,T) \cdot \frac{T_{j-1}^{ti+1} - T_j^{ti+1}}{dz^2} + \\ -k(RRR,T) \cdot \frac{T_j^{ti+1} - T_{j+1}^{ti+1}}{dz^2} = C_\mathrm{V}(B,T) \cdot \frac{T_j^{ti+1} - T_j^{ti}}{dt}. \end{aligned} \tag{3.28}$$

Equation (3.28) can be rearranged to

$$a(j,ti)\cdot T_{j-1}^{ti+1} + b(j,ti)\cdot T_{j}^{ti+1} + c(j,ti)\cdot T_{j+1}^{ti+1} = T_j^{ti} + d(j,ti), \tag{3.29}$$

with

$$a(j,ti) = -\frac{dt}{dz^2\cdot C_{\mathrm{V}}(B,T)}\cdot k(RRR,T), \quad b(j,ti) = 1 + \frac{dt}{dz^2\cdot C_{\mathrm{V}}(B,T)}\cdot 2k(RRR,T),$$

$$c(j,ti) = -\frac{dt}{dz^2\cdot C_{\mathrm{V}}(B,T)}\cdot k(RRR,T) \quad and \quad d(j,ti) = \frac{\varrho(RRR,B,T)\cdot J^2(t)\cdot dt}{C_{\mathrm{V}}(B,T)}.$$

The matrix equation which corresponds to the considered model takes the form of

$$\mathbf{A}_{jj}\cdot\mathbf{T}_j^{ti+1} = \mathbf{T}_j^{ti} + \mathbf{D}_j \quad \Rightarrow \quad \mathbf{A}\cdot\mathbf{X} = \mathbf{B}, \tag{3.30}$$

where:

$$\mathbf{A} = \begin{bmatrix} b(1) & c(1) & 0 & 0 & 0 & \dots & 0 & 0 \\ a(2) & b(2) & c(2) & 0 & 0 & \dots & 0 & 0 \\ \vdots & \vdots & \vdots & \vdots & \vdots & \dots & \vdots & \vdots \\ 0 & 0 & a(j) & b(j) & c(j) & \dots & 0 & 0 \\ \vdots & \vdots & \vdots & \vdots & \vdots & \dots & \vdots & \vdots \\ 0 & 0 & 0 & 0 & 0 & \dots & a(j_{\max}) & b(j_{\max}) \end{bmatrix}, \tag{3.31}$$

$$\mathbf{X} = \begin{bmatrix} T_1^{ti+1} \\ T_2^{ti+1} \\ \vdots \\ T_j^{ti+1} \\ \vdots \\ T_{j_{\max}}^{ti+1} \end{bmatrix}, \qquad \mathbf{B} = \begin{bmatrix} T_1^{ti} + d(1) \\ T_2^{ti} + d(2) \\ \vdots \\ T_j^{ti} + d(j) \\ \vdots \\ T_{j_{\max}}^{ti} + d(j_{\max}) \end{bmatrix}.$$

Since the matrix **A** is multi–diagonal, one can use dedicated algorithms in order to solve Eq. (3.30). The GSI quench calculation code is written in MATLAB® which enables to apply the bi–conjugate gradients stabilised method called “bicgstab” [53].

A quench occurs in the conductor at a certain current I_0. The relation between the current and the current density of the conductor is given by:

$$J(t) = I(t)/A_{\mathrm{cond}} = I(t)/(A_{\mathrm{NbTi}} + A_{\mathrm{Cu}} + \ldots). \tag{3.32}$$

In the following time step it is required to update the transient current according to the coil protection scheme. For instance for a magnet protected with an energy extraction resistor R_{d}, the electrical circuit is described by:

$$L_{\mathrm{d}}(I) \cdot \frac{dI(t)}{dt} + (R_{\mathrm{q}}(t) + R_{\mathrm{d}}) \cdot I(t) = 0 \tag{3.33}$$

Therefore:

$$I_{ti+1} = I_{ti} - \frac{(R_{\mathrm{q}}^{ti} + R_{\mathrm{d}}) \cdot I_{ti} \cdot dt}{L_{\mathrm{d}}(I_{ti})}, \tag{3.34}$$

where $L_{\mathrm{d}}(I)$ is the differential inductance (see Appendix J) which takes into account the yoke saturation. For a coarse calculation one can assume $L_{\mathrm{d}} = L_{\mathrm{d}}(I = 0) = \mathrm{const.}$ An example of the inductance dependence on current is shown in Fig. 3.6 where above 100 A the yoke saturation starts to be visible.

The quench resistance R_{q}^{ti} is computed at the macroscopic scale according to:

$$R_{\mathrm{q}}^{ti} = 2 \cdot \sum_{j=1}^{j_{\max}} \frac{\varrho(RRR, B(I_{ti}), T_j^{ti}) \cdot dz}{A_{cond}}, \tag{3.35}$$

where the "factor 2" is used to take into account the model symmetry (see Fig. 3.5).

Inserting the microscopic thermal model and the macroscopic electrical model into a common time loop, one can finally calculate the temperature distribution, quench resistance and magnet current at each time step.

3.2.2 Adaptive Time Stepping

Calculating the quench propagation with an implicit FDM software can be time consuming (there are many space elements[1] to be calculated at the large number of time steps). Furthermore, it may happen that from one time step to the other, ΔT at some mesh elements reaches few tens of Kelvin what might completely ruin the

---

[1] For numerical calculation, the volume of the model body needs to be divided into small space elements. A regular network that is created from the these space elements is called either a mesh grid or simply a mesh.

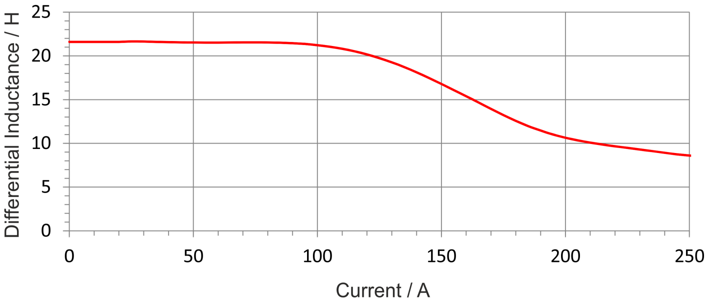

Figure 3.6.: Differential inductance measured on a Super–FRS dipole prototype ($I_\mathrm{n} = 232$ A).

calculation accuracy due the strong temperature dependence of material properties. Another threat for the computation is that despite of the unconditional stability of the implicit scheme, one can get close to the boundary of stability ($g \approx 1$, see Section L.2.2) what results in a large calculation error. Therefore, the arbitrary choice of the time step Δt could become an issue. In order to control and limit ΔT, an innovative adaptive time stepping algorithm was developed in the frame work of this Ph.D. [54].

Considering a single thermally isolated element in adiabatic conditions, it is true that:

$$\varrho(RRR, B, T) \cdot J^2(t) \cdot \Delta t = C_\mathrm{V}(B, T) \cdot \Delta T \tag{3.36}$$

and

$$\Delta T = \frac{\varrho(RRR, B, T) \cdot J^2(t)}{C_\mathrm{V}(B, T)} \cdot \Delta t. \tag{3.37}$$

When calculating the thermal model, it is desirable to have a small ΔT in the level of 1 K or lower. Let us call the desirable maximum temperature increase ΔT_max. In order to get $\Delta T \leq \Delta T_\mathrm{max}$ the time step shall not be longer than

$$\Delta t_\mathrm{max} = \frac{\Delta T_\mathrm{max}}{J^2(t)} / \left[\frac{\varrho(RRR, B, T)}{C_\mathrm{V}(B, T)}\right]_\mathrm{max}, \tag{3.38}$$

where $[\varrho(RRR, B, T)/C_\mathrm{V}(B, T)]_\mathrm{max}$ is the maximum ratio of $\varrho(RRR, B, T)/C_\mathrm{V}(B, T)$ calculated among all mesh elements.

The temperature dependence of $\varrho(RRR, B, T)/C_\mathrm{V}(B, T)$ is shown in Fig. 3.7, where three cases can be distinguished.

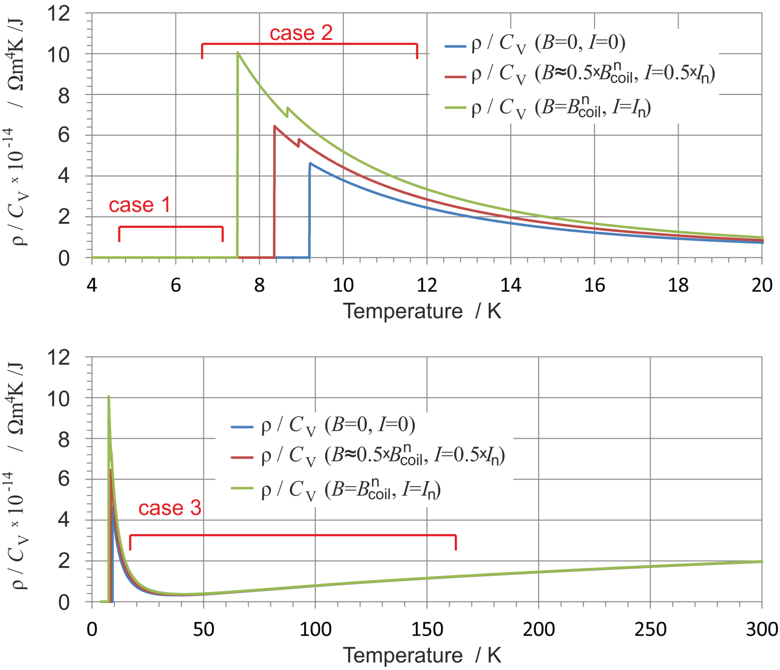

Figure 3.7.: Temperature dependence of $\varrho(RRR, B, T)/C_\mathrm{V}(B, T)$ (example of Super–FRS dipole magnet).

1. When the maximum temperature in the conductor T_max does not exceed the critical–surface temperature $T_\mathrm{cs}(I, B)$ (such a situation can only happen when either the resistive zone does not exist or it shrinks), the $\varrho(RRR, B, T)/C_\mathrm{V}(B, T)$ ratio equals to 0 and therefore the time step can not be calculated with the use of Eq. (3.38). In this case one can assume a minimum $\Delta t = \Delta t_\mathrm{min}$ which shall be arbitrary chosen.

2. When not all mesh elements have already quenched, then the maximum of $\varrho(RRR, B, T)/C_\mathrm{V}(B, T)$ appears for a temperature close to T_cs.

3. When all mesh elements have already quenched, then $[\varrho(RRR, B, T)/C_\mathrm{V}(B, T)]_\mathrm{max}$ appears for either the maximum or the minimum temperature in the conductor.

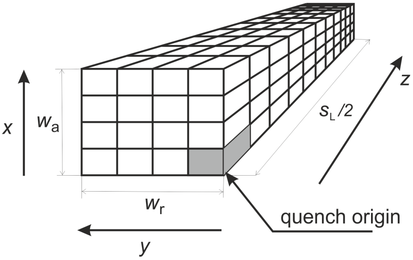

Figure 3.8.: Example of a 3D mesh grid applied to the slab that represents the half–coil: $w_\mathrm{a} \times w_\mathrm{r}$ – coil cross–section, s_L – average turn length in the coil.

3.2.3 Three–Dimensional Case

The 1D considerations presented in Section 3.2.1 can be expanded to a 3D case. Then, the magnet coil can be modelled as a homogeneous slab. For further considerations, it is assumed that a quench occurs in the middle of the slab length, in one of the corners. Such a location of the quench origin is chosen on purpose since in a real coil, the inner corner typically sees the maximum magnetic induction and, therefore, a quench in this location has a higher probability than elsewhere. In order to reduce the computation time, only half of the slab is modelled (the quench spreads symmetrically along the slab in both directions). The volume of the slab is characterised by averaged specific heat and anisotropic thermal conductivity. Figure 3.8 shows the regular mesh grid applied to the slab and the local coordinate system. A single mesh element has a size of $dx \times dy \times dz$.

The thermal model of the slab is described by

$$\begin{aligned} &\varrho(RRR,B,T)\cdot J^2(t)+\frac{\partial}{\partial x}\left[k_x(RRR,T)\cdot\frac{\partial T(x,y,z,t)}{\partial x}\right]+\\ &+\frac{\partial}{\partial y}\left[k_y(RRR,T)\cdot\frac{\partial T(x,y,z,t)}{\partial y}\right]+\frac{\partial}{\partial z}\left[k_z(RRR,T)\cdot\frac{\partial T(x,y,z,t)}{\partial z}\right]=\\ &=C_\mathrm{V}(B,T)\cdot\frac{\partial T(x,y,z,t)}{\partial t}. \quad (3.39)\end{aligned}$$

It is assumed that there is no heat exchange to the coolant (adiabatic conditions). Applying the finite difference method (implicit scheme) to Eq. (3.39), one obtains:

$$
\begin{aligned}
&J^2(t_i) \cdot \varrho(RRR, B^{ti}_{xi,yi,zi}, T^{ti}_{xi,yi,zi}) + \\
&+\frac{1}{dx^2} k_x \left(RRR, \frac{T^{ti}_{xi+1,yi,zi} + T^{ti}_{xi,yi,zi}}{2} \right) \cdot (T^{ti+1}_{xi+1,yi,zi} - T^{ti+1}_{xi,yi,zi}) + \\
&-\frac{1}{dx^2} k_x \left(RRR, \frac{T^{ti}_{xi,yi,zi} + T^{ti}_{xi-1,yi,zi}}{2} \right) \cdot (T^{ti+1}_{xi,yi,zi} - T^{ti+1}_{xi-1,yi,zi}) + \\
&+\frac{1}{dy^2} k_y \left(RRR, \frac{T^{ti}_{xi,yi+1,zi} + T^{ti}_{xi,yi,zi}}{2} \right) \cdot (T^{ti+1}_{xi,yi+1,zi} - T^{ti+1}_{xi,yi,z_i}) + \\
&-\frac{1}{dy^2} k_y \left(RRR, \frac{T^{ti}_{xi,yi,zi} + T^{ti}_{xi,yi-1,zi}}{2} \right) \cdot (T^{ti+1}_{xi,yi,zi} - T^{ti+1}_{xi,yi-1,zi}) + \\
&+\frac{1}{dz^2} k_z \left(RRR, \frac{T^{ti}_{xi,yi,zi+1} + T^{ti}_{xi,yi,zi-1}}{2} \right) \cdot (T^{ti+1}_{xi,yi,zi+1} - T^{ti+1}_{xi,yi,zi}) + \\
&-\frac{1}{dz^2} k_z \left(RRR, \frac{T^{ti}_{xi,yi,zi} + T^{ti}_{xi,yi,zi-1}}{2} \right) \cdot (T^{ti+1}_{xi,yi,zi} - T^{ti+1}_{xi,yi,zi-1}) = \\
&= C_\text{V}(B^{ti}_{xi,yi,zi}, T^{ti}_{xi,yi,zi}) \cdot \frac{T^{ti+1}_{xi,yi,zi} - T^{ti}_{xi,yi,zi}}{dt},
\end{aligned}
\tag{3.40}
$$

where xi and yi are the indexes for the position in the slab cross–section, zi is the index of the position along the slab and ti is the index for the digitalised time. Equation (3.40) can be rewritten as:

$$
\begin{aligned}
&a_x(xi, yi, zi, ti) \cdot T^{ti+1}_{xi-1,y_i,zi} + a_y(xi, yi, zi, ti) \cdot T^{ti+1}_{xi,yi-1,zi} + \\
&+a_z(xi, yi, zi, ti) \cdot T^{ti+1}_{xi,yi,zi-1} + b_{xyz}(xi, yi, zi, ti) \cdot T^{ti+1}_{xi,yi,zi} + \\
&+c_x(xi, yi, zi, ti) \cdot T^{ti+1}_{xi+1,yi,zi} + c_y(xi, yi, zi, ti) \cdot T^{ti+1}_{xi,yi+1,zi} + \\
&+c_z(xi, yi, zi, ti) \cdot T^{ti+1}_{xi,yi,zi+1} = T^{ti+1}_{xi,yi,zi} + d_{xyz}(xi, yi, zi, ti),
\end{aligned}
\tag{3.41}
$$

with the parameters:

$$
a_x(xi, yi, zi, ti) = -\frac{dt}{dx^2 C_\text{V}(B^{ti}_{xi,yi,zi}, T^{ti}_{xi,yi,zi})} \cdot k_x \left(RRR, \frac{T^{ti}_{xi,yi,zi} + T^{ti}_{xi-1,yi,zi}}{2} \right),
$$

$$a_y(xi, yi, zi, ti) = -\frac{dt}{dy^2 C_V(B^{ti}_{xi,yi,zi}, T^{ti}_{xi,yi,zi})} \cdot k_y\left(RRR, \frac{T^{ti}_{xi,yi,zi} + T^{ti}_{xi,yi-1,zi}}{2}\right),$$

$$a_z(xi, yi, zi, ti) = -\frac{dt}{dy^2 C_V(B^{ti}_{xi,yi,zi}, T^{ti}_{xi,yi,zi})} \cdot k_z\left(RRR, \frac{T^{ti}_{xi,yi,zi} + T^{ti}_{xi,yi,zi-1}}{2}\right),$$

$$\begin{aligned} b_{xyz}(xi, yi, zi, ti) = 1 + &\\ + \frac{dt}{dx^2 C_V(T^{ti}_{xi,yi,zi})} \cdot \left[k_x\left(RRR, \frac{T^{ti}_{xi,yi,zi} + T^{ti}_{xi-1,yi,zi}}{2}\right) + k_x\left(RRR, \frac{T^{ti}_{xi+1,yi,zi} + T^{ti}_{xi,yi,zi}}{2}\right)\right] + &\\ + \frac{dt}{dy^2 C_V(T^{ti}_{xi,yi,zi})} \cdot \left[k_y\left(RRR, \frac{T^{ti}_{xi,yi,zi} + T^{ti}_{xi,yi-1,zi}}{2}\right) + k_y\left(RRR, \frac{T^{ti}_{xi,yi+1,zi} + T^{ti}_{xi,yi,zi}}{2}\right)\right] + &\\ + \frac{dt}{dz^2 C_V(T^{ti}_{xi,yi,zi})} \cdot \left[k_z\left(RRR, \frac{T^{ti}_{xi,yi,zi} + T^{ti}_{xi,yi,zi-1}}{2}\right) + k_z\left(RRR, \frac{T^{ti}_{xi,yi,zi+1} + T^{ti}_{xi,yi,zi}}{2}\right)\right], & \end{aligned}$$

$$c_x(xi, yi, zi, ti) = -\frac{dt}{dx^2 C_V(B^{ti}_{xi,yi,zi}, T^{ti}_{xi,yi,zi})} \cdot k_x\left(RRR, \frac{T^{ti}_{xi+1,yi,zi} + T^{ti}_{xi,yi,zi}}{2}\right),$$

$$c_y(xi, yi, zi, ti) = -\frac{dt}{dy^2 C_V(B^{ti}_{xi,yi,zi}, T^{ti}_{xi,yi,zi})} \cdot k_y\left(RRR, \frac{T^{ti}_{xi,yi+1,zi} + T^{ti}_{xi,yi,zi}}{2}\right),$$

$$c_z(xi, yi, zi, ti) = -\frac{dt}{dz^2 C_V(B^{ti}_{xi,yi,zi}, T^{ti}_{xi,yi,zi})} \cdot k_z\left(RRR, \frac{T^{ti}_{xi,yi,zi+1} + T^{ti}_{xi,yi,zi}}{2}\right),$$

$$d_{xyz}(xi, yi, zi, ti) = \frac{\varrho(RRR, B^{ti}_{xi,yi,zi}, T^{ti}_{xi,yi,zi}) \cdot J^2(ti) \cdot dt}{C_V(B^{ti}_{xi,yi,zi}, T^{ti}_{xi,yi,zi})}.$$

In order to reduce the number of indexes, instead of xi, yi and zi, a single mi index is introduced. Figure 3.9 explains how a mesh element e_{xyz} with the location specified by indexes $xi/yi/zi$ refers to the new index mi. Marking $xi_{\max}$, $yi_{\max}$ and $zi_{\max}$ as the number of elements along x, y and z axis, respectively, the total number of mesh elements is marked by $mi_{\max} = xi_{\max} \cdot yi_{\max} \cdot zi_{\max}$. Referring to Fig. 3.9, it is true that:

$$(xi, yi, zi) \rightarrow (mi): \quad mi = xi + (yi-1)xi_{\max} + (zi-1)xi_{\max}yi_{\max}. \tag{3.42}$$

The matrix equation which corresponds to the considered 3D thermal model takes the form of:

$$\mathbf{A}_{mi,mi} \cdot \mathbf{T}_{mi}^{ti+1} = \mathbf{T}_{mi}^{ti} + \mathbf{D}_{mi} \quad \rightarrow \quad \mathbf{A} \cdot \mathbf{X} = \mathbf{B}, \tag{3.43}$$

where **A** is a multi–diagonal coefficient matrix. The thermal model defined by Eq. (3.43) is solved in MATLAB® with the use of bi–conjugate gradients stabilised method [53].

For instance, the **A** matrix for a model that consists of 27 ($3 \times 3 \times 3$) mesh elements is as following:

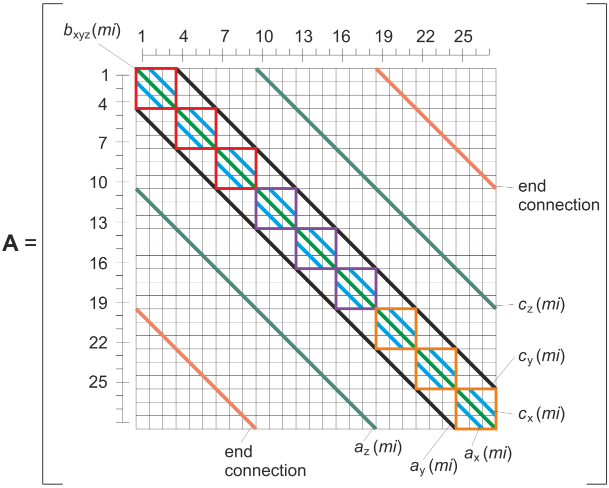

– the diagonal lines indicate the location of the matrix coefficients. The orange diagonals correspond to the end connections of the conductors. Along the z axis, the last mesh element is thermally coupled with the first one (these diagonals only exist when no model symmetry is applied). The square marks at the main diagonal correspond to the matrix coefficients along the x axis (in this case there are just three elements). The matrix elements beyond the marked diagonals are equal to zero.

X and **B** are 1D matrices are given by:

$$\mathbf{X} = \begin{bmatrix} T_1^{ti+1} \\ \vdots \\ T_{mi_{\max}}^{ti+1} \end{bmatrix}, \qquad \mathbf{B} = \begin{bmatrix} T_1^{ti} + d_{xyz}(1) \\ \vdots \\ T_{mi_{\max}}^{ti} + d_{xyz}(mi_{max}) \end{bmatrix}.$$

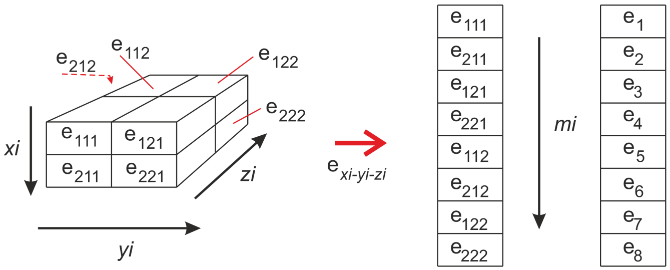

Figure 3.9.: Relation between $xi/yi/zi$ and mi indexes.

The GSI 3D quench calculation software gives the opportunity to check the temperature gradients that occur in the coil during the quench. For magnets with potted coils, the maximum temperature difference within the coil volume shall not exceed 100 K in order to do not cause mechanical deformations [24]. An example of a temperature distribution in the coil cross–section (the case of Super–FRS dipole prototype) calculated with the GSI 3D quench software is presented in Fig. 3.10.

The electrical model of the coil is considered at the macroscopic scale, hence for the 3D case, the electrical equations are consistent with the 1D case (see Section 3.2.1). The current density is computed as following:

$$J_{\mathrm{3D}}(t) = \frac{I(t) \cdot n_{\mathrm{tpp}}}{xi_{\max} \cdot dx \cdot yi_{\max} \cdot dy}. \tag{3.44}$$

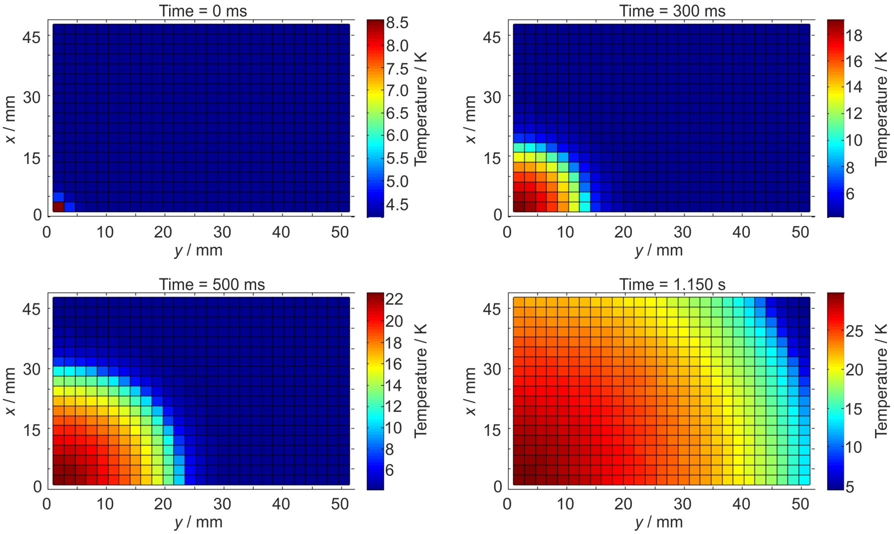

Figure 3.10.: Examples of temperature profiles in the coil cross–section (quench in the Super–FRS dipole magnet).

Optimal Mesh Size

In order to achieve the best correlation between the thermal model of the coil and reality, the number of mesh elements in the coil cross–section shall be equal to the number of turns [55]. The mesh size along the coil shall be adjusted to the temperature profile that occurs in the conductor. Since, the potted coil magnets have typically a few hundreds of turns, such an approach will lead to a very fine mesh for which the computation time will be relatively long. For instance in case of Super–FRS dipole, the coil has 560 turns (the conductor size equals to $\approx 2 \times 1$ mm). The average turn length is approximately 6.5 m. Therefore assuming the half–coil model represented in 325 elements along the z axis corresponding to the mesh element length of 10 mm, one gets the total number of mesh elements of 182000. Using the MATLAB® software, such a simulation will last for a few days on a typical office personal computer.

3.2.4 Heat Transfer to Helium

In the GSI 3D software, as an option, heat transfer to a helium bath can be taken into account. In order to explain how the cooling mechanism is applied to the thermal model of the coil, the properties of Helium and a short description of the physics behind the heat transfer to He are recalled.

Helium is used as a coolant for all LTS superconducting magnets. There are two stable isotopes available: ^{3}He and ^{4}He. ^{3}He is a very rare element, present on Earth only in trace amounts. Nevertheless because of its very low boiling point of 3.19 K at 1 atm (for comparison the boiling point of ^{4}He is 4.23 K), it is used for experiments at extremely low temperatures (< 1 K). Naturally, all large cryogenic installations operate with ^{4}He which is available in sufficient amounts [56].

The phase diagram of ^{4}He is presented in Fig. 3.11a. One can distinguish two different liquid states, gaseous phase and solid. The two liquid phases are: conventional liquid (He I) and superfluid (He II). The liquid phases are separated by the λ–line at which the transition from He I to He II takes place. At the λ–point located at 2.172 K and 5.043 kPa, there is a coexistence of the liquid He I, He II and gas. The properties of He I are similar to the classical fluid while the properties of the superfluid helium are characterised by very low viscosity and extremely high heat conductivity. The saturation curve separates the liquid phase from the gas phase. At the end of the saturation curve, the critical point is located ($T_\mathrm{c} = 5.23$ K and $P_\mathrm{c} = 0.227$ MPa). Above the critical point (at $T > T_\mathrm{c}$ and $P > P_\mathrm{c}$), ^{4}He goes to the supercritical state which means that the liquid He I and gaseous phase cannot be distinguished any–more. The solid phase occurs only at high pressure (> 25 bar) [56, 57].

The superfluid He is used as a coolant in LHC magnets [19, 38]. In the FAIR machines the two phase helium (He I/gas) is used for the force flow cooling of the SIS100 magnets while He I bath (at 1 bar) is used for the cooling of the Super–FRS magnets. Within this section, the case of the Super-FRS dipole in a liquid helium (He I) bath is considered.

When looking at the heat transfer at the coil/liquid He interface, the efficient cooling is lost when the liquid loses the contact with the coil surface. At very low heat flux q (in the range of 1 mW/cm^2), the heat transfer to helium is governed by convection (see Fig. 3.11b). At slightly higher heat flux ($\approx$ few mW/cm^2), the nucleate boiling starts. Many small gaseous bubbles occur at the surface level and detach, causing macroscopic turbulence (see Fig. 3.11c). When the heat flux is further increased, the nucleate boiling bubbles merge into a continuous gas film (layer). In this regime, the heat transfer is called the film boiling. The heat flux

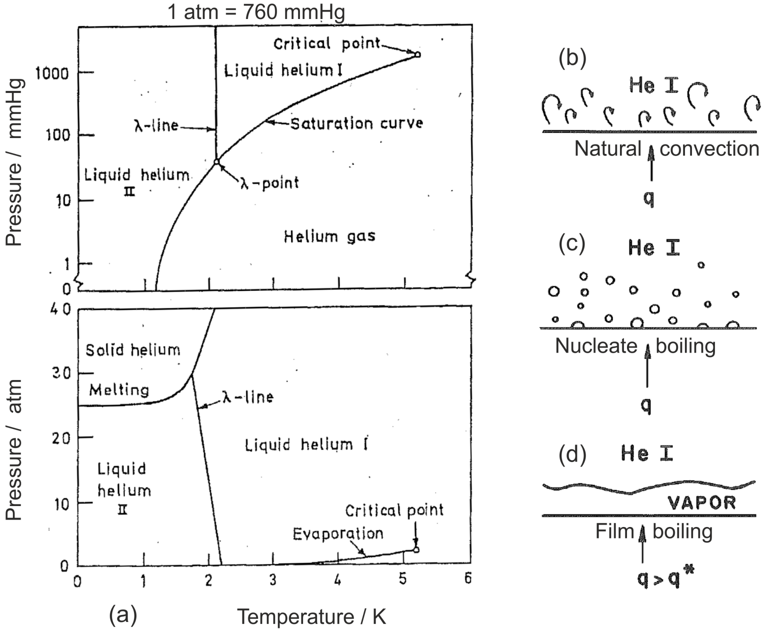

Figure 3.11.: Phase diagram for ^{4}He [58] (a) and regimes of heat transfer [56] (b-d).

that corresponds to the origin of the film boiling is called the peak boiling nucleate heat flux q^* (see Fig. 3.11d) [56,58–61].

A good experimental data set concerning the heat transfer to liquid He I is reported in [59] where measurements of the heat flux P_{sHe} from the heated aluminium plate to liquid He I can be found. Two aluminium samples with different surface condition were investigated under various orientation to the Helium (inclination angle). At 0° the aluminium surface points downwards which provides the worst cooling conditions. The fitting function for the heat flux in conjunction with the measurement data is presented in Fig. 3.12. The fit is based on the functions found in [56,57] and was proposed by Floch [24] to be used in the 3D quench calculation software. The expression for P_{sHe} can be found in Appendix K.

In order to introduce the heat transfer to He in the thermal model of the coil, one has to subtract from the Joule heating power density (ϱJ^2), the power that is taken over by the helium via the contact surface A_{He}. This action has to be

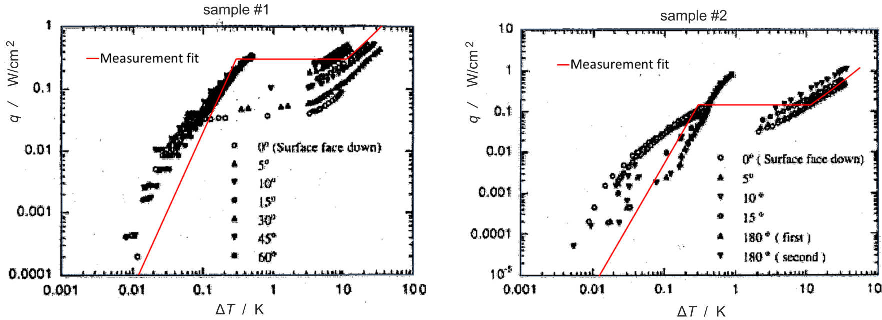

Figure 3.12.: Heat flux vs. temperature difference between the surface in He for high purity aluminium with texture (sample #1) and smooth (sample #2) surface, in liquid helium bath at 4.21 K with different sample orientation [59].

done for all mesh elements located at the interface coil/He. Then, the heat balance equation takes the form of:

$$\varrho(RRR, B, T) \cdot J^2(t) - \frac{1}{\mathrm{vol}} \oiint\limits_{A_{\mathrm{He}}} P_{\mathrm{sHe}}(\Delta T) \cdot dA_{\mathrm{q}} + \\ + \nabla \left[k(RRR, T) \cdot \nabla T(x, y, z, t) \right] = C_{\mathrm{V}}(B, T) \cdot \frac{\partial T(x, y, z, t)}{\partial t}, \tag{3.45}$$

where "vol" is the coil volume. Considering a single mesh element, the heat transfer to He is described by:

$$\frac{1}{\mathrm{vol}} \oiint\limits_{A_{\mathrm{He}}} P_{\mathrm{sHe}}(\Delta T) \cdot dA_{\mathrm{q}} = \frac{A_{\mathrm{He}} \cdot P_{\mathrm{sHe}}(T^{ti}_{xi,yi,zi} - T_{\mathrm{He}})}{dx \cdot dy \cdot dz}, \tag{3.46}$$

where $A_{\mathrm{He}} = 0$ or $A_{\mathrm{He}} = dx \cdot dz$ or $A_{\mathrm{He}} = dy \cdot dz$ depending on the mesh element position in the coil model.

Referring to the matrix equation of the 3D thermal model (3.41), the heat transfer to He has to be included in the d_{xyz} coefficients as following:

$$
d_{xyz}(xi, yi, zi, ti) = \\
= \left[\varrho(RRR, B^{ti}_{xi,yi,zi}, T^{ti}_{xi,yi,zi}) J^2(ti) - \frac{A_{\mathrm{He}} P_{\mathrm{sHe}} (T^{ti}_{xi,yi,zi} - T_{\mathrm{He}})}{dx \cdot dy \cdot dz} \right] \cdot \frac{dt}{C_V(B^{ti}_{xi,yi,zi}, T^{ti}_{xi,yi,zi})}. \tag{3.47}
$$

4 Validation of the GSI Quench Calculation Software

The GSI quench calculation software is validated by comparing with selected measurements performed on prototypes of FAIR magnets. At the time of writing this thesis, only several SIS100 dipole prototypes and one conceptual Super–FRS dipole prototype was manufactured and tested. The SIS100 dipole prototypes were tested at GSI while the Super–FRS dipole prototype was tested at IMP[1] and the test results were shared with GSI.

4.1 Quench Calculations and Measurements on SIS100 Dipole Prototype

This section presents quench measurements of the SIS100 dipole magnet (the latest design). These measurements were conducted in the course of this Ph.D. work. The SIS100 dipole magnet utilises a super–ferric, window–frame construction. The coil is wound with Nuclotron–type cable in a single layer of eight turns (four turns per magnetic pole). Since SIS100 is a fast–cycling machine (with the ramp rate of 4 T/s which corresponds to $\approx$ 28 kA/s), a special low AC loss superconducting cable is used for the coil [39]. On one hand, the AC losses were reduced by using CuMn inter–filamentary matrix in the superconducting strands and on the other hand by reducing the NbTi–filament size down to 3 μm. CuMn is characterised by higher resistance than Cu and therefore the path for the induced eddy currents is more resistive which decreases the inter–filament coupling in each strand [62, 63]. The SIS100 single–layer dipole magnet prototype is presented in Fig. 4.1.

The SIS100 dipole prototype (single layer) was intensively tested at the GSI test facility [64]. The results can be used to validate the GSI quench calculation software. During the quench study testing campaigns, the magnet was powered according to the scheme shown in Fig. 2.24 (Section 2.5). A variable energy extraction resistor (resistance range: 0–36 mΩ) was used for the magnet protection. Quench detection was assured by a balance bridge with a quench threshold of 200 mV which corresponds to a quench voltage (V_q) of 400 mV (see Section 2.6). The voltage signals were acquired via voltage taps. A voltage tap is a connection point on the superconducting circuit (e.g. coil, current lead, bus–bar, splice, etc.) which

---

[1] IMP – Institute of Modern Physics in Lanzhou/China.

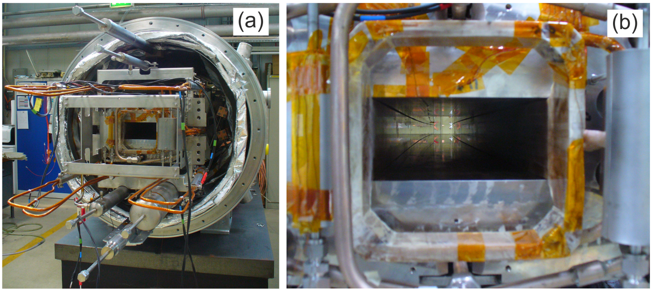

Figure 4.1.: SIS100 single layer dipole prototype: (a) view on the connection side, (b) coil–end connection, magnetic aperture and yoke curvature.

enables a measurement of the electrical potential. The quench signal was validated over a 10 ms–long time period (t_{v}). The procedure during the quench study measurements was as following. At first the magnet was operated at a certain DC current. Then, a quench was introduced via an inductive spot heater located on the coil bus–bar. After a quench trigger had been sent to the protection system, the dump resistor was activated and the magnet was discharged. At each quench the following signals were recorded:

- magnet current;
- bridge voltage V_{b} (which is equal to half of the quench voltage V_{q});
- quench propagation velocity v_{fp} (indirect measurement);
- hot–spot temperature T_{max} (indirect measurement).

The quench propagation velocity was measured indirectly via additional voltage taps (V–taps) installed at the coil bus–bar. The locations of the spot heater and additional V–taps are presented in Fig. 4.2. The spot heater is located between V–taps VQ01 and VQ02. In total, there are six V–taps dedicated to the quench propagation velocity measurement: VQ01–VQ06. For the considered prototype, the exact distance between V–taps is presented in Tab. 4.1.

An example of voltage signals induced by the expanding normal zone is presented in Fig. 4.2. The quench was introduced into the bus–bar at the current of 2 kA. v_{fp} is calculated by dividing the distance between VQ03–VQ05 by the time needed for the quench propagation between VQ03 and VQ05 (the corresponding voltages are marked with the red and green traces). It is also possible to compute v_{fp} with the use of VQ01/VQ02 and VQ03/VQ04. Then, a higher uncertainty has to be

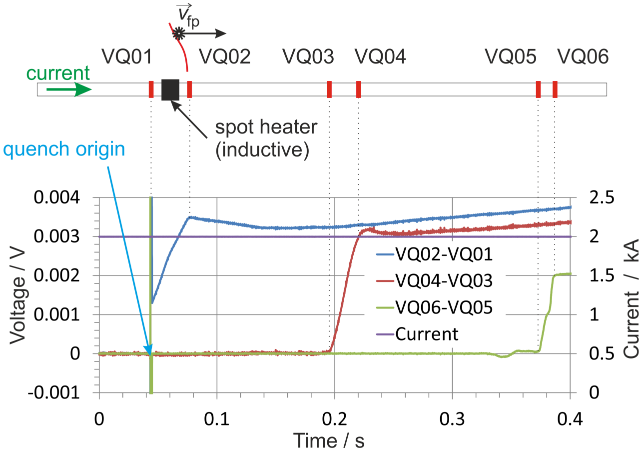

Figure 4.2.: Principle of quench propagation velocity measurement.

taken into account due to the forced transition to the resistive state coming from the discharge on the spot heater. During the measurement of v_{fp}, one has to assure that the quench voltage reaches VQ06 before the quench detection system gives the trigger for the current dump.

Table 4.1.: Distance between voltage taps dedicated to the quench study

V–tap	V–tap	distance (mm)
VQ01	VQ02	47.8 ± 1.0
VQ02	VQ03	214.7 ± 1.0
VQ03	VQ05	536.8 ± 1.0
VQ03	VQ04	47.8 ± 1.0
VQ05	VQ06	30.6 ± 1.0

During the quench study campaign, the magnet was always quenched by a spot heater located between voltage taps VQ01 & VQ02. Since in the considered magnet the hot–spot is located in the quench origin, the area between VQ01 & VQ02 will be featured with the maximum temperature. Knowing the magnet current and measuring the voltage across VQ02–VQ01, one can compute the resistance increase in the bus–bar piece between VQ01 & VQ02. Since the cable resistance is correlated with temperature, the temperature can be derived as follows:

$$R_{\mathrm{VQ01\text{–}VQ02}} = \frac{V_{\mathrm{VQ02\text{–}VQ01}}}{I_{\mathrm{magnet}}} = \varrho_{\mathrm{cable}}(RRR, T, B) \cdot \frac{L_{\mathrm{VQ01\text{–}VQ02}}}{A_{\mathrm{cond}}} \quad \Rightarrow$$
$$\Rightarrow \quad T = f^{-1}(R_{\mathrm{VQ01\text{–}VQ02}}), \qquad (4.1)$$

where A_{cond} is the cross–section of the conductor, $L_{\mathrm{VQ01\text{–}VQ02}}$ is the distance between the voltage taps VQ01 & VQ02 and ϱ_{cable} is the resistivity of the SIS100–type main cable given in Appendix H. f^{-1} is an inverse function of $R_{\mathrm{cable}}(T)$.

The hot–spot temperature depends on the quench detection threshold and on the overall resistance of the protection system (see Section 3.1.2). Figure 4.3 presents the MIITs, the hot–spot temperature, and the current decay measured on the SIS100 dipole prototype. During the measurements, the quench threshold was set to 400 mV (200 mV at V_{b}) and the validation time was fixed to 10 ms. The quench was introduced via an inductive spot heater. There are two measurements shown in Fig. 4.3:

- when R_{d} was fixed to 5.4 mΩ which corresponds to a time constant τ of 100 ms,
- when R_{d} was fixed to 36 mΩ which corresponds to $\tau = 15$ ms.

At the test facility, when a stand–alone magnet is powered, one uses the highest available R_{d} in order to discharge the current as fast as possible. Thus, the time period required for the magnet recovery from a quench is minimised. In the SIS100 dipole circuit (see Appendix O), there are 108 magnets (each magnet featured with inductance of $L_d = 0.56$ mH) connected in series. In order to obtain $\tau \approx 15$ ms, one would require a total dump resistance of:

$$R_{\mathrm{d}}^{\mathrm{total}} = \frac{108 \cdot L_{\mathrm{d}}}{\tau} \approx 4\ \Omega. \qquad (4.2)$$

Such a high $R_{\mathrm{d}}^{\mathrm{total}}$ at the nominal current of 13.1 kA would induce a total circuit voltage of 52.5 kV which even if divided in multiple resistors, would become impossible to handle (no HV switches available at this range, the magnet insulation cannot be designed for such a high voltage, etc.). Therefore, the dump resistors are fixed to the maximum value at which the temperature at the hot-spot stays below 350 K.

Considering the protection of a stand–alone magnet, a higher R_{d} dominates the current decay ($R_{\mathrm{d}} \gg R_{\mathrm{q}}$, $\tau \approx L_{\mathrm{d}}(I)/R_{\mathrm{d}}$) while for R_{d} in the range of few mΩ,

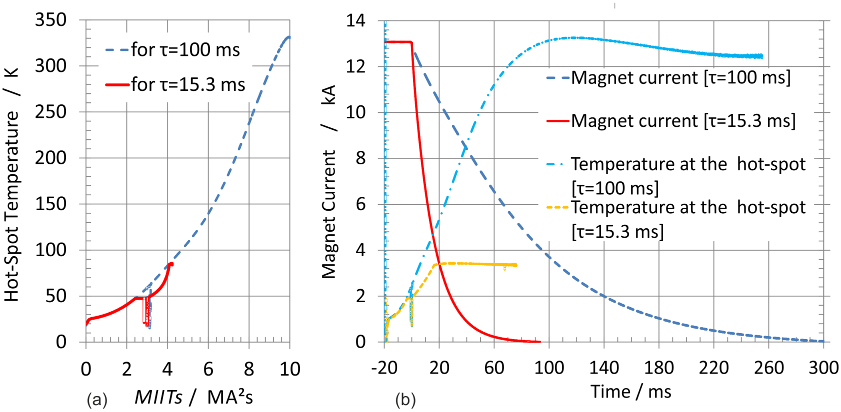

Figure 4.3.: Measurements on the SIS100 dipole prototype (single layer): (a) temperature at hot-spot vs. $MIIT$s , (b) current decay and hot–spot temperature increase.

the current decay is dominated by R_{d} only at the beginning. Later the developed quench resistance $R_{\mathrm{q}}(t)$ is no longer negligible and the current dump is accelerated by the developing R_{q} ($\tau \approx L_{\mathrm{d}}(I)/[R_{\mathrm{d}} + R_{\mathrm{q}}(t)]$).

Referring to Fig. 4.3, for $R_{\mathrm{d}} = 5.4$ mΩ ($\tau \approx 15$ ms) the temperature at the hot spot reaches ≈ 340 K which is close to the limit of 350 K being still considered as safe. Therefore, the measurements with $R_{\mathrm{d}} = 5.4$ mΩ were chosen as the reference for the software validation.

4.1.1 GSI Software Validation (1D)

The quench behaviour in the magnet coil is approximated by two various 1D models:

- “conductor model” which considers only the superconducting strands,
- “cable model” which takes into account 23 strands, the CuNi tube and the ground insulation (Kapton).

In both models the volumetric proportion of the involved material is taken into account according to the cable construction which is described in Appendix H. The cooling with the force–flow two–phase helium is not included in the thermal model. However adiabatic conditions are assumed. Both magnet models are featured with an inductance $L_{\mathrm{d}}(I)$ in order to include the characteristic of the magnetic yoke (see Fig. J.3). The protection scheme considers an energy extraction resistor R_d of 5.4 mΩ. The quench simulation considers a resistive zone occurrence at a fixed constant current. When the arising quench voltage exceeds the predefined threshold ($V_\mathrm{q} > 400$ mV), the current is still kept in the coil for a predefined validation time ($t_\mathrm{v} = 10$ ms) and then the dump resistor is activated.

In order to validate the GSI 1D quench calculation software, four quench measurements (at 13.1, 10, 7 and 4 kA) are compared to simulations.

Magnet Quench at 13.1 kA

A comparison between a quench recorded at 13.1 kA and the corresponding quench calculations ("conductor model" and "cable model") is presented in Figure 4.4 where the magnet current, temperature at the hot–spot, quench voltage and quench resistance behaviour are shown. For both models, the calculated current decays are very similar to each other and they are slightly faster than the measured decay. The highest temperature is obtained for the calculation with the "conductor model". The latter can be explained by the fact that the "conductor model" concerns the smallest volume of the conductor (only superconducting wires) which is warmed up by the Joule heating. Taking a glance at the quench voltage, the calculated voltages show a good agreement with the measured data up to the moment when a difference between the current curves occurs. The maximum of V_q for the "cable model" is slightly lower than for the "conductor model" equivalent and for the measured voltage. Figure 4.4 also shows the calculated quench resistance R_q which reaches 4.4–4.8 mΩ – the same order of magnitude as the dump resistance (5.4 mΩ).

Magnet Quench at 10 kA

A comparison between a quench recorded at 10 kA and the corresponding quench calculations ("conductor model" and "cable model") is presented in Figure 4.5 where the magnet current, temperature at the hot–spot, quench voltage and quench resistance behaviour are shown. Concerning the current and temperature the conclusion is the same as in case of quench at 13.1 kA. Looking at the quench voltage, the calculated V_q develops faster and its maximum is slightly higher than the measured V_q. For the both models, the quench resistance behaviour is similar and the maximum of R_q is calculated as 1.85 mΩ.

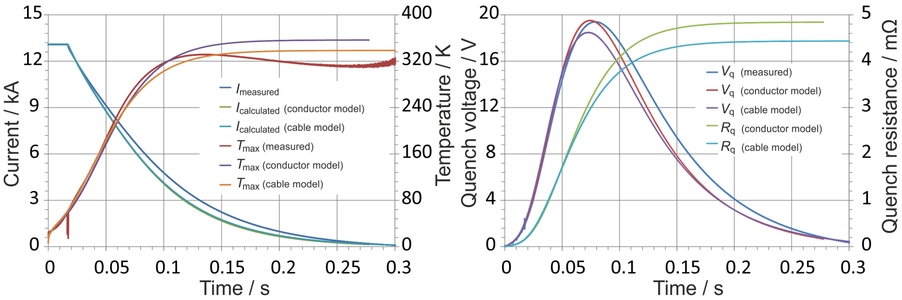

Figure 4.4.: Current decay, temperature at the hot–spot, quench voltage and quench resistance measured and calculated for the SIS100 dipole prototype. Case of a stand–alone magnet protected with an energy extraction resistor of 5.4 mΩ.

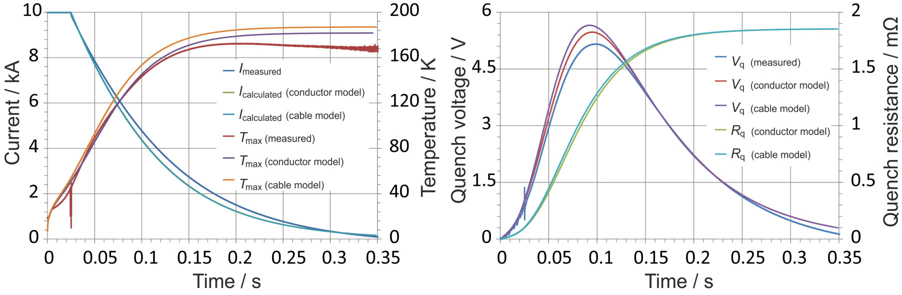

Figure 4.5.: Current decay, temperature at the hot–spot, quench voltage and quench resistance measured and calculated for the SIS100 dipole prototype. Case of a stand–alone magnet with an energy extraction resistor of 5.4 mΩ.

Magnet Quench at 7 kA

A comparison between a quench recorded at 7 kA and the corresponding quench calculations (“conductor model” and “cable model”) is presented in Figure 4.6 where the magnet current, temperature at the hot–spot, quench voltage and quench resistance behaviour are shown. The calculated current decay is in very good agreement with the measurement. So is the temperature calculated with the “cable model”. Similarly to quenches at 13.1 and 10 kA, the calculation with the “conductor model” features with the highest T_{max}. The computed R_{q} reaches

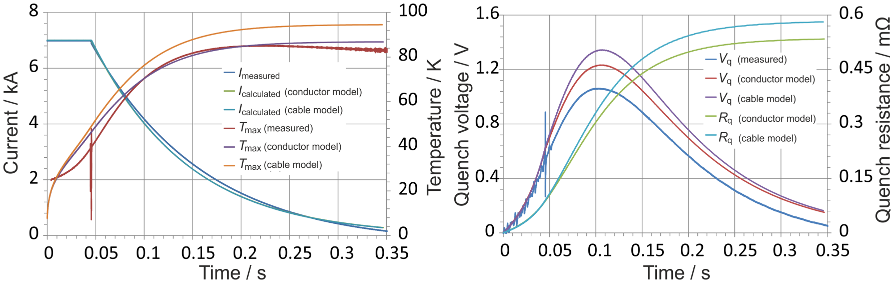

Figure 4.6.: Current decay, temperature at the hot–spot, quench voltage and quench resistance measured and calculated for the SIS100 dipole prototype. Case of a stand–alone magnet with an energy extraction resistor of 5.4 mΩ.

$\approx$ 0.5 mΩ which means that the current decay is dominated by R_d (5.4 mΩ). The calculated quench voltages are higher than the measured V_q.

Magnet Quench at 4 kA

A comparison between a quench recorded at 4 kA and the corresponding quench calculations ("conductor model" and "cable model") is presented in Figure 4.7 where the magnet current, temperature at the hot–spot, quench voltage and quench resistance behaviour are shown. In this case the calculated data are not in good accordance with the measurement. However the computed temperature and quench voltage can be treated as the worst case scenario because of their maximum values are higher than the measurement. The computed R_q reaches $\approx$ 0.23 mΩ which means that similarly to the quench recorded at 7 kA, the current decay is dominated by R_d (5.4 mΩ).

Quench Propagation Velocities

The measured and calculated quench propagation velocities are presented in Fig. 4.8. At higher currents (above 5 kA), the calculation with the "cable model" gives a much better fit to the measurement data than the "conductor model". The results obtained with the both models show a good agreement with the measured v_pf at currents lower than 5 kA.

Since in the SIS100 machine, dipole and quadrupole coils will be manufacturer

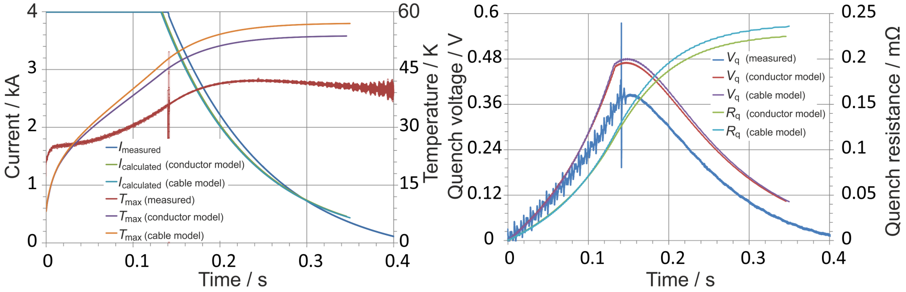

Figure 4.7.: Current decay, temperature at the hot–spot, quench voltage and quench resistance measured and calculated for the SIS100 dipole prototype. Case of a stand–alone magnet with an energy extraction resistor of 5.4 mΩ.

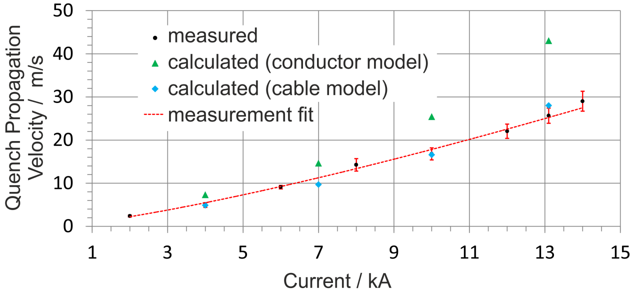

Figure 4.8.: Quench propagation velocity measured and calculated on the SIS100 dipole prototype.

from very a similar Nuclotron–type cable, it is useful to give a measurement fit for the quench propagation velocity of the SIS100 main cable:

$$v_{\text{pf}}^{(\text{SIS100 main cable})}\ [\text{m/s}] = 0.921095 \cdot (I\ [\text{kA}])^{1.28678}. \tag{4.3}$$

This measurement fit can be used i.a. for fast quench calculations of the dipole and quadrupole circuits of SIS100. For example, let us consider the dipole circuit in which the 108 magnets are powered in series. Due to the low AC loss Nuclotron–type cable, no quench back effect is expected because of $\mathrm{d}I/\mathrm{d}t$ at the current dump. That means if a quench originates in a particular dipole, it will spread over the circuit with v_{pf}. Most probably, no new normal zones will occur in other magnets. The study of v_{pf} revealed that during a quench, the quench propagation is slower than 30 m/s. Referring to Fig. 4.3b ($\tau = 100$ ms), the time counted from the quench origin to the end of the current dump is equal to approximately 300 ms. Hence, roughly calculating, within the quench time of 300 ms, only 9 m (30 m/s × 300 ms) of superconducting cable has a chance to become resistive. Taking into account the fact that the dipole coil is wound with approximately 51 m of cable, a quench in the dipole ring will be confined within a single magnet (only if the quench happens at the coil extremity it can spread towards the adjacent dipole). The latter is very important when calculating the overall dump resistance in the ring, since the current dump will not be accelerated by the quench resistance ($R_\mathrm{q}(t) \ll R_\mathrm{d}^\mathrm{total}$).

4.1.2 Calculation Summary and Software Limits

The comparisons presented in Figures 4.4–4.7 shows that quench calculations performed with the GSI software give a good estimation of the quench behaviour. The calculation can be also interpreted as the worst case scenario, since the measured temperature at the hot–spot was never higher than the calculated equivalent. The “cable model” gives a better approximation of the maximum temperature. On the other hand, the “conductor model” gives a quench voltage which is slightly closer to the measured V_q. When using the “cable model” the calculated quench propagation velocity is in very good agreement with the actual quench propagation velocity which was measured during the quench study testing campaign. The general conclusion is that the GSI 1D quench calculation software can successfully be used for quench calculations of the SIS100 dipole and quadrupole magnets (a very similar cable will be used for both magnets). The main software limitations is that the force–flow cooling with two–phase helium is not included in the model.

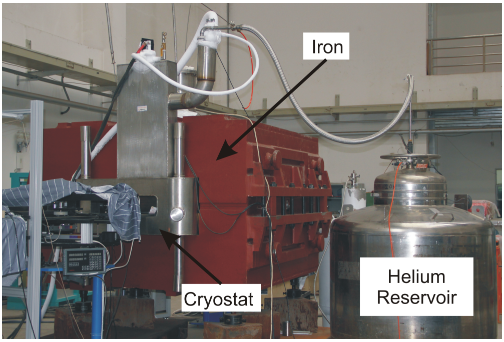

Figure 4.9.: Super–FRS dipole prototype (courtesy of IMP Lanzhou).

4.2 Quench Calculations and Measurements on Super–FRS Dipole Prototype

The first Super–FRS dipole prototype was designed and manufactured by the FAIR China Group[2] (FCG) in cooperation with GSI [65]. Figure 4.9 shows the magnet at the test stand at IMP. The prototype is a potted coil super–ferric H–type magnet. It has two coils, wound with 560 turns each (28 layers with 20 turns in each). The conductor used for the coil has a special construction called "wire in channel" (see Fig. 4.10) which is characterised by a very high copper–to–superconductor ratio ($\alpha = 10.8$). The conductor is built from a round superconducting strand (NbTi/Cu) immersed into a rectangular copper stabilizer (with a groove) and then soldered. The scheme of the coil cross–section is shown in Fig. 4.11. The main parameters of the dipole prototype are presented in Tab. 4.2.

The Chinese prototype was intensively investigated at IMP in years 2009–2010 and the test results were shared with GSI. The test program was oriented most of all on the cryogenic stability and mechanical issues. Nevertheless three sets of quench data were recorded. The analysis of the delivered quench measurements was performed in the frame work of this Ph.D. Figure 4.12 shows a scheme of the electrical circuit which was used during the testing campaigns. Although the magnet was designed as self–protecting, the protection system was equipped with an energy extraction resistor of 1.18 Ω. R_d could be activated (via a mechanical switch) in order to reduce the maximum temperature and minimize the time needed to cool down the system after occurrence of a quench.

---

[2] FCG is a collaboration of the Institute of Modern Physics (IMP Lanzhou), Institute of Plasma Physics (ASIPP, Hefei) and Institute of Electric Engineering (IEE, Beijing).

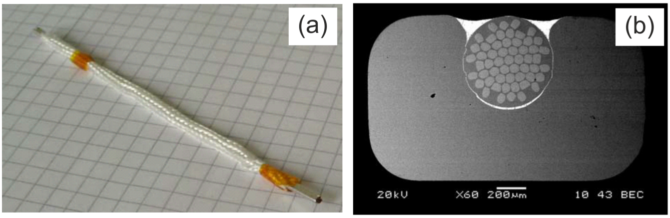

Figure 4.10.: The conductor used for the Super–FRS dipole prototype (courtesy of Oxford Instruments): a bus–bar piece made of the insulated conductor(a), cross–section of the conductor (b).

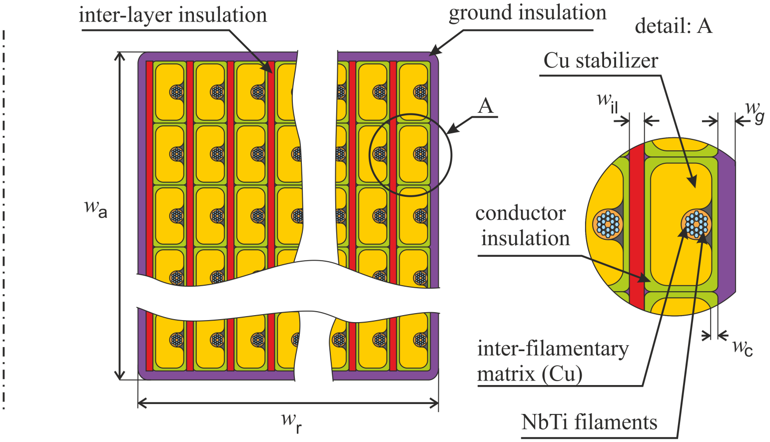

Figure 4.11.: Scheme of the coil cross–section of the Super–FRS dipole magnet.

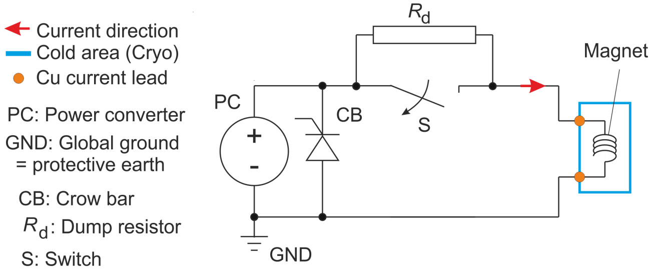

Figure 4.12.: Electrical circuit used during powering of the Super–FRS dipole prototype.

Table 4.2.: Main parameters of the Super–FRS dipole prototype [54]

Quantity	Value	Unit
I_n	232	A
L_d at $I = 0$	21.5	H
E_mag at I_n	414	kJ
B_n at the conductor	1.33	T
Number of turns	560	–
Average turn length	6.576	m
Pole cross–section ($w_\mathrm{a} \times w_\mathrm{r}$)	48.8×52.2	mm^2
NbTi cross–section (single conductor)	0.173	mm^2
Cu/NbTi ratio	10.8	–
Conductor insulation thickness	0.11	mm
Inter–layer insulation thickness	0.3	mm
Ground insulation thickness	2	mm

4.2.1 GSI Software Validation (3D)

The 3D thermal model of the magnet coil is approximated by a long straight slab as described in Section 3.2.3. The electrical model includes the inductance which reflects the magnetic yoke characteristics (see Fig. 3.6). Since only the maximum field on the conductor is known (B_{n} at I_{n}), a linear approximation is included in the simulation: $B_{\max}(I) = B_{\mathrm{n}} \cdot I/I_{\mathrm{n}}$. The maximum of the magnetic field which acts on the conductor is located at the inner surface of the coil and it decreases along the radial axis (y). In the model, it is assumed that $B(y) = B_{\max} \cdot (1 - y/w_{\mathrm{r}})$, where y is the axis along the radial direction. The quench measurements and calculations on the considered magnet are presented in [54, 66] and in the next paragraphs.

The first measurement data set considers a quench at 240 A. During the experiment, the energy extraction system was disabled ($R_{\mathrm{d}} = 0$) and the quench detection threshold was fixed to 4 V (2 V at V_{b}). The total delay time between detecting the quench and short–circuiting of the magnet, was approximately 50 ms (sum of t_{v} and delay of the mechanical switch). Figures 4.13 and 4.14 show a comparison between the measured data and corresponding 3D quench simulations performed with two quench calculation software solutions (GSI software and SQUID[3]). The current decay and the quench resistance behaviour are shown in Fig. 4.13 while the quench voltage and the temperature increase (at the hot–spot) are shown in Fig. 4.14. The quench calculations show a very good agreement with the measurements. Unfortunately no temperature measurement was provided in Lanzhou. Thus, instead of measured temperature, a temperature calculated with MIITs is superimposed (the worst case scenario).

---

[3] see Section I.

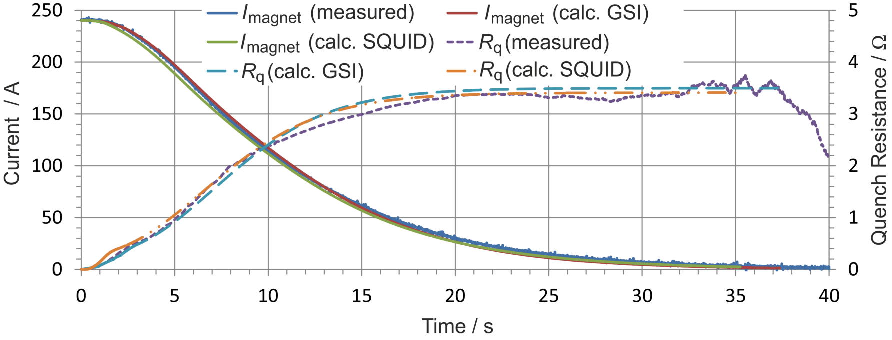

Figure 4.13.: Current decay and quench resistance behaviour measured and computed for the Super–FRS dipole. Case of a stand–alone magnet with no energy extraction system.

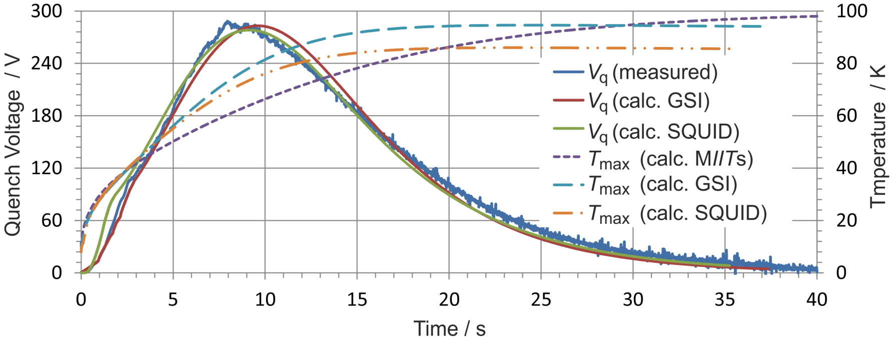

Figure 4.14.: Quench voltage and temperature at the hot–spot measured and computed for the Super–FRS dipole. Case of a stand–alone magnet with no energy extraction system.

Another quench was recorded at the current of 236 A. At the time of this measurement, the energy extraction was realised by two subsystems:

- activation of classical dump resistor ($R_\mathrm{d} = 1.18\ \Omega$),
- energy return to the electrical system by the power converter (reverse mode at $V_\mathrm{PC} = -158$ V).

The quench detection threshold was fixed to 4 V (2 V at V_b) and the summarised delay time between detecting the quench and activating the energy extraction was approximately 425 ms. Figure 4.15 shows a comparison between the measured quench and corresponding 3D quench simulations performed with two quench software solutions (GSI software and SQUID). The quench calculations show a very good agreement with the measurements.

The last received measurement data set concerns a quench at 278 A. In that case, the energy extraction was realised by returning the energy to the electrical system via the power converter in the reverse mode at $V_\mathrm{PC} = -158$ V. The quench detection threshold was fixed to 4 V (2 V at V_b) and the summarised delay time between detecting the quench and activating the energy extraction was approximately 445 ms. Figure 4.16 shows a comparison between the measured quench and corresponding 3D quench simulations performed with two quench software solutions (GSI software and SQUID). The quench calculations shows a very good agreement with the measurements.

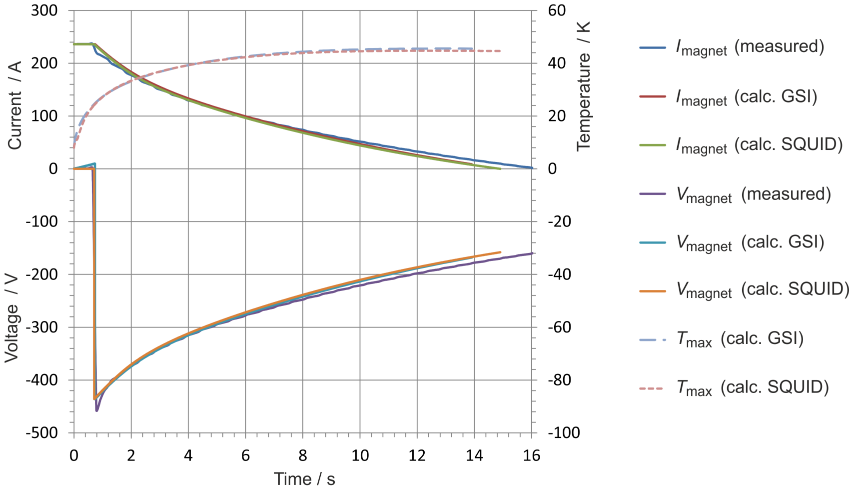

Figure 4.15.: Current decay, magnet voltage and temperature at the hot–spot measured and computed for the Super–FRS dipole. Case of $R_\mathrm{d} = 1.18\ \Omega$ and reverse operation of the power converter at -158 V.

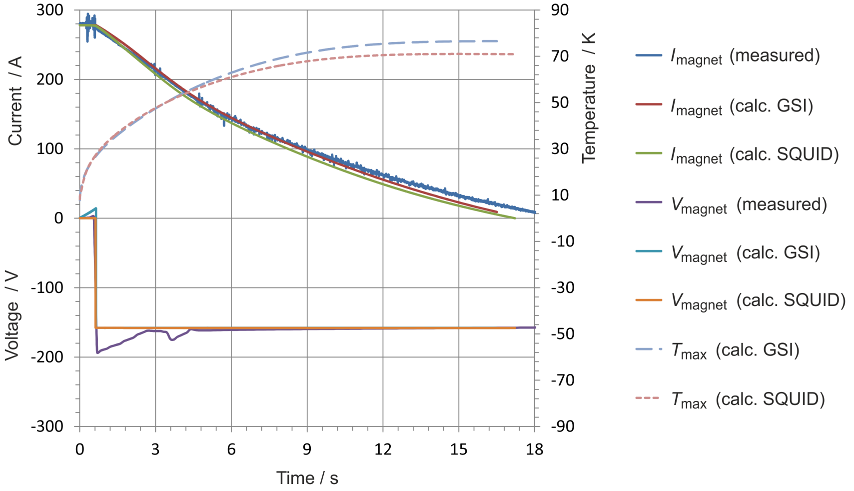

Figure 4.16.: Current decay, magnet voltage and temperature at the hot–spot measured and computed for the Super–FRS dipole. Case of $R_\mathrm{d} = 0$ and reverse operation of the power converter at -158 V.

4.2.2 Quench Calculation with and without Heat Transfer to He

In order to check the influence of the term which describes the heat transfer to He, two cases (with and without heat transfer to He bath) were considered for quench simulations. The following simulation parameters where adjusted:

- number of mesh elements: $20 \times 28 \times 325$;
- inductance characteristics that takes into account the yoke saturation – see Fig. 3.6;
- quench detection threshold at 600 mV, 10 ms of validation time, 40 ms delay for turning off the power converter (magnet short–circuit);
- no energy extraction system;
- quench was introduced to the coil model at the current of 240 A by assigning the initial temperature of 10 K in 200 out of 182000 mesh elements.

The calculation results are presented in Fig. 4.17 – the current decay and the hot–spot temperature and in Fig. 4.18 – quench voltage and quench resistance development. Paradoxically, the hot spot temperature for the computation including cooling is slightly higher than the one that assumed adiabatic conditions. This is due to the fact that the quench resistance for the case with cooling develops slower and therefore the current discharge takes longer time what heats up the conductor at the hot–spot to a higher temperature. It is worth to add that the difference between the two calculations would be even smaller if e.g. a dump resistor of 3 Ω is considered. In this case, the current discharge would be dominated by the dump resistor.

Energy Balance

In order to estimate the ratio between the energy initially stored in the magnet to the energy absorbed by He, the energy balance has to be considered. The energy stored in the magnet at 240 A is equal to E_{mag}. In adiabatic conditions E_{mag} is equal to the energy dissipated in the coil $E_{\mathrm{coil}}^{\mathrm{adiabatic}}$. Therefore:

$$E_{\mathrm{mag}} = E_{\mathrm{coil}}^{\mathrm{adiabatic}} \quad \Rightarrow \quad \frac{1}{2} \cdot L_{\mathrm{w}}(I_0) \cdot I_0^2 = \int\limits_{t=0}^{\infty} I^2(t) \cdot R_{\mathrm{q}}(t) \cdot \mathrm{d}t. \tag{4.4}$$

At 240 A, the magnet inductance L_{w} equals to 14.8 H.

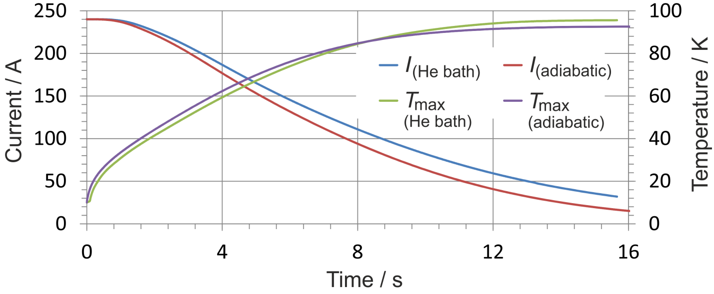

Figure 4.17.: Current decay and hot–spot temperature computed in adiabatic conditions and for a coil in an infinite He bath.

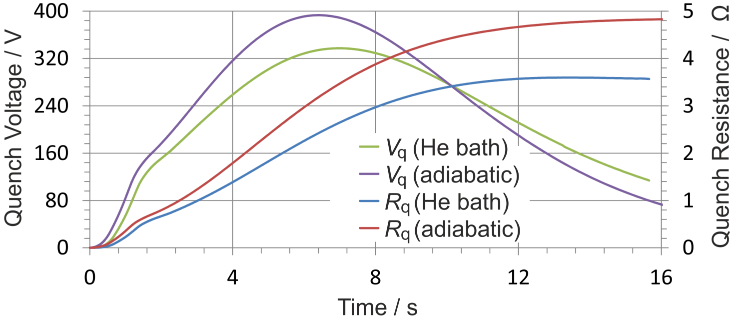

Figure 4.18.: Quench voltage and quench resistance development computed in adiabatic conditions and for a coil in an infinite He bath.

Hence $E_{\mathrm{mag}} = E_{\mathrm{diss}}^{\mathrm{adiabatic}} = 425.7$ kJ.

For the calculation with the heat transfer to He, a fraction of E_{mag} is absorbed by He (E_{He}) and the rest is dissipated within the coil (E_{coil}). Therefore, the energy balance is described by:

$$E_{\mathrm{mag}} = E_{\mathrm{coil}} + E_{\mathrm{He}} \quad \Rightarrow \quad \frac{1}{2} \cdot L_{\mathrm{w}}(I_0) \cdot I_0^2 = \int\limits_{t=0}^{\infty} I^2(t) \cdot R_{\mathrm{q}}(t) \cdot \mathrm{d}t + E_{\mathrm{He}}. \quad (4.5)$$

For the considered case: $E_{\mathrm{coil}} = \int\limits_{t=0}^{\infty} I^2(t) \cdot R_{\mathrm{q}}(t) \cdot \mathrm{d}t = 417.6$ kJ and $E_{\mathrm{He}} = 425.7 - 417.6 = 8.1$ kJ. Therefore the $E_{\mathrm{He}}/E_{\mathrm{mag}}$ ratio is equal to approximately 2% and one can conclude that the impact of the heat transfer to He is negligible to the extent of the considered constraints.

In the calculation with cooling, an infinite He bath is considered. Taking into account the latent heat of liquid He I which is 20.7 kJ/kg and the corresponding density 0.1247 kg/l – both at 4 K and 1 bar, an evaporation of 1 litre of He requires 2.6 kJ of energy (rough calculation). In the Super–FRS dipole, only the coil is immersed into the He bath. The cryostat is filled with approximately 20 litres of He. In order to vaporize 20 l of He, an energy of 51.6 kJ is required. One needs to remember that heating up the helium, increases the overall pressure in the cryostat. When the He pressure exceeds the design pressure of the cryostat, a safety valve opens and all the helium is released to the cryostat surroundings [67].

4.2.3 Calculation Summary and Software Limits

The GSI 3D quench calculation software gives reasonable results that are in very good agreement with the available quench measurements. It has to be said that the quench data recorded at 236 and 278 A, are strongly dominated by the extraction system which involves the reverse mode of the power converter. Therefore, validation of the 3D thermal model of the coil based on these measurements is limited. On the other hand, the quench recorded at 240 A considers a quenched short–circuit magnet which enables to compare the quench resistance and quench voltage behaviour to their equivalents obtained with simulations. A good agreement achieved for this case, enables to conclude that the GSI 3D software can be successfully used for quench study of the Super–FRS magnets and other potted coil magnets. The disadvantage of the software is a relatively long computation time (few days on a typical office personal computer) when using fine mesh. Mesh is considered as fine when the cross section of a single mesh element is comparable to the cross–section of a single superconducting wire.

5 Contributions to the Quench Detection System of SIS100

5.1 Main Circuits: Dipole and Quadrupole Magnets

The quench detectors that are planned for SIS100 (as for the most of superconducting machines built so far) rely on voltage signals acquired via voltage taps. Except the current leads, voltage taps are located directly at the superconducting cable. In order to measure the electrical potential, one needs to connect a signal wire (so called voltage tap wire) and bring it outside the cryostat via a dedicated feedthrough. The feedthrough needs to be vacuum tight and fulfil the requirements for high voltage, radiation hardness and, if applicable, Paschen tightness (see Appendix M).

Based on the experience gained from the other projects (Tevatron, Nuclotron, RHIC and LHC), the analogue bridge solution is always preferable for the protection of individual superconducting magnets. Therefore, the first proposal for the quench detection of SIS100 assumed resistive bridges. It was considered to use two layers of detection: the primary for individual magnets and the secondary for protection against symmetrical quenches and survey of bus–bars & splices [24]. After a detailed analysis of the main circuits, it turned out that with the initially planned amount of voltage taps, the estimated leakage current due to the equivalent parasitic capacitance reaches the level of current accuracy required for the machine operation. The equivalent parasitic capacitance of the circuit refers to:

- capacitance to ground of the coils and bus–bars (including coil assembly),
- capacitive coupling between coils and bus–bars to other independent circuits,
- capacitance introduced via the voltage taps.

The parasitic capacitance becomes the dominant source of current leaks whenever there is a change in voltage ($i_{\text{leakage}} = C\frac{dV}{dt}$). Figure 5.1 presents the current and overall voltage waveforms for the dipole circuit of SIS100 during the proton cycle. The most rapid change of the voltage takes part at the start of the ramp (50 ms rounding time).

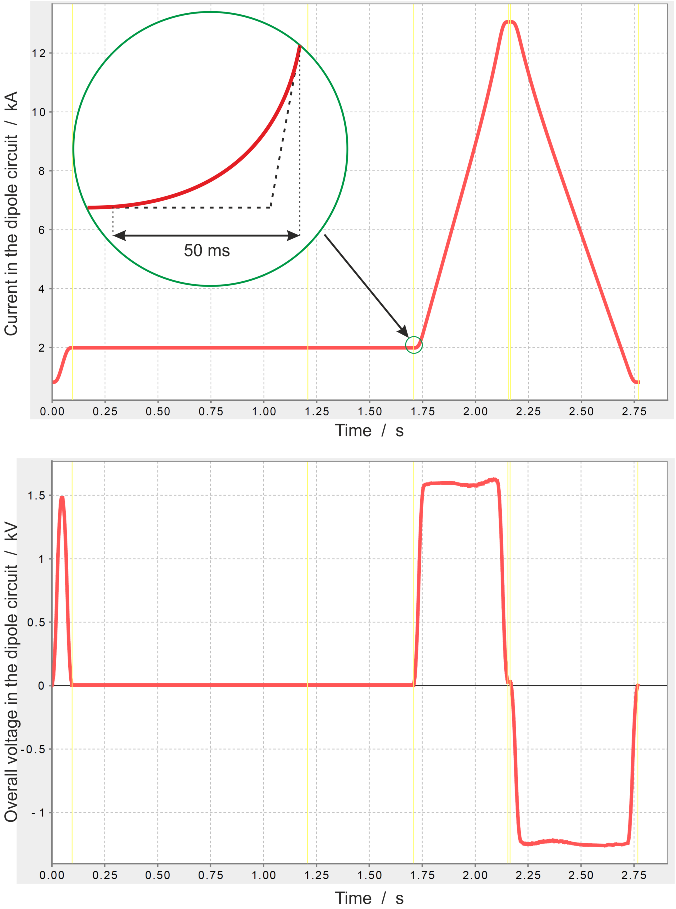

Figure 5.1.: Current and overall voltage in the dipole circuit of SIS100 during the proton cycle (calculation) [68].

The average parasitic capacitance which is introduced to the circuit via the voltage taps can be estimated as following. Each voltage tap wire (inside the cryostat) is 4–6 m long. The cables that transmit the signals from the cryostat feedthroughs to the quench detection cabinets can be up to 170 m. The capacitance of a typical cable with shield is equal to 250 pF/m. Considering a double layer structure of quench detection (an individual bridge for each magnet and a super–bridge across the two neighbouring magnets), the dipole circuit of SIS100 would have approxi-

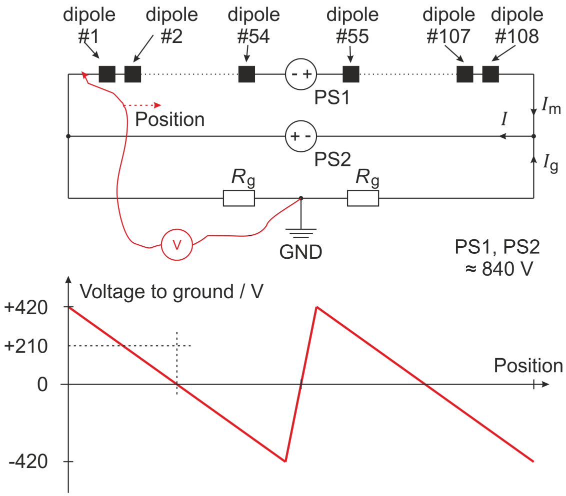

Figure 5.2.: Simplified voltage distribution over the dipole circuit of SIS100, PS1 & PS2 – power converters, R_g – grounding resistor, GND – ground.

mately 1100 voltage taps. Assuming 210 V as the average voltage in the circuit (see the simplified voltage distribution of the SIS100 dipole circuit presented in Fig. 5.2), the leakage current due to the voltage taps would be in the range of:

$$1100 \text{ voltage taps} \times 250 \text{ pF/m} \times 100 \text{ m (on average)} \times 210 \text{ V}/50 \text{ ms} \approx 115 \text{ mA}.$$

For the required current accuracy of 10^{-4} out of 1.5 kA which is the injection level (12 Tm → 0.228 T → 1.5 kA) , the summarised leakage current budget is equal to $10^{-4} \times 1.5$ kA = 150 mA. Since most of this budget would be consumed by the voltage taps (115 mA), the conclusion is that a quench detection system with large amount of long voltage tap cables shall not be used for SIS100.

5.1.1 Magnetic Amplifiers

One can reduce the parasitic capacitance by significantly limiting the length of the voltage taps wires. The simplest way is to apply isolation amplifiers and locate them close to the voltage tap feedthroughs (at the cryostat level). Taking into account the tough requirements for radiation hardness, no electronics (e.g. insulation amplifiers) is allowed in the machine tunnel in the direct surroundings of the cryo–modules. Another way of decoupling is a galvanic isolation with a transformer. Recalling late 1980s, a similar problem with too long cables dedicated to quench detection arose at

DESY when constructing the HERA accelerator [69]. There, the distance between the quench detection cabinets and the cryostats enclosing superconducting magnets was in the range of 700 m. Transmitting the low–value (mV range) signals over such a long distance, causes trouble with high noise which is picked up by the cable. Therefore, at HERA the quench detection was based on magnetic amplifiers (also called saturable reactors or in German nomenclature "Transduktoren") [70–72].

Magnetic amplifiers were developed at the beginning of XX century and mainly used for the regulation of high AC power circuits with low DC power control circuits. The control system of illumination in theatres (dimming) and speed controllers in electric motors became the basic applications for magnetic amplifiers. With the development of power electronics, the magnetic amplifiers could not longer compete with the transistor–based power amplifiers and they entered the path leading to forgotten technologies [70–74].

A magnetic amplifier is a special double core transformer. Its magnetic cores are manufactured from a special amorphous material which makes the hysteresis loop very narrow and steep ("Z"–shape). In the simplest version, the magnetic amplifier has two windings: control and load. The control winding (designed as a high voltage circuit) is connected in a bridge configuration to the live–circuit[1] of the magnet coil as shown in Fig. 5.3. It is wound either on both cores or separately on each core and connected in the manner of adding flux. The load winding is a low voltage signal–winding. It is wound separately on each core and connected in the manner of opposing flux. Thus, no signal can be transferred from the load side to the control side (assuming identical magnetic properties of the both cores). The load winding is connected to a circuit with an AC voltage source and load resistor R_{Load}. The amplitude of the voltage source V_0 is adjusted in order to operate the cores within the unsaturated part of the hysteresis loop. Therefore the impedance X_{Load} of the load winding stays at a very high level. R_{Load} is matched to X_{Load} that $X_{\mathrm{Load}} \gg R_{\mathrm{Load}}$. If there is no quench in the magnet, the current in the control winding i_{Control} equals zero and the cores remain non–magnetised. Since $R_{\mathrm{Load}} \ll X_{\mathrm{Load}}$, the current in the load circuit is limited to a very low value by the large X_{Load}. Therefore the voltage drop on R_{Load} is also low. When a quench occurs, a current starts to flow in the control winding and both cores saturate. As a consequence, the impedance of the load winding drops rapidly ("Z"–type cores). The relation between X_{Load} and R_{Load} changes and the current in the load circuit increases. Thereby, a higher voltage on R_{Load} occurs which indicates a quench. Fig. 5.4a shows few magnetic amplifiers prototypes designed and manufactured by

---

[1] Live–circuit – an electrical circuit which has power actively passing through it.

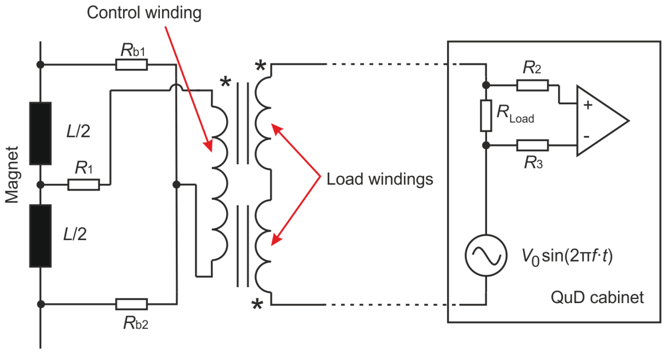

Figure 5.3.: Electrical scheme of a magnetic amplifier in the bridge configuration. QuD – quench detection; L – magnet inductance; R_{b1}; R_{b2} – resistors of the balance bridge; R_1 – current limiter in the control winding; R_{Load} – load resistance; R_2, R_3 – input impedance of the analogue amplifier.

VAC[2] (1–2) and in the course of this Ph.D. work (3-5). Fig. 5.4b–c shows original magnetic amplifier of HERA.

The operation principle of a magnetic amplifier is presented in Figures 5.5 and 5.6 (these are measurements on the prototype done at GSI). The signals shown on the graphs are:

- I_{Control} – the current in the control winding (measured on 350 Ω resistance in the control circuit),
- I_{Control} (mean) – mean value of the current in the control winding,
- $V_{\mathrm{L\_Load}}$ – voltage drop on the reactance of the load winding,
- $V_{\mathrm{R\_Load}}$ – voltage drop on the load resistor (R_{Load} fixed to 400 Ω),
- AC 300 Hz – sinusoidal voltage source: ±8 V amplitude and 300 Hz frequency[3].

Figures 5.5 and 5.6 show how the relation between $V_{\mathrm{L\_Load}}$ and $V_{\mathrm{R\_Load}}$ changes in respect to the control current. At $I_{\mathrm{Control}} = 0$ mA, $X_{\mathrm{Load}} \gg R_{\mathrm{Load}}$ and $V_{\mathrm{R\_Load}}$

---

[2] VAC – VACUUMSCHMELZE GmbH & Co. KG is a magnetic core manufacturer. VAC delivered special magnetic cores for the magnetic amplifier study performed within this Ph.D. work.

[3] 300 Hz is the optimum frequency regarding the long cable length and staying away from the 600 Hz frequency generated by the main power converter and odd harmonics of 50 Hz.

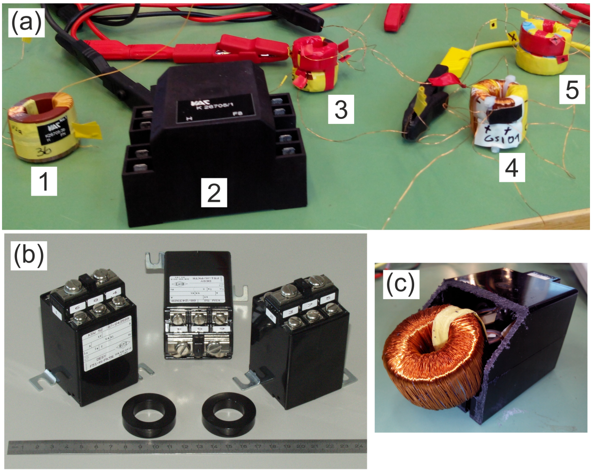

Figure 5.4.: Magnetic amplifiers: (a) 1, 2 – prototypes manufactured by VAC, 3, 4, 5 – selected prototypes designed and manufactured at GSI; (b,c) – magnetic amplifier and cores used at HERA.

is low (< 0.6 V). At $I_{\text{Control}} = 1$ mA, $V_{\text{R\_Load}}$ increases significantly (peak value of 2.8 V). When further increasing I_{Control}, $V_{\text{R\_Load}}$ also increases. Referring to Fig. 5.3 and assuming $R_1 = 50\ \Omega$ and $R_{\text{b1}} = R_{\text{b2}} = 300\ \Omega$, the quench detection at 1 mA corresponds to a voltage threshold of 175 mV (350 mV at V_{q}) when comparing to a balance bridge (see Section 2.6).

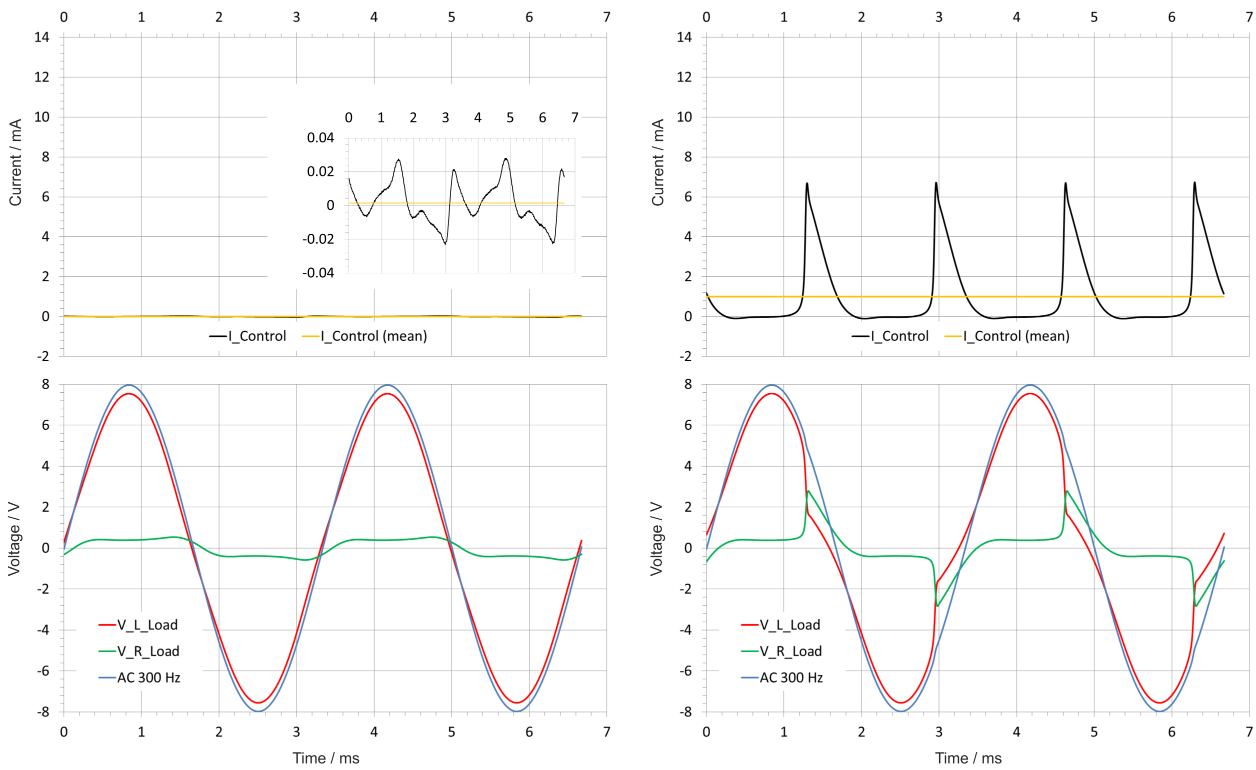

Figure 5.5.: Operating principle of a magnetic amplifier: behaviour at 0 and 1 mA in the control winding.

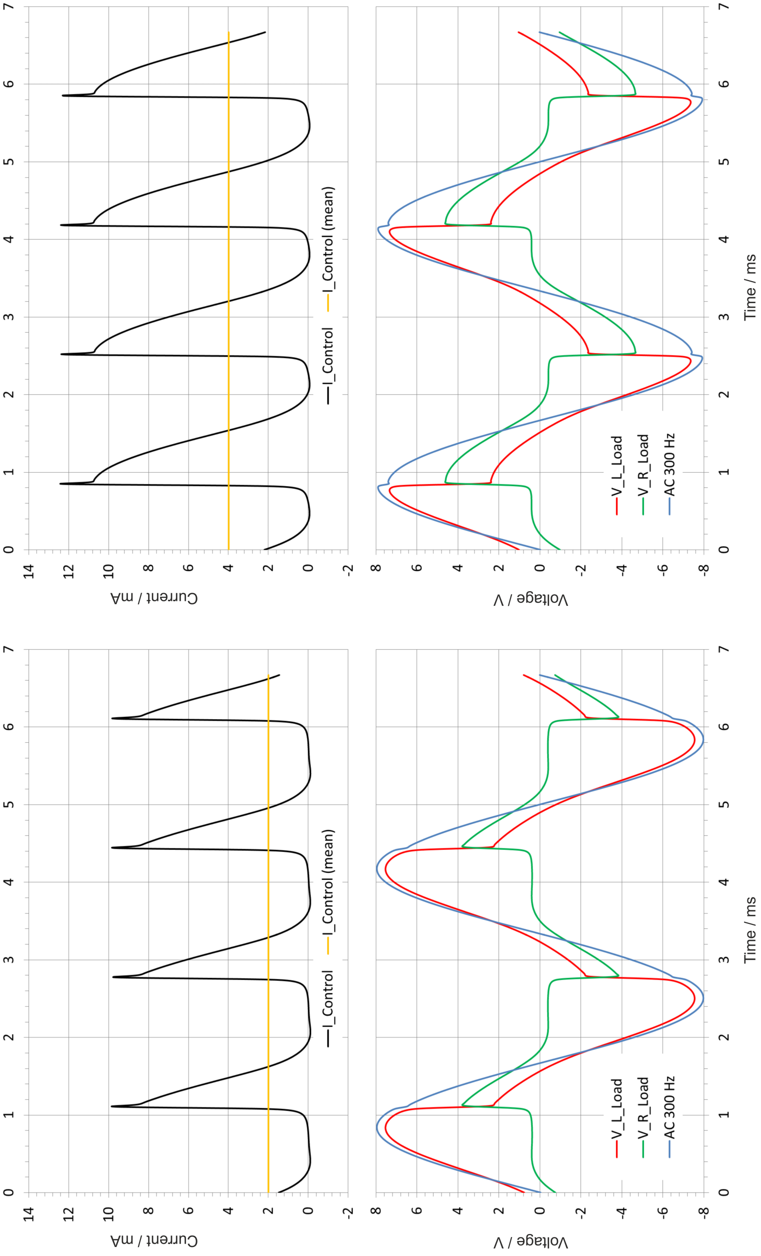

Figure 5.6.: Operating principle of a magnetic amplifier: behaviour at 2 and 4 mA in the control winding.

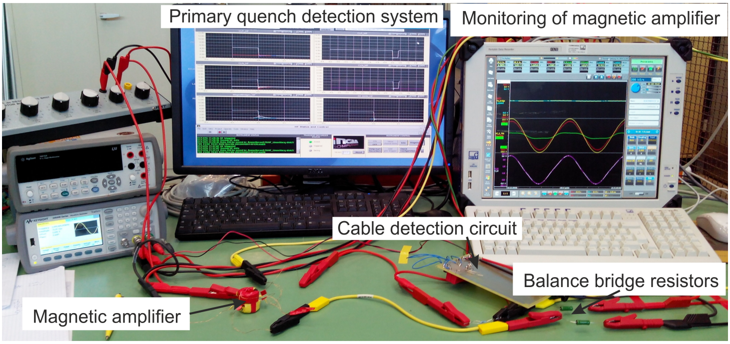

Figure 5.7.: GSI magnetic amplifier prototype during testing with the SIS100 dipole magnet.

The functionality of the GSI magnetic amplifier prototype was successfully tested on a stand–alone SIS100 dipole magnet. Fig. 5.7 shows a photo of the actual test stand at the test facility at GSI. During the experiment, the primary quench detection was provided by a resistive bridge (balance bridge) detector with a threshold of 200 mV (400 mV at V_q) and 10 ms of validation time. In order to check the behaviour of the magnetic amplifier, the magnet was charged to 12 kA and then a quench was initiated by an inductive spot heater. Fig. 5.8 shows the magnet current, the voltage of the balance bridge (primary quench detection) and the signals of the investigated magnetic amplifier. Looking at $V_{\mathrm{R\_Load}}$ one can see the voltage peaks which indicate the quench. For the quench validation one can either count 2–3 subsequent peaks or rectify and integrate the $V_{\mathrm{R\_Load}}$ signal. The second method is applied in the first prototype of the magnetic amplifier control board (see Fig. 5.9) where the rectified and integrated voltage signal is compared to a predefined threshold.

In 1990s, a quench detection system with magnetic amplifiers was also considered for the LHC machine. However it was rejected because of the non–linear characteristics which makes the magnetic amplifiers unsuitable as a monitoring system [75]. Nevertheless, the advantages such as:

- high radiation hardness,
- galvanic isolation of high voltage,
- good electrical insulation,
- relatively low cost, and
- high reliability,

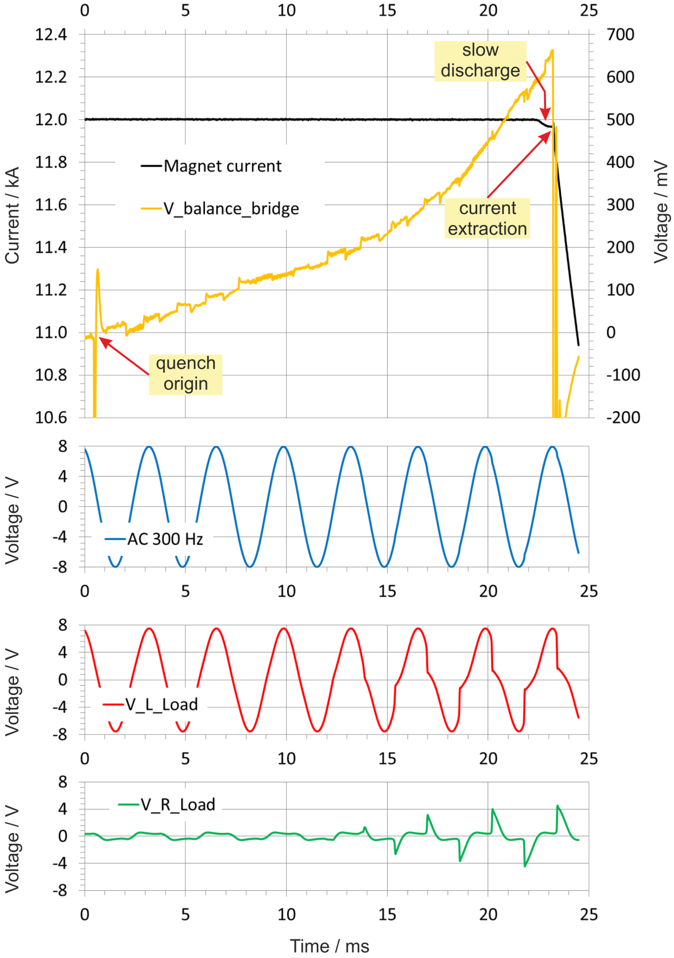

Figure 5.8.: Test results on magnetic amplifier connected to the magnet.

are highly appreciated. Although a system with magnetic amplifiers does not provide information concerning the quench voltage development, its switching functionality (no quench/quench) could be successfully used for the safety system which indeed the quench detection is. Considering a chain of magnets, a magnetic amplifiers–based system indicates which magnet has quenched and at which time.

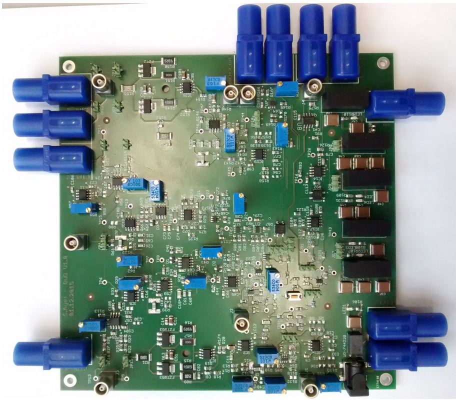

Figure 5.9.: Prototype control board for magnetic amplifiers (photo and design of S. Ayet).

5.1.2 Voltage Tap Detection

Voltage taps are very essential for the quench detection system. Therefore, it is very desirable to have a cable detection subsystem which monitors the presence of each voltage tap connection. A simple cable detection could be realised by applying pull–up resistors at the input of the quench detection card. An example of a bridge detector with pull–up resistors is presented in Fig. 5.10. The voltage taps “P” and “N” are fed with +15 V isolated voltage via 2 MΩ pull–up resistors. When all voltage taps are present, the parallel connection of the two pull–up resistors (“P” and “N”) gives 1 MΩ. The “middle” voltage tap is fed with −15 V (also isolated voltage) via a 1 MΩ pull-up resistor. Thus, under normal condition the circuit remains balanced and no voltage occurs across the bridge. In case any of the voltage taps is lost, an unbalanced voltage will occur and a quench trigger will be released.

In case of a system with magnetic amplifiers, the cable detection is more challenging compared to a system with pull–up resistors. The following concept for the cable detection was developed in the frame work of this Ph.D. (see Fig. 5.11). The magnetic amplifier is connected to the magnet in a standard bridge configuration with balance resistors $R_{\mathrm{b1}}/R_{\mathrm{b2}}$ (300 Ω each) and current limiting resistor R_1 (50 Ω) in the middle branch. The load circuit of the magnetic amplifier includes the AC voltage source ($V_0 = 8$ V, $f = 300$ Hz) and a load resistor R_{Load} (400 Ω). The cable detection subsystem considers an additional test voltage provided by an isolated DC line (a Graetz bridge and an isolation transformer). The voltage at the output of the rectifier is set to approximately 50 V. The cable detection cur-

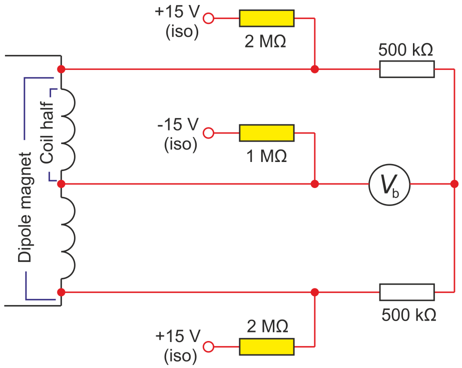

Figure 5.10.: Cable detection with pull-up resistors (iso – supplied from isolated power source).

rent is limited via two resistors R_{CD} (10 kΩ each). The isolation transformer can be powered either from the same voltage source as the load circuit (as shown in Fig. 5.11) or from a separate power line. When all three voltage taps are present, the current path for the cable detection closes via the magnet. If a voltage tap “P” or “N” is lost, the cable detection current will flow via the magnetic amplifier and a quench trigger will be released. Unfortunately, a lost of the "middle" voltage tap will not be recognised by the presented system. Thus, for the main circuits of SIS100, it is proposed to use a structure of magnetic amplifiers with 50% overlapping. In this case, each two adjacent magnets are compared to each other. If a one magnet quenches, the resistive zone is detected by two neighbouring magnetic amplifiers. Therefore, the presented structure is characterised by a high redundancy level. Thanks to the overlapping, the "middle" voltage tap of one magnetic amplifier becomes the “side” voltage tap (“P” or “N”) for the next magnetic amplifier and the missing of a “middle” voltage tap can be recognised. Figure 5.12 presents a section of SIS100 dipole circuit surveyed by magnetic amplifiers. The structure includes the cable detection subsystem. As indicated in the scheme, the polarity of the cable detection supply voltage has to be alternated along the magnet string. The system presented in Fig. 5.12 has following issues:

- Each magnet is by–passed by a two 300 Ω resistors which creates a by–pass current up to 100 mA at the maximum ramp rate (at 15.4 V / magnet). This by–pass current is equal over the whole magnet circuit. Therefore it can be compensated in the power converter controller.

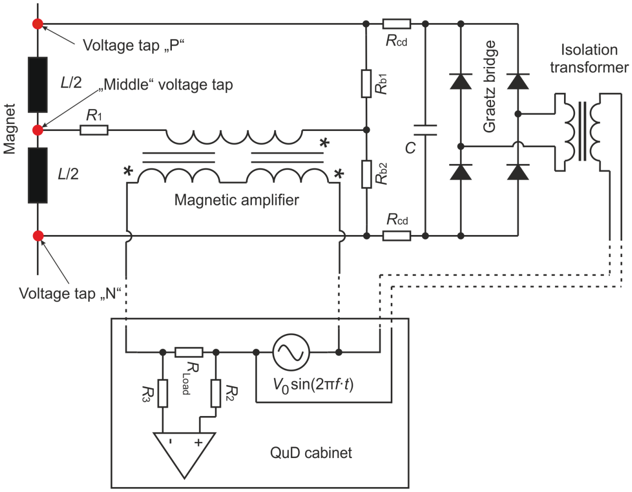

Figure 5.11.: Cable detection for a single magnetic amplifier.

- The cable detection system introduces a small error current to the magnets. The level of this disturbance is up to ±6 mA (calculated for a section of 18 magnets). Since the total budget for the leakage current is 150 mA (see Section 5.1), the disturbance of ±6 mA can be accepted.

Alternative to Magnetic Amplifiers

An overlapping quench detection structure as presented in Fig. 5.12 can be used with classical balance bridges instead of magnetic amplifiers. Due to the overlapping, the number of long cables can be minimised from initial ≈ 1100 to ≈ 240. Thus, the overall leakage current can be reduced by a factor of 4.5. One can also develop a new low–capacitance cable for further reduction of the capacitive effects. At the moment of writing this thesis, both options (magnetic amplifiers and balance bridges) are considered for the main magnets of SIS100. Figure 5.13 shows the overlapping quench detection structure with balance bridges.

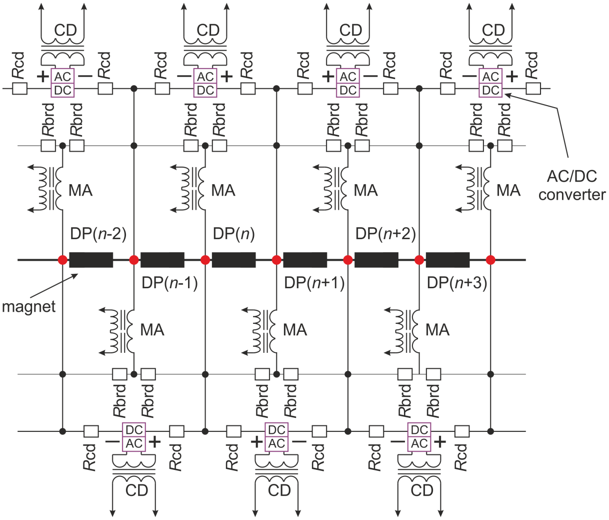

Figure 5.12.: Cable detection for magnet string surveyed by magnetic amplifiers with cable detection: MA – magnetic amplifier, CD – cable detection

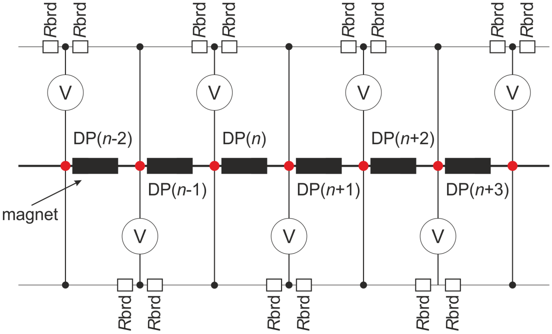

Figure 5.13.: Cable detection for magnet string surveyed by balance bridges.

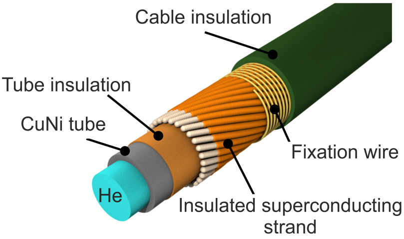

Figure 5.14.: Scheme of the SIS100 corrector cable [76].

5.2 Mutual Inductance Detector for Corrector Magnets

The corrector magnets of SIS100 are constructed from a Nuclotron–type cable which differs from the cable used for the main magnets, see Fig. 5.14. Apart from physical dimensions (size of the CuNi tube, number of strands, strand cross–section), the major difference is that the strands of the corrector cable are insulated as well as the CuNi tube. The concept of insulated strands was introduced to supply the corrector magnets from a power converter with a relatively small current (300 A). In order to achieve that, one needs to connect the superconducting strands in series as shown in Fig. 5.15. The strand connections require excellent cooling, e.g. Fig. 5.16 shows a cooling concept with a conduction plate. In superconducting systems, the cooling plate is not a very practical solution due to space limitations and issues concerning electrical insulation. Therefore, a special corrector terminal box was developed at GSI [76]. The terminal box is made from aluminium components and it encloses three cables: the two coil extremities and the bus–bar which supplies the current. At the side, a special ceramic plate is located where in the dedicated grooves all strands are connected. The terminal box model is presented in Fig. 5.17.

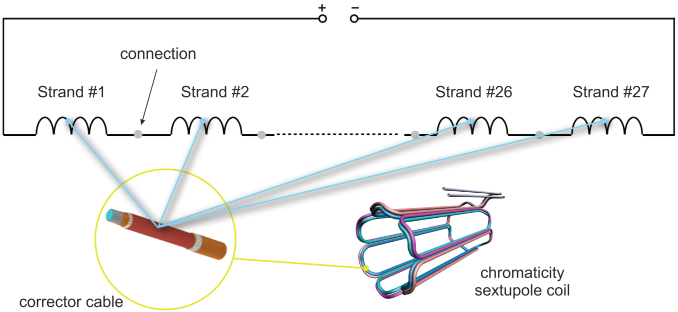

Figure 5.15.: Series connection of corrector strands [76].

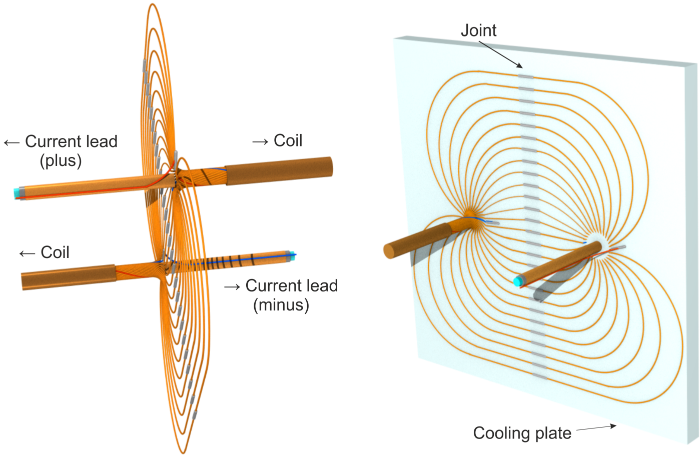

Figure 5.16.: Strand interconnection concept for SIS100 corrector magnets [76].

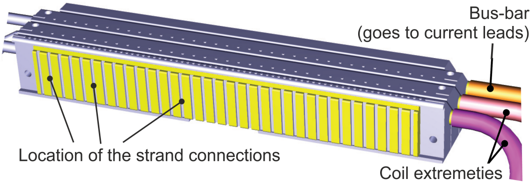

Figure 5.17.: Terminal box prototype [76].

It is planned that all SIS100 corrector magnets will be surveyed by mutual inductance detectors (MID), see Section 2.6. The decision concerning the use of MID has been taken due to the high risk of symmetrical quenches in the corrector magnets (e.g. beam loss induced quench) [24]. Since the corrector coil is wound from a cable with insulated strands connected in series, a local energy distribution might become an origin of a restive zones of the same volume in two or more strands. These resistive zones may preserve undetected when using a classical balance bridge – identical voltages at the bridge halves will be cancelled by the balance bridge configuration.

Measurements on Mutual Inductance Detector Prototype

The cable for the corrector coil has 28 strands: one strand is used as the pick–up coil of MID and the other 27 strands[4] are connected in series and carry the current (primary winding of MID). The construction of the corrector coil enables an easy implementation of the coupled coil for MID (pick–up coil).

A prototype of the MID electronic board was built at GSI (see Fig. 5.18) and tested on the SIS100 corrector model. This experiment was conducted in the course of this Ph.D. work. The corrector model is a superconducting solenoid (see Fig. 5.19) which has very similar parameters to the SIS100 chromaticity sextupole magnet. The cable used for the solenoid also has 28 insulated strands that are connected in series in a modified terminal box shown in Fig. 5.20. The experiment with the solenoid was conducted with the MID detector as the test object. The quench detection was provided by a standard bridge system. The test results are presented in Figures 5.21 and 5.22. Initially the solenoid was charged to 50 A DC (not shown in the graphs). Then the current was increased to 200 A with the ramp rate of 80 A/s. Figure 5.21 shows the voltage of the solenoid in comparison to the induced voltage in the MID strand. As expected, $V_{\mathrm{MID\_strand}}$ is 27 times lower than V_{Magnet} ($L_{\mathrm{magnets}}/M \approx 27$). A few seconds after the current reached 200 A, a quench occurred in the superconductor. The corresponding quench signals are shown in Fig. 5.22b. V_{Magnet} increases due to the developing resistive zone. This quench voltage is not transferred to the pick–up coil since only inductive voltage can be transferred. In the electronics of MID the normalised magnet voltage $V_{\mathrm{Magnet}}/27$ is compared to the voltage of the pick up coil $V_{\mathrm{MID\_strand}}$. When the difference $V_{\mathrm{Magnet}}/27 - V_{\mathrm{MID\_strand}}$ exceeds the adjusted threshold, a quench trigger is released. Taking a closer look at Fig. 5.22b, one can observe a small increase of $V_{\mathrm{MID\_strand}}$ in the negative direction. Most probably (since the signal is very

---

[4] In case of the chromaticity sextupole and steerer, 27 out 28 strands carry the current. In multipole corrector, for quadrupole, sextupole and octupole coil, the number of strands that carry the current is 13, 27 and 24, respectively. In the injection/extraction quadrupole 20 out of 21 strands carry the current.

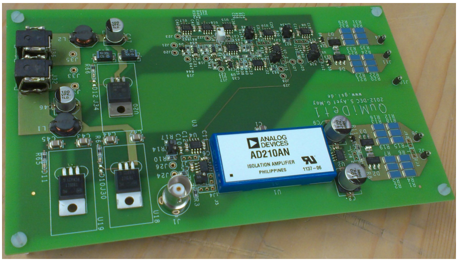

Figure 5.18.: Prototype of the electronic board for MID (photo and design S. Ayet).

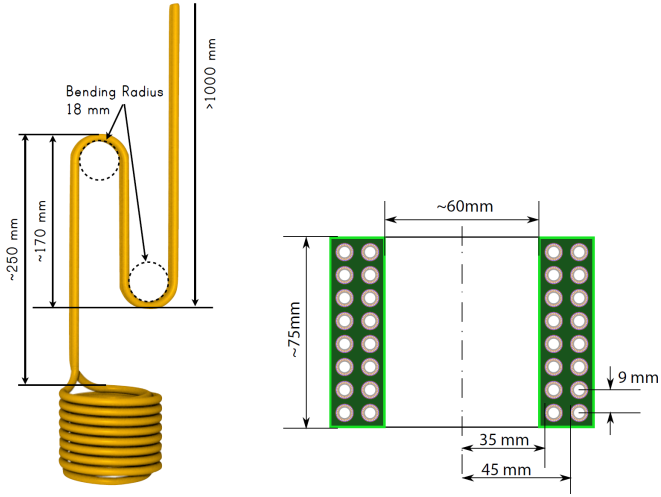

Figure 5.19.: Scheme of the superconducting solenoid (SIS100 corrector model) [76].

low in amplitude), the signal comes from the poor stabilization of the used power converter. Nevertheless this effect gives a positive impact on the MID detector functionality – it increases $V_{\text{magnet}}/27 - V_{\text{MID\_strand}}$.

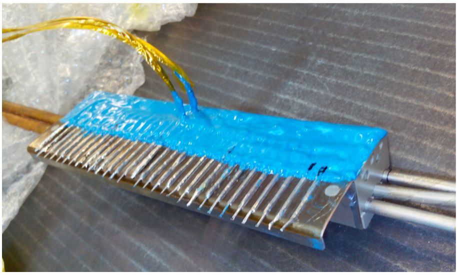

Figure 5.20.: Terminal box prototype (realisation and photo by V. Datskov).

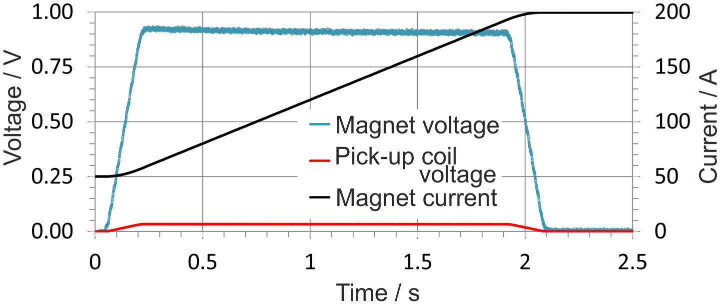

Figure 5.21.: Recording of the experiment with the corrector model and the MID detector.

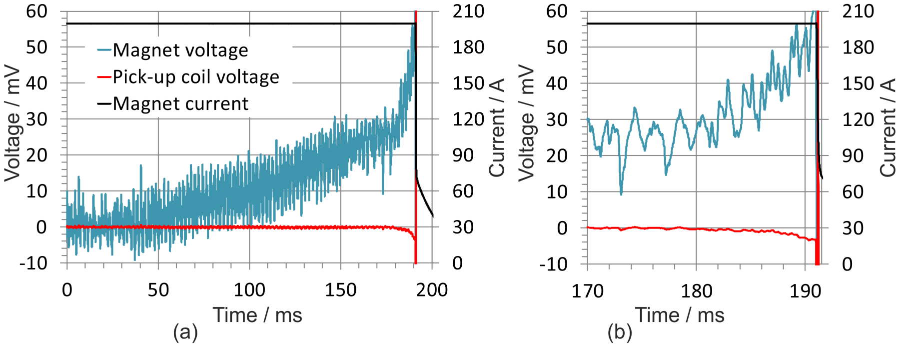

(a) (b)

Figure 5.22.: Zoom at the quench origin.

6 Conclusions and Outlook

The objectives of this dissertation have been successfully accomplished. A novel FDM[1] quench calculation software (called GSI quench software) was developed. This software utilises the unconditionally stable implicit scheme and an innovative adaptive time stepping algorithm which takes into account the maximum temperature increase estimated for the individual mesh elements. The implemented thermal model of the magnet coil gives the possibility to include cooling by a liquid helium bath (applicable for potted coils modelled with a fine mesh). The heat transfer at the interface coil/helium is computed with the use of a measurement fit of the experimental data reported in [59]. The electrical circuit topology including the magnet protection system (energy extraction resistors and/or by–pass diodes) is implemented. The properties of the magnet's yoke are taken into account in the inductance function $L_\mathrm{d}(I)$. The magnetic field on the individual mesh elements can be either implemented as a table data (e.g. a result of a 2D magneto–static simulation) or calculated as an arbitrary function of electrical current and the mesh element position in the cross section of the coil.

The electro–thermal model of the GSI quench software was verified, validated and compared to quench measurements performed on SIS100 dipole and Super–FRS dipole prototypes. The testing campaign on the SIS100 dipole prototype (magnet training, quench propagation velocity, hot–spot temperature, $\mathrm{M}IIT$s, RRR_Cu, magnet inductance, splice resistance, 14 kA HTS current leads) was performed at the GSI test facility in the scope of this Ph.D. work. The quench measurements on the Super–FRS dipole prototype were received from the FAIR China Group – nevertheless, the data analysis was conducted in the course of this work. The calculated current decays, quench voltages, quench resistances and hot–spot temperatures are either in good agreement with the measurement data or they represent the worst case scenario, e.g. the calculated hot–spot temperature or quench voltage is higher than measured. Based on the performed study, one can conclude that the GSI software can be utilised for quench calculations of all superconducting magnets of SIS100 (Nuclotron–type) and Super–FRS (potted coil). Currently, the quench calculations done with the GSI software serve as an input for the proper design of SIS100 and Super–FRS quench detection and energy extraction systems.

The second subject of the dissertation concerns the design challenges of the SIS100 quench detection system. An outstanding cycling rate of the dipole cir-

---

[1] FDM – finite difference method.

cuit (4 T/s), high voltage ($U_0/U = 1$ kV/2 kV), radiation hardness required for the equipment to be installed in the accelerator tunnel (≥ 1 MGy) and long signal lines between the magnets and quench detection racks (up to 200 m) implies a customised design of the key components of the system.

For the main magnet circuits of SIS100, the overall effect of parasitic capacitance (mainly due to long quench detection cables) might influence the current accuracy at the beginning and the end of the fast current ramp. In order to reduce the parasitic capacitance, a new structure of quench detectors is proposed. With the new detection lattice, a balance bridge surveys two adjacent magnets. Such a structure with 50% of overlapping, provides required hardware redundancy and reduces the number of voltage taps actively used by the system. Further reduction of capacitance can be achieved by applying a galvanic isolation barrier located in the accelerator tunnel (at the cryostat level). This can be realised by utilising magnetic amplifiers (MA) – inductive components known from the beginning of XX century and successfully used at HERA (DESY, Hamburg). Another advantage of MA is the high voltage decoupling which brings a significant reduction of the cabling cost – the long signal cables between the accelerator tunnel and the quench detection racks do not have to be specified for the very high voltage of the machine. The aptitude of MA for the modern quench detection system of SIS100 was investigated. A number of MA prototypes with special iron–dominated cores (“Z”–shape of the hysteresis loop) were constructed and tested (also with the SIS100 dipole magnet). The experiment shows that MA–based quench detectors can be applied for the main circuits of SIS100.

The corrector magnets of SIS100 are utilising a special Nuclotron–type cable with individual superconducting wires being insulated from each other. Such a construction is sensitive to symmetrical quenches, e.g. beam induced quenches that cannot be detected by a typical balance bridge detector. The issue can be resolved by utilising so–called mutual inductance detectors (MID). The concept of MID was investigated and proved experimentally on a SIS100 corrector magnet model. Since the MID prototype shows excellent performance, it is planned to use the MID concept for all SIS100 corrector magnets.

Outlook

The GSI quench calculation software was developed in order to study quench cases in superconducting magnet circuits of FAIR. The software code is written in a commercial programming language MATLAB. Transfer of the GSI code to the OCTAVE/SCILAB environment (free and open source software) in conjunction with the new graphical user interface (GUI) will significantly improve the accessibility and usability of the software. Further improvement of software can aim:

- development of a 3D thermal model of a Nuclotron–type cable which includes cooling with force–flow two–phase helium;
- adding cylindrical coordinate system as an option to the 3D thermal model;
- development of a de–centralised electrical model;
- upgrade of the electrical model (include the capacitance of the electrical circuit, warm cables, components of the power converter output and the grounding system);
- development of thermal models of SIS300 magnet coils (Rutherford cable).

The work concerning MA shall be continued including the design optimization (number of turns, electrical insulation, housing). The overlapping lattice of balance bridges shall be verified experimentally. A closer look shall be taken on electrical coupling between individual magnetic amplifiers. The cable detection (voltage tap detection) concept shall be also verified by experiment. Furthermore, a study concerning the long quench detection line shall be launched in order to investigate a possible use of higher frequency for the magnetisation of the MA cores (e.g. 1.2 kHz instead of currently used 300 Hz). Utilising a higher operating frequency will speed up the detection of a quench and will also enable to reconstruct the trend of the bridge voltage signal required for the *post mortem* analysis.

The next step for the MID development shall concentrate on analogue electronics of the detector and data acquisition.

Acknowledgements

I would like to express my very great appreciation to Dr. Eric Floch, Prof. Thomas Weiland, Prof. Oliver Boine-Frankenheim and Dr. Carsten Mühle for accepting me as a Ph.D. student at GSI and at TEMF/TU Darmstadt. I would also like to thank the management of the Helmholtz Graduate School for Hadron and Ion Research (HGS–HIRe for FAIR): Prof. Henner Büching, Dr. Gerhard Burau, Silvia Engel, Johanna Dilley, Sylke Schneider, Helena Santos and Dr. Sascha Vogel for excellent organisation of the graduate school program.

I am indebted to Prof. Dariusz Świsulski who established the contact between GSI and Gdańsk University of Technology. Due to this collaboration, I had a chance to participate in the GSI Summer Student Program 2008. I also thank Dr. Andrzej Stafiniak who was my first mentor at GSI and later become my good colleague. Many thanks to Dr. Isfried Petzenhauser who was my first office mate at GSI and helped a lot with the organisation of my life in Germany. I am very grateful to the GSI colleagues, namely Walter Freisleben, Dr. Christian Roux, Dr. Anna Mierau, Dr. Henning Raach, Dr. Kei Sugita, Farid Marzouki, Dr. Vladimir Datskov, Dr. Hans Müller, Jan Patrick Meier, Johann Macavei, Dr. Hanno Leibrock, Franz Walter, Klaus Schröder, Samuel Ayet, Prof. Gebhard Moritz, Heinz Ramakers, Horst Welker, Dr. Pierre Schnizer, Valentin Plyusnin and other colleagues for their help in the daily work and especially for the support in the test facility.

Special thanks to Dr. Fernando Toral for very fruitful discussions concerning quench calculations at CIEMAT/Madrid and to Prof. Rüdiger Schmidt for sharing the experience gained at CERN.

I would also like to thank Dr. Pradeep Ghosh, Dr. Ariel Dzwonkowski, Doc. Marek Wołoszyk, Dr. Michał Ziółko, Dr. Selim Seddiki, Dr. Giuseppe Colluci, Dr. Achim Heinz, Dr. Grzegorz Kalicy, Dr. Sebastian Kupny, Dr. Youssef Hayek, Eugen Bayer, Dr. Ioannis Bouras, Vasileios Velonas, Dr. Klaus Klopfer and others that I could have forgotten to mention by name, for their accompany and help during my long Ph.D.–path. I thank Dr. Paul Görgen, Dr. Uwe Niedermayer for the help with the TUD LaTeXtemplate.

Once again I would like to thank Dr. Erich Floch for all the energy and time he spent on my education concerning superconducting magnets, quenches and measurements at low temperatures.

At the end, I would like to express my gratitude to my lovely parents Tadeusz & Regina Szwangruber, my brother Tomasz Szwangruber & his wife Julita and my

friends Elżbieta Zięba & Przemysław Chrząstowski – they always believed in me and offered their support in the moments of doubt.

A Historical Steps of Superconductivity

The historical steps of superconductivity are presented in Tab. A.1.

Table A.1.: Historical steps of superconductivity

Year	Discovery	Discovered by
1908	Liquefying helium – opening the door of low temperature physics	H. K. Onnes
1911	Discovery of superconductivity in pure mercury	H. K. Onnes
1931	Discovery of superconductivity in alloys	W. J. de Haas, W. Keesom
1933	Discovery of the Meissner effect - expulsion of magnetic field from the interior of a superconductor	W. Meissner, R. Ochsenfeld
1935	Londons' equations – the first theory of superconductivity, based on classical equations of electromagnetism	F. London, H. London
1950	Ginzburg-Landau theory (alternative to Londons' theory), based on quantum mechanics	V. L. Ginzburg, L. D. Landau
1954	Discovery of superconductivity in Nb_3Sn, used for the high–field superconducting magnets	B. T. Matthias, T. H. Geballe, S. Geller, E. Corenzwit
1957	BCS theory – the microscopic theory of superconductivity, based on quantum mechanics, introduction of Cooper pairs – paired electrons that are carrying the "super–current"	J. Bardeen, L. Cooper, R. Schrieffer

Year	Discovery	Discovered by
1962	Discovery of the Josephson junction (superconductor–insulator–superconductor junction) in which the tunnelling of supper-current via an insulation barrier was observed. Multiple applications, i.a. the voltage standard [77]	B. Josephson
1962	Discovery of superconductivity in NbTi – the most popular material for superconducting magnets	T. G. Berlincourt, R. R. Hake
1986	Finding of superconductivity in ceramics	G. Bednorz, A. Müller
1987	Discovery of superconductivity in YBCO – the first material which is superconducting above the boiling point of nitrogen (77K)	P. Chu
1988	Discovery of BSCCO general class superconductors	H. Maeda, Y. Tanaka, M. Fukutomi, T. Asano
2001	Discovery of superconductivity in MgB_2	J. Akimitsu

B Meissner Effect

A superconductors in the superconducting state expels the magnetics field from its interior. The phenomenon is called the Meissner effect. Figure B.1 shows behaviours of a type I superconductor and, for comparison, of a "perfect" conductor[1] for a magnetic field B_a being applied ($B_\mathrm{a} < B_\mathrm{c}$) and when cooled down to low temperatures. The presented three vertical behaviour schemes (a), (b) and (c) are characterised as follows [15]:

- Behaviour (a) is observed for both type I superconductors and "perfect" conductors. At $B_\mathrm{a} = 0$, the sample has a zero total magnetic flux in its interior. In the next step, the sample is cooled down. It means:
  - approaching vanishing resistance for $T \to 0$ for a "perfect" conductor,
  - entering the superconducting state for a superconductor at $T < T_\mathrm{c}$.

  When an external magnetic field B_a is applied, screening currents are induced that reduce the magnetic flux inside the sample to zero (shielding effect). The magnetic field is expelled out of the sample. In the last step, B_a is reduced to zero. Screening currents vanish and the total magnetic flux inside the sample remains zero.

- Behaviour (b) is observed for "perfect" conductors. At first, the sample is at room temperature and an external magnetic field B_a is applied. The sample is fully penetrated by B_a. In the next step the sample is cooled down. The magnetic flux in the sample does not change (full penetration). When B_a is reduced to zero, screening currents are induced that create a magnetic flux inside the sample. The total magnetic flux in the interior is equal to that before the field reduction.

- Behaviour (c) is observed for superconductors of type I. At the beginning, the sample is at room temperature and a magnetic field B_a is applied ($B_\mathrm{a} < B_\mathrm{c}$). In the next step, the sample is cooled down below T_c. Screening currents are induced that reduce the magnetic flux inside the sample to zero. In the last step, B_a is reduced to zero. Screening currents vanish and total magnetic flux inside the sample remains zero.

---

[1] "perfect" conductor - an extremely pure metal without any defects of the crystal structure; at low temperature its resistivity is close to zero ($\varrho \approx 0$).

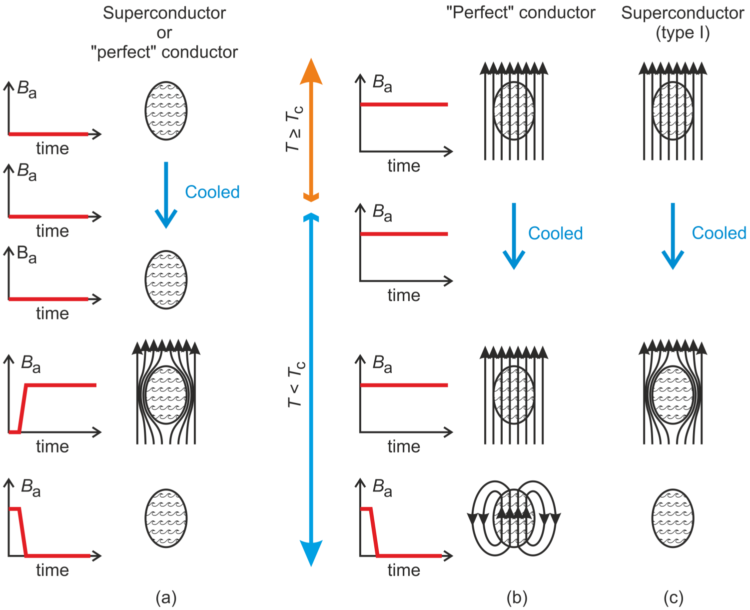

Figure B.1.: Behaviours of a “perfect” conductor and a type I superconductor when a magnetic field is applied and when cooled down to low temperatures.

The type I superconductor in the superconducting state never allows a magnetic flux density to exist in its interior and unlike in “perfect” conductors, the magnetic flux is expelled regardless of whether the external magnetic field was applied before or after cooling down. For magnetic fields higher than B_c, superconductivity is destroyed and the material gets normal conducting.

C Classification of Superconductors

Cooper pairs, BCS Theory

In the normal conducting state, electrons which flow through a conductor collide with the lattice and with each other which is observed as electrical resistance and Joule heating. In 1957, J. **B**ardeen, L. **C**ooper, and J. R. **S**chrieffer formulated a microscopic theory known as BCS theory which predicts occurrence of specific electron pairs that overcome the resistance. In the superconducting state, when a single electron passes through the lattice, the ions tend to slightly move due to the Coulomb interaction between the ions and the passing electron (the ions are attracted by the negative charge of the electron). This latter creates a lattice deformation in form of a local positively charged area which attracts another electron. Such paired electrons are called the Cooper pairs or super–electrons. The Cooper pairs are able to pass through the ion lattice without collisions which explains vanishing of the resistance. Since electrons within the Cooper pair are bound by a weak Coulomb interaction, the link can be easily broken by the thermal vibration of the ion lattice. This is why superconductivity is only observed at low temperatures at which the thermal energy (thermal vibration) of the ion lattice is low [15].

Type I or Type II

The classification of superconductors to either type I or type II requires introduction of two quantities that characterizes a superconducting material: a penetration depth and a coherence length. For a superconductor at $T < T_\mathrm{c}$ which is immersed into a magnetic field, screening/surface currents are induced at a certain surface thickness. Thus, the magnetic field penetrates the bulk into a certain penetration depth λ close to the surface. λ depends on the temperature and has a minimum called λ_0. When the temperature increases, the magnetic field gets into the bulk deeper and close to T_c it diverges to infinity (full penetration). Table C.1 shows theoretical values of λ at temperature of 0 K for indium, aluminium and lead [15].

At the surface of the superconductor bulk (type I) or at the interface between the normal region and the superconducting region (type II), the Cooper pair density does not jump abruptly from zero to a certain maximum value[1]. The number of

---

[1] The maximum Cooper pair density varies for different materials.

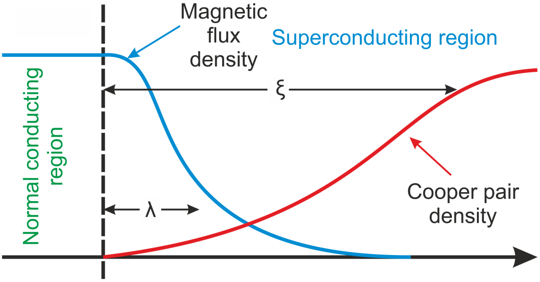

Figure C.1.: Penetration depth λ and coherence length ξ at the interface between normal-conducting and superconducting regions.

Cooper pairs increases smoothly over a finite distance ξ called the coherence length as presented in Figure C.1.

Table C.1.: Theoretical values of the penetration depth at temperature of 0 K [15]

Element	In	Al	Pb
λ_0 (cm)	$6.4{\cdot}10^{-6}$	$5.0{\cdot}10^{-6}$	$3.9{\cdot}10^{-6}$

The type of superconductor can be classified by the Ginzburg–Landau parameter κ defined by $\kappa = \lambda/\xi$. A superconductor is of type I for $\kappa < 1/\sqrt{2}$ and of type II for $\kappa \geq 1/\sqrt{2}$. The characteristics of superconductors with respect to κ is shown in Fig. C.2. The boundary between type I and type II superconductors is at $\kappa = 1/\sqrt{2} = 0.71$. The higher κ is, the lower is H_{c1} and the higher is H_{c2} with respect to H_c. A specific mechanism of superconductivity called surface superconductivity can occur in materials for which $\kappa > 0.42$. The phenomenon is limited by the maximum field strength H_{c3}. Surface superconductivity only occurs at the interface between a superconductor and an insulator and it does not occur at the interface between a superconductor and a normal conductor [15].

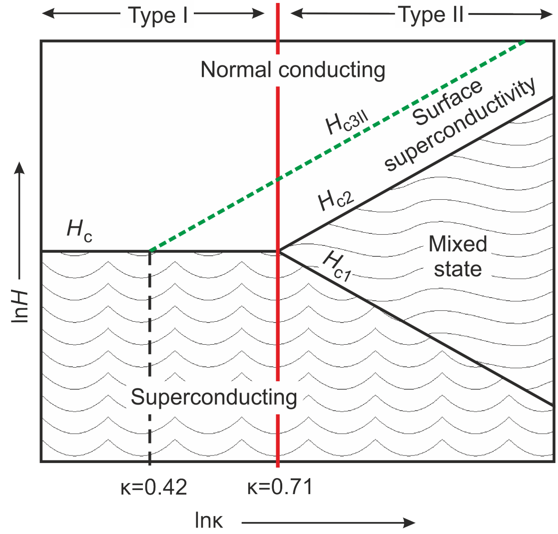

Figure C.2.: Characteristics of a superconductor as a function of the Ginzburg-Landau parameter κ [15].

D Current Leads

A current lead is a special designed conductor which brings the electrical current from the power supply circuit, located at ambient temperature, to the magnet which is located in the cryostat and operated very often at 4 K. The current lead design goal is to minimize the impact on the cryogenic system. In order to achieve that, one needs to simultaneously reduce the heat conduction (from the ambient temperature to the temperature at which the magnet is operated) and heat generation (Joule heating). Since:

- reducing heat conduction (reducing cross–section, increasing length, reducing thermal conductivity) increases heat generation and
- reducing heat generation (increasing cross–section, decreasing length, reducing electrical resistivity) increases heat conduction,

the design goal becomes challenging and a compromise (parameter optimisation) is required.

Assuming the temperature of the warm and cold terminal to be 300 K and 4 K, respectively, Eq. (D.1) can be used to estimate the power which is transferred through a copper current lead with a cross-section A_{Cu} and a length L_{Cu}. In many designs A_{Cu} varies over the current lead length in order to get more optimal correlation between the electrical resistivity and thermal conduction of the lead[1].

$$P_{\mathrm{in}} = \frac{A_{\mathrm{Cu}}}{L_{\mathrm{Cu}}} \int\limits_{4\ \mathrm{K}}^{300\ \mathrm{K}} k_{\mathrm{Cu}}(T) dT \tag{D.1}$$

For low current applications (currents up to few kilo Amperes), conventional copper current leads are used. There are three cooling options for Cu current leads: conduction cooled, vapour cooled and force flow cooled as presented in Fig. D.1.

---

[1] For metals, the relation between the thermal conductivity and electrical resistivity is described by the Wiedemann–Franz law – see Appendix K.

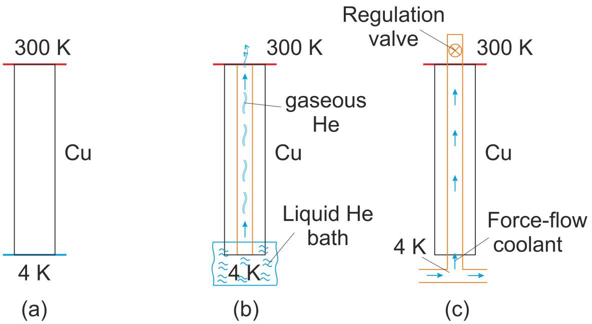

Figure D.1.: Cooling options for conventional copper current leads: (a) conduction cooled, (b) vapour cooled, (c) force flow cooled.

In applications where a very high current is required (> 10 kA) or the heat load due to conduction becomes a critical issue, one could implement HTS current leads. A HTS current lead is divided into two sections: Cu part operated at temperature range of 300–70 K (sometimes 50 K) and HTS part operated at 70–4 K (50–4 K). In most of the designs, the HTS section is conduction cooled and the Cu part is vapour or force flow cooled. HTS current leads are often called hybrid and its HTS part is usually made from stacks fabricated from BISCCO or YBCO tapes. Figure D.2 presents two various cooling options for HTS current leads.

In the FAIR project, the conventional copper current leads will be used for the Super–FRS magnets (current in the range of 300 A) while the hybrid HTS current leads will be used for the SIS100 magnets [78]. There are two variants of HTS current leads in SIS100:

- 14 kA main current leads (MCL) for the main magnets (linear optics: dipole and quadrupoles),
- 250 A conduction cooled local current leads (LCL) for corrector magnets (chromaticity sextupoles, multipole correctors and steering magnets).

Figure D.3 shows a prototype of HTS current leads designed for the main electrical circuits of SIS100. In these leads, the Cu part is vapour cooled while the HTS part is conduction cooled. The structure of the HTS part and the connection to the LTS cable is shown in Fig. D.4.

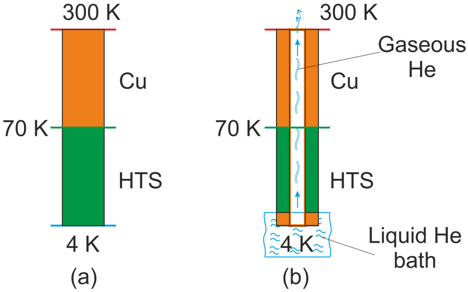

Figure D.2.: Cooling options for HTS current leads: (a) the Cu part and the HTS part cooled by heat conduction, (b) hybrid cooling, conduction cooling for the HTS part and vapour cooling for the Cu part.

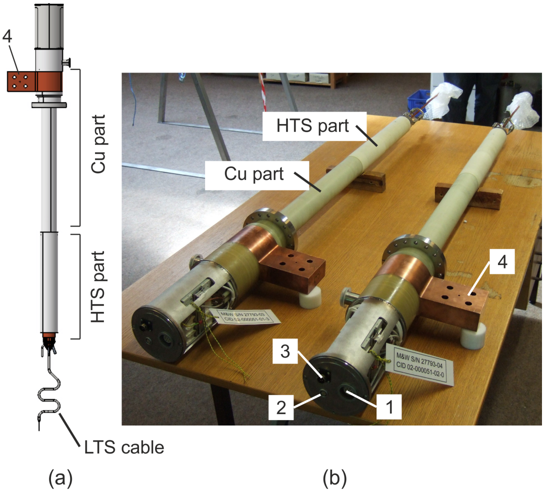

Figure D.3.: SIS100 main current leads (courtesy of Mark&Wedell): (a) 3D model, (b) the 1^{st} pair that was manufactured; 1 – voltage tap socket, 2 – temperature sensors socket, 3 – socket for heaters powering, 4 – warm terminal connection for electrical current.

The conventional copper current leads as well as the Cu parts of the HTS current leads require a protection against thermal runaway. This is an uncontrolled positive feedback where an increase in temperature caused by the Joule heating results

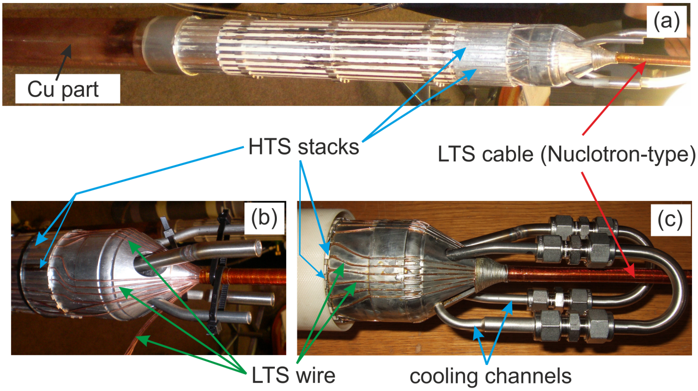

Figure D.4.: SIS100 main current leads (courtesy of Mark&Wedell): (a) HTS section, (b, c) HTS/LTS interface (cold terminal).

in further increase in temperature and leads to a destructive effect. The thermal runway of the copper part could be detected by measuring voltage directly on the conductor. The start of the thermal runway will be visible in the increased voltage drop.

The HTS part of the hybrid current lead requires a protection against quench. Similarly to the Cu part, a quench in HTS could be detected by a voltage measurement. Figure D.5 presents a typical detection scheme for a stand–alone magnet powered via HTS current leads. Each current lead is monitored by two voltage recording cards (or single ended resistive bridges): one for the Cu part and another for the HTS part. Typically, the HTS part is stabilised (by–passed) by a stainless steel or brass conductor. Since the by–pass increases the cross–section of the thermal bridge between the interception point at 70 K (50 K) and the cold region at 4 K, the static head load is increased. However, in case of a quench, the by–pass takes over the current and protects the HTS section. Figure D.6 shows the thermal conductivity of various HTS tapes (Bi2223) in reference to brass, stainless steel, silver and copper. As one can see, for Bi tapes the additional silver layer significantly increases the thermal conductivity in comparison to pure Bi2223. Brass and stainless steel are the preferred materials for HTS stabilisers since their thermal conductivity coefficients are lower than that of copper.

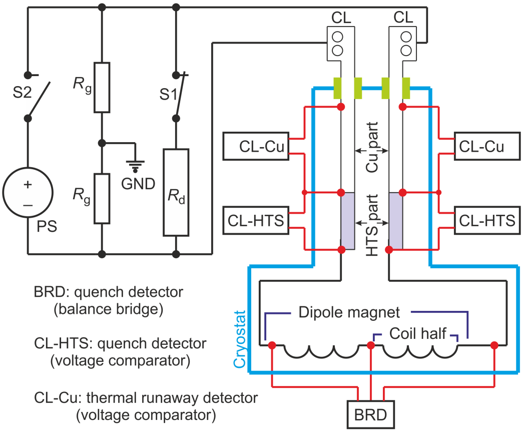

Figure D.5.: Quench detection concept for a stand–alone magnet and its current leads.

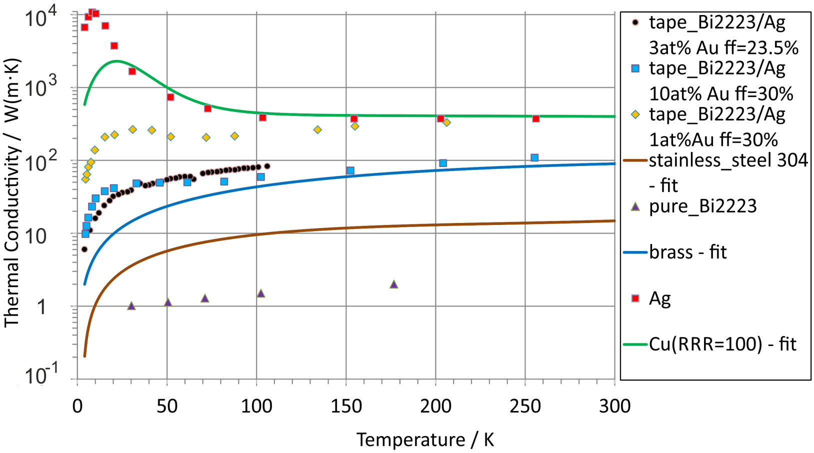

Figure D.6.: Thermal conductivity of HTS tapes in reference to brass, stainless steel, silver and copper. “ff” – filling factor [79].

E NbTi Alloy Composition

T_{c0} and B_{c2} of niobium–titanium depend on the Ti content in the alloy. Figures E.1 and E.2 show a summary of the bibliographic study concerning T_{c0} and B_{c2} of NbTi. All data points are measured values reported in the years 1961–1994. One finds that the 46.5 weight percent Ti alloy is the most popular because of its highest B_{c2}. For commercially available conductors (nominal composition of 44 to 48 weight percent Ti) one can deduce:

- $9.0 \text{ K} \leq T_{c0} \leq 9.4 \text{ K}$,
- $10.2 \text{ T} \leq B_{c2}(4.2 \text{ K}) \leq 11.8 \text{ T}$.

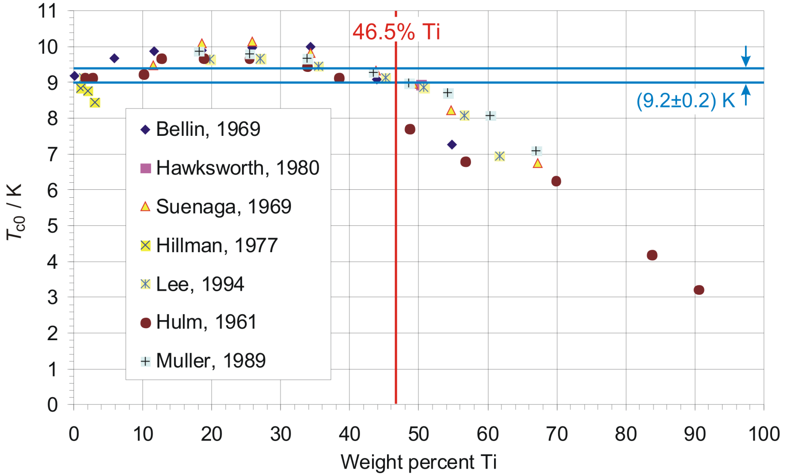

Figure E.1.: Measured T_{c0} for NbTi [80–86].

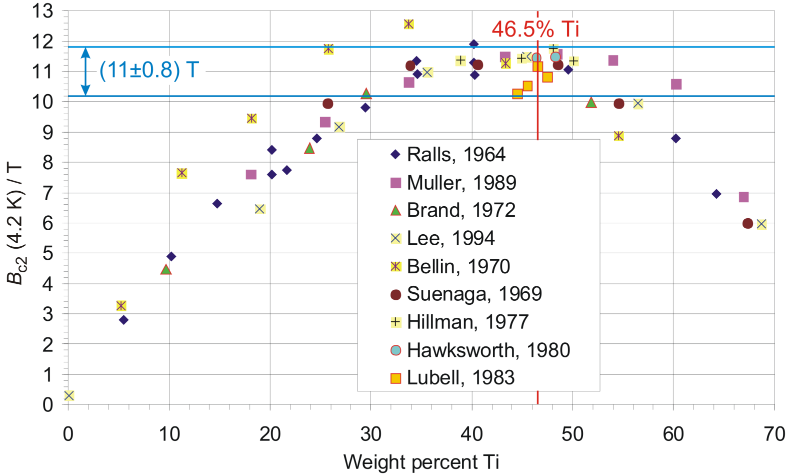

Figure E.2.: Measured B_{c2}(4.2 K) for NbTi [20, 80, 82–85, 87–89].

F Fundamentals of Electromagnetism and Synchrotrons

The magnetic field B and the electric field E act on charged particles by means of the Lorentz force F_L given by

$$\overrightarrow{F_\mathrm{L}} = q \cdot (\overrightarrow{E} + \overrightarrow{v} \times \overrightarrow{B}), \tag{F.1}$$

where q is the electrical charge of the particle and v is the particle velocity. The first term $(q \cdot \overrightarrow{E})$ gives the acceleration force to the particles while the second term $(q \cdot \overrightarrow{v} \times \overrightarrow{B})$ guides the particles through the space. The electric and magnetic fields are governed by the Maxwell's Equations (F.2–F.5) that form the fundamentals of electromagnetism [90]:

$$\nabla \cdot \overrightarrow{D} = \varrho_q, \tag{F.2}$$

$$\nabla \cdot \overrightarrow{B} = 0, \tag{F.3}$$

$$\nabla \times \overrightarrow{E} = -\frac{\partial \overrightarrow{B}}{\partial t}, \tag{F.4}$$

$$\nabla \times \overrightarrow{H} = \overrightarrow{J} + \frac{\partial \overrightarrow{D}}{\partial t}, \tag{F.5}$$

where $\overrightarrow{D} = \epsilon \overrightarrow{E}$ is the electric displacement field[1], ϱ_q is the charge density in the considered volume, $\overrightarrow{H} = \overrightarrow{B}/\mu$ is the magnetic field strength[2] and J is the current density.

The first two equations describe the static situation, where the Gauss' law for electric fields (F.2) states that the electric field E leaving a unit volume is propor-

---

[1] $\epsilon = \epsilon_0 \epsilon_\mathrm{r}$ is the electric permittivity where ϵ_0 is the permittivity of free space and ϵ_r is the relative permittivity.

[2] $\mu = \mu_0 \mu_\mathrm{r}$ is the magnetic permeability where μ_0 is the permeability of free space, μ_r is the relative permeability

tional to the charge q within this volume. The Gauss' law for magnetism (F.3) shows that there is no singular source of magnetic fields (in other words, there are no magnetic monopoles). The third Maxwell's Equation (F.4) is Faraday's law. It describes the induction of an electric field by an alternating magnetic field. Equation (F.5) is Ampere's law with Maxwell's addition. It describes the induction of a magnetic field due to the electrical current (in conductors) and/or displacement current (in capacitors).

If a charged particle passes through a vertical magnetic field B_y, its trajectory is deflected due to the Lorentz force F_L, see Fig. F.1. The particle's trajectory is described by

$$\left|\overrightarrow{F_\mathrm{c}}\right| = \left|\overrightarrow{F_\mathrm{L}}\right| \quad \Rightarrow \quad \frac{m_q \cdot v^2}{\varrho} = q \cdot v \cdot B_y \quad \Rightarrow \quad \frac{1}{\varrho} = \frac{q}{p} \cdot B_y, \tag{F.6}$$

where F_c is the centripetal force, m_q is the particle mass, $\overrightarrow{p} = m_q \cdot \overrightarrow{v}$ is the particle momentum and ϱ is the bending radius.

Synchrotrons

In synchrotrons, an equilibrium between the Lorentz force and the centripetal force is required in order to bend the beam along the desired path. One can define an ideal or reference trajectory (orbit, path) for which the ions are guided with only dipole field components. In reality, the ions are oscillating around the ideal orbit and form an ellipse in transverse direction. The ideal trajectory and the beam ellipse define the so–called beam envelope. For ions that move in the vicinity of ideal orbit, the magnetic field induction can be described with the use of Taylor's series as given by

$$B(x) = B_0 + \frac{dB}{dx} \cdot x + \frac{1}{2!} \cdot \frac{d^2B}{dx^2} \cdot x^2 + \frac{1}{3!} \cdot \frac{d^3B}{dx^3} \cdot x^3 + \ldots \tag{F.7}$$

In order to perceive the essence of the Taylor's expansion, Eq. (F.7) was multiplied by q/p:

$$\begin{aligned} \frac{q}{p} \cdot B(x) = \frac{q}{p} \cdot B_0 + \frac{q}{p} \cdot \frac{dB}{dx} \cdot x + \frac{1}{2!} \cdot \frac{q}{p} \cdot \frac{d^2B}{dx^2} \cdot x^2 + \frac{1}{3!} \cdot \frac{q}{p} \cdot \frac{d^3B}{dx^3} \cdot x^3 + \ldots = \\ = \frac{1}{\varrho} + k \cdot x + \frac{1}{2!} \cdot m \cdot x^2 + \frac{1}{3!} \cdot o \cdot x^3 + \ldots \end{aligned} \tag{F.8}$$

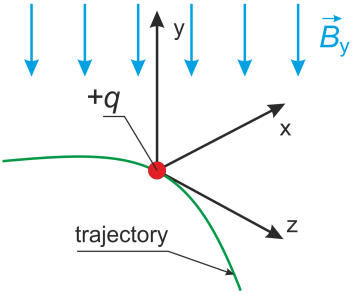

Figure F.1.: Particle trajectory and the local coordinate system.

Then each term of Eq. (F.8) corresponds to a different magnetic field component and its coefficient represents [40]:

- $1/\varrho$ – the dipole strength (bending component),
- $k \cdot x$ – the quadrupole strength (focusing component),
- $1/2! \cdot m \cdot x^2$ – the normalised sextupole strength,
- $1/3! \cdot o \cdot x^3$ – the normalised octupole strength.

Therefore the ions can be hold within the desired beam envelop by using magnets that provide the required magnetic field components at right locations. Such a magnetic structure along the synchrotron ring is called magnetic lattice. A part of the magnetic lattice which only contains dipole and quadrupole magnets is called linear optics. Since a single quadrupole focuses the beam in only one axis (parallel to the beam) and simultaneously de–focuses in the other, the quadrupole magnets are assembled into doublets (two quadrupole magnets rotated by 90° in respect to each other).

Magnetic Rigidity

Typically, in synchrotrons and as well as in fragment separators, the maximum beam energy is given by the machine size (bending radius) and maximum magnetic field that can be generated by the dipole magnets. The latter is taken into account by the machine parameter called magnetic rigidity $B\varrho$. The higher the rigidity is, the harder is to bend the particle path through a given radius. $B\varrho$ is defined by

$$B\varrho = p/e, \tag{F.9}$$

where p is the momentum, e is the elementary charge and ϱ is the effective radius of the synchrotron. ϱ is smaller than the ring radius since the dipole magnets are not continuously distributed over the machine circumference [40]. The significant part of the synchrotron circumference is occupied by quadrupole and corrector magnets, accelerating units, injection & extraction units, beam position instrumentation, etc.

For instance, the SIS100 synchrotron is designed to accelerate protons up to 30 GeV which means a particle velocity which is very close to the velocity of light c ($c \approx 3 \cdot 10^8$ m/s). Applying Eq. (F.9) one gets the magnetic rigidity of SIS100 equal to

$$B\varrho_{\mathrm{SIS100}} = \frac{30\ \mathrm{GeV}}{e \cdot 3 \cdot 10^8\ \mathrm{m/s}} \approx 100\ \mathrm{Tm}.$$

Equation (F.9) holds for proton and electron beams while for heavy ion beams, the magnetic rigidity is defined by

$$B\varrho = 3.3356 \cdot \beta \cdot \frac{A}{Q} \cdot E_{\mathrm{u}}, \tag{F.10}$$

where $B\varrho$ is expressed in [Tm], β is the particle velocity relative to the velocity of light in vacuum, A is the mass number (number of nucleons), Q is the particle charge in units of the electron charge e and E_{u} is the total beam energy given in GeV/u. The factor $3.3356 = 1/0.2998$ results from the units conversion: kg·m/s → GeV/c.

G World's Superconducting Particle Accelerators and Fragment Separators

World's Superconducting Particle Accelerators

Up to now (2016), only five high energy superconducting particle accelerators have been constructed in the world:

- the Tevatron at the Fermi National Accelerator Laboratory (Fermilab) in Illinois, USA;
- the Hadron-Electron-Ring-Anlage (HERA) at the German Electron Synchrotron research center (DESY) in Hamburg, Germany;
- the Nuclotron at the Joint Institute for Nuclear Research (JINR) in Dubna, Russia;
- the Relativistic Heavy Ion Collider (RHIC) at the Brookhaven National Laboratory (BNL) in Upton, New York, USA;
- the Large Hadron Collider (LHC) at the Centre Européen pour la Recherche Nucléaire (CERN) in Geneva, Switzerland.

All of them have a synchrotron construction. This list will be complemented with two more machines that will be constructed in the frame of the FAIR project. These machines are called SIS100 and SIS300 after their designed magnetic rigidities that are 100 and 300 Tm, respectively. The main parameters of world's superconducting synchrotrons are presented in Tab. G.1.

Table G.1.: World's superconducting synchrotrons [17, 24, 91–93]

Accelerator	Circumference (km)	B_{dipole} (T)	$B\varrho$ (T·m)	$\frac{dB_{\text{dipole}}}{dt}$ (T/s)	Years of operation
Tevatron	6.300	4.4	$3.3{\cdot}10^3$	0.29	1987-2011
HERA	6.336	4.682	-	0.007	1992-2007
Nuclotron	0.252	1.98	45	2	1993-
RHIC	3.834	3.45	839.5	0.07	2000-
LHC	27	8.36	$23{\cdot}10^3$	0.008	2009-
SIS100	1.0836	1.9	100	4	2022-
SIS300	1.0836	4.5	300	1	-

Dipole Magnets in Superconducting Synchrotrons

The dipoles of the Tevatron, HERA, RHIC, LHC and SIS300 are of $\cos\vartheta$–type, see Fig. G.1. Their main parameters are presented in Tab. G.2. One of the most important parameter is the effective length along the longitudinal field profile given by

$$L_{\text{eff}} = \frac{1}{B_{\text{n}}} \cdot \int\limits_{-\infty}^{\infty} B(z) \cdot dz, \tag{G.1}$$

where B_{n} is the nominal magnetic field in the gap and $B(z)$ is the actual field in the gap with respect to the position z along the dipole axis.

The dipole magnets of the Nuclotron and SIS100 are of super–ferric window–frame type as shown in Fig. G.2. The main parameters of the Nuclotron dipole and three different prototypes of SIS100 dipoles are presented in Tab. G.3.

Quadrupole Magnets in Superconducting Synchrotrons

Typically within a superconducting machine a same type of magnets is used for all magnets. In the Tevatron, HERA, RHIC, LHC and SIS300, the main quadrupole magnets are of $\cos(2\vartheta)$ and in the Nuclotron and SIS100 are of super–ferric type. The main electrical parameters of superconducting quadrupole magnets used in the Tevatron, HERA, RHIC, LHC, SIS300, Nuclotron and SIS100 are presented in Tables G.4 and G.5.

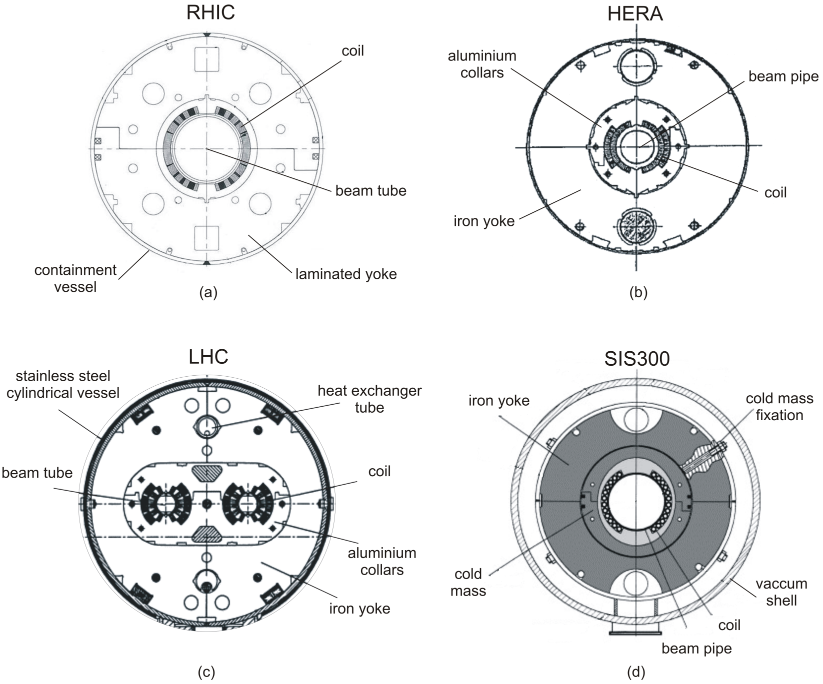

Figure G.1.: $\cos\vartheta$ dipole magnets in various accelerators: (a) RHIC dipole (courtesy of BNL), (b) HERA dipole [17], (c) LHC twin dipoles [19], (d) SIS300 dipole prototype (courtesy of GSI).

Table G.2.: $\cos\vartheta$ dipole magnets [17, 24, 91–93]

Dipole	B (T)	L_{eff} (m)	Dipole shape	I_{n} (kA)	L (mH)	E_{mag} (kJ)
RHIC	3.45	9.46	straight	4.56	43	490
Tevatron	4.4	6.1	straight	4.40	-	-
HERA	4.682	8.824	straight	5.027	58	820
LHC	8.33	14.312	curved	11.85	2×51	7021
SIS300	4.5	7.757 3.878	curved	8.924	22.5 11.25	896 448

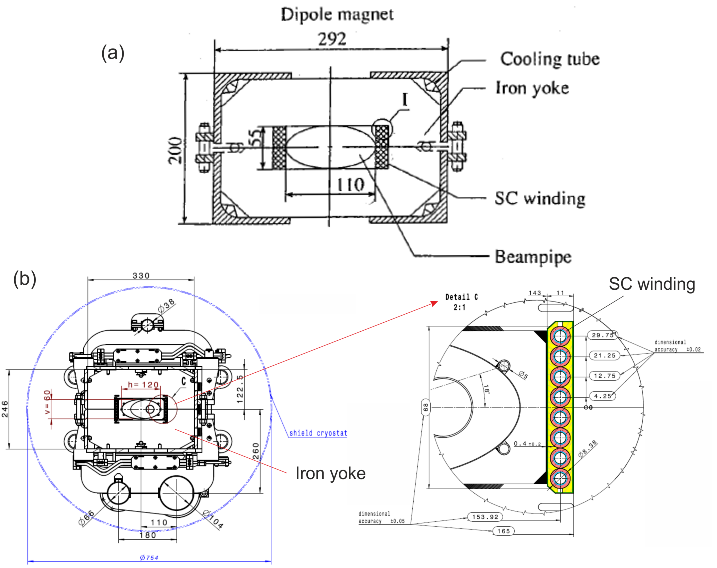

Figure G.2.: Designs of super–ferric window–frame dipole magnets: (a) Nuclotron dipole [94], (b) SIS100 dipole (courtesy of J. Macavei/GSI) .

Table G.3.: Super-ferric window-frame dipole magnets [39, 76, 94]

Dipole	B (T)	L_{eff} (m)	Dipole shape	I_{n} (kA)	L (mH)	E_{mag} (kJ)
Nuclotron	1.98	-	straight	6	1.1	19.8
SIS100 2 layer ver. 1	2.1	2.76	straight	7.535	2	56.8
SIS100 2 layer ver. 2	1.9	3.06	curved	6.5	2	42.3
SIS100 1 layer	1.9	3.06	curved	13.093	0.56	48

Table G.4.: cosϑ quadrupole magnets [91–93, 95, 96]

Quadrupole	Field gradient (T/m)	I_n (kA)	L (mH)	E_{mag} (kJ)
RHIC	71	4.7	2	22
Tevatron	76	4.44	-	-
HERA	90.2	5.027	5.5	69.5
LHC	223	12.12	5.6	411.3
SIS300	45	6.3	2.4	47.5

Table G.5.: Super-ferric window–frame quadrupole magnets [76, 94]

Quadrupole	Field gradient (T/m)	I_n (kA)	L (mH)	E_{mag} (kJ)
Nuclotron	33.4	5.6	0.44	6.9
SIS100	27	10.5	0.41	22.7

World's Superconducting Fragment Separators

The aim of fragment separators is rare isotope production and selection. Up to now only two fragment separators utilising superconducting magnets exist:

- A1900 at National Superconducting Cyclotron Laboratory (NSCL), Michigan State University (MSU), USA [97];
- BigRIPS at Institute of Physical and Chemical Research (RIKEN) in Japan [98].

In both separators, the primary beam is accelerated in a cyclotron and then hits the thin foil target to produce a secondary beam (in–flight technique) which is driven into the fragment separator. The available primary beam energy is in the range of 100–350 MeV/u with the rigidity between 6 and 9 Tm [99]. The A1900 separator consists of four superconducting dipoles and 24 superconducting quadrupoles (5 sizes) arranged in triplets. Correction multipoles are added to some of the quadrupoles. In case of the BigRIPS separator, only the quadrupoles are superconducting. There are three sizes of super–ferric type and three sizes of air–core type. The air–core quadrupoles are radiation resistant and are placed at the first section of the separator.

As a part of the FAIR facility, a new superconducting fragment separator called Super–FRS is constructed. In contrast to A1900 and BigRIBS, the primary beam for the injection into Super–FRS will be accelerated in a synchrotron (SIS100/SIS300). At Super–FRS, the available primary beam energy will range up to 1.5 GeV/u with the rigidity up to 20 Tm. The Super–FRS machine will consist of 24 superconducting dipoles (4 different bending radii) and 33 superconducting multiplets. A single multiplet has from two up to nine magnets enclosed within the common cryostat [100].

The main parameters of the superconducting dipoles and quadrupoles (the largest) used in A1900, BigRibs and Super–FRS are presented in Tables G.6 and G.7, respectively.

Table G.6.: Characteristics of dipoles used in superconducting fragment separators [97,100]

	A1900	Super-FRS
B_{gap} (T)	2	1.6
Gap (mm)	90	140
Bend Angle (°)	45	9.75
ϱ (m)	3.1	12.5
$B\varrho$ (T·m)	6.2	20
I_n (A)	171	245
L (H)	36.25	15
E_mag (kJ)	530	450

Table G.7.: Characteristics of the quadrupoles used in superconducting fragment separators [97,98,100]

Machine	Field Grad. (T/m)	I_n (A)	L (H)	E_mag (kJ)
A1900 Type QD	11	404.5	5.08	372
BigRIPS Q1000	14.1	135	18-33	270
Super–FRS “long”	10	291	26.5	1120

H RRR Measurements

The residual resistance ratio RRR is defined by

$$RRR = \frac{\varrho(300\ \mathrm{K})}{\varrho(4\ \mathrm{K})}. \tag{H.1}$$

Since in superconducting cables, the copper plays the role of a thermal stabilizer, it is important to verify RRR by measurement. The thermal conductivity of Cu in respect to RRR is shown in Fig. H.1. The higher RRR is, the lower resistivity and the higher thermal conductivity the conductor (Cu) has.

The RRR ratio can be measured on a superconducting cable sample according to the setup presented in Fig. H.2, where the cable sample is connected to a small power supply via current leads. The sample is equipped with two voltage taps that enable a voltage measurement. The distance between the voltage taps (L) is well–defined. The power supply feeds the circuit with a well–stabilised DC current. The temperature of the sample is measured via a dedicated temperature sensor. Since during the cooling process the temperature changes from a room temperature to 4 K, one has to use an adequate sensor that covers the full temperature range, e.g. CERNOX or CLTS. The measurement controller acquires and stores the data from the digital voltmeter (DVM) and from the temperature sensor (time synchronisation is required). The resistance of the sample is calculated as $R_{\mathrm{cable}}(T) = V/I$ and its resistivity can be computed by

$$\varrho_{\mathrm{cable}} = \frac{R_{\mathrm{cable}}(T) \cdot A_{\mathrm{cond}}}{L}, \tag{H.2}$$

where A_{cond} is the cross–section of the conductor.

Let us now present an example of a RRR measurement performed on the main cable of SIS100 magnets. The cable scheme is presented in Fig. H.3. The cable is constructed with 23 superconducting strands equally distributed around a CuNi tube in which the cooling two–phase helium is flowing (force flow). The strands are mechanically stabilised with a nickel–chrome wire. The cable is insulated with d polyimide insulation (Kapton®). The cable resistivity can be calculated by combining the resistivity characteristics of the involved conductors. In this case the involved conductors are: NbTi, CuMn, Cu (strand composition) and CuNi of which

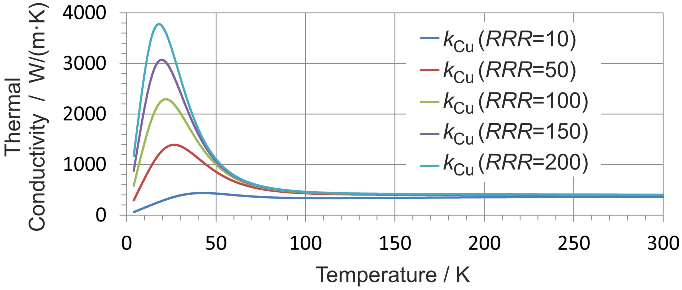

Figure H.1.: Thermal conductivity of Cu – measurement data given by the National Institute of Standards and Technology (NIST).

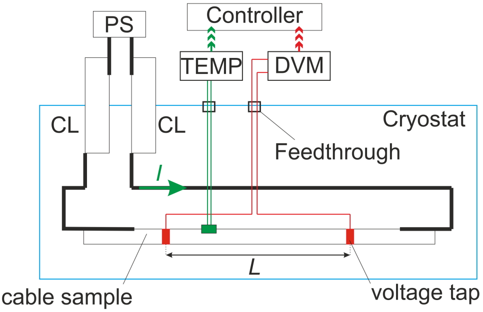

Figure H.2.: Experimental setup for RRR measurement: CL – current lead, PS – power supply, DVM – digital voltmeter, TEMP – acquisition card for temperature read out, L – distance between the voltage taps.

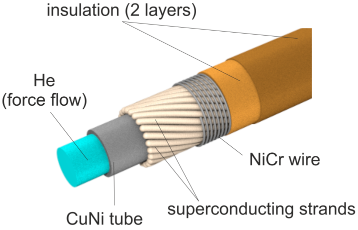

Figure H.3.: Scheme of the SIS100 main cable (courtesy of K. Sugita).

the cooling tube is made of. Therefore, the resistivity of the SIS100 main cable is equal to

$$\begin{aligned} &\varrho_{\text{cable}}(RRR,B,T) = \\ = A_{\text{cond}} \cdot \Bigg(&\frac{n_{\text{s}} \cdot A_{\text{NbTi}}}{f_{\text{tp}} \cdot \varrho_{\text{NbTi}}(T)} + \frac{n_{\text{s}} \cdot A_{\text{Cu}}}{f_{\text{tp}} \cdot \varrho_{\text{Cu}}(RRR,B,T)} + \\ &+ \frac{n_{\text{s}} \cdot A_{\text{CuMn}}}{f_{\text{tp}} \cdot \varrho_{\text{CuMn}}(T)} + \frac{A_{\text{CuNi}}}{\varrho_{\text{CuNi}}(T)} \Bigg)^{-1}, \end{aligned} \tag{H.3}$$

where A is the cross–section of the involved material, n_{s} is the number of superconducting strands and f_{tp} is the strand twist pitch factor. The total cross–section of the conductor in the cable equals to

$$A_{\text{cond}} = n_{\text{s}} \cdot A_{\text{NbTi}} + n_{\text{s}} \cdot A_{\text{Cu}} + n_{\text{s}} \cdot A_{\text{CuMn}} + A_{\text{CuNi}}. \tag{H.4}$$

The twist pitch t_{pf} is the axial length at which a wire/strand/filament returns to its original position in the conductor/cable as it is explained in Fig. H.4. Therefore, referring to the cable length, the twisted strands are longer than in case there would be no twist at all. This length increase is taken into account by the twist pitch factor as following:

$$f_{\text{tp}} = \frac{\sqrt{(\pi d)^2 + t_{\text{pf}}^2}}{t_{\text{pf}}}. \tag{H.5}$$

The following MATLAB® code describes the resistivity model of the SIS100 main cable:

```
function rlFoSD=rlSIS100maincable(RRR,T,Tcs,B) %  [Ohm/m]
di=4.7e-3; % inner diameter of the CuNi tube in [m]
do=5.7e-3; % outer diameter of the CuNi tube in [m]
ACuNi=pi*(do^2-di^2)/4; % cross-section of the CuNi tube in [m^2]
ds=0.8e-3; % superconducting strand diameter in [m]
ns=23; % number of strands
tp=0.05; % twist peach (strands) [m]
As=pi*ds^2/4; strand cross-section in [m^2]
alpha=1.4; % (Cu+CuMn)/NbTi ratio
ftps=(((pi*(do+ds))^2+tp^2)^0.5)/tp; % factor that takes into account the
% strand tp
ACu=0.403*As; % Cu cross-section (strand) in [m^2]
ACuMn=0.18*As; % CuMn cross-section (strand) in [m^2]
ANbTi=0.417*As; % NbTi cross-section (strand )in [m^2]
Acond=ns*ACu+ACuNi+ns*ACuMn+ns*ANbTi; % conductor cross-section in [m^2]
rlFoSD=1/(ACuNi/roCuNi(T)+ns*ACu/rhoCuF(RRR,T,B)/ftps+ns*ACuMn/rhoCuMnB(T)
/ftps+ns*ANbTi/rhoNbTi2(T,Tcs)/ftps);
% linear resistance (SIS100 main cable) in [Ohm/m]
end
```

The measurement of SIS100 main cable RRR was conducted in conjunction with the cold test of the first single–layer dipole prototype. Figures H.5 and H.6 show

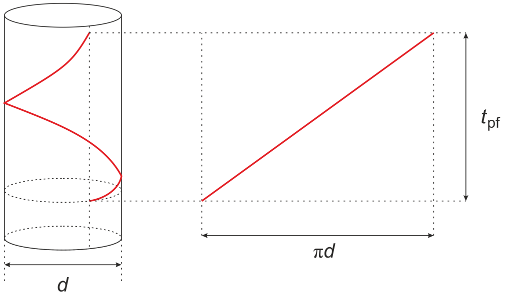

Figure H.4.: Explanation of the twist pitch and the twist pitch factor.

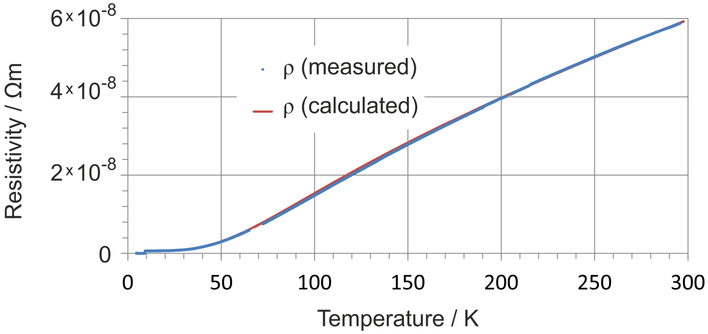

Figure H.5.: Temperature dependence on resistivity of the SIS100 main cable.

the measured and calculated values of the cable resistivity when cooling the magnet from the room temperature (300 K) to the operating temperature of 4 K. During the measurement the current was fixed to 5 A. At such a low current the critical temperature of NbTi is equal to its maximum of 9.2 K. A good agreement between the calculation and the measurement data was obtained for a cable model with $RRR_{\mathrm{Cu}} = 125$.

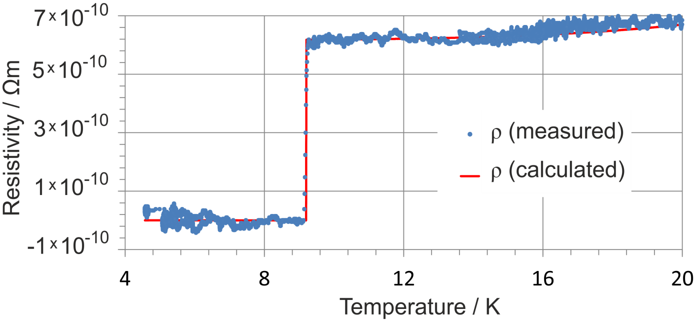

Figure H.6.: Temperature dependence on resistivity of the SIS100 main cable – zoom at the transition to the superconducting state.

I Existing Quench Calculation Software Solutions

Within this section, a short survey through the existing quench calculation software solutions is presented.

QUENCH – First Quench Calculation Software

The QUENCH calculation program was written in 1968 by Martin Wilson and his assistants at Rutherford Laboratory, UK [3, 4]. Over a period of five decades, the code was modified by variety of users, e.g. [5–7]. In spite of all the changes in the code, the core calculation engine of the original version has been preserved. The QUENCH software is able to provide the following information:

- temperature distribution along the conductor;
- time and spatial dependence of voltage including the peak value;
- total energy deposited in the magnet.

The software uses quench the propagation velocity as an input parameter. The velocity along the conductor can be calculated as follows:

$$v_{\mathrm{fp}}^{\mathrm{Wilson}} = \frac{J}{C_{\mathrm{V}}} \cdot \sqrt{\frac{\varrho \cdot k}{T_{\mathrm{cs}} - T_{\mathrm{op}}}}, \tag{I.1}$$

where T_{op} is the operating temperature (e.g. 4.2 K when operating in liquid He). T_{cs} is the current–sharing temperature. The transverse propagation velocity is characterised by the α factor defined by Equation (I.2).

$$\alpha = \frac{v_{\mathrm{fp}}^{\mathrm{Transverse}}}{v_{\mathrm{fp}}^{\mathrm{Longitudinal}}} \approx \sqrt{\frac{k_{\mathrm{Transverse}}}{k_{\mathrm{Longitudinal}}}} \tag{I.2}$$

The major disadvantages of the QUENCH software are:

- high uncertainty of quench propagation velocities (v_{fp} and α),

- use of the Lubell's fit for the critical surface (not very precise at low magnetic fields),
- saturation of the magnetic yoke is not taken into account (constant inductance is assumed).

QUABER – Quench Software for cosϑ Magnets

The QUABER is a quench software developed for the LHC magnets (cosϑ–type) in the 1990s [8, 9]. The software takes into account:

- coil geometry and cable characteristics;
- non-linear material properties;
- electrical circuit of the magnet system and its parameters: initial current, self- and mutual inductance of the magnet poles, etc.;
- magnetic field map and the load line.

ROXIE – Quench Software for LHC Magnets

The ROXIE software was developed at CERN for electromagnetic simulation and optimisation of the LHC magnets (Rutherford cable) [10]. ROXIE is an advanced computer code that uses a sophisticated BEM–FEM[1] method. The following features are considered:

- thermal model with non–linear material properties;
- Bottura's fit for the critical surface of NbTi;
- coil and cable geometry;
- magnet protection scheme (quench heaters, dump resistors, cold diodes, etc.).

SQUID – Quench Calculation Software developed at CIEMAT

The quench calculation software developed at CIEMAT[2] was invented for potted coil magnets [2]. The implicit finite difference method (FDM) is the calculation core of the software. The time steps are variable, depending on the number of iterations that are necessary to solve the equation system. The following features are considered:

---

[1] BEM – boundary element method, FEM – finite element method.

[2] Centro de Investigaciones Energéticas, Medioambientales y Tecnológicas in Madrid, Spain

- coil and cable geometry;
- thermal model with non-linear material properties;
- Bottura's fit for the critical surface of NbTi;
- magneto–resistive effect in copper;
- magnetic field map and the load line;
- AC losses between the filaments (optional);
- magnet protection scheme (quench heaters, dump resistors, cold diodes, etc.).

Opera 3D with Quench Module (Vector Fields)

Opera 3D with the quench module is the only commercial quench software available nowadays on the market. The software uses the finite element method (FEM) in order to model the transient thermal and electromagnetic behaviour of a superconducting magnet system. The model contains superconducting coils, associated fixation structure, magnetic yoke, etc. – these are the elements of the thermal and electromagnetic model where the discrete mesh grid is applied. The electrical circuit of the magnet system (including magnet protection) is considered at the macroscopic scale (no mesh). For example, a 3D thermal model of the Super-FRS dipole prototype and its electrical scheme is presented in Fig. I.1. During the calculation, the software uses adaptive time stepping. Nevertheless, the computation time is relatively long. Non–linear material properties (including the B–H curve) can be implemented in the model in form of tables or user–defined functions. The user has no possibility to control the internal algorithm of the program.

Other Software Solutions

Apart from the quench calculation software solutions mentioned above, there exist a large number of "home–made" quench programs that were created over the years [11–14]. However, many of these programs are either not available for public or no user-friendly interface exists.

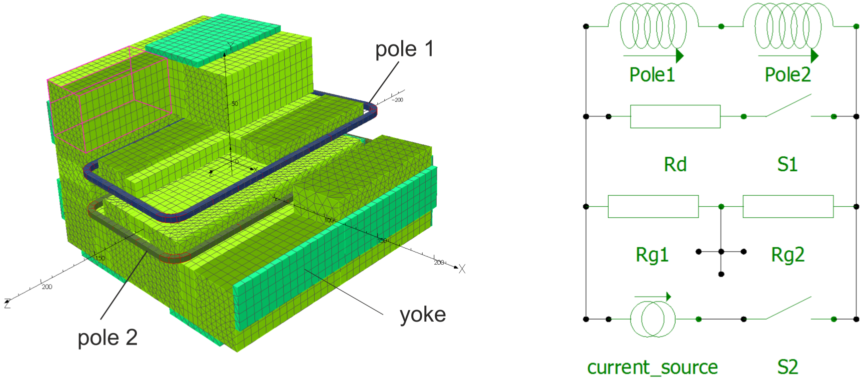

(a)

(b)

Figure I.1.: Super-FRS dipole model done in Opera: (a) mesh for the thermal model, (b) macroscopic scale electrical model.

J Inductance in Electro–Magnets

Definition

The fundamental definition of the inductance considers the flux correlated with the current in the coil windings:

$$L_\mathrm{s}(i) = N\frac{\Phi}{i} \quad \Rightarrow \quad , \Phi = L_\mathrm{s}(i) \cdot i/N, \tag{J.1}$$

where the index “s” states for secant or large signal and N is the number of turns associated with the flux Φ.

When calculating the electrical circuits, one uses the differential (or small signal) inductance L_d derived from the Faraday’s Law:

$$V(t) = -N\frac{\mathrm{d}\Phi}{\mathrm{d}t} = -L_\mathrm{d}(i)\frac{\mathrm{d}i}{\mathrm{d}t} \quad \Rightarrow \quad L_\mathrm{d}(i) = N\frac{\mathrm{d}\Phi}{\mathrm{d}i}. \tag{J.2}$$

On the other hand:

$$V(t) = -N\frac{\mathrm{d}\Phi}{\mathrm{d}t} = -\frac{\mathrm{d}[L_\mathrm{s} \cdot i]}{\mathrm{d}t} = -\left[i \cdot \frac{\mathrm{d}L_\mathrm{s}}{\mathrm{d}t} + L_\mathrm{s} \cdot \frac{\mathrm{d}i}{\mathrm{d}t}\right] = -\left[\frac{\mathrm{d}L_\mathrm{s}}{\mathrm{d}i} \cdot i + L_\mathrm{s}\right]\frac{\mathrm{d}i}{\mathrm{d}t}. \tag{J.3}$$

Therefore, there exist a correlation between L_s and L_d described by

$$L_\mathrm{d} = \frac{\mathrm{d}L_\mathrm{s}}{\mathrm{d}i} \cdot i + L_\mathrm{s}. \tag{J.4}$$

During the design phase of an electro–magnet, one performs magneto–static calculation (most of the time with the use of a 2D or 3D FEM software) from which the magnet inductance[1] L_w is calculated. L_w is derived from the magnetic energy calculation as follows:

$$E_\mathrm{mag} = \iiint\limits_\mathrm{volume} \frac{B^2}{2\mu_0\mu_\mathrm{r}}\,\mathrm{d}x \cdot \mathrm{d}y \cdot \mathrm{d}z = \frac{1}{2} \cdot L_\mathrm{w} \cdot i^2 \quad \Rightarrow \quad L_\mathrm{w} = 2 \cdot E_\mathrm{mag}/i^2. \tag{J.5}$$

---

[1] The symbol L_w was used by S. Russenschuck [10] where the index “w” states for work.

Assuming no losses in the magnetic yoke, the energy used for charging the magnet equals to

$$E_{\mathrm{PS}} = \int\limits_{t=0}^{t} V \cdot i \,\mathrm{d}t = \int\limits_{t=0}^{t} L_{\mathrm{d}} \frac{\mathrm{d}i}{\mathrm{d}t} \cdot i \,\mathrm{d}t = \int\limits_{i(t=0)=0}^{i(t)=I} L_{\mathrm{d}} \cdot i \,\mathrm{d}i. \tag{J.6}$$

Since $E_{\mathrm{PS}} \approx E_{\mathrm{mag}}$, it is true that

$$L_{\mathrm{w}} = \frac{2}{i^2} \cdot \int\limits_{i(t=0)=0}^{i(t)=I} L_{\mathrm{d}} \cdot i \,\mathrm{d}i = 2 \cdot \left[L_{\mathrm{s}} - \frac{1}{i^2} \int\limits_{0}^{I} \cdot L_{\mathrm{s}} \cdot i \,\mathrm{d}i \right]. \tag{J.7}$$

Looking at the power balance, one can derive the *vice versa* L_{d} dependence on L_{w}:

$$P_{\mathrm{PS}} = P_{\mathrm{mag}} \quad \Rightarrow \quad L_{\mathrm{d}} = L_{\mathrm{w}} + \frac{1}{2} \cdot \frac{\mathrm{d}L_{\mathrm{w}}}{\mathrm{d}i} \cdot i, \tag{J.8}$$

where the power generated in order to charge the magnet equals to

$$P_{\mathrm{PS}} = V \cdot i = L_{\mathrm{d}} \frac{\mathrm{d}i}{\mathrm{d}t} \cdot i \tag{J.9}$$

and the power rate at which the magnet stores the energy is calculated as

$$P_{\mathrm{mag}} = \frac{\mathrm{d}E}{\mathrm{d}t} = \frac{\mathrm{d}}{\mathrm{d}t} \left[\frac{1}{2} \cdot L_{\mathrm{w}} \cdot i^2 \right] = \frac{1}{2} \left[\frac{\mathrm{d}L_{\mathrm{w}}}{\mathrm{d}t} \cdot i^2 + 2 \cdot L_{\mathrm{w}} \cdot i \cdot \frac{\mathrm{d}i}{\mathrm{d}t} \right]. \tag{J.10}$$

When there is no iron yoke or only the linear range of the B–H characteristics is used (unsaturated region), all three mentioned inductances are identical and constant ($L_{\mathrm{s}} = L_{\mathrm{w}} = L_{\mathrm{d}} = \mathrm{const}$). When taking into account the iron saturation, the relation between the inductances changes to $L_{\mathrm{s}} > L_{\mathrm{w}} > L_{\mathrm{d}}$. The correlation between L_{s}, L_{w} and L_{d} for a given flux Φ variation is illustrated in Fig. J.1 [24].

Measurements

The inductance measurement with the use of a standard RLC meter only gives coarse result comparable to the inductance at zero current. Since the inductance measurement is often used to judge the quality of the coil and the yoke, a more accurate measurement method is required. When a series production of magnets of

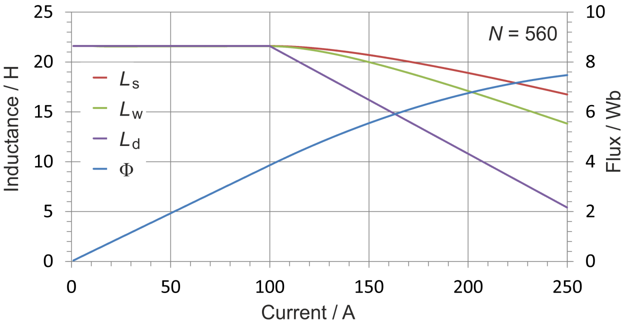

Figure J.1.: Inductance dependence on current for a given flux including yoke saturation.

the same type is launched, the inductance variation from one magnet to the other can indicate:

- turn–to–turn short–circuit in coil or insulation weakness,
- issues with the reproducibility of the yoke and coil parameters.

It is recommended that the inductance measurement ($V - I$ method) is performed on each magnet at cryogenic conditions (4 K) during magnet ramping to the nominal current. The magnet current and its voltage shall be recorded with two synchronised high precision digital volt–meters (DVM). Then the differential inductance can be calculated as follows:

$$L_{\mathrm{d}}(i) = V_{\mathrm{measured}}(t) / \frac{di_{\mathrm{measured}}(t)}{dt} \tag{J.11}$$

A typical shape of the $V - I$ characteristics of the magnet is presented in Fig. J.2. Since the magnet voltage changes very rapidly at the starting points of magnet charging and discharging, a high speed recording is necessary. Very often, before calculating the inductance, the measured voltage signal requires filtering (smoothing, noise reduction). Figure J.3 shows the measured inductance ($V - I$ method) for the SIS100 dipole magnet prototype. The inductance was calculated for the magnet charging (positive slope) and discharging (negative slope) and then a measurement fit was calculated. The measurement fit will be later used as the reference for the series SIS100 dipole magnets.

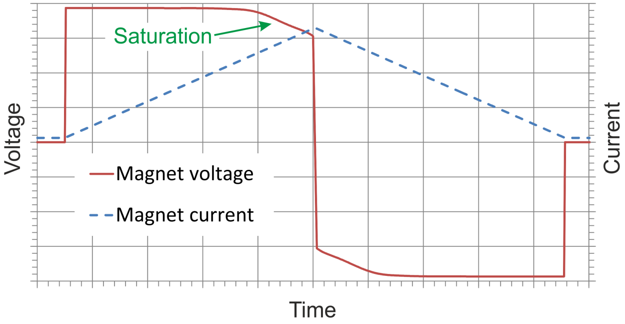

Figure J.2.: Typical shape of voltage and current recorded during superconducting magnet cycling.

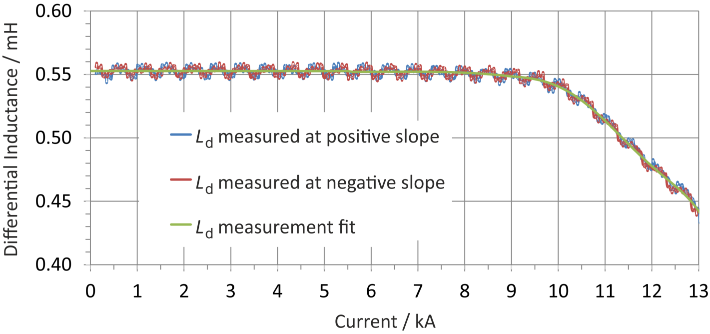

Figure J.3.: Differential inductance measured on the SIS100 dipole magnet.

K Wiedemann–Franz Law and Material Properties

Wiedemann–Franz Law and Lorenz Number

The Wiedemann–Franz Law, applicable for the most of conductive metals, states that the product of the thermal conductivity and the resistivity is proportional to the temperature of the metal [101]:

$$k(RRR, T) \cdot \varrho(RRR, B, T) = L_{\mathrm{L}} \cdot T. \tag{K.1}$$

The proportional factor L_{L} is the so–called Lorenz number defined by

$$L_{\mathrm{L}} = \left[\frac{\pi k_{\mathrm{B}}}{e\sqrt{3}}\right]^2 = 2.45 \times 10^{-8}\ \mathrm{W\Omega/K^2}, \tag{K.2}$$

where k_{B} is the Boltzmann's constant and e is the electronic charge. Figure K.1 presents the Lorenz number measured for copper, silver and aluminium in comparison to the theoretical value deduced from the free electron model of metals.

Selected Material Properties

A database of thermal and electrical properties of materials involved in superconducting magnet construction is presented within this section. For convenience, fitting functions are given (MATLAB® code).

Electrical Resistivity of Cu [45]

```
function rhoCuF=rhoCuF(RRR,T,B) % [Ohm*m]
rho_0T_293K = (1.7 /RRR + 1 / (2325470000 / 273 ^ 5 + 957137 / 273 ^ 3 +
162.735 / 273)) * 0.00000001;
rho_0T_T = (1.7 / RRR + 1 / (2325470000 / T ^ 5 + 957137 / T ^ 3 +
162.735 / T)) * 0.00000001;
x = B * rho_0T_293K / rho_0T_T;
  if x < 2
    y = 1 + 0.0031 * x;
  else
```

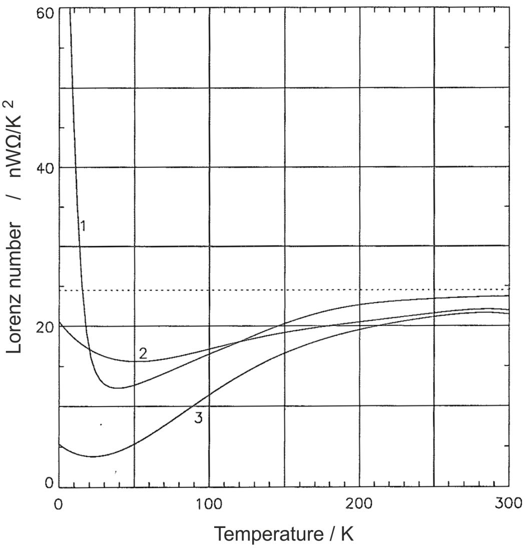

Figure K.1.: Lorenz number measured for: 1 – Cu ($RRR = 100$), 2 – Ag (99.99%) and 3 – Al (99.99%). The dotted line is a theoretical value based on the free electron model [101].

```
    z = log10(x);
    gaux = 0.016446 * z ^ 4 - 0.189163 * z ^ 3 + 0.700421 * z ^ 2 +
    0.091182 * z - 2.290249;
    y = 1 + 10 ^ gaux;
  end
rhoCuF = rho_0T_T * y;
```

Electrical Resistivity of NbTi [24]

```
function rhoNbTi2=rhoNbTi2(T,Tcs) % [Ohm*m]
 if T < Tcs
     rhoNbTi2 = 2e-31;
 elseif T < 150
     rhoNbTi2 = (-0.00000163 * T ^ 3 + 0.000288 * T ^ 2 + 0.0493 * T
     + 59.7) * 0.00000001;
 else
     rhoNbTi2 = (0.03017 * T + 63.55) * 0.00000001;
 end
```

Electrical Resistivity of CuNi [37]

```
function roCuNi=roCuNi(T); % [Ohm*m]
%roCuNi in Ohm.m
roCuNi = ((40 - 38) / (293 - 77) * (T - 293) + 40) * 0.00000001;
```

Electrical Resistivity of CuMn [24]

```
function rhoCuMnIF=rhoCuMnIF(sodf, df, rhoCuMn4K, rhoCuMn300K, T) % [Ohm*m]
% linear resistance of a single wire, only CuMn inter-fil matrix
aux = 6.56E-16;
rhoCuMnIF = rhoCuMn4K + (rhoCuMn300K - rhoCuMn4K)/(300 - 4) * (T - 4) +
aux/(sodf) * 1 / df;
```

Specific Heat of Cu [24]

```
function CvCuCern = CvCuCern(T); % [J/m3/K]
  if T < 10
    CvCuCern = -0.0000000308 * T ^ 4 + 0.000007229 * T ^ 3 -
     0.0000021286 * T ^ 2 +              0.0001018921 * T + 0.0000025631;
  elseif T < 40
    CvCuCern = -0.0000003045 * T ^ 4 + 0.000029871 * T ^ 3 -
     0.0004556091 * T ^ 2 + 0.003469536 * T - 0.0082503293;
  elseif T < 125
    CvCuCern = 0.0000000419 * T ^ 4 - 0.0000140237 * T ^ 3 +
     0.0015088935 * T ^ 2 - 0.0315948413 * T + 0.1784321698;
  elseif T < 300
    CvCuCern = -0.000000000848 * T ^ 4 + 0.000000841873 * T ^ 3 -
     0.000325517748 * T ^ 2 + 0.060590034121 * T - 1.285138694752;
  elseif T < 500
    CvCuCern = -0.000000000048 * T ^ 4 + 0.0000000917333 * T ^ 3 -
     0.00006412 * T ^ 2 + 0.0203626666678 * T + 1.028;
  elseif T < 1001 %valable jusqu'a 1000 K
    CvCuCern = 0.00000000012 * T ^ 3 - 0.000000214857 * T ^ 2 +
     0.001003841536 * T + 3.182253581765;
  else
    CvCuCern = 0.0009208 * T + 3.1703101; %'prolongation ajoute par moi
  end
CvCuCern = 1000000*CvCuCern; %'change les J/cm3.K ou MJ/m3.K en J/m3.K
```

Specific Heat of NbTi [24, 102]

```
function CvNbTiColinsB=CvNbTiColinsB(T,B); % [J/m3/K]
% for 1.8K - 100 K
if T < 20
  %----------------up to 20 K, values taken form collins collins en J/m3.K---
  %Alloy: 47 % wt in Nb = 31.4 %at in Nb, jusq^'a 20 K
  %E.W. Collins. "Applied superconductivity, metallurgy and Physics of
  %titanium alloys". Page 232, Plenium Press, New-york, 1986.
  %'attention , c 'est un Tc a I = 0
  TcBaux = 9.2 * (1 - B / 14.5) ^ 0.59;
  if T < (TcBaux + 0.001)
    aux = 49.1 * T ^ 3 + 64 * B * T;
  else
    aux = 16.4 * T ^ 3 + 928 * T;
  end
%------------------------------------------------------------------------------
elseif T < 50
   %-----between 20 and 50 K we make a junction between the values of
   %Collins and thus used for SSC
```

```
    %' in J/m3.K
        aux = -0.217724*T^4 + 11.983792*T^3 + 553.712993*T^2 - 7846.120813*
                          T + 41382.928569;
%-----------------------------------------------------------------------------
    % ' above 50 K we take the SSC values given here in J/cm3
elseif T < 175
        Cv = -0.00000000482 * T ^ 4 + 0.00000297583 * T ^ 3 - 0.00071625148
                          * T^2 + 0.08302230116 * T - 1.53178;
elseif T < 500
        Cv = -0.0000000000629 * T ^ 4 + 0.0000000929657 * T^3 -
                          0.0000516653121*T^2 + 0.0137062419692 * T + 1.23554;
elseif T < 1001
        Cv = -0.000000257 * T ^ 2 + 0.000955466 * T + 2.450087571;
else

     Cv = 0;% 'rien '; %nothing
end
if T < 50
    CvNbTiColinsB = aux;
else
    CvNbTiColinsB = 1000000 * Cv;     %conversion  to J/m3.K
end
```

Specific Heat of CuNi [24]

```
function CvCuNi=CvCuNi(T)
if T < 300
    if T <= 20
         CvCuNii=0.005214*T^3-0.02364 * T ^ 2 + 0.6418 * T - 1.73;
    else
       if T <= 80
         CvCuNii = -0.0076797 .* T ^ 3 + 1.2731 * T ^ 2 - 37.91 * T+353.7;
       else
         CvCuNii = 0.0002434 .* T ^ 3 - 0.18854 * T ^ 2 + 49.78 * T-1337;
       end
    end
    if T <= 20
       CvCuNia = 0.0050737 * T ^ 3 + 0.03497 * T ^ 2 + 0.9012 * T -2.6;
    else
       if T <= 40
         CvCuNia = 0.0048333 * T ^ 3 + 0.295 * T ^ 2 - 6.733 * T + 48;
       else
         CvCuNia = 0.0002222 * T ^ 3 - 0.184 * T ^ 2 + 50.86 * T -1200.0;
       end
    end
CvCuNi=(CvCuNia+CvCuNii)/2 * 1000; %'this Cv was initially given in kJ/m3.K
else
CvCuNi=833.5*T+3098750.0;
end
```

Specific Heat of Fiber Glass Epoxy G11 [24]

```
function  CvG11 = CvG11(T) % [J/m3/K]
if T <= 25.7
  CvG11 = 0.000044908 * T ^ 6 + 0.00117996 * T ^ 5 - 0.20029*T^4
        +2.72245 *T^3 + 194.657 * T ^ 2 - 699.191 * T + 817.749;
elseif T <= 273.8
   CvG11 = 0.0000000176492 * T ^ 6 - 0.0000164728 * T ^ 5 +
        0.00613783 * T ^ 4 - 1.16156 * T ^ 3 + 108.155 * T ^ 2 + 2997.29 * T
        - 34649.5;
else
  CvG11 = (4840.29 * T + 312808) * 0.998;
end
```

Specific Heat of Polyimide (Kapton) [103]

```
function CvKapton=CvKapton(t) % [J/m3/K]
%TP95HY, Cryogenics, Vol37,N12,1997, p799,
%from 20 to 300K,  J/m3.K
aux = -0.016 + 0.002074 * t + 0.00017738 * t ^ 2;  % J/cm3.K
CvKapton = aux * 1000000; %   J/m3.K
end
```

Thermal Conductivity of Cu [24]

```
function kCuNist = kCuNist(RRR, T) % [W/m/K]
% valid from 0.2 a 1250 K
% the NIST function is given with RRR = RRR_273K=r273/r4K, since we want
% to use RRR_293K=r293K/r4K
% we use RRR_273K=RRR_293K/1.082
RRR = RRR / 1.082; % change I made compared to what NIST used
beta = 0.634 / RRR;
p1 = 0.00000001754;
p2 = 2.763;
p3 = 1102;
p4 = -0.165;
p5 = 70;
p6 = 1.756;
betar = beta / 0.0003;
p7 = 0.838 / betar ^ (0.1661);
Wo = beta / T;
Wi = p1 * T ^ p2 / (1 + p1 * p3 * T ^ (p2 + p4) * exp(-(p5 / T) ^ p6));
Wio = p7 * Wi * Wo / (Wi + Wo);
kCuNist = 1 / (Wo + Wi + Wio);
```

Thermal Conductivity of NbTi [104]

```
function kNbTi = kNbTi(T); % [W/m/K]
if T <= 288.5
x = log(T) / log(10);
aux = 0.54249077 * x ^ 6 - 4.70877184 * x ^ 5 + 15.82488323 * x ^ 4 -
25.82624416*  x ^ 3 + 20.76901962 * x ^ 2 - 6.1357121 * x - 0.66963755;
kNbTi = 10 ^ aux;
else
kNbTi = 10.0112 + (14.544 - 10.0112) / (600 - 288.5) * (T - 288.5);
end
```

Thermal Conductivity of CuMn [24]

```
function kCuMn=kCuMn(sodf, df, rhoCuMn4K, rhoCuMn300K, T) % [W/m/K]
LWF=2.44e-8; %in W.Ohm/K^2 Wiedemann-Franz Law
kCuMn=LWF*T/rhoCuMnIF(sodf, df, rhoCuMn4K, rhoCuMn300K, T);
```

Thermal Conductivity of G10 [105]

```
function kG10CRpa=kG10CRpa(T) % [W/m/K]
% "pa" means parallel to the fibers,
if T <= 300
x = log(T) / log(10);
aux = 0.2839039 * x ^ 6 - 2.6006308 * x ^ 5 + 9.4683181 * x ^ 4
- 17.3392328 * x ^ 3 + 16.6101228 * x ^ 2 - 7.2383359 * x - 0.0161117;
kG10CRpa = 10 ^ aux;
else
kG10CRpa = 0.9047 + (1.5057 - 0.9047) / (600 - 300) * (T - 300);
end
```

```
function kG10CRpe=kG10CRpe(T) % [W/m/K]
% "pe" means perpendicular to the fibers,
if T <= 300
x = log(T) / log(10);
aux = 0.1322538 * x ^ 6 - 1.0849068 * x ^ 5 + 3.574754 * x ^ 4
- 5.9695994 * x ^ 3 + 5.1262453 * x ^ 2 - 1.4634311 * x - 1.2523286;
kG10CRpe = 10 ^ aux;
else
kG10CRpe = 0.6383 + (1.18 - 0.6383) / (600 - 300) * (T - 300);
end
```

Thermal Conductivity of CuNi [37]

```
function kCuNi=kCuNi(T); % [W/m/K]
if T < 40
    kCuNi = 0.35 * T;
elseif T < 80
    kCuNi = 0.000015 * T ^ 3 - 0.0053 * T ^ 2 + 0.63 * T - 3.7;
else
    kCuNi = 0.029 * T + 17.6;
 end
```

Heat Transfer to He I – Heat Flux $P_{\text{sHe}}(\Delta T)$ [59]

```
function PsHe=PsHe(DT) %W/m^2
THeaux=4.21;
d = 0.0504; %diameter of heater surface [m]
L = 20787.6; % latent heat [J/kg]
Cp = 5208.168; % specific heat LHe [J/Kg*K]
Muv = 0.00000124; % viscousity of vapor helium [Pa-s]
kv = 0.008998; % conductivity of vapor helium [W/(m-K)]
rhov = 16.64742076; %1/vtx(THeaux,1) density vapor helium [kg/m^3]
% at 4.4 K and 1 atm
rhoL = 125.1809512; %1 / vtx(THeaux, 0) density liquid helium [kg/m^3]
gravity = 9.81; % 'gravity [m/s^2]
sigma = 0.00008858; % surface tension [N/m]
L2 = L * (1 + (0.34 * Cp * DT) / L) ^ 2;
baux = (Muv * DT / (kv ^ 3 * rhov * (rhoL - rhov) * gravity * L2)) ^ 0.25;
a = (sigma / (gravity * (rhoL - rhov))) ^ 0.125;
C = (sigma / (gravity * d ^ 2 * (rhoL - rhov))) ^ 0.5;
if DT <= 1e-6
PsHe=0;
elseif DT <= 0.3
PsHe = 60000 * DT ^ 2.5;
elseif DT <= 11.19
  PsHe = 60000 * 0.3 ^ 2.5;
else
  PsHe = ((0.37 + 0.28 * C) / (a * baux)) * DT;
end
```

L Solution for the Heat–Balance Problem

L.1 Analytical Approach

The heat propagation in a 1D homogeneous wire which carries an electrical current is governed by the heat–balance equation as follows:

$$\varrho(RRR,B,T)\cdot J^2(t)+\frac{\partial}{\partial x}\left(k_x(RRR,T)\cdot\frac{\partial T(x,t)}{\partial x}\right)=C_\mathrm{V}(B,T)\cdot\frac{\partial T(x,t)}{\partial t} \tag{L.1}$$

In order to facilitate the analytical approach let us introduce the following simplifications and boundary & initial conditions:

- the temperature at both wire extremities is fixed to 0 °C (the Dirichlet boundary conditions):

  $$T(0,t)=T(L,t)=0,\ \text{where } L \text{ is the wire length;} \tag{L.2}$$

- the material properties k_x, C_V and ϱ do not depend on temperature and magnetic field;
- the electrical current in the wire does not vary with time (I =const $\Rightarrow$ J =const);
- the temperature distribution at $t=0$ is given as the initial condition:

  $$T(x,0)=f(x). \tag{L.3}$$

Then Eq. (L.1) simplifies to:

$$\varrho\cdot J^2+k\cdot\frac{\partial T^2(x,t)}{\partial x^2}=C_\mathrm{V}\cdot\frac{\partial T(x,t)}{\partial t}. \tag{L.4}$$

The solution of Eq. (L.4) can be expressed as a sum of two functions [106]:

$$T(x,t)=T_1(x)+T_2(x,t), \tag{L.5}$$

where:

- $T_1(x)$ is the solution for the steady state (at time $\to \infty$),
- $T_2(x,t)$ is the solution for the transient (unsteady state).

Solution for the Steady State

For the steady state, $T_1(x)$ satisfies Eq. (L.6).

$$\frac{\partial T_1^2(x)}{\partial x^2} = -\frac{\varrho \cdot J^2}{k} \tag{L.6}$$

When solving Eq. (L.6), one gets:

$$T_1(x) = -\frac{\varrho \cdot J^2}{2 \cdot k} \cdot x^2 + c_1 \cdot x + c_2, \tag{L.7}$$

where c_1 and c_2 are the integration constants that cab be derived with use of the boundary conditions (L.2). Hence c_1 and c_2 are equal to:

$$c_1 = \frac{\varrho \cdot J^2 \cdot L}{2 \cdot k}, \qquad c_2 = 0. \tag{L.8}$$

Solution for the Transient State

Considering the transient state, $T_2(x,t)$ satisfies equation

$$\frac{k}{C_\mathrm{V}} \cdot \frac{\partial T_2^2(x,t)}{\partial x^2} = \frac{\partial T_2(x,t)}{\partial t}, \tag{L.9}$$

which can be solved by separation of variables:

$$T_2(x,t) = A(x) \cdot B(t). \tag{L.10}$$

Substituting Eq. (L.10) into Eq. (L.9), one obtains:

$$\frac{B'(t)}{B(t)} = \frac{k}{C_\mathrm{V}} \cdot \frac{A''(x)}{A(x)}. \tag{L.11}$$

Since the left side of Eq. (L.11) only depends on time and the right side on x, both sides are equal to a certain constant value $-\lambda$ (minus is taken for more convenient representation). Thus, one can rewrite Eq. (L.11) with a system of two ordinary differential equations:

$$A''(x) + \lambda \cdot A'(x) = 0, \tag{L.12}$$

$$B'(t) + \frac{k}{C_{\mathrm{V}}} \cdot \lambda \cdot B(t) = 0. \tag{L.13}$$

One has to consider three cases with respect to the sign of λ when solving Eq. (L.12):

1. For $\lambda < 0$:

   $$A(x) = C_1 \mathrm{exp}(\sqrt{-\lambda} \cdot x) + C_2 \mathrm{exp}(\sqrt{-\lambda} \cdot x). \tag{L.14}$$

   Taking into account the boundary conditions that are valid for both steady and unsteady state, $A(0) = 0$ only when $C_1 = C_2 = 0$. Hence only a trivial solution exists.

2. For $\lambda = 0$:

   $$A(x) = C_1 x + C_2. \tag{L.15}$$

   Again, because of $A(0) = A(L) = 0 \Rightarrow C_1 = C_2 = 0$ (only trivial solution).

3. For $\lambda > 0$:

   $$A(x) = C_1 \mathrm{cos}(\sqrt{\lambda} \cdot x) + C_2 \mathrm{sin}(\sqrt{\lambda} \cdot x). \tag{L.16}$$

   Considering the boundary conditions (L.2), one obtains:

   - $A(0) = C_1 \Rightarrow C_1 = 0$,
   - $A(L) = C_2 \mathrm{sin}(\sqrt{\lambda} \cdot L) = 0 \Rightarrow \mathrm{sin}(\sqrt{\lambda} \cdot L) = 0 \Rightarrow \lambda_n = \left(\frac{\pi n}{L}\right)^2$, where n =1, 2, 3...

   Therefore:

   $$A(x) = C_n \mathrm{sin}\left(\frac{\pi n}{L} \cdot x\right), \tag{L.17}$$

   where C_n represents a series of constants for n =1, 2, 3...

When solving Eq. (L.13) one gets:

$$B(t) = D_n \exp\left(-\frac{k}{C_\mathrm{V}} \cdot \lambda \cdot t\right) \quad \Rightarrow \quad B(t) = D_n \exp\left(-\frac{k}{C_\mathrm{V}} \cdot \left(\frac{\pi n}{L}\right)^2 \cdot t\right), \tag{L.18}$$

where D_n represents a series of constants, $n = 1, 2, 3\ldots$

Combining Equations (L.10), (L.16) and (L.18), one gets:

$$T_2(x,t) = \sum_{n=1}^{\infty} G_n \sin\left(\frac{\pi \cdot n}{L} \cdot x\right) \exp\left(-\frac{k}{C_\mathrm{V}} \cdot \left(\frac{\pi \cdot n}{L}\right)^2 \cdot t\right), \tag{L.19}$$

where $G_n = C_n \cdot D_n$. One can calculate the G_n coefficients when applying the initial condition (L.3) as follows:

$$T_2(x,0) = \sum_{n=1}^{\infty} G_n \sin(\frac{\pi \cdot n}{L} \cdot x) = f(x). \tag{L.20}$$

The initial temperature distribution $f(x)$ can be described in a general Fourier series representation –

$$f(x) = \sum_{n=1}^{\infty} F_n \cdot X_n(x), \tag{L.21}$$

or simplified in a particular Fourier series as:

$$f(x) = \sum_{n=1}^{\infty} F_n \sin(\frac{\pi \cdot n}{L} \cdot x) \quad \Rightarrow \quad f(x) = \sum_{n=1}^{\infty} G_n \sin(\frac{\pi \cdot n}{L} \cdot x), \tag{L.22}$$

from where G_n can be derived using the following expression:

$$G_n = \frac{\int_0^L f(x) \sin(\frac{\pi \cdot n}{L} \cdot x) dx}{\int_0^L \sin^2(\frac{\pi \cdot n}{L} \cdot x) dx} \tag{L.23}$$

Combination of the Steady State and Transient – the Final Solution

Finally one can insert Equations (L.7) and (L.20) n Eq. (L.5) and obtains the analytical solution of the heat–balance problem (L.4):

$$T(x,t) = -\frac{\varrho \cdot J^2}{2 \cdot k} x^2 + \frac{\varrho \cdot J^2 \cdot L}{2 \cdot k} x + \sum_{n=1}^{\infty} D_n \sin\left(\frac{\pi \cdot n}{L} \cdot x\right) \exp\left(-\frac{k}{C_\mathrm{V}} \cdot \left(\frac{\pi \cdot n}{L}\right)^2 \cdot t\right). \tag{L.24}$$

L.2 Numerical Approach

L.2.1 Explicit Scheme

The heat propagation in a 1D homogeneous wire which carries an electrical current is governed by the heat–balance equation as follows:

$$\varrho(RRR, B, T) \cdot J^2(t) + \frac{\partial}{\partial x}\left(k_x(RRR, T) \cdot \frac{\partial T(x,t)}{\partial x}\right) = C_\mathrm{V}(B,T) \cdot \frac{\partial T(x,t)}{\partial t} \tag{L.25}$$

In the explicit scheme, the rate of temperature change $\partial T(x,t)/\partial t$ and the temperature gradients take the following forms:

$$\frac{\partial T(x,t)}{\partial t} = \frac{T_{x,t+dt} - T_{x,t}}{dt}, \tag{L.26}$$

$$\frac{\partial T(x,t)}{\partial x}|_\mathrm{forward} = \frac{T_{x+dx,t} - T_{x,t}}{dx}, \tag{L.27}$$

$$\frac{\partial T(x,t)}{\partial x}|_\mathrm{backward} = \frac{T_{x,t} - T_{x-dx,t}}{dx}. \tag{L.28}$$

Therefore, Eq (L.25) can be rewritten as:

$$J^2 \cdot \varrho + k \cdot \frac{T_{x-dx,t} - T_{x,t}}{dx^2} - k \cdot \frac{T_{x,t} - T_{x+dx,t}}{dx^2} = C_\mathrm{V} \cdot \frac{T_{x,t+dt} - T_{x,t}}{dt}, \tag{L.29}$$

and transformed to:

$$J^2 \cdot \varrho + k \cdot \frac{T_{x-dx,t} - 2 \cdot T_{x,t} + T_{x+dx,t}}{dx^2} = C_\mathrm{V} \cdot \frac{T_{x,t+dt} - T_{x,t}}{dt}. \tag{L.30}$$

Finally one obtains a formula for the temperature profile at the time moment $t+dt$:

$$T_{x,t+dt} = T_{x,t} + \frac{k \cdot dt}{C_\mathrm{V} \cdot dx^2} \cdot (T_{x-dx,t} - 2 \cdot T_{x,t} + T_{x+dx,t}) + \frac{J^2 \cdot \varrho \cdot dt}{C_\mathrm{V}}, \qquad \text{(L.31)}$$

where dt is the elementary time step.

Introducing the indexes for the discrete space elements $j = 1,\ 2\ldots$ and for the discrete time moments $n = 1,\ 2\ldots$ to be: $x(j) = \{dx/2,\ 3dx/2,\ 5dx/2\ldots\}$ and $t(n) = \{0,\ dt,\ 2dt\ldots\}$, one gets:

$$T_j^{n+1} = T_j^n + \frac{k \cdot dt}{C_\mathrm{V} \cdot dx^2} \cdot \left(T_{j-1}^n - 2 \cdot T_j^n + T_{j+1}^n\right) + \frac{J^2 \cdot \varrho \cdot dt}{C_\mathrm{V}}, \qquad \text{(L.32)}$$

which is is the numerical (explicit scheme) solution of the considered 1D problem. When the temperature profile at the time moment n is known, the temperature profile at the time moment $n+1$ can be computed.

Stability of the Explicit Scheme

In order to check the stability of Eq. (L.32), let us consider a temperature function represented by a Fourier mode in independent variables (such an approach is presented in [107]):

$$T = \hat{T}^n \mathrm{e}^{iwx}, \qquad \text{(L.33)}$$

where w is the wave–number and i is the imaginary unit ($i^2 = -1$). Taking into account the linearity of Eq. (L.4), the numerical errors at the time step n (ϵ^n) and at the time step $n{+}1$ (ϵ^{n+1}) are given by:

$$T^{n+1} + \epsilon^{n+1} = g \cdot (T^{n+1} + \epsilon^n) \quad \Rightarrow \quad \epsilon^{n+1} = g \cdot \epsilon^n, \qquad \text{(L.34)}$$

where g represents the amplification factor of the numerical error. If ϵ increases from one time step to another, the calculation will quickly reveal instability. Thus, for a stable solution the condition:

$$|g| \leq 1 \qquad \text{(L.35)}$$

has to satisfied. Substituting Eq. (L.33) into Eq. (L.32) one obtains:

$$\hat{T}^{n+1}\mathrm{e}^{iwx} = \hat{T}^{n}\mathrm{e}^{iwx} + \frac{kdt}{C_{\mathrm{V}}dx^2}\left(\hat{T}^{n}\mathrm{e}^{iw(x-dx)} - 2\hat{T}^{n}\mathrm{e}^{iwx} + \hat{T}^{n}\mathrm{e}^{iw(x+dx)}\right) + \frac{J^2\varrho dt}{C_{\mathrm{V}}}. \tag{L.36}$$

Including

$$\mathrm{e}^{iw(x-dx)} = \mathrm{e}^{iwx}\cdot\mathrm{e}^{-iwdx}, \qquad \mathrm{e}^{iw(x+dx)} = \mathrm{e}^{iwx}\cdot\mathrm{e}^{iwdx}, \tag{L.37}$$

one gets

$$\hat{T}^{n+1}\mathrm{e}^{iwx} = \hat{T}^{n}\mathrm{e}^{iwx}\left(1 + \frac{2kdt}{C_{\mathrm{V}}dx^2}\left(\frac{1}{2}\mathrm{e}^{-iwdx} - 1 + \frac{1}{2}\mathrm{e}^{iwdx}\right)\right) + \frac{J^2\varrho dt}{C_{\mathrm{V}}}. \tag{L.38}$$

With

$$\frac{1}{2}\mathrm{e}^{-iwdx} + \frac{1}{2}\mathrm{e}^{iwdx} = \cos(wdx), \tag{L.39}$$

$$\cos(wdx) = 1 - 2\sin^2\frac{wdx}{2} \quad\Rightarrow\quad \cos(wdx) - 1 = -2\sin^2\frac{wdx}{2}, \tag{L.40}$$

one finally obtains the expression for the amplification factor g:

$$g(dx,dt) = 1 + \frac{2kdt}{C_{\mathrm{V}}dx^2}\left(\cos(wdx) - 1\right) = 1 - \frac{4kdt}{C_{\mathrm{V}}dx^2}\sin^2\frac{wdx}{2}. \tag{L.41}$$

Since the term $J^2\varrho dt/C_{\mathrm{V}}$ is not amplified, it is omitted in the expression for g. Using Eq. (L.35), one gets the stability condition of the explicit scheme as:

$$\left|1 - \frac{4kdt}{C_{\mathrm{V}}dx^2}\sin^2\frac{wdx}{2}\right| \leq 1. \tag{L.42}$$

Equation (L.42) must be fulfilled for every wave–number w. Therefore taking the maximum value of the sine function, one gets the final condition for the stability of the explicit scheme:

$$dt \leq \frac{C_{\mathrm{V}}dx^2}{2k}. \tag{L.43}$$

L.2.2 Implicit Scheme

In the implicit scheme, the heat conduction term is calculated at the time step $n+1$. Hence, the heat–balance problem of Eq. (L.25) takes the form of:

$$J^2 \cdot \varrho + k \cdot \frac{T_{x-dx,t+dt} - T_{x,t+dt}}{dx^2} - k \cdot \frac{T_{x,t+dt} - T_{x+dx,t+dt}}{dx^2} = C_{\mathrm{V}} \cdot \frac{T_{x,t+dt} - T_{x,t}}{dt}. \tag{L.44}$$

Introducing indexes for the discrete space elements $j = 1,\ 2, \ldots$ and for the discrete time moments $n = 1,\ 2, \ldots$ as $x(j) = \{dx/2\ , 3dx/2\ ,\ 5dx/2, \ldots\}$ and $t(n) = \{0,\ dt,\ 2dt, \ldots\}$, respectively, one obtains:

$$J^2 \cdot \varrho + k \cdot \frac{T_{j-1}^{n+1} - T_{j}^{n+1}}{dx^2} - k \cdot \frac{T_{j}^{n+1} - T_{j+1}^{n+1}}{dx^2} = C_{\mathrm{V}} \cdot \frac{T_{j}^{n+1} - T_{j}^{n}}{dt}. \tag{L.45}$$

Equation (L.45) can be rewritten as

$$a \cdot T_{j-1}^{n+1} + b \cdot T_{j}^{n+1} + c \cdot T_{j+1}^{n+1} = T_j^n + d, \tag{L.46}$$

with the parameters:

$$a = -\frac{dt}{dx^2 \cdot C_{\mathrm{V}}} \cdot k, \quad b = 1 + \frac{dt}{dx^2 \cdot C_{\mathrm{V}}} \cdot 2k, \quad c = -\frac{dt}{dx^2 \cdot C_{\mathrm{V}}} \cdot k \quad \text{and} \quad d = \frac{\varrho \cdot J^2 \cdot dt}{C_{\mathrm{V}}}.$$

In the explicit scheme, all the required temperature values are known from the previous time moment n in order to calculate the temperature profile at the time moment $n+1$. In contrast, in the implicit scheme, the computation is more sophisticated because of the unknown temperatures of elements $j-1$ & $j+1$ when computing the temperature of the element j at the time moment $n+1$. This latter is described by Eq. (L.46) and schematically shown in Fig. L.1, where, the temperature of the red elements is required to be known in order to compute the temperature of the space element marked in blue. That is why Eq. L.46 is never considered as a stand–alone equation and one creates an array of equations (matrix equation) which takes into account all the space elements $(1, \ldots,\ j, \ldots,\ j_{\max})$ at once. The matrix equation for the considered 1D problem takes the following form:

$$\mathbf{A} \cdot \mathbf{X} = \mathbf{B}, \tag{L.47}$$

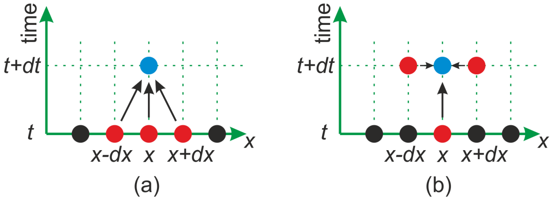

Figure L.1.: Explicit (a) and implicit (b) schemes.

where:

$$\mathbf{A} = \begin{bmatrix} b & c & 0 & 0 & 0 & \dots & 0 & 0 \\ a & b & c & 0 & 0 & \dots & 0 & 0 \\ \vdots & \vdots & \vdots & \vdots & \vdots & \dots & \vdots & \vdots \\ 0 & 0 & a & b & c & \dots & 0 & 0 \\ \vdots & \vdots & \vdots & \vdots & \vdots & \dots & \vdots & \vdots \\ 0 & 0 & 0 & 0 & 0 & \dots & a & b \end{bmatrix}, \tag{L.48}$$

$$\mathbf{X} = \begin{bmatrix} T_1^{n+1} \\ T_2^{n+1} \\ \vdots \\ T_j^{n+1} \\ \vdots \\ T_{j\max}^{n+1} \end{bmatrix}, \qquad \mathbf{B} = \begin{bmatrix} T_1^n + d \\ T_2^n + d \\ \vdots \\ T_j^n + d \\ \vdots \\ T_{j\max}^n + d \end{bmatrix}.$$

When solving Equation (L.47), one gets the temperature profile at the time moment $n+1$ when knowing the temperature profile at the moment n. Therefore it is the numerical (implicit scheme) solution of the considered 1D problem.

Stability of the Implicit Scheme

Equation (L.45) is the implicit representation of the 1D heat balance problem. After a rearrangement one gets

$$T_j^{n+1} = T_j^n + \frac{k \cdot dt}{C_\mathrm{V} \cdot dx^2} \cdot \left(T_{j-1}^{n+1} - 2 \cdot T_j^{n+1} + T_{j+1}^{n+1}\right) + \frac{J^2 \varrho dt}{C_\mathrm{V}}. \tag{L.49}$$

In order to check the stability of the implicit scheme, an identical approach as for the explicit scheme is used. Applying the Fourier mode (L.33) one gets:

$$\hat{T}^{n+1}\mathrm{e}^{iwx} = \hat{T}^{n}\mathrm{e}^{iwx} + \\ +\frac{k \cdot dt}{C_\mathrm{V} \cdot dx^2} \cdot \left(\hat{T}^{n+1}\mathrm{e}^{iw(x-dx)} - 2 \cdot \hat{T}^{n+1}\mathrm{e}^{iwx} + \hat{T}^{n+1}\mathrm{e}^{iw(x+dx)}\right) + \frac{J^2 \varrho dt}{C_\mathrm{V}}. \tag{L.50}$$

Implementing Equations (L.37), one obtains

$$\hat{T}^{n+1}\mathrm{e}^{iwx} = \hat{T}^{n}\mathrm{e}^{iwx} + \\ +\frac{k \cdot dt}{C_\mathrm{V} \cdot dx^2} \cdot \hat{T}^{n+1} \cdot \left(\mathrm{e}^{iwx} \cdot \mathrm{e}^{-iwdx} - 2 \cdot \mathrm{e}^{iwx} + \mathrm{e}^{iwx} \cdot \mathrm{e}^{iwdx}\right) + \frac{J^2 \varrho dt}{C_\mathrm{V}}, \tag{L.51}$$

and further

$$\hat{T}^{n+1}\mathrm{e}^{iwx} = \hat{T}^{n}\mathrm{e}^{iwx} + \frac{2 \cdot k \cdot dt}{C_\mathrm{V} \cdot dx^2} \cdot \hat{T}^{n+1}\mathrm{e}^{iwx} \cdot \left(\frac{1}{2}\mathrm{e}^{-iwdx} + \frac{1}{2}\mathrm{e}^{iwdx} - 1\right) + \frac{J^2 \varrho dt}{C_\mathrm{V}}, \tag{L.52}$$

$$\hat{T}^{n+1}\mathrm{e}^{iwx} = \hat{T}^{n}\mathrm{e}^{iwx} + \frac{2 \cdot k \cdot dt}{C_\mathrm{V} \cdot dx^2} \cdot \hat{T}^{n+1}\mathrm{e}^{iwx} \cdot (\cos(wdx) - 1) + \frac{J^2 \varrho dt}{C_\mathrm{V}}, \tag{L.53}$$

$$\hat{T}^{n+1}\mathrm{e}^{iwx}\left(1 - \frac{2 \cdot k \cdot dt}{C_\mathrm{V} \cdot dx^2} \cdot (\cos(wdx) - 1)\right) = \hat{T}^{n}\mathrm{e}^{iwx} + \frac{J^2 \varrho dt}{C_\mathrm{V}}. \tag{L.54}$$

Taking into account Eq. (L.40) one gets the formula for the amplification factor g (term $J^2 \varrho dt / C_V$ is omitted since it is not amplified):

$$g(dx, dt) = \frac{1}{1 - \frac{2 \cdot k \cdot dt}{C_\mathrm{V} \cdot dx^2} \cdot (\cos(wdx) - 1)} = \frac{1}{1 + \frac{4 \cdot k \cdot dt}{C_\mathrm{V} \cdot dx^2} \cdot \sin^2 \frac{wdx}{2}}. \tag{L.55}$$

Since the sine function can take values between 0 and 1, it is true that:

$$\left|\frac{1}{1 + \frac{4 \cdot k \cdot dt}{C_\mathrm{V} \cdot dx^2} \cdot \sin^2 \frac{wdx}{2}}\right| \leq 1 \quad \Rightarrow \quad |g(dx, dt)| \leq 1. \tag{L.56}$$

Therefore, the implicit method is unconditionally stable.

L.3 Comparison between Analytical and Numerical Methods

In this section, the analytical and numerical solutions of the heat-balance problem (L.4) are presented. In order to present the results, it is required to specify the conductor dimensions and properties. Let us consider a conductor of 1 m long which is characterised by the following physical properties:

- $\varrho = 1.74 \cdot 10^{-8}$ Ωm,
- $k = 400$ W/m/K,
- $C_{\mathrm{V}} = 3.5 \cdot 10^{6}$ J/m^3/K.

Furthermore, it is assumed that the temperature at the conductor extremities is fixed to 0 °C and the heating is caused by the constant current density J of 10 A/mm^2. The initial temperature distribution is given by:

$$T(x, 0) = -40 \cdot x^2 + 40 \cdot x. \tag{L.57}$$

Figure L.2 presents the temperature profiles in the considered conductor at the time moments 0, 25 and 50 seconds calculated with analytical and numerical (explicit and implicit) methods. Since for the all three methods, the obtained temperature distributions at the defined time are on top of each other, a perfect agreement is achieved between the analytical and numerical approaches. For the explicit scheme, the calculation is within the stability range only when $dt \leq 4.375 \cdot 10^3 \cdot dx^2$. For example, for dx =5 cm, the time step shall be lower than 110 ms.

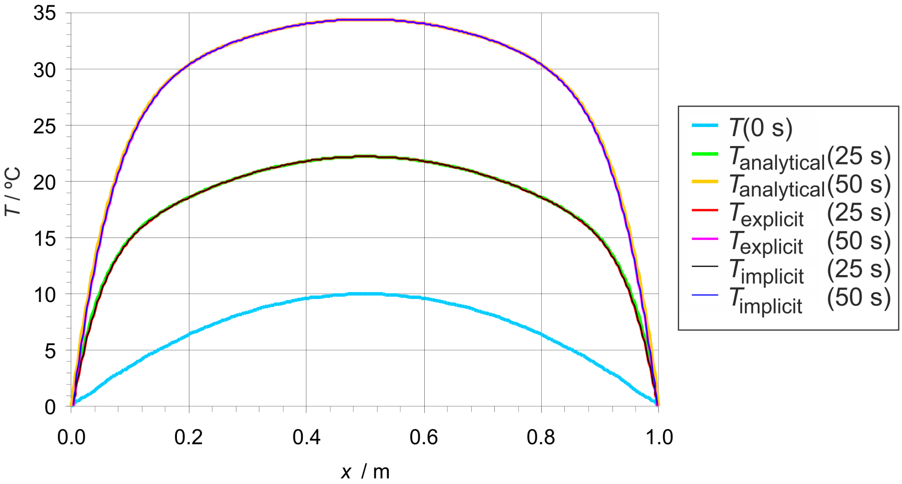

Figure L.2.: Analytical and numerical solution of the considered heat–balance problem (for numerical approach: dx =5 cm, dt =10 ms).

M Paschen's Law

The Paschen's law is an empiric equation that gives the breakdown voltage in a gaseous environment as a function of the pressure–distance product. The breakdown voltage is defined as the voltage at which the electrical discharge starts. It is measured between the test electrodes that are spaced apart with a defined distance. The experimental data of the breakdown voltage in air, SF_6[1], nitrogen and helium are presented in Figures M.1 and M.3. The Paschen's curves are characterised with a minimum. The breakdown voltage is significantly higher either at very low pressure (high vacuum) or when the gas is pressurised.

In electrical systems, the requirement for the Paschen tightness shall be considered whenever there is a probability to approach the minimum area at the Paschen's curve. In the FAIR magnets the Paschen tightness is considered for:

- SIS100 cryo-modules where the space in cryostat is kept at a good air vacuum (10^4 mbar or better). If the vacuum isolation is compromised, an interlock will be activated causing emergency switching off of the machine (emergency beam dump and discharge of the electrical circuit). In addition, the feedthroughs for the voltage tap wires are reinforced with a special epoxy glue.
- SIS100 main current leads that are designed to be Paschen tight.
- Super–FRS magnets that operate in helium bath at 1.2–1.3 bar and up to 20 bar at quench. Paschen tightness is required for the voltage tap feedthrouhgs and current leads.

Fig. M.2 shows an example of a voltage tap feedthrough for which the electrical insulation (pin–to–pin and pin–to–ground) was reinforced by applying an epoxy glue.

---

[1] SF_6 – Sulfur hexafluoride, inorganic, non-flammable gas often used for insulation in high voltage switching installations.

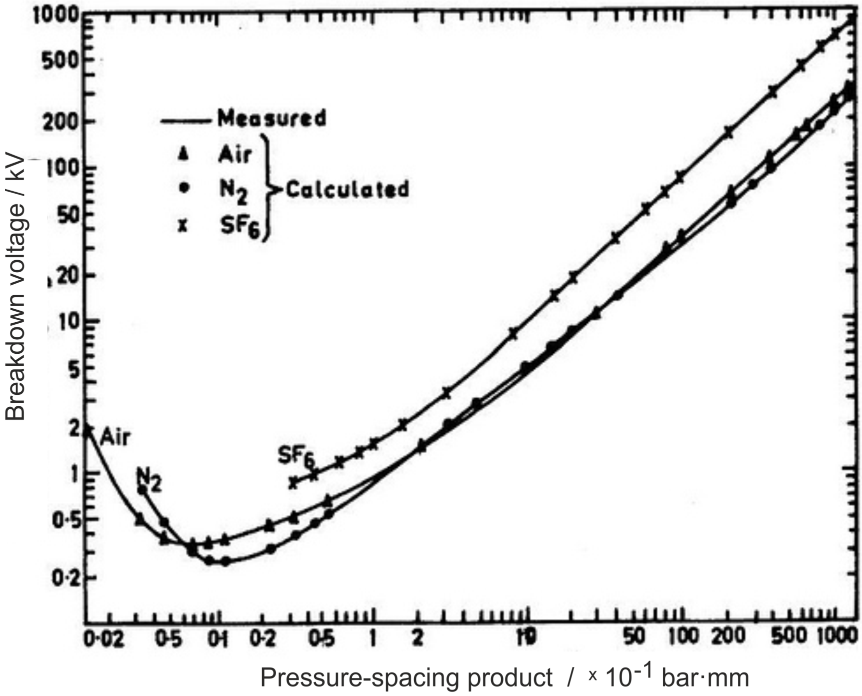

Figure M.1.: Paschen curve for air, nitrogen and SF_6 in a log–log scale (measurements at 20°C) [108].

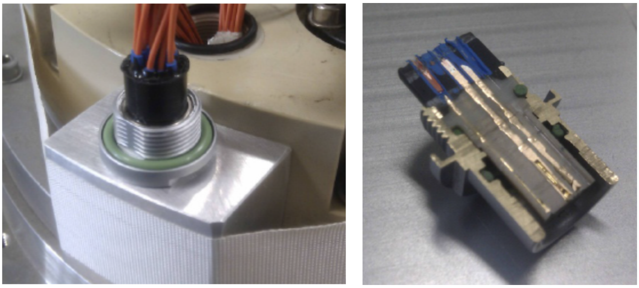

Figure M.2.: Possible insulation upgrade applied to an electrical feedthrough in order to fulfil the requirement for Paschen tightness [109].

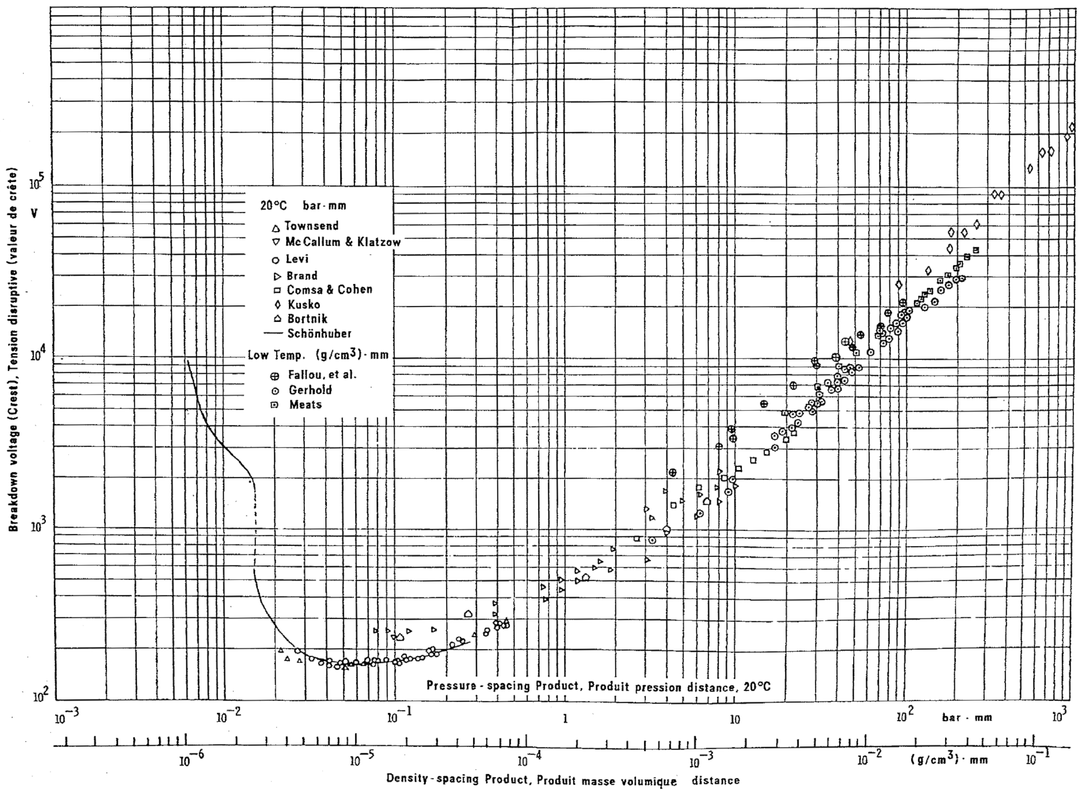

Figure M.3.: Paschen curve for helium in a log log scale (measurements at 20° C) [110].

N Magnet Protection at LHC

In order to meet the tough requirements for the beam parameters (strong bending field, high focusing gradients, etc.), the design of modern superconducting machines is pushed towards the quench limit of superconducting wires and cables. A very small temperature margin in conjunction with a very high operating current (in the range of 10-15 kA) increases the probability of a quench. In the history of superconducting accelerators, the most catastrophic (in terms of consequences) quench happened at CERN on September 19th 2008 during the last stage of the Large Hadron Collider (LHC) commissioning. In order to understand what exactly happened, let us take a closer look at the magnet protection and quench detection at the LHC machine.

N.1 Superconducting Circuits at LHC and their Protection

The Large Hadron Collider (LHC) is a double aperture superconducting synchrotron with the circumference of 27 km. The machine accelerates proton bunches[1] in two parallel beam pipes. The two beams travel in opposite directions. The LHC ring is divided into octants numbered from 1 to 8 as shown in Fig. N.1. Each octant contains two half–arc sections and one straight section. In the straight sections of the octants 1, 2, 5 and 8, the two beam pipes intersect. The crossing points are the locations where the particles collide with each other. Therefore at these locations, the main detectors are installed. Table N.1 presents the main detectors of LHC and their field of study. There is also another naming convention for the sections of the LHC ring that refers to sectors, called: 1–2, 2–3, 3–4, 4–5, 5–6 and 7–8. Each sector contains the full arc section and two halves of the straight sections at the arc extremities.

The electrical system of the LHC magnets is extremely large and contains more than 1600 different circuits of superconducting and normal–conducting magnets. In total, there are 3286 current leads, among them 1070 are of HTS type. The linear optics is constructed from 1232 (154 in each sector) double aperture dipole magnets and 392 twin quadrupole magnets (a single twin quadrupole magnet combines two coils: one of focusing and the other of defocusing family). Figure N.2 presents the

---

[1] With other control settings, it also is possible to accelerate ions, as it was done for Pb–Pb collisions study reported in [111].

Table N.1.: Main detectors of the LHC machine

Detector	Full name	Field of Study
ATLAS	A Toroidal LHC Apparatus	Wide range of Physics. Looking for signs of new physics, origin of mass (Higgs boson[a]) and extra dimensions.
ALICE	A Large Ion Collider Experiment	Study of the quark–gluon plasma.
CMS	A Compact Muon Solenoid	A competitor to ATLAS.
LHCb	LHC–beauty	Study the matter–antimatter asymmetry in the Universe.

[a] – So called God Particle discovered recently – the last element of the Standard Model (theory of particle physics that assumes that the universe is made up from elementary particles – fermions and mediators of interactions – bosons). So far it is known that the Higgs boson gives the mass to quarks and to W and Z bosons as well [112].

main dipole circuit of the LHC machine. There are eight circuits of this type, one per each arc section. The main quadrupole circuits are presented in Fig. N.3. In the whole ring, there are eight RQF and eight RQD circuits [113].

The quench protection system of the main circuits of LHC considers quench heaters, cold diodes (a diode for each twin aperture dipole magnet and for each quadrupole coil) and energy extraction resistors. At LHC, the functionality of quench heaters is combined with the cold diode [114]. When a quench in the magnet coil is detected, the heaters are fired in order to increase the overall resistive zone in the coil. Then the turn on voltage of the cold diode will be reached faster and the current will be overtaken by the by–pass in shorter time. The shorter the time within the quenched magnet conducts the current, the lower is the temperature at the quench origin. The principle of protection with the quench heaters and cold diodes is explained separately in Section 2.5.

The energy extraction resistors of the LHC main circuits (Figures N.2 and N.3) are activated by opening mechanical circuit breakers [46]. Figure N.4 shows an example of dump resistors and a cold diode (turn on voltage of 6–8 V) used at LHC.

N.2 Quench Detection at LHC

The quench detection system at the main circuits at LHC is based on analogue resistive bridge detectors. In the dipole circuit, the voltages across the two magnet

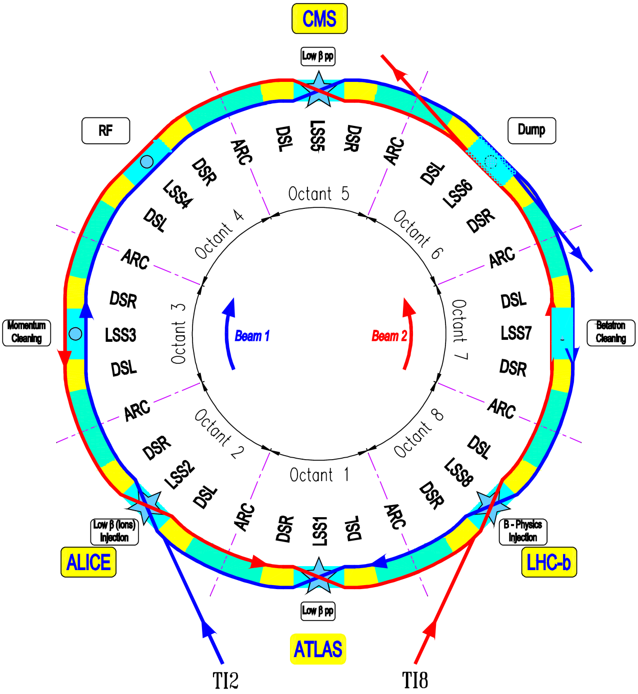

Figure N.1.: General scheme of the LHC ring [113].

apertures are compared to each other (see Fig. N.2). In the quadrupole circuits, each quadrupole is monitored by a single detector (with the use of a voltage tap installed in the middle of the coil). Quench detection of the quadrupoles differs from the dipoles due to the fact that the quadrupole coils in the neighbouring apertures belong to two independent circuits (focusing and defocusing families) and they cannot simply be combined (see Fig. N.3). For dipole and both quadrupole circuits the quench detection threshold is fixed to 100 mV with the validation time of 10 ms. The described analogue bridges belong to the so-called local quench detection system which gives the trigger for quench back heaters [19, 113, 115].

Quench detection for the main current leads is realised with voltage recording cards. For each lead, the voltage drop along the Cu part and the HTS part is monitored and recorded via a separate channel. The quench detection thresholds

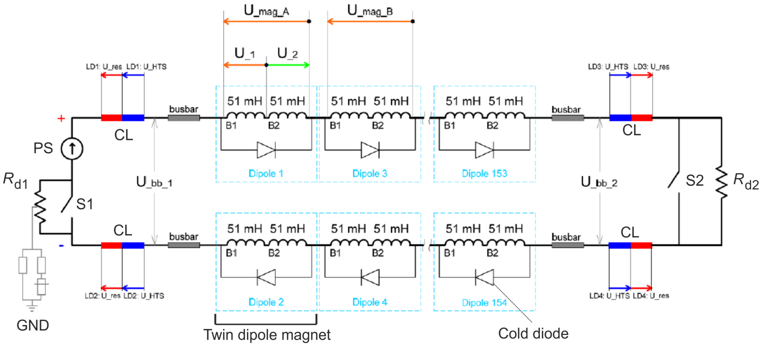

Figure N.2.: Main dipole circuit of LHC. There are 154 dipole magnets that cover a full arc section (courtesy of Alexandre Erokhin).

are set to 100 mV and 3 mV for the Cu part and the HTS part, respectively. In both cases the validation time is fixed to 100 ms [113, 116].

At LHC, the probability of quench in splices (superconducting joints) and bus–bars was considered as very low due to the heavy stabilization by soldered copper sections [117]. The survey of these elements was included in the so–called global quench detection which monitors the voltage across the complete electrical circuit [19, 116]. A scheme of a splice which connects the two bus–bars of the LHC dipole circuit is shown in Fig. N.5. The splices are located in low magnetic field regions which creates more relaxed conditions for the superconductor than in a coil (in the superconducting state, higher B decreases the temperature margin). It was assumed that if a quench occurs in the joint section, the Cu stabilizer shall take over the current and simultaneously conduct the heat away from the superconductor causing either recovery or slow thermal runaway of the Cu stabilizer [117]. In case of a thermal runaway of the Cu stabilizer, the resistive voltage will increase which will be detected by the global quench detection system at a certain threshold. For the dipole and quadrupole circuits, the threshold is fixed to 1 V with 1 s of validation time.

The local and global quench detection fully covers all the circuits of LHC with the assumption that all the circuits are healthy. The system is not able to generate an early warning in case of manufacturing faults, e.g. bad magnet interconnections.

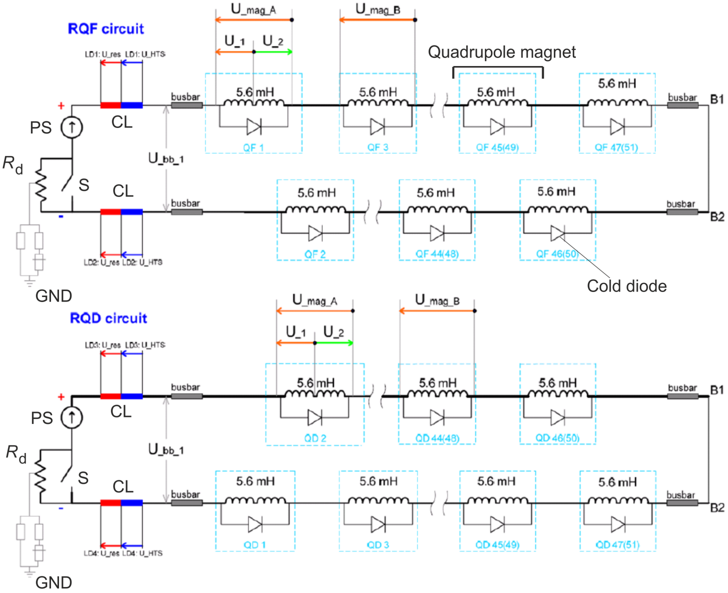

Figure N.3.: Main quadrupole circuits of LHC. In each sector there are two quadrupole circuits that power 47(51) quadrupole coils of the focusing family – RQF circuit and 51(47) quadrupole coils of the defocusing family – RQD circuit (courtesy of Knud Dahlerup-Petersen).

N.3 Incident at LHC

During the commissioning of LHC, the quench detection system provided:

- local quench detection (analogue bridges) on individual magnets with the threshold of 100 mV and 10 ms validation time;
- global quench detection at the electrical circuit level (1 V threshold with 1 s of validation time).

Until the middle of September 2008, seven out of eight LHC sectors successfully passed all the hardware commissioning tests. On September 15th, the commissioning of sector 3–4 started. The dipole circuit of sector 3–4 was powered up to 7 kA DC for a period of one hour. No suspicious behaviour was noticed at that time. On September 19th, the powering test were continued and during the ramping of the dipole circuit up to 9.3 kA (at nominal rate of 10 A/s), suddenly at 8.7 kA,

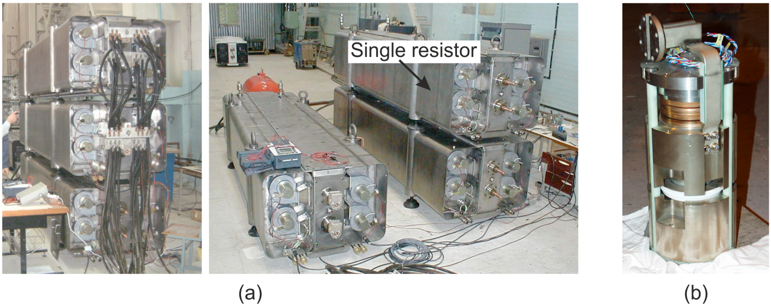

Figure N.4.: Quench protection elements; (a) 225 mΩ dump resistor (courtesy of Knud Dahlerup–Petersen), (b) cold diode of the by–pass system (courtesy of CERN).

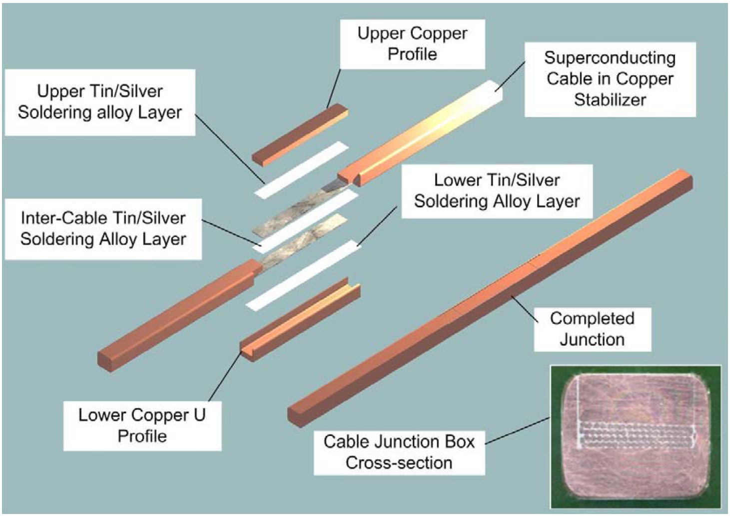

Figure N.5.: Superconducting joint assembly on main bus–bars (Rutherford–type cable) at LHC [117].

a quench occurred in the magnet interconnection section (dipole bus–bar). Based on the CERN report [117], the sequence of events could be summarised as follows:

1. A 300 mV resistive voltage signal appeared in the dipole circuit. The corresponding time will be used in the presented chronology as the reference. The

signal analysis done after the incident revealed that this resistive voltage came from the magnet interconnections, since the local detection did not register any unbalanced voltage at the analogue bridges.

2. After 0.39 s, the resistive voltage exceeded the 1 V level and the power converter could not maintain the required current any–more. As a consequence it went into the slow discharge mode at 0.46 s. The current started to slowly decrease.

3. At 0.86 s the energy extraction system was triggered by the global quench detection. The fast extraction of the current began.

Figure N.6 shows the current decay during the incident recorded at the two dump resistors of the dipole circuit (see Fig. N.2). First of all, the current decay time is much shorter ($\tau \approx 15$ s) than nominal value ($\tau \approx 104$ s at 11.85 kA) which indicates an abnormal behaviour of the circuit. Furthermore, the decay curve differs from one dump resistor to the other. This is an evidence of current fragmentation and probably an appearance of alternative current paths (e.g. insulation breakdown, short circuits, electrical arcs, etc.). The post–incident analysis revealed that 104 out of 154 dipole magnets were quenched because of firing the quench heaters. The triggers for the quench heaters were given by the individual local quench detectors of which many were excited by the noise induced due to too fast extraction, helium release, bus–bar ruptures, secondary arcs, ground faults or cryostat displacements.

Already in the first report concerning the incident [115], a bad splice has been considered as the most likely quench origin. Later this hypothesis was confirmed by the *post mortem* analysis [117]. After many tests and simulations it was discovered that only a bad splice with the resistance level of around 220 nΩ could stay undetected at 7 kA (maximum current reached on September 15th) and provoke a very fast thermal runaway of the Cu stabilizer at 8.7 kA that was observed on September 19th (see Fig. N.7). Such a high resistance joint[2] points to an absence of the soldering material [117].

Figure N.8 shows the scale of damage at the location of the faulty splice. The energy of the primary arcs was so high that a section of the dipole bus–bar (splice, copper stabilizer, Rutherford cable) was simply evaporated. One can also see the destroyed bellows around the “missing” bus–bar (M3 line) and the damaged beam vacuum pipes (V lines). At the time of energy extraction, the energy stored in the dipole circuit was equal to 595 MJ. The post–incident energy balance revealed that only 30% of the stored energy was dissipated in the dump resistors. Around 24%

---

[2] In the LHC specification it is required that the splice resistance shall be below <0.6 nΩ. Measurements done on the reference samples indicate a mean value of <0.2 nΩ and peak value of <0.3 nΩ [117].

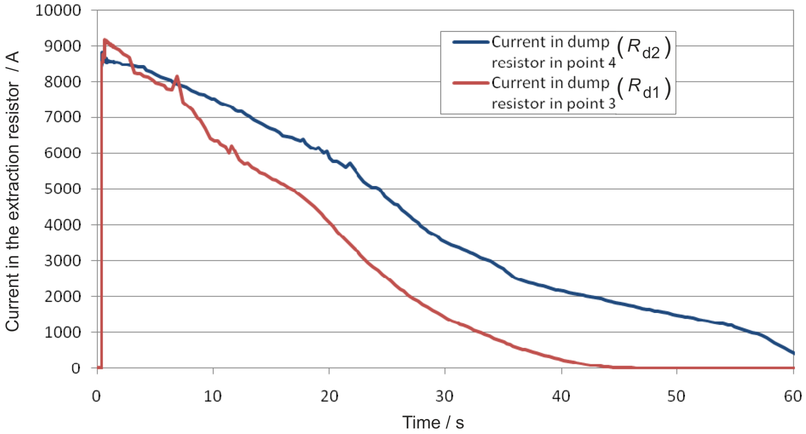

Figure N.6.: Current decay measured during the incident in the both dump resistors of the dipole circuit in sector 3–4 [117].

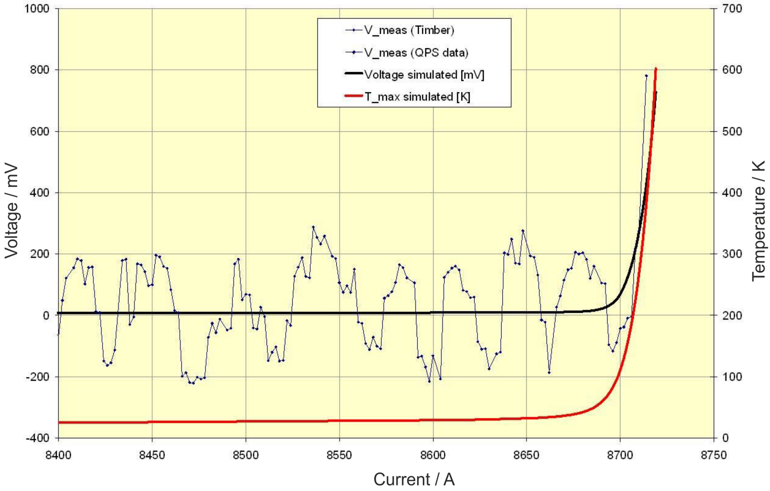

Figure N.7.: Measured and simulated voltage and temperature of the faulty bus–bar section with 220 nΩ splice (splice specification: <0.6 nΩ) [117].

of the energy was absorbed by the Helium coolant. The missing 46% were "most

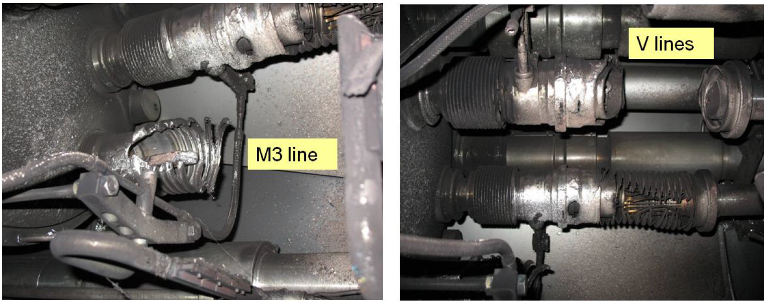

Figure N.8.: Vaporised dipole bus–bar, destroyed bellows around it (M3 line) and damaged beam vacuum pipes (V lines) at the location of the primary electrical arcs [117].

certainly" consumed by the electrical arcs [117]. As a consequence of the primary electrical arcs, the helium enclosure and the insulation vacuum were broken. This latter led to pressure increase in these volumes and appearance of large axial forces on the vacuum barriers. Due to these axial forces, at some places the cryostats were kicked out from their concrete anchors and in many other locations, the connections (cryostat bellows, bus–bars, process pipes, vacuum pipes, etc.) between the adjacent cryo–modules were damaged or deformed (see Fig. N.9). The damaged bus–bar connections caused secondary arcs that developed in other cryo–modules.

As a result of the incident, over 50 superconducting magnets (including their mounting) were damaged and about six tonnes of helium was released into the accelerator tunnel. In addition, the vacuum pipes were contaminated by soot. After spending around 14 months on repairs and upgrades, the LHC machine successfully passed all the commissioning tests and was brought into its first operational run (2009–2013).

After the incident, the structure of iQPS[3] was intensively investigated and as an outcome a decision was made to equip the detection system with additional hardware [118, 119]. "More than 14600 extra cables and 6000 new detectors and control cards" [119] were introduced in order to complete the old detection system. First of all, a second layer detection was added in order to detect symmetrical quenches. The second layer detection considers dipole super–bridges that compare to each other four dipole magnets and quadrupole super–bridges that compare two quadrupole magnets of the same family. In contrast to the analogue bridges of iQPS, the new super–bridges are digital. They are made with the use of specially

---

[3] In the present nomenclature the quench detection before the incident is called iQPS (old Quench Protection System) [118, 119].

(a)

(b)

Figure N.9.: Damage after the incident at LHC [117]: (a) displacement of cryostat support structure and damage of concrete anchors, (b) cryostat interconnection damage.

developed radiation hard FPGA[4] electronics. The threshold and the validation time for the second layer detection is fixed to 200 mV (double value of the first layer detection) and 10 ms, respectively [118]. Apart from the super–bridges, special high resolution nano-ohmmeter cards were installed for precise measurements of bus–bars and superconducting joints. Whenever the voltage across the bus–bar segment exceeds 500 μV (assuming LHC operation at 3.5 TeV) or 300 μV (at 6.5 TeV) for longer than 10 seconds, a quench trigger will be released [119]. After the upgrade the quench detection of LHC is called nQPS (“n” states for “new”).

In addition to nQPS, the energy extraction systems for dipole and quadrupole circuits were upgraded. The upgrade concerns an increase of the total dump resistance from 75 mΩ to 147 mΩ for the dipole circuits and from 7.7 mΩ to 30 mΩ for quadrupole circuits. Such a change is possible by adapting the opening switches in order to work at higher voltages (1 kV for dipoles and 240 V for quadrupoles) [119].

---

[4] FPGA – Field–Programmable Gate Array

O Magnet Protection at FAIR

O.1 SIS100

In contrast to LHC (see Appendix N), SIS100 is a fast cycling machine with capability to accelerate very wide spectrum of ions (from protons to uranium). Table O.1 presents a comparison between the dipole circuits of LHC and SIS100. The feature which makes the SIS100 unique (worldwide) is the very high ramp rate in the dipoles (28 kA/s corresponding to 4 T/s). In order to achieve such a ramp rate, the overall voltage across the SIS100 circuit exceeds ten times the voltage of the LHC dipole circuit (despite of more magnets and much higher inductance at LHC). Taking into account the primary features of both machines, the input parameters for the SIS100 quench protection design differ a lot from those at LHC.

Table O.1.: Comparison of the dipole circuit parameters of LHC and SIS100

Machine	LHC	SIS100
Number of magnets	154/circuit	108
Number of power converters	1/circuit	2
Nominal current (kA)	11.85	13.1
Nominal ramp rate (A/s)	10	28000
Total inductance of the circuit (mH)	$154 \times 2 \times 51 =$ $= 15.7 \times 10^3$	$108 \times 0.55 =$ $= 59.4$
Inductive voltage at cycling (V) per twin dipole / overall in the circuit	$1/\approx 160$	$15.4/\approx 1660$
Energy extraction system	$2 \times R_\mathrm{d}$ per circuit	$6 \times R_\mathrm{d}$
Cold by–pass	cold diode per twin dipole	none
Quench back heaters	on each coil	none

The magnetic lattice of SIS100 considers the following types of superconducting magnets:

- main dipole;

- main quadrupole;
- chromaticity sextupole;
- steering magnet (two autonomic coils: SH – horizontal coil and SV – vertical coil);
- multipole corrector (three autonomic coils: MQ – quadrupole coil, MS – sextupole coil, MO – octupole coil);
- injection/extraction (in/ex) quadrupole.

The electrical parameters of these magnet are summarised in Tab. O.2.

Table O.2.: Electrical parameters of superconducting magnets of SIS100

Magnet	Nominal current (A)	Inductance (mH)	Inductive voltage (V)	Quantity
Main dipole	13100	0.55	15.4	108
Main quad.	10512	0.41	7.5	83 (QD) 36 (F1) 47 (F2)
Chrom. sext.	250	43	62	42
Steering magnet	245 (SH) 241 (SV)	21	25	83 magnets 166 coils
Multipole corrector	250 (MQ) 250 (MS) 250 (MO)	1.1 (MQ) 5.6 (MS) 7.4 (MO)	1.8 (MQ) 5.8 (MS) 7.7 (MO)	12 magnets 36 coils
In/ex quad.	507	139	147	4

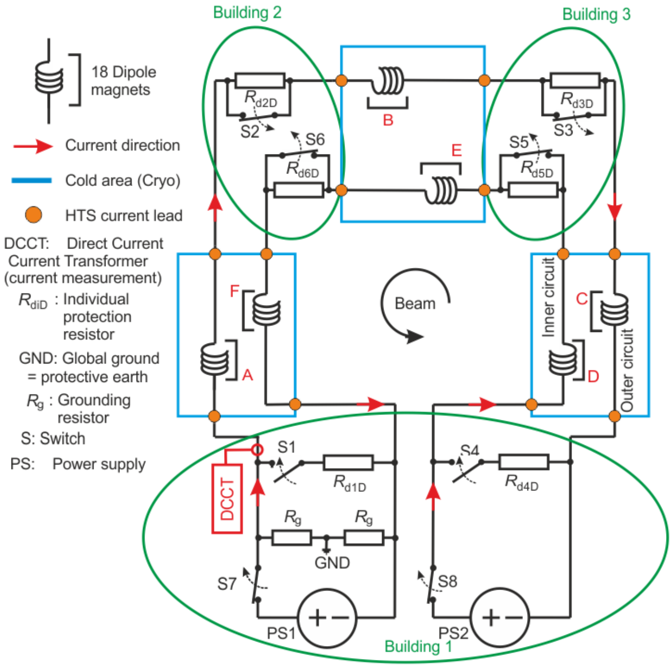

Figure O.1.: Dipole circuit of the SIS100 machine.

Superconducting Circuits at SIS100 and their Protection

Main Magnet Circuits

The 108 dipoles will be connected in series in a common electrical circuit powered by two power converters PS1 and PS2, as shown in Fig. O.1. There are six magnet strings (18 dipoles in each) marked from “A” to “F” and connected in the manner of two large loops along the accelerator ring: inner and outer. One half of the dipoles are connected to the outer and the other half to the inner loop. PS1 provides the reference ground. The circuit is protected by six energy extraction resistors ($R_{\mathrm{d1D}} - R_{\mathrm{d6D}}$) located at ambient temperature. These dump resistors in conjunction with the fast high voltage switches are the only protection elements that are considered for the dipole ring. No cold diode by–pass is foreseen due to space constrains within the cryostat (the cryo–modules of SIS100 have a very compact construction).

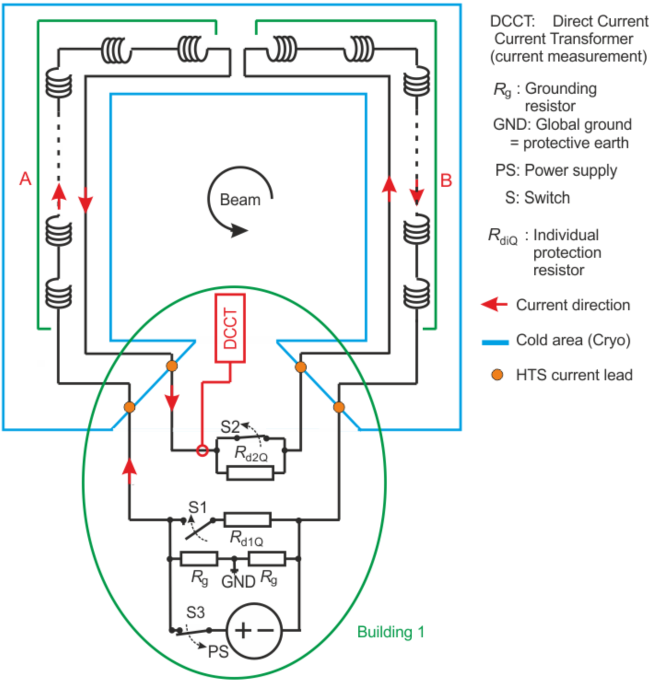

Figure O.2.: Quadrupole circuit of the SIS100 machine (example of the QD family: 42 magnets in section A and 41 in section B).

The three families (QD, F1 and F2) of SIS100 main quadrupoles are connected according to the scheme presented in Fig. O.2. The circuit is powered by a single power converter with the reference ground at the middle point. The quadrupoles are evenly distributed over to the outer loop of the circuit. The inner loop is a return line without connection to the magnets. The circuit is protected by two energy extraction resistors (R_{d1Q} and R_{d2Q}) and similar to the dipole circuit, these are the only quench protection elements that are used.

In order to provide galvanic connections of the individual magnet modules within the electrical circuit, a robust mechanically stable connection shall be provided. Such a connection is called a splice or simply a superconducting joint. A description of SIS100–type splices including results of the resistance measurements at cold condition is presented in Appendix P.

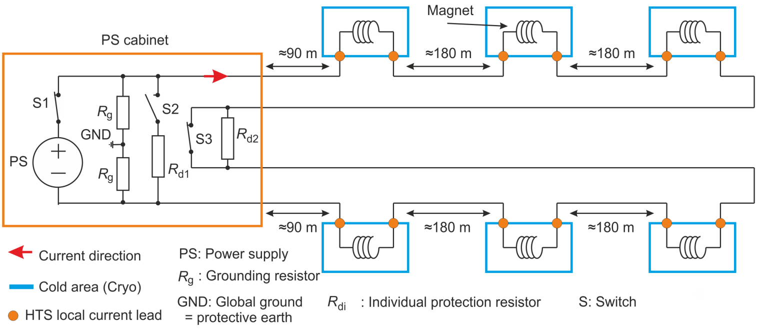

Figure O.3.: Protection scheme for the chromaticity sextupole circuit.

Corrector Magnets

The chromaticity sextupole magnets are powered in series of six according to the scheme presented in Fig. O.3. Since the magnets that belong to the same electrical circuit are evenly distributed over the accelerator circumference (one magnet per sector), there is approximately 180 m of warm connection between each two magnets. The magnet protection is provided by two energy extraction resistors.

The coils of the steering magnets and the multipole correctors are powered individually as presented in Fig. O.4. Each coil is protected against a quench with a single dump resistor.

Injection/Extraction Quadrupole Magnets

The injection/extraction (in/ex) quadrupoles are special magnets that will be installed in Y–cryostats at the location of beam injection and extraction. The in/ex quadrupole magnets are powered individually and their protection is provided by a single damp resistor, as shown in Fig. O.5. The magnet is supplied via two pairs of current leads. Such a solution was chosen in order to use a standard SIS100 local current leads with the rated current of 250 A instead of developing new current leads adequate for the current of 500 A.

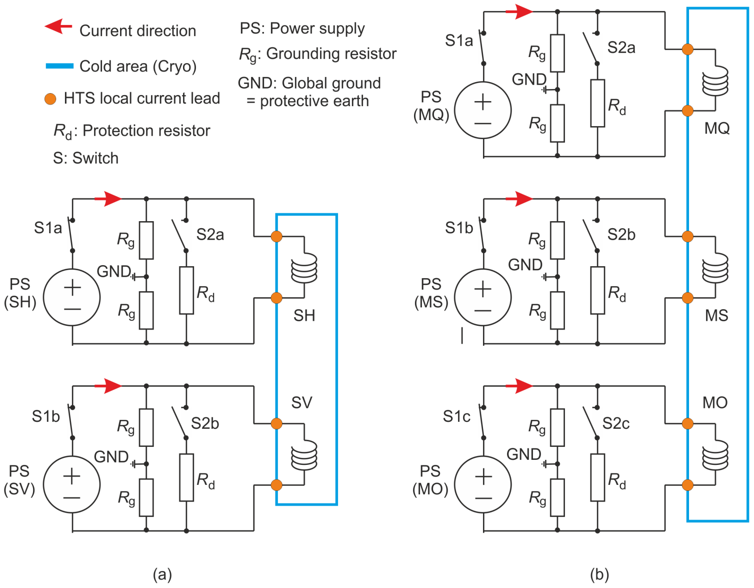

Figure O.4.: Protection scheme for: (a) steering magnets (two coils) and (b) multipole corrector (three coils).

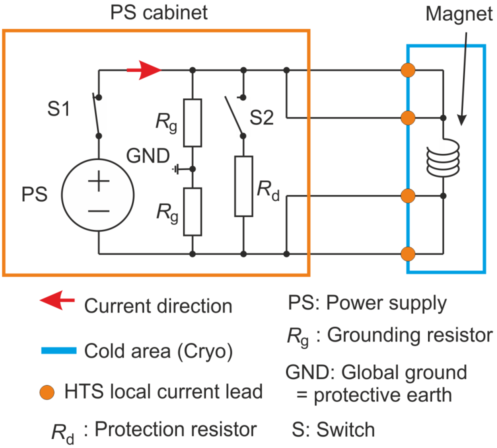

Figure O.5.: Protection scheme for the injection/extraction quadrupole magnets.

Main and Local Current Leads

There are two types of HTS current leads in SIS100. The 14 kA main current leads (MCL) and the 250 A local current leads (LCL). Currently, it is planned to use a voltage comparator with isolation amplifier at the input for the voltage survey of:

- the Cu part of MCL with a threshold set to 130 mV (estimated);
- the HTS part of MCL with a threshold set to 10 mV (estimated) ;
- the complete section of LCL (the HTS part is protected by the brass by–pass) with a threshold set to 50 mV (estimated).

O.2 Super–FRS

The superconducting modules of Super–FRS are categorised in two groups: dipoles and multiplets. In the dipoles only the coil is enclosed within the cryostat (He bath) while the yoke remains warm. A model of the Super–FRS main dipole is presented in Fig. O.6. The multiplets are multi–magnet systems that may contain up to nine magnets enclosed within a single cryostat. All magnets enclosed within the multiplet are immersed into a common He bath. The largest multiplet is presented in Figures O.8 and O.7. Table O.3 presents the electrical parameters of the superconducting magnets of Super–FRS. Each magnet is powered via an own pair of copper current leads (300 A).

Table O.3.: Electrical parameters of Super–FRS superconducting magnets

Magnet	$I_\mathrm{n}/I_\mathrm{max}$ (A)	Inductance at $I = 0$ (H)	Quantity
Main dipole	250/275	21.6	$21 + 3^*$
Long quadrupole	300/330	43	34
Short quadrupole	300/330	30.4	46
Octupole**	204/225	0.031	42
Sextupole	291/320	0.85	41
Steering dipole	280/310	0.0665	14

* – *two bending radii*
** – *embedded within the short quadrupole*

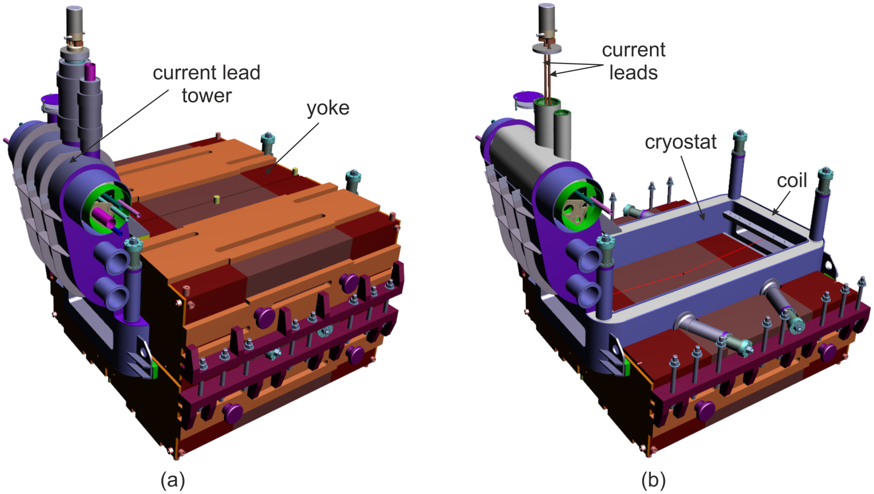

Figure O.6.: 3D model of the Super–FRS dipole prototype (courtesy of GSI): (a) overview , (b) closer look at the cryostat.

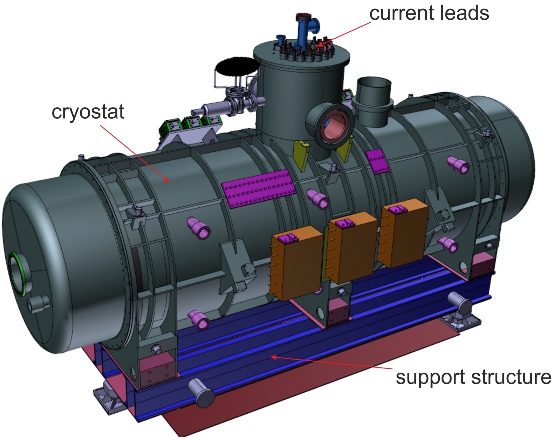

Figure O.7.: 3D model of the largest multiplet (9 superconducting magnets enclosed within a common cryostat) – courtesy of GSI.

Dipoles

The dipoles of Super–FRS are powered in series of three as shown in Fig. O.9. Although the magnets are designed as self–protecting, the electrical scheme considers two protection resistors that are activated with the use of mechanical switches in order to extract most of the magnet energy and limit the amount of the heat transferred to the coolant (He). Each dipole magnet has own pair of current leads and the interconnections between the magnets are provided with a "warm" cable.

Multiplets

Each magnet which belongs to any of the multiplets is powered individually. The long/short quadrupoles are also designed as self–protecting. For the same reasons as the dipoles, the quadrupole circuits are equipped with two energy extraction resistors that will be activated in case of quench as shown in Fig. O.10a. The corrector magnets (steering dipoles, sextupoles and octupoles) are self–protecting, too. Due their low energy their protection system only considers a crowbar at the power converter. The crowbar short–circuits the magnet when a quench occurs. The corresponding protection scheme is shown in Fig. O.10b.

Quench Detection at Super–FRS

At the moment two options of quench detection are considered for the individual magnets of Super–FRS. The first option is to use modified MID board and compare the magnet halves in similar manner as it is done for the magnet coil and the pick–up coil of MID. The second option is to use standard resistive bridges (already developed for the GSI test facility). Magnetic amplifier–based bridges are not considered for the Super–FRS since in quadrupoles and dipoles a very high quench voltage (up to 1.2 kV) could develop what would create too tough requirements for the control winding of the magnetic amplifier (demand for a large Cu cross–section and a very high insulation level). The voltage monitoring of the current leads will be provided by voltage comparators (isolation amplifier) with a threshold of "maximum expected voltage drop +10 mV".

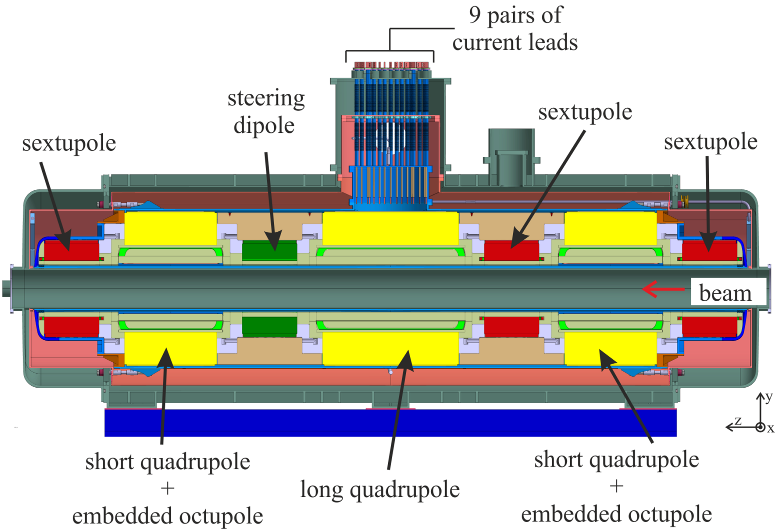

Figure O.8.: Content of the largest multiplet of Super–FRS: a single long quadrupole, two short quadrupoles with embedded octupole coils, three sextupoles and a single steering dipole (courtesy P. Neufingerl).

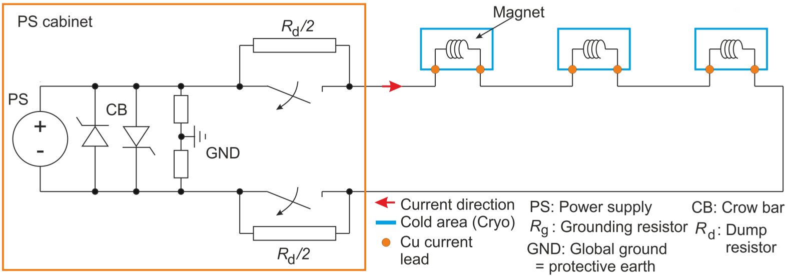

Figure O.9.: Protection scheme for the three Super–FRS dipole powered in series of three.

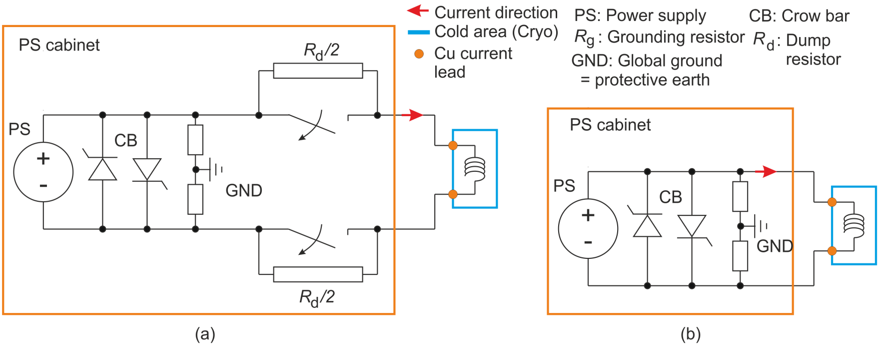

Figure O.10.: Protection schemes for Super–FRS multiplets: (a) long/short quadrupole circuit, (b) sextupole/octupole/steering dipole protection circuit.

P Splices (Superconducting Joints) at SIS100

In order to connect individual superconducting magnets into a chain, the magnet bus–bars must be soldered together in the way that an excellent galvanic connection is warranted. Such a connection is called splice or simply a superconducting joint (although it is not really superconducting). The structure and technology for the splice connection depends, above all, on a cable type used for the bus–bars. In SIS100 a splice connects two bus–bars made of Nuclotron–type cable. Figure P.1a shows the cross–section of a SIS100–type splice. The cables are assembled on top of each other and then a pre–shaped Cu stabilising clamp is attached. Such an assembly is soldered together with $Sn_{96}Ag_4$ tin. Figures P.1b and P.1c show the joint scans created with the use of computer tomography (CT). During the soldering of the junction it might happen that a void (lack of soldering) occurs at some section. Such a defect is shown in Figures P.1b–c.

Since the splice resistance equals to few nΩ, it is required to apply a current of few kA to be able to detect the resistive voltage across the joint which is in the level of tens of μV. Moreover the resistance computed from a single $V - I$ measurement suffers from high uncertainty of the voltage. The voltage accuracy at the μV level is affected by the noise (introduced by the power converter) and presumably by the thermo–electric potentials at the junction itself. Therefore the resistance shall be deduced from the $V - I$ characteristics of the junction. The simplest way to do so, is to compute the resistance from the slope of the $V - I$ curve. It is recommended to measure the splice voltage at minimum three currents and then apply a linear fit [120, 121]. The slope of the linear fit indicates the resistance of the splice. Figure P.2 shows measurement data of the two SIS100–type superconducting joints.

In particle accelerators the quality of the splices is of extreme importance what the history taught us during the incident at LHC (see Section N.3). It is very desired to have a tool/method which enables junction quality check at ambient temperature. Unfortunately, there is no correlation between the resistance at warm and at cold for the SIS100–type splices. This is due to the fact that at warm, the Cu clamp has a large contact–surface with the both cables within the joint while at cold, the low–ohmic contact area from the strands of the one bus–bar to the strands of the other bus–bar is limited and concentrated around the small area close to the

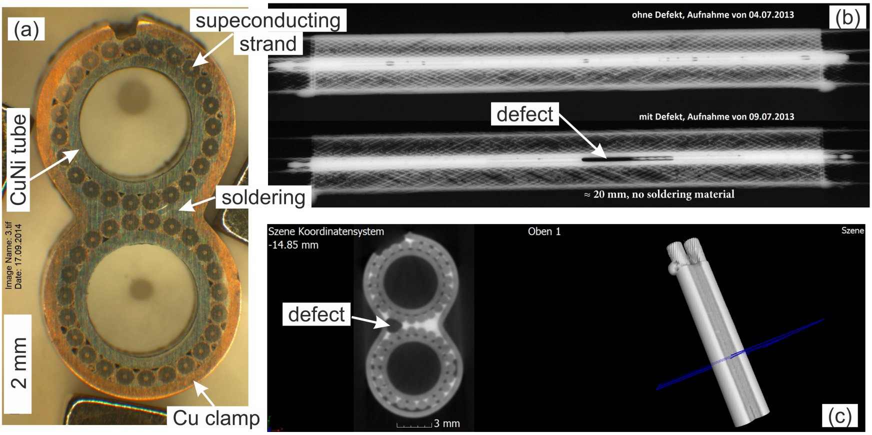

Figure P.1.: Splice which merges the two Nuclotron–type cables: (a) cross–section, (b–c) computer tomography and defect detection (CT by TU Darmstadt).

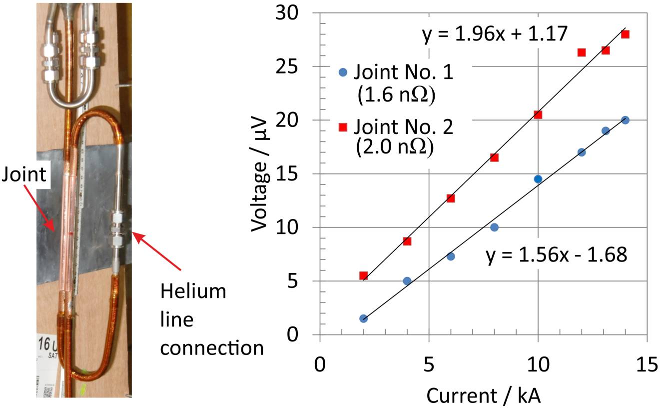

(a) (b)

Figure P.2.: DC resistance measurements of splices done on Nuclotron–type cable: (a) photo of splice, (b) measurement result obtained with $V - I$ method.

contact point. Table P.1 presents the resistance data of splices that was measured at:

- ambient temperature (4 wire $V - I$ method at 10 A) and
- at 4 K (slope of the $V - I$ characteristics, measurements at 4, 7, 10 and 13 kA) .

Looking at splice no. 3 with a defect, one can see that there is no correlation between the resistance measured with four wire method (at 10 A) at ambient temperature to the measurements at cold. The very high error at cold (±0.5 nΩ) comes from the uncertainty of the voltage measurement. Table P.1 shows a good reproducibility of splices when using the construction with Cu clamp.

Table P.1.: DC resistance of SIS100–type splices: measured data at 300 and 4 K

Splice	Cu plate size [mm]	R_{DC}(300 K) [$\mu\Omega$]	R_{DC}(4 K) [nΩ]
No. 1	$120 \times 38.5 \times 0.5$	73.7 ± 0.2	1.6 ± 0.5
No. 2	$120 \times 38.5 \times 0.5$	73.8 ± 0.2	2.0 ± 0.5
No. 3*	$120 \times 38.5 \times 0.5$	75.1 ± 0.2	9.6 ± 0.5
No. 4	$120 \times 38.5 \times 0.5$	74.9 ± 0.2	1.6 ± 0.5
No. 5	$120 \times 38.5 \times 0.5$	76.8 ± 0.2	1.7 ± 0.5
No. 6	$120 \times 38.5 \times 0.5$	75.5 ± 0.2	1.4 ± 0.5
No. 7	$120 \times 38.5 \times 0.3$	88.1 ± 0.2	0.9 ± 0.5
No. 8	$120 \times 38.5 \times 0.3$	99.2 ± 0.2	1.1 ± 0.5
No. 9	$120 \times 38.5 \times 0.3$	96.2 ± 0.2	1.2 ± 0.5
No. 10	$120 \times 38.5 \times 0.3$	98.7 ± 0.2	1.2 ± 0.5

* – defect: soldering void

Nomenclature

Roman Symbols

A	mass number (number of nucleons), [-]
A_{nosc}	total cross–section of none–superconductor in a superconducting naked wire, [mm^2]
A_{sc}	total cross–section of superconductor in a superconducting naked wire, [mm^2]
B	magnetic induction (magnetic field), [T]
B_0	reference magnetic field, [T]
B_{a}	applied magnetic field, [T]
B_{c}	critical magnetic field, [T]
B_{c1}	lower critical magnetic field, [T]
B_{c2}	upper critical magnetic field, [T]
B_{c20}	critical magnetic field of a type II superconductors defined at a zero temperature and zero transport current, [T]
B_{max}	maximum magnetic field, [T]
B_{n}	nominal magnetic field, [T]
B_{op}	magnetic field at which a conductor is operated, [T]
c	velocity of light, in vacuum c =299792.458 km/s
C_0	normalization constant for the Bottura's fit, [T]
c_1/c_2	integration constants, [-]
C	electrical capacitance, [F]
C_V	volumetric specific heat, [J/(K·m^3)]
d_{f}	diameter of a filament, [μm]
D	electric displacement field, [C/m^2]
d_{s}	diameter of a strand or wire, [mm]
e	elementary charge, $e = 1.602176565(35) \cdot 10^{-19}$ C

E	1. electric field strength, [V/m] 2. energy, [J]
E_{mag}	energy stored in a magnet, [J]
E_{u}	total beam energy, [GeV/u] (GeV per nucleon)
$E_{\mathrm{mag}}/V_{\mathrm{vol}}$	energy density, [J/m^3]
f	1. frequency, [Hz] 2. arbitrary function, [-]
F_{c}	centripetal force, [N]
F_{L}	Lorentz force, [N]
f_{tp}	twist pitch factor, [-]
g	amplification factor (numerical error), [-]
H	magnetic field strength, [H/m]
H_{c}	1. critical magnetic field strength (superconductors of type I), [H/m] 2. thermodynamic critical magnetic field strength, [H/m]
H_{c1}	lower critical magnetic field strength, [H/m]
H_{c2}	upper critical magnetic field strength, [H/m]
H_{c3}	critical magnetic field strength (surface superconductivity), [H/m]
I or i	electrical current or transport current, [A]
I_0	reference or initial current, [A]
I_{c}	critical current, [A]
I_{max}	maximum current, [A]
I_{n}	nominal current, [A]
J or j	electrical current density or transport current density, [A/m^2]
J_{c}	critical current density, [A/mm^2]
J_{cref}	reference current density for the Bottura's fit, [A/mm^2]
J_{op}	operating current density, [A/mm^2]
k	1. thermal conductivity, [W/(K·m)] 2. quadrupole strength 3. magnetic coupling factor (mutual inductance), [-]

k_B	Boltzmann's constant, $k_\mathrm{B} = 1.38064852(79) \cdot 10^{-23}$ J/K
L	1. inductance, [H] 2. distance or length, [m]
$l_\text{1-turn}$	average length of a single turn in a magnet coil, [m]
L_d	differential inductance, [H]
L_eff	effective length (longitudinal profile), [m]
L_L	Lorenz number, $L_\mathrm{L} = 2.45 \times 10^{-8}$ WΩ/K^2
L_s	self inductance, [H]
L_w	inductance, derived from an energy stored in a magnet, [H]
M	mutual inductance, [H]
m_q	particle mass, [kg]
m	sextupole strength
n	Lubell's fit parameter, [-]
N	1. number of magnets, [-] 2. number of turns, [-]
n_s	number of superconducting strands, [-]
n_tpp	number of turns per magnet pole
o	octupole strength
p	particle momentum, [GeV/c]
P_h	hysteresis loss, [W/m^3]
P_ifc	inter–filamentary coupling loss, [W/m^3]
P_c	critical pressure, [Pa]
P	1. electrical power, [W] 2. pressure, [Pa]
P_sHe	heat flux (heat transfer to He I), [W/m^2]
Q	particle charge in units of the electron charge e
q	1. electric charge, [C] 2. heat flux, [W/m^2]
R	resistance, [Ω]

R_b	resistance of a balance bridge resistor, [Ω]
R_d	resistance of a dump resistor (energy extraction resistor), [Ω]
R_g	resistance of a grounding resistor, [Ω]
R_q	quench resistance, [Ω]
RRR	residual–resistivity ratio, [-]
T	temperature, [K]
T_c	critical temperature, [K]
T_c0	critical surface temperature at a zero magnetic field and zero transport current, [K]
T_cB	critical surface temperature at a zero transport current, [K]
T_cs	current–sharing temperature, [K]
$T_\text{hot-spot}$	hot-spot temperature, [K]
t	time, [s]
T_max	maximum temperature, [K]
t_o	delay of an energy extraction system, [ms]
T_op	operating temperature of a superconductor, [K]
t_pf	twist pitch of filaments or strands, [mm]
t_q	total time between the quench start and the end of the energy extraction, [s]
t_Rd	time between the quench start and the start of an energy extraction, [s]
t_rt	time to reach a threshold (quench detection), [ms]
t_v	validation time (quench detection), [ms]
V_b	bridge input voltage, [V]
V_CLq	resistive voltage of a current lead, [V]
V	voltage, [V]
v_fp	quench propagation velocity, normal front propagation velocity, [m/s]
V_vol	volume of a coil or pole, [m^3]
V_0	reference voltage or amplitude, [V]
v	velocity of a particle, [m/s]

V_{PS}	voltage of a power supply, [V]
V_{q}	quench voltage, [V]
V_{th}	voltage threshold (quench detection), [V]
V_{thCL}	voltage threshold (thermal runaway in a current lead), [V]
w/o	weight percent, i.e. Cu-30w/oNi – means that Ni is 30 weight % in this particular CuNi alloy [%]
w	wave–number
X	reactance, could be capacitive ($1/[2\pi f C]$) or inductive ($2\pi f L$), [Ω]

Greek Symbols

α	1. non–superconductor to superconductor ratio in a wire, [-] 2. Bottura's fit parameter, [-]
β	1. Bottura's fit parameter, [-] 2. particle velocity to velocity of light ratio, [-]
κ	Ginzburg–Landau parameter, [-]
ϵ_0	permittivity of free space, $\epsilon_0 = 8.854187817\times10^{-12}$ [F/m]
ϵ	1. permittivity, [F/m] 2. numerical error
ϵ_{r}	relative permittivity, [-]
γ	Bottura's fit parameter, [-]
λ	1. penetration depth, [cm] 2. eigenvalue (in differential equations), [-]
μ_0	permeability of free space $= 4 \cdot \pi \cdot 10^{-7}$ [H/m]
μ_{r}	relative permeability, [-]
μ	magnetic permeability, $\mu = \mu_0 \cdot \mu_{\mathrm{r}}$, [H/m]
$\boldsymbol{\Phi}$	magnetic flux, [Wb]
ϱ	1. electrical resistivity, [Ωm] 2. bending radius of a dipole, [m]
ϱ_0	residual electrical resistivity, [Ωm]
ϱ_q	charge density in the considered volume, [C/m^3]
ϱ_{IF}	inter–filamentary matrix resistivity, [Ωm]

τ	time constant (energy extraction), [s]
ξ	coherence length, [cm]

Other Symbols

$B\varrho$	magnetic rigidity, [Tm]

List of Figures

List of Tables

Bibliography

[1] "Website FAIR-center." Internet: www.fair-center.eu, 2016.

[2] F. Toral Fernández. "Design and Calculation Procedure for Particle Accelerator Superconducting Magnets: Application to an LHC Superconducting Quadrupole." Ph.D. thesis, Universidad Pontificia de Comillas, Madrid, 2001.

[3] M. N. Wilson. *Superconducting Magnets.* New York: Oxford University Press, ISBN 0-19-854805-2, 1983.

[4] M. N. Wilson. "Computer Simulation of the Quenching of a Superconducting Magnet." Science Research Council, RHEL/M 151, August 1968.

[5] W. V. Hassenzahl. "QUENCHS - Users' Manual." *Advanced Energy Analysis*, Piedmont California, 2004.

[6] A. F. Zeller, J. C. DeKamp, and J. Delauter. "A Radiation Resistant Dipole." *IEEE Transactions on Applied Superconductivity*, vol. 15, no. 2, June 2005.

[7] S. Chuhan A. F. Zeller, J. C. DeKamp, P. Brindza, S. Lassiter, and M. Fowler. "A Superconducting Horizontal Bend Magnet for JLab's 12 GeV/c Super High Momentum Spectrometer." *IEEE Transactions on Applied Superconductivity*, vol. 18, no. 2, June 2008.

[8] D. Hagedorn and F. Rodriguez-Mateos. "Modeling of the Quenching Process in Complex Superconducting Magnet Systems." *IEEE Transactions on Magnetics*, vol. 28, no. 1, pp. 366-369, 1992.

[9] F. Rodriguez-Mateos, G. Gerin, and A. Marquis. "Quench Protection Test Results and Comparative Simulations on the First 10 Metre Prototype Dipoles for the Large Hadron Collider." *IEEE Transactions on Magnetics*, vol. 32, no. 4, pp. 2109-2112, 1996.

[10] S. Russenschuck. *Electromagnetic Design and Mathematical Optimization Methods in Magnet Technology.* ISBN 92-9083-242-8, 2006.

[11] R. Yamada, E. Marscin, A. Lee and M. Wake. "3D ANSYS Quench Simulation of Cosine Theta Nb_3Sn High Field Dipole Magnets." *IEEE Transactions on Applied Superconductivity*, vol. 14, no. 2, pp. 291-294, 2004.

[12] H. J. Lee, et al. “Quench Analysis of the KSTAR TF Magnets and Bus Lines for the First Campaign.” *IEEE Transactions on Applied Superconductivity*, vol. 19, no. 3, pp. 2399-2402, 2009.

[13] A. Ishiyama, H. Matsumora, W. Takita, and Y. Iwasa. “Quench Propagation Analysis in Adiabatic Superconducting Windings.” *IEEE Transactions on Magnetics*, vol. 27, no. 2, pp. 2092-2095, 1991.

[14] J. Chen and X. Jiang. “Protection Circuit and Quench Simulation of a 7 T Superconducting Magnet for Animal MRI.” *IEEE Transactions on Applied Superconductivity*, vol. 23, no. 3, 2012.

[15] A. C. Rose and E. H. Rhoderick. *Introduction to Superconductivity.* Perganom Press, ISBN 0-08-021652-8, 1978.

[16] D. Larbalestier. “The Long Road to High Current Density Superconducting Conductors” in *100 Years of Superconductivity,* H. Rogalla, P. H. Kes, CRC Press, ISBN 978-1-4398-4946-0, pp. 627-642, 2012.

[17] K.-H. Mess, P. Schmüser, and S. Wollf. *Superconducting Accelerator Magnets.* World Scientific, ISBN 981-02-2790-6, 1996.

[18] P. H. Kes. *100 Years of Superconductivity.* CRC Press, ISBN 978-1-4398-4946-0, 2012.

[19] F. Sonnemann. “Resistive Transition and Protection of LHC Superconducting Cables and Magnets.” Ph.D. thesis, CERN, 2001.

[20] M. S. Lubell. “Empirical Scaling Formulas for Critical Current and Critical Field for Commercial NbTi.” *IEEE Transactions on Magnetics*, vol. MAG-19, no. 3, pp. 754-757, May 1983.

[21] P. A. Hudson, F. C. Yin, and H. Jones. “Evaluation of the Temperature and Magnetic Field Dependence of Critical Current Densities of Multifilamentary Superconducting Composites.” *IEEE Transactions on Magnetics*, vol. MAG-17, no. 5, 1981.

[22] T. Boutboul. “Critical Current Density in Superconducting Nb-Ti Strands in the 100 mT to 11 T Applied Field Range.” *IEEE Transactions on Applied Superconductivity*, vol. 16, no. 2, 2006.

[23] L. Bottura. “A Practical Fit for the Critical Surface of NbTi,” *LHC Project Report 358*, presented at the 16th International Conference on Magnetic Technology. 26 September – 2 October 1999, Ponte Vedra Beach, 1999.

[24] E. Floch. Private communication, GSI, Darmstadt, 2010-2013.

[25] L. Muzzi. "Test Results of a NbTi Wire for the ITER Poloidal Field Magnets: A Validation of the 2-pinning Components Model," in *Proc. IEEE/CSC & ESAS European Superconductivity News Forum (ESNF),* no. 15, 2011.

[26] S. Hong. "High Current Density of NbTi Composite." *IEEE Transactions on Magnetics*, vol. 25, no. 2, 1989.

[27] K. Susai. "Critical Current Properties of Fine Filament Superconducting Wires for the SSC." *IEEE Transactions on Applied Superconductivity*, vol. 3, no. 1, 1993.

[28] G. P. Vedernikov. "Superconducting Properties of Wires Based on NbTi and NbTiTa Alloys at 2 K and 4.2 K." *IEEE Transactions on Applied Superconductivity*, vol. 10, no. 1, 2000.

[29] G. P. Vedernikov. "Comparative Study of NbTi Strands Developed for ITER PF Coils." *IEEE Transactions on Applied Superconductivity*, vol. 12, no. 1, 2002.

[30] C. R. Spencer, P. A. Sanger, and M. Young. "The Temperature and Magnetic Field Dependence of Superconducting Critical Current Densities of Multifilamentary Nb_3Sn and NbTi Composite Wires." *IEEE Transactions on Magnetics*, vol. MAG-15, no. 1, 1979.

[31] K. F. Hwang and D. C. Larbalestier. "Generalized Critical Current Density of Commercial Nb46.5, Nb50 and Nb53 w/o Ti Multifilamentary Superconductors." *IEEE Transactions on Magnetics*, vol. MAG-15, no. 1, 1979.

[32] Li Cheng-ren, Wu Xiao-zu, and Shou Nong." NbTi Superconductive Composite with High Critical Current Density." *IEEE Transactions on Magnetics*, vol. MAG-19, no. 3, 1983.

[33] H. H. J. ten Kate, A. J. M. Roovers, and L. J. M. ven de Klundert. "Critical Current and Stability Effects between 0 and 6 Tesla in Mono and Multifilamentary NbTi Conductors Having a CuNi Matrix." *IEEE Transactions on Magnetics*, vol. MAG-21, no. 2, 1985.

[34] L. Zani. "$J_C(B,T)$ Characterization of NbTi Strands Used in ITER PF-Relevant Insert and Full-Scale Sample." *IEEE Transactions on Applied Superconductivity*, vol. 15, no. 2, 2005.

[35] J. W. A. Somerkoski. "Structure and Superconducting Property Characterization of MF Cu/Nb-46.5 w% Ti Superconductors." *IEEE Transactions on Magnetics*, vol. MAG-23, no. 2, 1987.

[36] M. A. Green. "Calculating the J_c, B, T Surface for Niobium Titanium Using a Reduced-State Model." *IEEE Transactions on Magnetics*, vol. MAG-25, no. 2, 1989.

[37] E. Floch. "Conception d'un transformateur impulsionnel supraconducteur Modélisation de la transition Validations." Ph.D. thesis, Université de Franche-Comté, 1999.

[38] J. N. Schwerg. "Numerical Calculation of Transient Field Effects in Quenching Superconducting Magnets." Ph.D. thesis, Technischen Universität Berlin, 2010.

[39] H. G. Khodzhibagiyan. "Design of New Hollow Superconducting NbTi Cables for Fast Cycling Synchrotron Magnets." *IEEE Transactions on Applied Superconductivity*, vol. 13, no. 2, pp. 3370–3373, 2003.

[40] J. Rossbach and P. Schmüser. "Basic Course on Accelerator Optics." CERN Accelerator School: 5th General Accelerator Physics Course, pp. 17-88, 1994.

[41] S. Wolff. "Superconducting Accelerator Magnet Design." CERN Accelerator School: 5th General Accelerator Physics Course, vol. 2, pp. 755-790, 1994.

[42] S. Russenschuck. "Design of Accelerator Magnets." CERN Accelerator School: Basic Course on General Accelerator Physics, pp. 118-153, 2005.

[43] "Website of Canada's national laboratory for particle and nuclear physics and accelerator-based science." Internet: http://www.triumf.ca/home/about-triumf/about-us/faq-about-triumf/triumf-backgrounder, 2016.

[44] R. P. Reed and A. F. Clark. *Materials at Low Temperatures.*, ISBN 0-87170-146-4, American Society for Metals, Ohio, 1983.

[45] F. R Fickett. "Magnetoresistivity of Copper and Aluminum at Cryogenic Temperature," in *Proc. of the 4th International Conference on Magnet Technology, AEC–Conf720908,* pp. 539-541, Upton, USA, 1972.

[46] K. Dahlerup-Petersen. Private communication, CERN, Genova, 2015.

[47] P. Fazilleau, C. Berriaud, F–P Juster, and B. Gastineau. "The R3B–GLAD Quench Protection System." *IEEE Transactions on Magnetics*, vol. 20, no. 3, pp. 2074–2077, 2010.

[48] H. Ramakers. Private communication, GSI, Darmstadt, 2014.

[49] F. Bordry, V. Montabonnet, Y. Thurel and A. Dupaquier. "Earthing of The LHC DC Electrical Circuits," *Engineering Specification*, LHC Project Document No. LHC-D-ES-0001 rev 2.0, EDMS Document No. 309372, CERN, Geneva, December 2002.

[50] E. Ravaioli. "CLIQ – A New Quench Protection Technology for Superconducting Magnets." Ph.D. thesis, University of Twente, June 2015.

[51] L. Coull, D. Hagedom, V. Remondino, and F. Rodriguez-Mateos. "LHC Magnet Quench Protection System," in *Proc. of the 13th International Conference on Magnet Technology (MT–13)*, Victoria, Canada, 20-24 September 1993.

[52] X. L. Guo, F. Y. Xu, L. Wang, M. A. Green, H. Pan, H. Wu, X. K. Liu, L. X. Jia, and K. Amm. "Quench Protection for the MICE Cooling Channel Coupling Magnet." *IEEE Transactions on Applied Superconductivity*, vol. 19, no. 3, 2008.

[53] "MATLAB® documentation." Internet: http://se.mathworks.com, 2017.

[54] P. Szwangruber, E. Floch, F. Toral, and T. Weiland. "Three-Dimensional Quench Calculations for the FAIR Super–FRS Main Dipole." *IEEE Transactions on Applied Superconductivity*, vol. 23, no. 3, June 2013.

[55] F. Toral Fernández. Private communication, Centro de Investigaciones Energéticas, Medioambientales y Tecnológicas (CIEMAT), Madrid, 2011.

[56] S. W. Van Sciver. *Helium Cryogenics.* 2nd Edition, International Cryogenics Monograph Series, ISBN 978-1-4419-9978-8, Springer, 2011.

[57] J. W. Ekin. *Experimental Techniques for Low-Temperature Measurements: Cryostat Design, Material Properties and Superconductor Critical-Current Testing.* ISBN 10: 0198570546, Oxford University Press, 2006.

[58] R. V. Smith. "Review of Heat Transfer to Helium I". *Cryogenics*, pp. 11-19, 1969.

[59] Y. Huang and S. W. Van Sciver. "Heat Transfer from Aluminium Surfaces to Pool Boiling He I." *Advances in Cryogenic Engineering*, vol. 41, pp. 211-216, 1996.

[60] O. Tsukamoto and S. Kobayashi. "Transient Heat Transfer Characteristics of Liquid Helium." *Journal of Applied Physics*, vol. 46, no. 3, pp. 1359-1364, March 1975.

[61] C. Schmidt. “Review of Steady State and Transient in Pool Boiling Helium I.” Institut International du Froid, pp. 17-31, France, 1981.

[62] E. Fischer, P. Schnizer, K. Sugita, J. P. Meier, A. Mierau, A. Bleile, P. Szwangruber, H. Müller, and C. Roux. “Fast-Ramped Superconducting Magnets for FAIR. Production Status and First Test Results.” *IEEE Transactions on Applied Superconductivity*, vol. 25, no. 3, June 2015.

[63] E. Fischer, W. Freisleben, A. Mierau, P. Schnizer, and P. Szwangruber. “Thermodynamic Properties of the Superconducting Dipole Magnet of the SIS100 Synchrotron,” in *Proc. of the 25th International Cryogenic Engineering Conference and International Cryogenic Materials Conference 2014 (ICEC 25–ICMC 2014)*, vol. 67, pp. 781-784, 2015.

[64] P. Schnizer, A. Mierau, A. Bleile, V. Marusov, A. Stafiniak, W. Freisleben, H. Raach, J. P. Meier, K. Sugita, P. Szwangruber, H. Müller, and E. Fischer. “Low-Temperature Test Capabilities for the Superconducting Magnets of FAIR.” *IEEE Transactions on Applied Superconductivity*, vol. 25, no. 3, June 2015.

[65] H. Leibrock, E. Floch, G. Moritz, L. Ma, W. Wu, P. Yuan, W. Weiyue, and Q. Wang. “Prototype of the Superferric Dipoles for the Super-FRS of the FAIR-Project.” *IEEE Transactions on Applied Superconductivity*, vol. 20, no. 3, June 2010.

[66] P. Szwangruber, F. Toral, E. Floch, I. Rodriguez, H. Leibrock, X. Yu, W. Wu, M. Lizhen, W. Wei, X. Zhang, B. Guo, A. Zeller, and T. Weiland. “Quench Calculations and Measurements on the FAIR Super-FRS Dipole,” in *Proc. of the Superconductivity Centennial Conference 2011*, vol. 36, pp. 872-877, 2012.

[67] Y. Xiang, M. Kauschke, C. H. Schroeder, E. Floch, H. Leibrock, and G. Moritz. “Conceptual Design of Cryogenic Facilities for Super–FRS of FAIR.” *IEEE Transactions on Applied Superconductivity*, vol. 20, no. 3, 2010.

[68] H. Liebermann and D. Ondreka. “SIS100 Cycles.” GSI Primary Beams - System Planning, version 2.3, Darmstadt, September 2013.

[69] K. H. Mess. “Quench Protection at HERA,” in *Proc. of PAC*, CH2387-9/87/0000-1474 IEEE, 1987.

[70] P. Mali. *Magnetic Amplifiers – Principles and Applications.* John F. Rider Publisher, Inc., New York, 1960.

[71] United States Navy. *Magnetic Amplifiers – Another Lost Technology*, Edited by G. Trinkaus, ISBN 0-9709618-5-5, High Voltage Press, Portland (Oregon), USA, 1951.

[72] W. Schilling. *Der Transductor*, R. Oldenbourg Press, München, Germany, 1958.

[73] C. W. Lucy. "A Survey of Magnetic Amplifiers", in *Proc. IRE*, USA, 1955.

[74] R. Lee. *Electronic Transformers and Circuits.* John Wiley & Sons, Inc., New York, USA, 1955.

[75] L. Coull, D. Hagedorn, V. Remondino, and F. Rodriguez Mateos. "LHC Magnet Quench Protection System." CERN Internal Note AT-MA/LC 93-81, July 1993.

[76] K. Sugita. Private communication, GSI, Darmstadt, 2015.

[77] C. A. Hamilton, R. L. Kautz, R. L. Steiner, and F. L. Lloyd. "A practical Josephson voltage standard at 1 V." *IEEE Electron Device Letters*, vol. 6, no. 12, pp. 0741-3106, December 1985.

[78] H. Raach, C. H. Schroeder, E. Floch, A. Bleile, P. Schnizer, and T. P. Andersen. "14 kA HTS Current Leads with one 4.8 K Helium Stream for the Prototype Test Facility at GSI," in *Proc. of the 25th International Cryogenic Engineering Conference and International Cryogenic Materials Conference 2014 (ICEC 25–ICMC 2014)*, vol. 67, pp. 1098-1101, 2015.

[79] V. Datskov. Private communication, GSI, Darmstadt, 2015-2016.

[80] H. J. Muller. "The Upper Critical Field of Niobium-Titanium." Ph.D. thesis, University of Wisconsin-Madison, 1989.

[81] P. H. Bellin, V. Sadagopan, and H. C. Gatos. "Ternary Superconductors Alloys of the Titatanium-Niobium-Vanadium System. Transition Temperature Variation." *Journal of Applied Physics*, vol. 40, no. 10, pp. 3982-3984, 1969.

[82] M. Suenaga and K. M. Ralls. "Some Superconducting Properties of Ti-Nb-Ta Ternary Alloys." *Journal of Applied Physics*, vol. 40, no. 11, pp. 4457-4463, 1969.

[83] H. Hillmann and K. J. Best. "New Measurements of Critical Data of Optimized NbTi Superconductors." *IEEE Transactions on Magnetics*, vol. MAG-13, no. 5, pp. 1568-1570, 1977.

[84] D. G. Hawksworth and D. C.Larbalestier. *Advances in Cryogenic Engineering*, vol. 26, p. 479, 1980.

[85] P. J. Lee. *Composite Superconductors*, ISBN 0824791177, New York, Chapter 5, 1994.

[86] J. K. Hulm and R. D. Blaugher. *Phys. Rev.*, vol. 123, pp. 1569-1961, 1961.

[87] P. H. Bellin, V. Sadagopan and H. C. Gatos. “Critical Field in the Ti-Nb-V System.” *Journal of Applied Physics*, vol. 41, no. 5, pp. 2057-2059, 1970.

[88] K. M. Ralls. Ph.D. Thesis, Massachusetts Institute of Technology, 1964.

[89] R. A. Brand. Ph.D. Thesis, University of Wisconsin-Madison, 1972.

[90] J. D. Kraus and K.R. Carver. *Electromagnetics*, 2^{nd} edition, McGraw-Hill, 1973.

[91] M. Anerella, J. Cozzolino, J. Escallier, G. Ganetis, A. Ghosh, R. Gupta, M. Harrison, A. Jain, S. Kahn, E. Killian, W. Louie, A. Marone, J. Muratore, S. Plate, M. Rehak, W. Sampson, J. Schmalzle, R. Thomas, P. Thompson, P. Wanderer, and E. Willen. “Magnet note: the RHIC Magnet System,” Broohaven National Laboratory, Superconducting Magnet Division, November 2001.

[92] R. Meinke. “Superconducting Magnet System for HERA.” *IEEE Transactions on Magnetics*, vol. 27, no. 2, March 1991.

[93] D. Leroy, R. Perin, N. Siegel, T. Taylor, T. Tortschanoff, and J. Vlogaert. “The Superconducting Magnets for LHC,” CERN, LHC Division, Geneva, Switzerland, 1996.

[94] A. A. Smirnov. “Physics of Particles and Nuclei”, vol. 32, no. 1, pp. 49-76, 2001. Translated from in *Fizika Elementarnykh Chastits i Atomnogo Yadra*, vol. 32, no. 1, pp. 96-142, 2001.

[95] W. E. Cooper, H. E. Fisk, D. A. Gross, R. A. Lundy, E. E. Schmidt, and F. Turkot. “Fermilab Tevatron Quadrupoles,” TM-1183, March 1983.

[96] L. Tkachenko, I. Bogdanov, S. Kozub, P. Shcherbakov, P. Slabodchikov, V. Sytnik, and V. Zubko. “Development of Fast-Cycling Superconducting Quadrupole and Corrector Magnets for the SIS300,” in *Proc. of RuPAC-2010*, Protvino, Russia, 2011.

[97] A. F. Zeller. “Magnetic Elements for the A1900 Fragment Separator at the NSCL.” *Advances in Cryogenics Engineering*, vol. 43, pp. 245-252, 1998.

[98] T. Kubo. “Status and Overview of Superconducting Radioactive Isotope Beam Separator BigRIPS at RIKEN.” *IEEE Transactions on Applied Superconductivity*, vol. 17, no. 2, pp. 1069-1077, 2007.

[99] M. Winkler. Private communication, GSI, Darmstadt, 2013.

[100] “Technical Design Report, FAIR Super Fragment Separator.” GSI, Darmstadt, 2008.

[101] Y. Iwasa. *Case Studies in Superconducting Magnets, Design and Operation Issues. Selected Topics in Superconductivity*, ISBN 0-306-44881-5, Plenum Press, New York, 1994.

[102] E.W. Collings. “Applied Superconductivity, Metallurgy, and Physics of Titanium Alloys.” *International Cryogenics Monograph Series*, 1986.

[103] H. Lim and Y. Iwasa. “Two-Dimensional Normal Zone Propagation in BSCCO-2223 Pancake Coils.” *Cryogenics*, vol. 37, No. 12, pp. 799, 1997.

[104] K. Flachbart, T. A. Feher ,Z. Malek, and A. Rysea. “Thermal Conductivity of Nb-Ti Alloy in the Low-Temperature Range.” *Physica Status Solidi (b)*, vol. 85, no. 2, pp. 545-551, 1978.

[105] “Materials Studies for Magnetic Fusion Energy. Applications at Low Temperatures-II.” Technical report NBSIR 79-1609. National Bureau of Standards, Boulder, CO, 1983.

[106] Je-Chin Han. *Analytical Heat Transfer*, CRC Press, ISBN 9781439861967, 2011.

[107] D. Potter. *Computational Physics*, John Wiley & Sons, ISBN 0-471-69555-6, 1973.

[108] E. Husain and R. S. Nema. “Analysis of Paschen Curves for Air, N2, and SF6 using the Townsend Breakdown Equation.” *IEEE Trans. on Elect. Insul.*, EI-17(4), pp. 350-353, 1982.

[109] S. Pemberton. “MP3 Recommendation on the Fischer Connector of the 80–120 A Circuits in the LHC,” CERN Engienering/Technical Note, LHC-MP3-EN-0008, EDMS no. 1333823 rev. 1.1, Geneva, January 2014.

[110] J.Gerhold and T.W. Dakin. “Paschen–Curve of Helium.” *Electra*, no. 52, pp. 80-86, 1977.

[111] “CERN Completes Transition to Lead-Ion Running at the LHC.” CERN press release. Internet: http://press.web.cern.ch/press-releases/2010/11/cern-completes-transition-lead-ion-running-lhc, 8th November 2010.

[112] R. Oerter. *The Theory of Almost Everything: The Standard Model, the Unsung Triumph of Modern Physics*. Penguin Group. p. 2, ISBN 0-13-236678-9, 2006.

[113] “LHC Design Report.” Internet: http://ab-div.web.cern.ch/ab-div/Publications/LHC-DesignReport.html, 2004.

[114] F. Rodriguez-Mateos, L. Coull, K. Dahlerup-Petersen, D. Hagedorn, G. Krainz, A. Rijllart, and A. McInturff. “Electrical Performance of a String of Magnets Representing a Half-cell of the LHC Machine,” presented at Magnet Technology (MT–14), Tampere, Finland, June 11–16, 1995.

[115] “Interim Summary Report on the Analysis of the 19 September Incident at the LHC.” CERN/AT/PhL Document EDMS 973073, 15 October 2008.

[116] R. Denz and F. Rodriguez-Mateos. “Electronic Systems for the Protection of Superconducting Elements in the LHC,” presented at the 6th European Conference on Applied Superconductivity (EUCAS 2003), Sorrento Napoli – Italy, 14–18 September 2003.

[117] M. Bajko, F. Bertinelli, N. Catalan Lasheras, S. Claudet, P. Cruikshank, K. Dahlerup-Petersen, R. Denz, P. Fessia, C. Garion, J. M. Jimenez, G. Kirby, M. Koratzinos, Ph. Lebrun (chair), S. Le Naour, K. H. Mess, M. Modena, V. Montabonnet, R. Nunes, V. Parma, A. Perin, G. de Rijk (scientific secretary), A. Rijllart, L. Rossi, R. Schmidt, A. Siemko, P. Strubin, L. Tavian, H. Thiesen, J. Ph. Tock, E. Todesco, R. Veness, A. Verweij, L. Walckiers, R. van Weelderen, R. Wolf, S. Feher, R. Flora, P. Limon, and J. Strait. “Report of the Task Force on the Incident of 19 September 2008 at the LHC.” LHC Project Report 1168, Geneva, 31 March 2009.

[118] A.Priebe. “Quench Tests of LHC Magnets with Beam: Studies on Beam Loss Development and Determination of Quench Levels.” Ph.D. thesis, École Polytechnique Fédérale de Lausanne, January 2015.

[119] F. Formenti, Z. Charifoulline, G-J Coelingh, K. Dahlerup-Petersen, R. Denz, A. Honma, E. Ravaioli, R. Schmidt, A.P. Siemko, and J. Steckert. “Upgrade

of the Quench Protection Systems for the Superconducting Circuits of the LHC Machine at CERN: from Concept and Design to the First Operational Experience," presented at the International Particle Accelerator Conference (IPAC), pp. MOPD013, Kyoto, Japan, 23–28 May 2010.

[120] A. Stafiniak, E. Floch, C. Schroeder, F. Marzouki, and F. Walter. "The GSI Cryogenic Prototype Test Facility – First Experience Gained on 2-Phase-Flow Superconducting Prototype Magnets of the FAIR Project." *IEEE Transactions on Applied Superconductivity*, vol. 19, no. 3, 2009.

[121] A. Stafiniak, P. Szwangruber, W. Freisleben, and E. Floch. "Electrical Integrity and its Protection for Reliable Operation of Superconducting Machines," in *Proc. of the 25th International Cryogenic Engineering Conference and International Cryogenic Materials Conference 2014 (ICEC 25–ICMC 2014)*, vol. 67, pp. 1106-1111, 2015.

Piotr Szwangruber

☎ +49 157 88976709
☎ +48 790 589 115
✉ p.szwangruber@gmail.com

Experience

09.2013– **Researcher. Since 2016, work package leader SIS100 quench detection/magnet protection**, GSI Helmholtzzentrum für Schwerionenforschung GmbH, Darmstadt, Germany.
Quench calculations. Working on the design of the quench detection and magnet protection systems for SIS100 and Super–FRS. Preparing test programs for magnets in terms of electrical measurements and quench study. Providing quench detection service in the test facilities. Writing technical documentation.

10.2008–07.2010 **Research assistant/lecturer**, Gdańsk University of Technology, Gdańsk, Poland.
Teaching (laboratory training): *electrical measurements*, *diagnostics and monitoring systems*, *security systems*. Research on digital signal processing, i.a. discrete wavelet analysis.

07.2007–09.2007 **Electrician**, CASPA Polska, Gdańsk, Poland.
Installation of a large electrical system in an office building.

07.2006–08.2006 **Military Service**, Communication and Informatics Training Center, Zegrze, Poland.
Basic military training. Specialisation on radio–communication. Promoted to Corporal rank.

Education

2010–2017 **Ph.D. candidate**, Computational Electromagnetics Laboratory TEMF, TU Darmstadt/GSI, Darmstadt, Germany.
Thesis on superconducting magnets, topic: “Quench Study for FAIR magnets” (in English).

2005–2011 **Dipl.-Ing. in Physics**, Faculty of Applied Physics and Mathematics / Gdańsk University of Technology, Gdańsk, Poland, final grade: very good.
Master thesis on “Automation of Residual Magnetization Measurements for Metal Diagnostics Applications.” (in Polish)

2003–2008 **Dipl.-Ing. in Electrical Engineering**, Faculty of Electrical and Control Engineering / Gdańsk University of Technology, Gdańsk, Poland, final grade: very good.
Master thesis on “Wavelet Analysis in Vibration Diagnostics.” (in Polish)

Languages

English	**Fluent** (TOEFL certificate)	German	**Intermediate** (TELC DTZ B1)
Polish	**Native**	Russian	**Beginner**

Computer skills

Programming:	LabVIEW, Matlab, Scilab, C++	Graphics:	Corel Draw, GIMP, MS Visio
Office:	LaTeX, MS Office, Libre Office	Construction:	AutoCAD, Inventor

Publications

Peer–reviewed

[1] A. Stafiniak, P. Szwangruber, W. Freisleben, and E. Floch. "Electrical Integrity and its Protection for Reliable Operation of Superconducting Machines." *Physics Procedia*, vol. 67, pp. 1106-1111, 2015.

[2] A. Bleile, E. Fischer, W. Freisleben, A. Mierau, P. Schnizer, and P. Szwangruber. "Thermodynamic Properties of the Superconducting Dipole Magnet of the SIS100 Synchrotron." *Physics Procedia*, vol. 67, pp. 781-784, 2015.

[3] P. Szwangruber, F. Toral, E. Floch, I. Rodriguez, H. Leibrock, X. Yu, W. Wu, M. Lizhen, W. Wei, X. Zhang, B. Guo, A. Zeller, and T. Weiland. "Quench Calculations and Measurements on the FAIR Super–FRS Dipole." *Physics Procedia*, vol. 36, pp. 872-877, 2012.

Conference Proceedings

[4] M. Michna, A. Wilk, M. Ziółko, M. Wołoszyk, L. Swędrowski, and P. Szwangruber. "Investigation of inter-turn fault in transformer winding using discharge method," in *Proc. 2017 18th International Symposium on Electromagnetic Fields in Mechatronics, Electrical and Electronic Engineering (ISEF)*, Lódź 2017, Book of Abstracts, pp. 1-2.

[5] C. Roux, A. Mierau, A. Bleile, E. Fischer, F. Kaether, B. Körber, P. Schnizer, K. Sugita, and P. Szwangruber. "The optimised sc dipole of SIS100 for series production," in *Proc. IOP Conference Series: Materials Science and Engineering*, vol. 171, no. 1, pp. 012108, 2017.

[6] L. Serio, P. Schnizer, M. Arnaud, C. Bertone, E. Blanco, D. Calcoen, M. Charrondiere, E. J. Cho, G.-J. Coelingh, K. Dahlerup-Petersen, F. Dhalla, R. Denz, J. H. Derking, G. Golluccio, D. Hay, A. Henriques, V. Inglese, A. Kosmicki, V. Mertens, D. Missiaen, H. Mueller, Y. Muttoni, S. Moccia, R. Necca, A. Perin, I. Pschorn, S. Russenschuck, J. Steckert, P. Szwangruber, H. Thiesen, V. Velonas, F. Wamers, G. Willering, and Y. Xiang. "A New Cryogenic Test Facility for Large and Heavy Superconducting Magnets." *IEEE Transactions on Applied Superconductivity*, issue 99, 2016.

[7] P. Schnizer, A. Mierau, A. Bleile, V. Marousov, A. Stafiniak, W. Freisleben, H. Raach, J. P. Meier, K. Sugita, P. Szwangruber, H. Mueller, and E. Fischer. "Low-Temperature Test Capabilities for the Superconducting Magnets of FAIR." *IEEE Transactions on Applied Superconductivity*, vol. 25, issue 3, June 2015.

[8] E. Fischer, P. Schnizer, K. Sugita, J. P. Meier, A. Mierau, A. Bleile, P. Szwangruber, H. Müller, and C. Roux. "Fast-Ramped Superconducting Magnets for FAIR Production Status and First Test Results." *IEEE Transactions on Applied Superconductivity*, vol. 25, issue 3, June 2015.

[9] P. Szwangruber, E. Floch, F. Toral, and T. Weiland. "Three-Dimensional Quench Calculations for the FAIR Super-FRS Main Dipole." *IEEE Transactions on Applied Superconductivity*, vol. 23, issue 3, June 2013.

Scientific Reports

[10] E. Fischer, V. Bezkorovaynyy, A. Bleile, J. Ceballos, E. Floch, W. Freisleben, V. Maroussov, F. Marzouki, H. Müller, J. P. Meier, A. Mierau, H. Raach, P. Schnizer, F. Seifert, A. Stafiniak, K. Sugita, and P. Szwangruber. "Status of the Superconducting Magnets for FAIR." GSI Scientific Report 2014, 2015.

[11] M. Winkler,S. Althoff, F. Amjad, K. Behr, A. Bergmann, T. Blatz, A. Brünle, E. J. Cho, W. Freisleben, H. Geissel, M. Gleim, C. Karagiannis, B. Kindler, H. Kollmus, E. Kozlova, A. Krämer, A. Kratz, J. Kurdal, H. Leibrock, H. Müller, G. Münzenberg, C. Mühle, I. Mukha, C. Nociforo, L. M. Orona, S. Pietri, A. Prochazka, S. Purushotaman, M. V. Ricciardi, C. Scheidenberger, F. Schirru, C. Schlör, P. Schnizer, H Simon, P. Szwangruber, F. Wamers, H. Weick, C. Will, J. Winfield, and Y. Xiang. "Super–FRS Design Status Report." GSI Scientific Report 2014, 2015.

[12] S. Ayet, E. Floch. W. Freisleben, K. Koch, and P. Szwangruber. "Design of a Mutual Inductance Based Quench Detector for the Corrector Magnets of the SIS100." GSI Scientific Report 2013, 2014.

[13] P. Kurilkin, P. Szwangruber, H. Ramakers, E. Floch, and F. Toral. "Quench Detection and Protection System for the CBM Dipole Magnet." GSI Scientific Report 2013, 2014.

[14] P. Kurilkin, P. Szwangruber, E. Floch, F. Toral, A. Malakhow, and V. Ladygin. "Quench Calculation for the CBM Dipole Magnet." GSI Scientific Report 2013, 2014.

[15] E. Fischer, A. Bleile, E. Floch, W. Freisleben, V. Maroussov, F. Marzouki, H. Müller, J. P. Meier, A. Mierau, H. Raach, P. Schnizer, A. Stafiniak, K. Sugita, S. Y. Shim, P. Szwangruber, and D. Theuerkauf. "FAIR Realisation - Superconducting Magnets Production Start." GSI Scientific Report 2012, 2013.

[16] P. Akishin, A. Bychkov, E. Floch, Y. Gusakov, V. Ivanov, P. Kurilkin, V. Ladygin, H. Leibrock, A. Malakhow, G. Moritz, C. Mühle, W. F. J. Müller, W. Niebur, I. Pschorn, P. Senger, P. Szwangruber. Y. Xiang, C. Will, and A. Shabunov. "Superconducting Dipole Magnet for the Compressed Baryonic Matter (CBM) Experiment at FAIR." GSI Scientific Report 2012, 2013.

[17] P. Akishin, A. Bychkov, E. Floch, Y. Gusakov, V. Ivanov, P. Kurilkin, V. Ladygin, H. Leibrock, A. Malakhow, G. Moritz, C. Mühle, W. F. J. Müller, W. Niebur, I. Pschorn, P. Senger, P. Szwangruber. Y. Xiang, C. Will, and A. Shabunov. "Design Calculations for the Superconducting Dipole Magnet for the Compressed Baryonic Matter (CBM) Experiment at FAIR." GSI Scientific Report 2012, 2013.

Other

[18] R. Roskosz and P. Szwangruber. "Magnetic measurements," in *Electrical Measurements – Textbook for Electrical Engineering Students*. Available in Polish only, original tile: "Pomiary wybranych wielkości magnetycznych," in *Metrologia – skrypt do laboratorium dla studentów kierunku elektrotechnika*. Faculty of Electrical and Control Engineering, Gdańsk University of Technology, Gdańsk, 2009.

[19] P. Szwangruber. “Wavelet Analysis in Signal Compression and Denoise.” Available in Polish only, original title: “Wykorzystanie analizy falkowej do odszumiania oraz kompresji sygnałów.” Scientific Report of the Faculty of Electrical and Control Engineering / Gdańsk University of Technology, vol. 26, pp. 109–112, 2009.

Interests

magnetism, analog electronics, cycling, hiking, automotive, aviation

Additional information

Driving license cat. B (2003)

Private pilot license–airplane PPL(A) (2017)

Index